Nanowire Josephson junctions in superconducting circuits

Bargerbos, A.

DOI
10.4233/uuid:efcc21a7-1d28-48bd-be94-be44fc8d5458

Publication date
2023

Document Version
Final published version

Citation (APA)
Bargerbos, A. (2023). *Nanowire Josephson junctions in superconducting circuits*. [Dissertation (TU Delft), Delft University of Technology]. https://doi.org/10.4233/uuid:efcc21a7-1d28-48bd-be94-be44fc8d5458

NANOWIRE JOSEPHSON JUNCTIONS IN SUPERCONDUCTING CIRCUITS

ARNO BARGERBOS

NANOWIRE JOSEPHSON JUNCTIONS IN SUPERCONDUCTING CIRCUITS

NANOWIRE JOSEPHSON JUNCTIONS IN SUPERCONDUCTING CIRCUITS

Proefschrift

ter verkrijging van de graad van doctor
aan de Technische Universiteit Delft,
op gezag van de Rector Magnificus prof. dr. ir. T.H.J.J. van der Hagen,
voorzitter van het College voor Promoties,
in het openbaar te verdedigen op vrijdag 14 april 2023 om 15:00 uur

door

Arno BARGERBOS

Master of Science in Physics
Eidgenössische Technische Hochschule Zürich, Switzerland
geboren te Zoetermeer, Nederland

Dit proefschrift is goedgekeurd door de promotoren.

Samenstelling promotiecommissie:

Rector Magnificus	voorzitter
Dr. M. T. Wimmer	Technische Universiteit Delft, promotor
Dr. C. K. Andersen	Technische Universiteit Delft, copromotor
Onafhankelijke leden:	
Prof. dr. ir. L. DiCarlo	Technische Universiteit Delft
Prof. dr. A. Levy Yeyati	Universidad Autónoma de Madrid
Prof. dr. G. Katsaros	Institute of Science and Technology Austria
Prof. dr. M. Kjaergaard	University of Copenhagen
Prof. dr. G. Steele	Technische Universiteit Delft, reservelid
Overige leden:	
Prof. dr. A. Kou	University of Illinois at Urbana-Champaign

Casimir PhD Series, Delft-Leiden **2023-08**

ISBN **978-90-8593-556-8**

An electronic version of this dissertation is available at
`http://repository.tudelft.nl/`.

CONTENTS

SUMMARY

The Josephson effect is a quintessential topic of condensed matter physics. It has stimulated decades of fundamental research, leading to a plethora of applications from metrology to outer space. In addition, it is set to play a crucial role in the development of quantum computers, forming the dissipationless non-linear inductance that lies at the core of superconducting qubits.

While they are traditionally realized using oxide based tunnel barriers, in this thesis we construct Josephson junctions from non-insulating materials such as semiconducting nanowires and quantum dots. We investigate how their highly nontrivial interplay with superconductivity can lead to new effects, both of fundamental interest and of relevance for quantum applications. To study these effects we make use the exhaustive toolbox available for superconducting circuits, allowing us to probe the junction behavior to beyond what is possible with conventional transport techniques.

The first experimental chapter of this thesis examines the behaviour of a transmon that hosts a highly transparent semiconducting weak-link as the Josephson junction. In this system we find spectroscopic evidence for the predicted vanishing of Coulomb effects in open superconducting islands, in accordance with theoretical predictions from 1999.

In the second experiment we deterministically place a quantum dot inside the junction of a transmon circuit. We then demonstrate that by using microwave spectroscopy we are able to accurately probe the energy-phase relationship of the Josephson junction over a vast regime of parameter space. This reveals the remnants of a quantum phase transition, and allows us to probe the time dynamics of the junction parity.

We subsequently use the same type of device to reveal the predicted spin-splitting of the Andreev bound states in a quantum dot with superconducting leads, as brought about by the spin-orbit interaction. When combined with a magnetic field, this is shown to result in the anomalous Josephson effect. Furthermore, we demonstrate that transitions between the spin-split quantum dot states can be directly driven with microwaves.

This motivated the investigation of a novel superconducting spin qubit, performed in the fourth experiment. Here we demonstrate rapid, all-electric qubit manipulation in addition to detailed coherence characterization. We ultimately show signatures of strong coherent coupling between the superconducting spin qubit and the transmon into which it is embedded, setting the stage for future research of this nascent qubit platform.

In the fifth and final experiment, we utilize a different approach compared to the preceding chapters. While we once-more construct transmons based on semiconducting weak-links, we now do so to leverage the intrinsic magnetic field resilience of semiconducting nanowires. This allows us to use a single device to study the mitigation of phonon-induced quasiparticle losses by trapping the phonons using both super and normal-state conductors.

This thesis concludes by discussing several ideas and proposals that aim to leverage the alternative Josephson junctions studied in this thesis. Combined with the results of the preceding chapters, this shows that hybrid superconducting circuits can be used to obtain deep insights into the fundamental physics governing their constituent junctions, and opens avenues towards building better qubits.

SAMENVATTING

Het Josephson-effect is een paradigmatisch fenomeen uit de vastestoffysica. Het stimuleert al decennia lang fundamenteel onderzoek, en heeft tot toepassingen geleid die reiken van metrologie tot in de ruimte. Bovendien belooft het een cruciale rol te spelen in de ontwikkeling van kwantumcomputers, waarbij het als een dissipatieloze en niet-lineaire spoel fungeert die de kern van supergeleidende qubits vormt.

Hoewel ze traditioneel worden vervaardigd uit op oxide gebaseerde barrières, maken we in dit proefschrift Josephson-juncties van elementen zoals halfgeleidende nanodraden en kwantumdots. We tonen aan dat de complexe interacties van deze systemen met supergeleiding tot nieuwe effecten kunnen leiden die zowel van fundamenteel belang zijn evenals relevant voor kwantumtoepassingen. Om deze effecten te bestuderen maken we bovendien gebruik van het uitgebreide instrumentarium van supergeleidende circuits. Daardoor kunnen we het gedrag van de juncties nauwkeuriger onderzoeken dan mogelijk is met conventionele transporttechnieken.

Het eerste experimentele hoofdstuk van dit proefschrift gaat over het gedrag van een transmon-circuit gevormd uit een zeer transparante, halfgeleidende junctie. In dit systeem vinden we spectroscopisch bewijs voor het verdwijnen van Coulomb-effecten in open supergeleidende eilanden, in overeenstemming met theoretische voorspellingen uit 1999.

In het tweede experiment plaatsten we bewust een kwantumdot binnenin de junctie van een transmon-circuit. Vervolgens hebben we kunnen aantonen dat we met behulp van microgolven de energie-faserelatie van de Josephson-junctie nauwkeurig kunnen onderzoeken. Dit maakt het mogelijk om de restanten van een kwantumfaseovergang te meten, en stelt ons in staat de dynamica van de junctie pariteit te onderzoeken.

We gebruiken hetzelfde type experiment om de voorspelde spin-splitsing van de Andreev-toestanden in een kwantumdot met supergeleidende elektrodes aan te tonen, veroorzaakt door spin-baankoppeling. We laten vervolgens zien dat het zogenaamde anomale Josephson-effect optreedt wanneer dit systeem wordt gecombineerd met een magnetisch veld. Daarnaast tonen we aan dat overgangen tussen de spin-gesplitste kwantumdot-toestanden direct kunnen worden aangestuurd met microgolven.

Dit motiveert het onderzoek naar een nieuwe supergeleidende spin-qubit, uitgevoerd in het vierde experiment. We laten snelle, volledig elektrisch gecontroleerde qubit-manipulatie zien, evenals gedetailleerde karakterisering van de coherentie eigenschappen. Ten slotte tonen we sterke coherente koppeling aan tussen de supergeleidende spin-qubit en de transmon waarin deze zich bevindt. Deze resultaten maken de weg vrij voor toekomstig onderzoek van dit opkomende qubit-platform.

In het vijfde en laatste experiment hebben we een andere benadering gebruikt dan in de voorgaande. We hebben opnieuw transmons gemaakt op basis van halfgeleidende juncties, maar nu om gebruik te maken van de intrinsieke veldbestendigheid van halfgeleidende nanodraden. Dit stelt ons in staat om de vermindering van fonon-geïnduceerde quasideeltjesverliezen te bestuderen, door op dezelfde chip de fononen op te vangen met zowel supergeleidende als normale geleiders.

Dit proefschrift besluit met een bespreking van verschillende ideeën en voorstellen die tot doel hebben de bestudeerde alternatieve Josephson-juncties te benutten. In combinatie met de resultaten van de voorgaande hoofdstukken wordt aangetoond dat hybride supergeleidende circuits gebruikt kunnen worden om dieper inzicht te krijgen in de fundamentele fysica van hun onderliggende juncties, en uiteindelijk om betere qubits te bouwen.

1

INTRODUCTION

> *Where men build on false grounds, the more they build, the greater is the ruin.*
>
> Thomas Hobbes, Leviathan

1.1. PREFACE

The central topic of this thesis is the study of the Josephson effect, which is largely motivated by the plethora of applications the Josephson effect enables. Indeed, it lies at the core of some of the most accurate measurements of the constants of nature, allows for the construction of highly sensitive detectors which find applications from biology to mining and even outer space, and is poised to play a crucial role in the development of quantum computers [40].[1] We will expand on these concepts in the sections that follow.

Before doing so, however, we allow ourselves to wax somewhat poetic and remark that the topic of this thesis is also the study of fundamental physics. This perhaps does not match its traditional interpretation, in which fundamental physics is often seen as the study of the laws of nature obeyed by one, two, or maybe ten elementary particles. Instead, we adopt the point of view argued by Philip W. Anderson, put forward in his celebrated article titled “More is different” [10]. Published in Science in 1972,[2] in a time-period where the largest scientific budgets were reserved for high energy physicists and astronomers, it is an insightful exposition on the nature of fundamental science that remains just as relevant today. The central message is essentially that scientists (and in

---

[1] A quantum computer is a type of computer based on the peculiar features of quantum physics, such as superpositon and entanglement. The core conjecture is that such a device is able to perform tasks that traditional computers cannot efficiently do, because it makes use of a different set of rules. See Ref. [258] by John Preskill for a recent discussion.

[2] In celebration of the 50 year anniversary, Nature recently published a viewpoint in which scientists discuss “emergent phenomena” in their respective fields [305].

particular physicists) tend to conflate reductionism and constructionism. Here reductionism refers to the hypothesis that all matter obeys certain fundamental laws of nature, such as those of electromagnetism and gravity. So far we have no strong reason to believe that this is not the case.[3] Constructionism is the hypothesis that one can start from those fundamental laws and reconstruct the universe. While perhaps theoretically possible, this is practically unfeasible in almost all many-particle scenarios, as modern physics has shown time and again. From the universal frequency response of dielectric materials to the quantized plateaus of the fractional quantum Hall effect, it appears that whenever we change scale (be it temporal or spatial), entirely new properties and phenomena appear. These "emergent phenomena" often require their own novel framework in order to be understood, even though the very same fundamental laws apply to their constituents. This thesis focuses on the study of such an emergent phenomenon, the Josephson effect.

We return to the physics underlying this phenomenon in the next section. Before we do so, we find it instructive to examine a case closer to our everyday life, in which constructionism appears to fail just as spectacularly. Let us start with life itself. Most would agree that a human cell is alive, but that its parts are not. A commonly held belief is then that life is somehow encoded in these parts, such as in the approximately 3×10^9 DNA base pairs that make up the human genome, or perhaps a little more accurately, in the 10^5 or so relevant proteins that they encode.[4] It was once thought that mapping out the genome would provide "the book of life"[230]; not unlike the standard model of particle physics, it was to be a complete blueprint of all we need to explain the higher lying levels of functioning, from calcium pumps to heart rhythms. This is essentially what the human genome project set out to do; one of the largest collaborative biology projects undertaken to date, its goal was to determine all of the base pairs that make up human DNA, and to sequence the entire human genome. The mapping was recently completed,[5] both from a physical and functional standpoint; an unquestionable marvel of molecular biology. But from our everyday lives it is of course evident that the central research questions of human physiology, let alone psychology or sociology, remain unsolved. Instead, the appreciation for the complexity of interactions that form above the protein level has given rise to a whole new field of study. Known as systems biology, it aims to model and understand the emergent properties of biological systems, not unlike how modern condensed matter physics is often centered around the emergent properties of physical systems. This is of course not to say "higher" lying domains do not benefit from research done "below"; certainly genetic testing is invaluable in identifying predispositions to a variety of illnesses, and high energy physics remains as important as ever in furthering our understanding of the universe. The point is, however, that it is all fundamental science. At each level, entirely new laws emerge, for which new concepts and generalizations are required, demanding just as much creativity and hard work. And, as we will see, this process of discovery is not unidirectional. It often even provides novel

---

[3] Eugene Wigner once dubbed the existence of the laws of nature as "one of two miracles", with the other being the human mind's capacity to divine them [336].

[4] The analogy with the fundamental laws of physics is not entirely apt, however, as the genome is not static, while the laws of nature appear to be.

[5] Although it was declared complete already in 2003, the final gapless assembly of the genome was made only last year in January 2022.

insight into the lower lying levels.

1.2. SUPERCONDUCTIVITY

Let us now briefly examine such an emergent phenomenon that lies at the core of this thesis: superconductivity. As we expand on below, superconductivity is a many-body quantum effect that generally takes place in cold metals, and is able to persist even at everyday "macroscopic" length and timescales. It is one of the central examples in Anderson's article; while the phenomenon of vanishing resistivity, one of the hallmarks of superconductivity, was first detected by Heike Kamerlingh Onnes in 1911, Anderson points out that it took until the 1950's for it to be theoretically understood. It was only then that the phenomenological Ginzburg-Landau (GL) theory and the microscopic Bardeen-Cooper-Schrieffer (BCS) theory were formulated, even though the traditionally-fundamental laws of nature required to understand this phenomenon had been put forward by the mid-1920s.[6] Examining how these theories came about is a humbling exposition of how the behavior of a large aggregate of many particles could not be understood as a simple extrapolation of the properties of just a few particles, instead requiring entirely novel ideas and ansatzes.

Succinctly stating what exactly superconductivity entails is somewhat challenging, as it is a phenomenon with many different faces. As put forward (in approximately chronological order) in Ref. [96], superconductivity can be characterized as

- A state of matter that, when cooled below a critical temperature T_c, exhibits perfect conductivity (zero resistance flow of electrical current) as well as perfect diamagnetism (the absence of magnetic permeability). These are among the prime physical observables detected in experiments. The first effect was discovered by Kamerlingh Onnes in 1911, while the second was discovered by Meissner and Ochsenfeld in 1933.

- Almost a Bose-Einstein condensate (BEC) of charged particles. This is how one can interpret the constitutive relations put forward by the London brothers in 1935, as later remarked by older brother Fritz in a discussion on superfluidity [198]. We use the word almost here to emphasize that the effective bosons that give rise to superconductivity are composite particles with a spatial extent of many lattice periods. They are essentially bound in momentum-space rather than in real-space, and are thus not simply combined together into diatomic molecules consisting of two fermions.[7]

- A second order phase transition driven by spontaneous $\mathrm{U}(1) \to \mathbb{Z}_2$ gauge-symmetry breaking. While the implications of this statement are somewhat contentious when taken literally (see Refs. [111, 254] for a detailed discussion), it is a crucial insight that informed both the GL and the BCS theories. Indeed, the first line of the seminal BCS paper states that "the main facts which a

---

[6] With this we do not do justice to the contribution of the London brothers, whose constitutive equations put forward in 1935 offered the first explanation of the perfect diagmagnetism observed by Meissner and Ochsenfeld.

[7] As stated by Bardeen "the idea of paired electrons, though not fully accurate, captures the sense of it." [20]

theory of superconductivity must explain are (1) a second-order phase transition at the critical temperature, . . . ” [21]

- An emergent quantum phenomenon described by a complex order parameter field $\psi(r) = |\psi(r)|e^{i\varphi(r)}$, where the quantity $|\psi(r)|^2$ is a measure of the local density of charge carriers. This is the core of the Ginzburg-Landau theory published in 1950 [103], a phenomenological model which brings together Landau’s theory of second order phase transitions with what Gor’kov later showed to essentially be a macroscopic wavefunction describing the collective many-body state of the superconductor [109].

- A phenomenon where the phonon-mediated attractive interaction known as Cooper pairing transmutes fermionic electrons into a condensate of bosonic pairs, separated from excitations by an energy gap. This is the central idea of the theory of Bardeen, Cooper, and Schrieffer published in 1957 [21]. We examine these concepts in more detail in Sec. 2.1.

- . . . a phenomenon encompassing several more concepts we will not expand on, such as a phase of matter with topological defects known as Abrikosov vortices, an instance of the Anderson-Higgs phenomenon which gives the photon field a mass, or as put forward in recent years, a topologically ordered state of matter in and of itself [117].

Given the above description, which is by no means exhaustive, it is safe to say that superconductivity is a highly complex, fundamental-in-the-Anderson-sense phenomenon that has kept physicists busy for most of the past century. Even today there are still various open questions, in particular with regard to so-called unconventional superconductors, which can display peculiar pairing symmetries and surprisingly large critical temperatures.

1.3. THE JOSEPHSON EFFECT

Ever since their discovery (and indeed even before they were properly understood), superconducting materials have found a plethora of applications. Superconducting magnets, for example, are electromagnets that rely on the fact that superconductors can conduct very large electric currents with negligible heat dissipation, producing some of mankind’s most powerful magnetic fields. They enable a broad range of measurement techniques and apparatuses, from the (almost) everyday MRI machine and the magnetic levitation train to the more traditionally-fundamental fusion reactor and the particle accelerator.

Another broad class of applications results from the effects that occur when two superconductors are brought into close proximity, traditionally separated only by a thin and insulating barrier. Schematically depicted in Fig. 1.1, this system is known as superconductor-insulator-superconductor (SIS) junction or the tunnel junction. It is essentially this geometry that Brian Josephson considered in his seminal work of 1962, in which he put forward the eponymous effect that would later earn him the Nobel prize

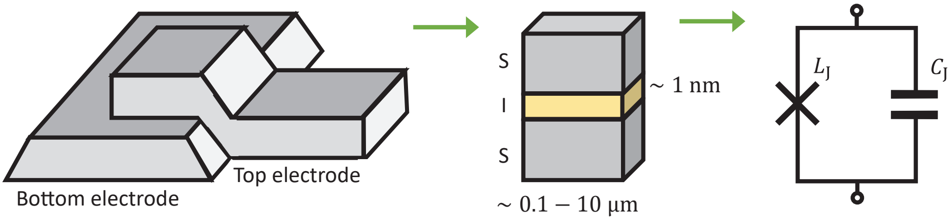

Figure 1.1: The Josephson tunnel junction at different levels of abstraction. At the surface level, the Josephson tunnel junction consists of superconducting bottom and top electrodes separated by a thin oxide layer (not shown), all of which can be a rather disordered collections of grains and boundaries. This is modeled as an idealized, uniform junction, leading to the Josephson relations. At the highest level of abstraction, the junction can then finally be decomposed into an electrical circuit containing the nonlinear Josephson inductance (cross element) in parallel to a linear capacitance. Image adapted from [81].

of 1973 [142].[8] Josephson was originally motivated by finding observable signatures of a type of symmetry breaking he learned about during his lectures on superconductivity by Anderson.[9],[10] As the symmetry breaking related to the phase φ of a superconductor, known to be unobservable in isolation, he postulated that two superconductors brought into close proximity could exchange single electrons via quantum tunneling events in a fashion that would be dependent on the phase difference $\phi = \varphi_1 - \varphi_2$. Instead, what he ended up with was two novel effects governed by the tunneling of *electron pairs*, previously thought to be a process with too small of a probability to be of physical relevance. He derived what became known as the two Josephson equations:

$$I(t) = I_c \sin\big(\phi(t)\big) \tag{1.1}$$

$$V(t) = \frac{\hbar}{2e}\frac{\partial\phi}{\partial t} \tag{1.2}$$

where $V(t)$ and $I(t)$ are the voltage across and current through the Josephson junction, $\hbar$ is the reduced Planck constant, e is the elementary unit of charge, and I_c is known as the critical current, governing the maximal amount of charge that can be transferred per unit of time.[11]

Taking $\phi(t) = \phi$ to be independent of time leads to what what is known as the DC Josephson effect; the voltage across the junction is zero by virtue of the second relation, but the current can still be finite by virtue of the first: $I = I_c \sin\phi$. Counter to intuition, this results in a non-Ohmic and disipationless current of electron pairs flowing across the junction. Known as supercurrent, it is dependent only on the phase difference ϕ, with I_c fixed by choice of materials and geometry. The existence of this effect was ex-

---

[8] This is not an entirely accurate reconstruction; Josephson initially considered a metallic weak link as the junction, but oxide based devices turned out to be easier to realize [251].

[9] Note that the symmetry breaking Josephson had in mind was that found in Anderson's pseudo-spin formulation of BCS theory [8, 251].

[10] We suggest reading Anderson's first-hand account of the discovery, whose reconstruction of Josephson's derivation gives appreciable historic context [9].

[11] When I_c is exceeded, a resistive current instead flows across the junction. For reasons made clear in chapters 2 and 8, this also occurs when the applied voltage exceeds a certain threshold $|eV| \geq |2\Delta|$.

perimentally verified only a year later by Anderson and Rowell, showing that indeed the superconducting phase φ is more than a mathematical curiosity [11].[12]

As implied by the naming convention, there is also an AC Josephson effect. This deals with the case in which a fixed voltage $V(t) = V_{\mathrm{DC}}$ is applied across the junction, which causes the phase difference $\phi(t)$ to vary linearly with time, producing a sinusoidal AC current of amplitude I_{c} and frequency $\frac{2e}{h}V_{\mathrm{DC}}$. The Josephson junction is thus a voltage-to-frequency converter. The inverse also holds: radiation at angular frequency ω incident on the junction can induce quantized DC voltages $V_{DC} = n\frac{\hbar}{2e}\omega$ across the junction, making the Josephson junction a frequency-to-voltage converter. These effects were first verified by Shapiro, also in 1963 [289].

The fact that such constants of nature appear in the behavior of a device involving a very large number of atoms was unique at the time, and has earned the Josephson effect the name of macroscopic quantum phenomenon [81]. After the verification of the Josephson relations, initial thoughts of applications predominantly focused on the AC Josephson effect [9]. As frequency can be defined both accurately and practically through the so-called caesium standard, the AC Josephson effect has since been put to use to provide the standard representation of the volt, a method known as the Josephson voltage standard. When combined with independent measurement of the integer quantum Hall effect, the AC Josephson effect can furthermore be used to accurately determine the value of the elementary charge e.[13] This essentially provides a corollary to Anderson's argument: macroscopic phenomena can provide highly accurate details of the fundamental constants of nature.

In this thesis, however, we primarily concern ourselves with the DC Josephson effect, which also has a plethora of applications. One such application is in superconducting quantum interference devices (SQUIDs), which contain one or multiple Josephson junctions in a loop. Enabled by the connection between the allowed values of the phase difference ϕ and screening currents, these devices transduce flux to current, and form some of the most sensitive magnetic field detectors available.[14] Such SQUIDs will also make an appearance throughout this thesis, albeit for a different purpose. However, the main application of the DC Josephson effect employed in this thesis is its recasting as a dissipation-free, nonlinear inductance.[15] To understand why such a recasting can be done, we recall that an inductance L is defined through its constitutive relation as $V = L\frac{dI}{dt}$. By manipulating the Josephson equations, one can show that they result in

$$V = \frac{\hbar}{2eI_{\mathrm{c}}\cos\left(\phi\right)}\frac{\partial I}{\partial t} \rightarrow L(\phi) = \frac{\hbar}{2eI_{\mathrm{c}}\cos(\phi)}. \tag{1.3}$$

We emphasize that the analogy to a traditional inductor does not mean that in a Josephson junction energy is stored in a magnetic field, however. It is instead stored in the

---

[12] Note that phase-dependent supercurrents had likely already been experimentally observed in 1960 by Giaever [101] as well as by Nicol, Shapiro, and Smith [229], however the authors had not recognized them as such.

[13] The AC Josephson effect is proportional to $2e/h$, while the integer quantum hall effect results in resistance proportional to h/e^2.

[14] Implicit in this relation between phase and flux is the somewhat technical gauge-invariant nature of ϕ, for which we refer to e.g. Ref. [81].

[15] Tunnel junctions typically also include a linear capacitance in parallel to the nonlinear inductance.

kinetic energy of the electron pairs, and is given by

$$E(\phi) = -\frac{\hbar I_{\mathrm{c}}}{2e}\cos\phi = -E_{\mathrm{J}}\cos\phi, \tag{1.4}$$

where E_{J} is known as the Josephson energy, a characteristic energy scale we will frequently return to.[16]

The fact that both the effective inductance and energy are non-linear functions of ϕ can have profound consequences. For example, if one were to create an effective LC circuit containing such a nonlinear inductor, the resulting energy spectrum is not that of the constant-spacing harmonic oscillator. Instead, it forms a non-linear ladder of levels that can be used to encode quantum bits, or qubits, the constituent elements of a quantum computer. In passing we further remark that implicit in such a circuit description is that we can (and must) treat ϕ not as a classical but as a quantum mechanical variable. This rather profound subject was discussed by Anderson already in 1964 [7]. He put forward that since the superconducting phase is essentially the sum of the phases of all individual electrons in the condensate, it must therefore also be conjugate to the electric charge of the condensed particles.

The specific implementation of a Josephson junction-based nonlinear LC oscillator is colloquially known as the transmon [162], and it is discussed in detail in Sec. 2.4. It has been a highly popular topic of research for the past two decades, filling numerous PhD theses, and has given rise to some of the most advanced quantum computing devices made to date [13, 133]. The construction of transmons out of Josephson junctions is in fact also the main research methodology of this thesis. However, this is not with the (immediate) goal of building a well-performing qubit, with long lifetimes and high gate fidelities. Rather than using the established properties of the SIS junction to build highly coherent and predictable qubits, we invert the construction; we use the exhaustive toolbox available for transmon measurements to probe the behavior of alternative Josephson junctions, embedded within the qubits. These junctions are based on barriers made out of non-insulating materials, such as semiconducting nanowires and quantum dots. Their highly nontrivial interplay with superconductivity is predicted to lead to new effects distinct from those of SIS junctions, expected to be both of fundamental interest and relevant for various quantum computing applications.

We finally note that Josephson junctions based on semiconducting nanostructures can and have previously been studied without transmons, e.g. using low-frequency transport techniques. While such techniques have proven to be invaluable for initial exploration, their resolving abilities are typically limited to timescales of many milliseconds (a result of $1/f$ noise), as well as to energy scales of several μeV (bounded by thermal fluctuations of size $k_{\mathrm{B}}T$). They are therefore unsuitable for validation of a range of predicted phenomena, particularly when rapid dynamics of the junction are involved. It is in these scenarios that the value of the transmon is most clear; through decades of research, its circuit parameters can be engineered with percent-level accuracy, the transition frequencies can be probed down to neV-level accuracy[17], and

---

[16] The physically equivalent expression $E(\phi) = E_{\mathrm{J}}\left(1-\cos\phi\right)$ is often employed as well.

[17] In this thesis we will often use energy and frequency interchangeably, as implied by the Planck relation $E = hf$.

the state of the system can be manipulated and read out on nanosecond timescales. And ultimately, because the conventional Josephson effect is such a well-understood and thoroughly studied phenomenon, any deviation from SIS-like behaviour can be readily quantified.

1.4. THESIS OUTLINE

We now provide an outline for the remainder of this thesis.

- **Chapter 2** reviews the theoretical concepts pertinent to the experiments performed: superconducing islands, Andreev bound states in semiconducting weak-links, quantum dots with superconducting leads, and finally transmons.

- **Chapter 3** discusses the details of the material platform used to host our Josephson junctions: InAs-Al nanowires. We furthermore discuss the nanofabrication of the samples measured in this thesis, and specify details regarding the experimental setup, such as nuances in cryogenics and shielding.

- **Chapter 4** contains our results on a transmon that hosts a highly transparent semiconducting weak-link as the Josephson junction. In this system we probe and resolve the predicted vanishing of Coulomb effects in superconducting islands as the junction transparency approaches unity, in accordance with theoretical predictions from 1999.

- **Chapter 5** demonstrates how a SQUID-based transmon is able to accurately probe the energy-phase relationship of quantum dots with superconducting leads. This reveals the finite temperature remnants of a quantum phase transition, which is explored over a vast range of device parameters and found to be in agreement with numerical calculations. We furthermore probe the time dynamics of the junction parity across the phase transition.

- **Chapter 6** uses the same techniques as chapter 5 to study the predicted spin-splitting of the Andreev bound states in a quantum dot with superconducting leads, as brought about by spin-orbit interaction. When combined with a magnetic field, this is shown to result in the anomalous Josephson effect, for which supercurrent can flow even in the absence of a phase difference, i.e. at $\phi = 0$. Furthermore, we demonstrate that direct transitions between the spin-split quantum dot states can be driven with microwaves, motivating the investigation of a novel superconducting spin qubit.

- **Chapter 7** details the investigation of the aforementioned superconducting spin qubit. We read out its state by embedding it in the junction of a transmon, and demonstrate rapid, all-electric qubit manipulation in addition to detailed coherence characterization. We ultimately show signatures of strong coherent coupling between the superconducting spin qubit and the transmon into which it is embedded.

- **Chapter 8** utilizes a different approach compared to the preceding chapters. Here we once-more construct transmons based on semiconducting weak-links, but this time not to probe the properties of the junction. Instead, we leverage the intrinsic magnetic field resilience of semiconducting nanowires to study the mitigation of phonon-induced quasiparticle losses by trapping the phonons using both super and normal-state conductors.

- **Chapter** 9 contains reflections on the results of each chapter, and additionally puts forward several ideas and proposals that aim to leverage the alternative Josephson junctions studied in this thesis. This is both with the goal of gaining deeper insight into the physics governing the constituent materials, as well as to build better qubits.

2

THEORY

Nothing new comes out of rigor, and in fact, we cannot recall a single great theory in physics which is rigorous.

Condensed Matter Theory Center, Twitter

Throughout this thesis various theoretical concepts come together, from superconductivity to Coulomb repulsion, and from Andreev bound states to quantum information processing. Each of these topics is (at the bare minimum) deserving of its own thesis, and in fact, has already been extensively reported on. Instead, the novelty of our work lies in the experimental examination of the combination of these topics, as detailed in the next chapters. In this chapter we therefore repeat only the pertinent theoretical concepts and ideas, explicitly referring the reader to other works for derivations and more elaborate discussion.

2.1. SUPERCONDUCTING ISLANDS

In the theses of experimental PhD candidates that study topics similar to those discussed in this work, an introduction to the theory of superconductivity tends to start by considering electrons freely propagating as plane waves, present in an ideal and translationally-invariant medium. In this case the electron spectrum is continuous, and the density of states is a function of energy. The theses by Breathau [43] and Hays [121] are excellent expositions that take this approach, which we recommend reading. Foreshadowing a connection to the sections that come later, however, we will instead follow the example of a recent review by Glazman and Catelani [105], which studies superconductivity in a confined medium. This is the guiding reference of this section, and should be referred to for detailed derivations.

As in their work, we start by considering electrons confined to some large (in units of Fermi wavelength), galvanically isolated box: an island. On such an island, confinement to the box renders the electron spectrum discrete, albeit closely-spaced. Indeed, the islands studied in this thesis are generally large enough that the spacing is a small energy scale, $\delta\epsilon \sim 1\,\mu\mathrm{K} \ll k_{\mathrm{B}}T$, even at millikelvin temperatures. Furthermore, in the absence of magnetic effects, we make the assumption that each of these discrete levels is doubly-degenerate, formed by a pair of spin-up and spin-down electrons.[1] The Hamiltonian for such an island then takes on the generic, second-quantized form

$$H = \sum_{n,\sigma=\uparrow,\downarrow} \xi_n c^\dagger_{n\sigma} c_{n\sigma} + H_{\mathrm{int}} \tag{2.1}$$

where the operators $c^\dagger_{n\sigma}$ and $c_{n\sigma}$ create and annihilate electrons with spin σ and energy ξ_n, as measured from the Fermi level. In turn, H_{int} governs the interactions between these electrons. Although various interactions can be taken into account, for our purposes it will be sufficient to consider two primary contributions. First, the electrostatic potential arising from the distribution of charge carriers endows the island with a charging energy E_{c}, the electrostatic cost of adding an additional electron to the island. Second, we incorporate the phenomena of superconductivity by including an attractive interaction between electrons of opposite spin and energies that are within some range $|\xi_n| < \hbar\omega_{\mathrm{D}}$. While the underlying mechanism is not crucial for the derivation, such an interaction is typcally phonon-mediated, with ω_{D} is of the order of the materials' Debye frequency. This is the basis of the Bardeen-Cooper-Schrieffer (BCS) theory of superconductivity, briefly touched upon in Sec. 1.2. Under these assumptions, the interaction term takes the form

$$H_{\mathrm{int}} = E_{\mathrm{c}} \left(N^e - N_{\mathrm{g}}\right)^2 + (\lambda\delta\epsilon)\, O^\dagger O. \tag{2.2}$$

Here $N^e = \sum_{n,\sigma} c^\dagger_{n\sigma} c_{n\sigma}$ is the number operator counting the number of electrons on the island, and N_{g} is a polarization charge, which for an isolated island only affects the value from which the energies are measured. In turn, λ is a dimensionless interaction constant, while the operator $O = \sum_{|\xi_n|<\hbar\omega_{\mathrm{D}}} c_{n\downarrow} c_{n\uparrow}$ captures the salient features of BCS super-

---

[1] Additional accidental degeneracies between levels can be removed by considering scattering with randomly-placed non-magnetic impurities on the island [105]. The fact that superconductivity is robust with respect to such impurities is known as Anderson's theorem.

conductivity.[2] Indeed, the term $O^\dagger O$ is the counterpart of the BCS interaction term that is typically written in the basis of plane waves. It describes an attractive interaction that couples spin-singlet pairs of electrons to $\sim \hbar\omega_{\mathrm{D}}/\delta\epsilon$ of other pairs, which is typically a very large number.

The fact that such a large number of pairs is coupled to one-another suggests that there will be non-negligible correlations between the electrons. While it is a notion of appreciable subtlety,[3] this motivates applying a mean-field treatment to simplify the quartic-in-c-operators Hamiltonian of Eq. (2.2) such that one can then study e.g. its ground-state properties. To do so, we examine Eqs. (2.1) and (2.2) for a fixed, even number of electrons N^e, so that the charging energy results in a constant offset which for now can be ignored. In a procedure that is essentially equivalent to that employed for a bulk superconductor, we substitute in the average

$$\Delta = (\lambda\delta\epsilon)\langle O\rangle = (\lambda\delta\epsilon)\sum_{|\xi_m|<\hbar\omega_{\mathrm{D}}}\langle c_{m\downarrow}c_{m\uparrow}\rangle \tag{2.3}$$

while omitting small fluctuations around this average, resulting in a Hamiltonian that is bilinear in electron operators rather than quartic:

$$H_{\mathrm{BCS}} = \sum_{n,\sigma}\xi_n c^\dagger_{n\sigma}c_{n\sigma} + \Delta^*\sum_{|\xi_m|<\hbar\omega_{\mathrm{D}}} c_{m\downarrow}c_{m\uparrow} + \Delta\sum_{|\xi_m|<\hbar\omega_{\mathrm{D}}} c^\dagger_{m\uparrow}c^\dagger_{m\downarrow} + \mathrm{const.} \tag{2.4}$$

Here $\Delta = |\Delta|e^{i\varphi}$ is a complex-valued quantity that can evaluated self-consistently after diagonalizing the Hamiltonian. The latter step proceeds via the celebrated Bogoliubov transformation

$$c_{n\uparrow} = u_n^*\gamma_{n\uparrow} + v_n\gamma^\dagger_{n\downarrow} \tag{2.5}$$

$$c_{n\downarrow} = -v_n^*\gamma_{n\uparrow} + u_n\gamma^\dagger_{n\downarrow} \tag{2.6}$$

where $\gamma^\dagger_{n\sigma}$ and $\gamma_{n\sigma}$ are creation and annihilation operators for Bogoliubov quasiparticles.[4] The result is that the Hamiltonian of Eq. (2.4) is transformed into a Hamiltonian for quasiparticle excitations:

$$H_{\mathrm{BCS}} \to H_{\mathrm{qp}} = \sum_{n,\sigma}\epsilon_n\gamma^\dagger_{n\sigma}\gamma_{n\sigma}. \tag{2.7}$$

Here $\epsilon_n = \sqrt{\xi_n^2 + |\Delta|^2}$ is the quasiparticle excitation energy. It is separated from the Fermi level by an energy gap of at least $|\Delta|$, such that $|\Delta|$ is often referred to as the superconducting gap. We further note that both the ground-state energy and the excitation spectrum are independent of φ.[5]

---

[2] In this thesis we generally do not make use of the notation where quantum operators such as O are written with hats as $\hat{O}$; the particular meanings of the symbols are intended to be clear from context.

[3] Much discussion arises from the fact that the mean-field treatment only approximately conserves the number of electrons. For a more intricate derivation that nevertheless conserves electron number throughout, we have been advised to refer to the textbook by Leggett [189].

[4] While various quasiparticles exist in condensed matter physics, these Bogolyubov quasiparticles are the ones we will refer to when we talk about quasiparticles throughout this thesis.

[5] At this stage the physical relevance of the φ degree of freedom is not obvious. As we treat in the next section, we require a second island to have a reference for the phase as well as a Josephson junction between both superconductors in order to physically detect a relative difference in the phases. This is somewhat like the difference between the concept of a voltage and a voltage-drop.

We point out that the diagonlization procedure described above also fixes the magnitude of Bogolyubov coefficients u_n and v_n; governed by the canonical (anti)commutation relations of the electron operators, their magnitudes are constrained to obey $|v_n|^2 = 1-|u_n|^2 = \frac{1}{2}\left(1-\frac{\xi_n}{\epsilon_n}\right)$. In turn, their phase depends on the phase of Δ, for which one can take $u_n = u_n^*$ and $v_n = |v_n|e^{i\varphi}$ for convenience. With this in mind, inverting Eq. (2.5) is also instructive: these relations imply that a quasiparticle excitation is not simply a charge eigenstate, but rather an energy-dependent, coherent superposition of both electron creation and annihilation operators. In other words, a quasiparticle is a superposition of both electrons and holes, and for $\xi_n = 0$ this is an equal superposition. This remarkable "particle-hole coherence" property of superconductors is essentially what underlies the microscopic description of the Josephson effect, which is discussed in the next section.

We now examine the ground state of Eq. (2.4), for which we adopt what is known as the excitation picture of superconductivity; the ground state is the zero-energy state defined by the condition $\gamma_{n\sigma}|\psi\rangle = 0$, i.e. it is the state devoid of quasiparticle excitations.[6] It can be shown that this condition is satisfied by the celebrated BCS wave function

$$|\psi_\varphi\rangle = \prod_n \left(u_n + v_n c^\dagger_{n\uparrow} c^\dagger_{n\downarrow}\right)|0\rangle\,, \tag{2.8}$$

where $|0\rangle$ is the vacuum of electronic excitations, and the subscript φ is there to remind us that the coefficients u and v depend on the phase of Δ. While this state is devoid of quasiparticles, it is not empty; indeed, upon closer inspection we see that this equation describes a large ensemble of levels combined in a coherent superposition of $|0\rangle$ and $|2\rangle$ states.

The attentive reader will note that such a state constitutes a violation of the superselection rule for charge, or alternatively, that the number of electron pairs on the galvanically isolated island is not well-defined. This can be construed as problematic, given that in principle we should be able to count the number of charges on the isolated island both before and after the normal-to-superconducting phase transition. As such, the BCS wavefunction does not offer an entirely physical description of a superconducting island. It remains widely useful however, given that exact particle-number conservation is often not crucial for macroscopic samples. Nevertheless, if one desires to remedy this situation we can make use of the fact that both the ground state energy and the excitation spectrum are independent of φ, so that we can construct a new state which is a linear combination of $|\psi_\varphi\rangle$ states; known as the Anderson projection, this state is given by

$$|\psi_N\rangle = \int_0^{2\pi} \frac{d\varphi}{2\pi} e^{-iN\varphi}|\psi_\varphi\rangle\,. \tag{2.9}$$

This state does correspond to a definite number of electron pairs N, which from now on we will refer to as *Cooper pairs*, for it was Cooper that first envisioned them [63]. This state then constitutes our approximation to the ground state of Eq. (2.4), a valid description for islands with a small level spacing.

Even if the φ representation is nonphysical for an isolated island, it remains a highly convenient tool even for a different reason than approximate validity for macroscopic

---

[6] We return to a different picture of superconductivity, known as the one-particle picture, in the next section.

samples. Indeed, the $|\psi_\varphi\rangle$ and $|\psi_N\rangle$ wavefunctions essentially form two bases in the Hilbert space of Cooper pairs, such that the N and φ representations are dual, similar to position and momentum in single-particle mechanics.[7] The related operators satisfy the canonical commutation relation $\left[N, e^{-i\varphi}\right] = e^{-i\varphi}$, which will be of importance when we connect several islands together.[8]

Before we move on, we first examine a re-introduction of electrostatic interactions into the quasiparticle Hamiltonian. In principle this can lead to a complex interplay between superconductivity and Coulomb effects, a topic that has recently regained experimental and theoretical interest [239, 271]. However, at the surface level intuition can already be gained by simply adding back the charging energy term to Eq. (2.7) and making the assumption that an even occupation of the island always corresponds to zero quasiparticle excitations, with all electrons paired up into Cooper pairs. In turn, we assume that odd occupation corresponds to a single, non-interacting quasiparticle which has the minimal excitation energy $\epsilon = |\Delta|$. This allows us to write down a minimal Hamiltonian that captures the salient features of several of our experiments:

$$H_{\mathrm{isl}} = E_{\mathrm{c}}\left(N^e - N_{\mathrm{g}}\right)^2 + \begin{cases} 0 & \text{even} \\ |\Delta| & \text{odd}. \end{cases} \tag{2.10}$$

The energy spectrum of this Hamiltonian for different electron occupations is shown in Fig. 2.1, both for the case $|\Delta| > E_{\mathrm{c}}$ (panel a) and $|\Delta| < E_{\mathrm{c}}$ (panel b). As the islands studied in this thesis all fall firmly into the former range, with $\frac{|\Delta|}{E_{\mathrm{c}}} \gg 1$ and often even exceeding 100, the figure illustrates that the ground state of the system should always corresponds to an even number of electrons, for any N_{g}.

In principle this situation is relaxed at finite temperatures, where ionization of Cooper pairs results in a higher number of quasiparticles on the island. This effect can be quantified through the partition functions of even and odd electron occupation [105], which govern the ratio x_{qp}, denoting the ratio between the density of quasiparticles and the density of Cooper pairs on the island

$$x_{\mathrm{qp}} = \sqrt{2\pi T/|\Delta|}\exp\left(-|\Delta|/T\right). \tag{2.11}$$

The actual *number* of quasiparticles on the island is then an increasing function of the volume of the island. However, this number is still expected to be very small for the devices studied in this thesis, given that we operate them at cryogenic temperatures of tens of mK (see Sec. 3.3). For example, for an aluminium island of volume $10^{-2}\,\mu\mathrm{m}^3$ one expects $x_{\mathrm{qp}} \sim 10^{-23}$ at $T = 40\,\mathrm{mK}$ [105]. In stark contrast to this, experiments on superconducting islands (including our own) tend to find x_{qp} in the range 10^{-7} to 10^{-5}, corresponding to an effective temperature in the range 120 to 210 mK [285]. Yet recent measurements that probe the energy distribution of these quasiparticles has made it clear that this excess density cannot simply be explained by poor thermalization of the devices [287]. It must rather be of a different, non-thermal origin, primary candidates

---

[7] A difference with the position and momentum space representation is that $\varphi \in [0, 2\pi)$ is a compact variable, rendering N discrete.

[8] This is an instance where leaving out the hat notation leads to ambiguity, as the result of a commutator can be a number rather than an operator. For clarity, $\left[\hat{N}, e^{-i\hat{\varphi}}\right] = e^{-i\hat{\varphi}}$.

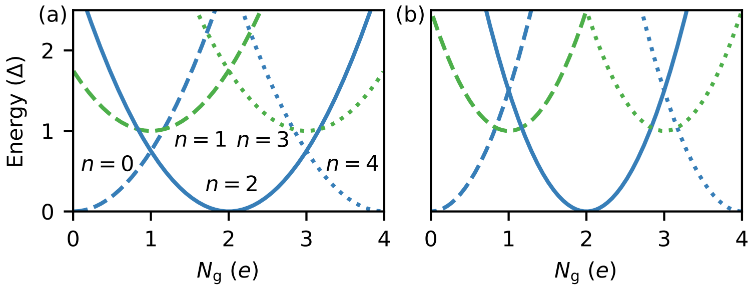

Figure 2.1: Energy versus induced charge of a superconducting island. Panel (a) shows the case of $E_c = 0.75|\Delta|$, panel (b) shows the case of $E_c = 1.5|\Delta|$. Blue colors indicate even island parity, green colors indicate odd island parity. Note that the number of charges n are labeled up to an even offset.

for which are ionizing events due to cosmic rays and ambient radioactivity [214], as well as photon-assisted tunneling events due to stray infrared radiation coming down the control lines [286]. There is much recent interest in the elucidation and mitigation of these mechanisms, which primarily stems from the fact that excess quasiparticles can induce dissipation and thereby limit qubit coherence.[9] In particular, the mitigation of increased quasiparticle densities following cosmic ray impacts is the primary topic of chapter 8.

CONNECTING THE ISLANDS

Once-more following [105], we now consider what happens when two superconducting islands are connected together using a coupling element that allows Cooper pairs to move from one island to the next. Such a coupling element has already been discussed in chapter 1, and in fact is part of the title of this thesis; this is the Josephson junction. In what follows we provide a brief phenomenological motivation for its constituent relations, while we perform a microscopic examination in the next section.

Following the notation established above, a generic process that moves charges between two superconducting islands at energies below $|\Delta|$ cannot make use of quasiparticle excitations. It must instead do so via transfer of the Cooper pairs that make up the ground state, and thus takes on the general form [105]

$$H_\mathrm{J} = \sum_{n=1}^{\infty} \left(C_n T_\mathrm{R}^{\dagger n} T_\mathrm{L}^{n} + C_n^* T_\mathrm{L}^{\dagger n} T_\mathrm{R}^{n} \right) + \mathrm{const.} \tag{2.12}$$

Here each term in the sum corresponds to the transfer of n Cooper pairs, mediated by the operator $T_\mathrm{L,R} = \sum_N |N+1\rangle\langle N|$ which increases the number of Cooper pairs N on the corresponding island by one. C_n is then the complex-valued coefficient for this process. For now we will assume to be dealing with a weak coupling element, such that only terms of order $n = 1$ have a significant contribution. Furthermore, we assume that the coupling element to obeys time-reversal symmetry, which enforces $C_n = C_n^*$. Using the conjugate relationship between N and φ, one can furthermore show that $T_j = e^{-i\varphi_j}$ [105]. When

---

[9] As long as quasiparticles do not tunnel between different islands, their presence generally does not affect the dynamics of the qubit degree of freedom [105].

combined, we obtain the phase basis representation of the (simplified) coupling Hamiltonian:

$$H_{\mathrm{J}} = -E_{\mathrm{J}} \cos\phi + \mathrm{const}, \tag{2.13}$$

where $\phi = \varphi_{\mathrm{R}} - \varphi_{\mathrm{L}}$, and $E_{\mathrm{J}} = -C_1$ is the Josephson energy. Here the sign is motivated by considering that at $\phi = 0$ connecting the islands constrains the motion of Cooper pairs less than on isolated islands, so that the transfer term should reduce the ground state energy of the system. We thus see that by connecting the islands and enforcing the innate relationship between ϕ and N we have recovered the SIS Josephson junction behaviour discussed in chapter 1.

2.2. ANDREEV BOUND STATES

Having discussed a motivation in terms of the allowed tunneling events, we now examine the microscopic origin of the Josephson effect. That this is nontrivial might not be obvious at first sight; for the case of a very thin oxide separating two superconductors (as considered in chapter 1) one can argue that Cooper pair transfer simply proceeds via direct quantum tunneling.[10] However, this type of reasoning cannot hold for every type of Josephson junction, which exist in various different sandwiches of the type superconductor-X-superconductor. Here X does not have to be thin nor insulating; it can for example be a normal metal, a semiconductor, or even a spinful quantum dot. We refer the reader to Ref. [108] by Golubov et al. for a an elaborate review of a plethora of different junctions, but in what follows we restrict ourselves to the aforementioned types.

Given that each of these materials X can impart their own properties on the Josephson effect, one might instead worry that a unified microscopic description is simply not feasible. What is common across various junctions, however, is that much of their properties can be recast as a spatial variation in Δ, and in turn, a variation in the Bogolyubov amplitudes u_n and v_n [276]. The latter implies that the electron-hole character of quasiparticles is modified in the vicinity of the junction. As we show below, this generally gives rise to a special kind of reflection at the junction's interfaces. Known as Andreev reflection, it leads to the formation of Andreev bound states, and ultimately to the Josephson effect. We motivate this below; for their description we refer to the theses of Bretheau [43] and Hays [121], which contain extensive calculations and derivations using what is known as the Bogoliubov-de Gennes formalism for inhomogeneous superconductors.[11]

To illustrate of Andreev bound states, we first consider a junction of the superconductor-normal metal-superconductor (SNS) type. The problem is then essentially that of particles (electrons and holes) confined in a normal-state metallic box with superconducting walls. As before, this confinement renders the energy spectrum discrete, while the energy levels themselves can be found e.g. by enforcing that the wavefunctions (and their derivatives) of the particles match what is imposed by the boundary conditions.

---

[10] We note that the direct tunneling of a Cooper pair is still of appreciable subtlety, as one has to realize that the wave-functions of the electrons in the pair are phase-coherent. The electrons thus do not tunnel independently, but rather as if they were single particle, so that the tunneling probability is comparable to that of a single electron [251].

[11] The recent thesis of Metzger also contains a wealth of information on these topics, but was not yet available at the time of writing [220].

What sets this box apart is the type of boundary condition imposed by a superconductor. Take a rightward traveling electron with an energy smaller than $|\Delta|$, which imparts on the normal-superconducting interface on one side of the box. As it does not have have enough energy to enter the superconductor, it must be reflected backwards. However, rather than reflecting specularly from a right-moving electron into a left-moving electron, it can instead undergo “branch conversion scattering”; better known as Andreev reflection (AR), the right-moving electron becomes a left-moving hole. As electrons and holes carry opposite charge, this has important ramifications: the Andreev reflection of an electron into a hole is additionally accompanied by the creation of a Cooper pair in the superconductor. This process is schematically depicted in Fig. 2.2(a).

The figure furthermore illustrates how multiple of such Andreev reflections can together give rise to the Josephson effect. When the resulting hole has traversed the junction in the opposite direction the reverse process can take place, where the hole Andreev reflects into an electron. This removes a Cooper pair in the other superconductor, and one cycle of these events thus transfers a Cooper pair between the superconductors.[12] It is constructive interference of many of these cycles that leads to the formation of the aforementioned ABS; spatially localized near the Josephson junction, they are the states that are ultimately responsible for carrying the supercurrent of the DC Josephson effect.

Up to now we have only considered Andreev reflection at the normal-superconducting interface, but the properties of the normal metal and the quality of the interface also impact the Andreev bound states. To simplify matters, we consider junctions that are short compared to the superconducting coherence length, so that the properties of the metal have no appreciable contribution. This is known as the short junction limit.[13] We do allow for the junction and its interfaces to have some degree of disorder, such that electrons (holes) moving to the right can also scatter into electrons (holes) moving to the

---

[12] we note that at $\phi = 0$ a time-reversed trajectory of Cooper pair transfer exists, such that there is no net current, in line with Eq. (1.3).

[13] A description of long SNS junctions is beyond the scope of this thesis, for which we refer the reader to Refs. [121] and [220].

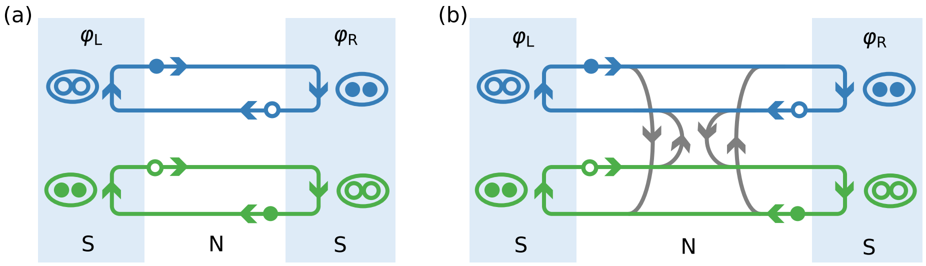

Figure 2.2: Andreev bound state formation in an SNS junction without (a) and with (b) scattering. Each panel depicts two loops of Cooper pair transfer mediated by electrons and holes, made possible by Andreev reflection. The top (bottom) loop shows right-moving (left-moving) electrons. Panel (b) additionally includes the effect of scattering in the normal section (gray arrows), coupling left and right-moving electrons as well as left and right-moving holes. The image adapted from Ref. [121], and we additionally note that the colors used in this figure do not imply a connection to the figures that come before or after.

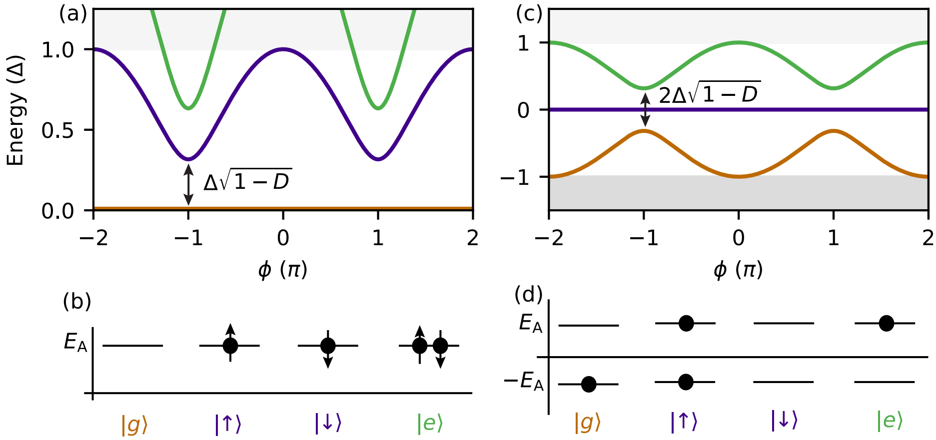

Figure 2.3: Andreev bound state energy spectra in the excitation picture (a) and in the one-particle picture (c). ABS levels are evaluated for $D = 0.9$. (b,d) Junction occupation diagram in the excitation (b) and one-particle (d) pictures, showing the even ground state $|g\rangle$ (orange), the spin-degenerate odd excited states $|\uparrow,\downarrow\rangle$ (purple), and the even excited state $|e\rangle$ (green). Note that in the latter the $|\uparrow,\downarrow\rangle$ designation is arbitrary.

left, without transferring a Cooper pair.[14] This is schematically depicted in Fig. 2.2(b). Mathematically, this scenario is well-described by assigning the transmission process a certain tunneling amplitude t, or a junction transparency $D = |t|^2$. Under these assumptions, one finds that the interference process of multiple reflections gives rise to two spin-degenerate Andreev bound states, with their excitation energy given by [26]

$$E_A^e = |\Delta|\sqrt{1 - D\sin^2\left(\phi/2\right)}. \tag{2.14}$$

The resulting energy spectrum is shown in Fig. 2.3(a), from which we see that for finite ϕ, populating an Andreev bound state in the junction has an energy cost that can be lower than $|\Delta|$. Indeed, for $D = 1$ this energy cost even goes down to 0 at $\phi = \pi$, at which point there is no longer an energy cost associated with a quasiparticle excitation. Andreev bound states are therefore also known as *subgap states*, a concept we will encounter again in Sec. 2.3.

We furthermore note that, given that there are two spin-degenerate ABS, one can consider up to four different junction occupations; see Fig. 2.3(b). There are the states occupied by zero or two quasiparticles, which have an even parity of quasiparticles and no net spin, and are therefore known as singlet states. In addition, there are also two degenerate states with an odd parity and spin-1/2, known as doublet states. As proposed in Refs. [59, 234, 348] and experimentally probed in [122, 123, 136], one can therefore build qubits out of both the singlet and doublet subspaces.

---

[14] Specular reflection might also take place in the absence of disorder if the chemical potential of the junction is smaller than $|\Delta|$; this is known as a violation of the Andreev approximation [300].

PICTURES OF SUPERCONDUCTIVITY

At this stage we make a subtle but important remark. As touched upon in the previous section, we have thus far employed what is known as the excitation picture of superconductivity. We defined the ground state to be the vacuum state devoid of excitations, formed by a large coherent superposition of $|0\rangle$ and $|2\rangle$ states on top of which Bogolyubov quasiparticles can be added. This is a useful description when one wants to emphasize the spinful nature of these excitations, as done above. However, such a picture obfuscates any potential parameter dependence of e.g. the ground state energy, which is essentially taken to be a constant energy reference. While this procedure has little impact for the case of e.g. an isolated superconducting island, it is of consequence for the case of Andreev bound states.

To see this, we change our frame of reference to that known as the one-particle picture of superconductivity. Similar to the method often employed for the free electron gas or for Fermi liquids, in this picture one defines the ground state to be a highly excited "sea" of quasiparticle states, here occupied up to an energy $-|\Delta|$ below the Fermi energy (for which we take $E=0$). In this formalism one defines separate fermion operators that act on states above or below the Fermi level, a procedure which removes the spin-degeneracy of positive-energy excitations and instead results in particle-hole symmetry; each state with energy E has a counter-part at energy $-E$. Within this picture, the Andreev spectrum is thus instead given by [26]

$$E_{\mathrm{A}}^{s} = \pm|\Delta|\sqrt{1-D\sin^2\left(\phi/2\right)}, \tag{2.15}$$

which is depicted in Fig. 2.3(c). In contrast to the excitation picture, the ground state now corresponds to a quasi-continuum of levels filled up to $-|\Delta|$, together with a single phase-dependent and discrete state with energy $-E_{\mathrm{A}}^{e}$. Additionally, what we previously interpreted as the state of a single excitation can now be seen as the state in which either zero or two ABS are occupied, both with energy $E=0$; see Fig. 2.3(d).

While initially counter-intuitive, we emphasize that the two pictures are complementary. They highlight different properties of the same system, as is shown more rigorously in e.g. Sec. 6.7 of Ref. [121]. Indeed, while in the one-particle picture the spinful nature of the states is obfuscated, the current-carrying character of the ground state is clearly revealed; from the conjugate relation between N and ϕ one finds the current across the junction to be given by $I_{\mathrm{A}} = \frac{1}{\phi_0}\frac{dE_{\mathrm{A}}}{d\phi}$ (with $\phi_0 = \hbar/2e$, the reduced flux quantum), such that the ground state carries a current[15]

$$I_{\mathrm{A}} = \frac{|\Delta|}{4\phi_0}\frac{D\sin\left(\phi\right)}{\sqrt{1-D\sin^2\left(\phi/2\right)}}. \tag{2.16}$$

The latter is clearly non-zero for $\phi \neq 0, \pi$, in line with expectation from the Josephson equations discussed in chapter 1. In contrast, for the junction occupation with $E=0$ the current is zero for any ϕ, so that spinful occupation of the junction generally does not carry any current.[16]

---

[15] Here we neglect the contribution from the states in the continuum. This is a good approximation in the short junction limit, but does not generally hold.

[16] The ability for the spinful states to carry current is recovered in Sec. 2.3.

SIS JUNCTIONS AND SEMICONDUCTING WEAK-LINKS

With this subtle but important distinction between pictures of superconductivity elucidated, we now continue with the one-particle picture and investigate two different limits of Eq. (2.15), each of which govern a different type of Josephson junction. We first consider a junction hosting many independent channels n, each of which has a very small transparency $D_n \ll 1$.[17] According to the Landauer formalism, we can describe their collective behaviour by summing up the contribution of the individual channels. If we furthermore perform a series expansion in the small parameters D_n, the Josephson potential and current can be approximated as

$$H_{\mathrm{SIS}} = \frac{|\Delta|}{4}\sum_n D_n(1-\cos\phi) \tag{2.17}$$

$$I_{\mathrm{SIS}} = \frac{|\Delta|}{4\phi_0}\sum_n D_n \sin\phi. \tag{2.18}$$

Identifying $E_{\mathrm{J}} = \frac{|\Delta|}{4}\sum_n D_n$, we recover the form of the phenomenological Josephson Hamiltonian of Eq. (2.13) (up to an irrelevant constant), as well as the zero-voltage expression for the current given by the first Josephson relation of Eq. (1.3). Indeed, a valid picture for the SIS junction considered in chapter 1 is that of a weak connection containing many independent and low transparency channels. Interesting to note is that through the sheer number of modes involved they are in principle able to overcome the smallness in D_n and achieve a large effective E_J, which can even be comparable to $|\Delta|$ [105].

The second limit we consider is that of a junction consisting of a few or even a single channel, now with a potentially large transparency. Such is the case for the semiconducting weak-links studied in chapters 4 and 8, which utilize a Josephson junction of the form superconductor-semiconductor-superconductor (see Sec. 3.1 for details on the material platform of choice). For the purposes of this section these junctions can be thought of in the same way as an SNS junction, except that the number of relevant transport channels and their transparencies can now be tuned with a nearby gate electrode through the field effect [83]. They are therefore often still referred to as SNS junctions, and Eq. 2.15 is an appropriate description of their physics, up to a few nuances. For example, such a junction can no longer simply be treated as a low transparency element that transfers single Cooper pairs, which can be motivated as follows. As E_{A} is an even function of ϕ, it can be written in terms of a cosine decomposition

$$E_{\mathrm{A}}^{\cos} = \pm\sum_n E_{\mathrm{J}}^n \cos(n\phi) \tag{2.19}$$

with components

$$E_{\mathrm{J}}^n = \frac{2|\Delta|}{\pi}\int_0^\pi d\phi\sqrt{1-D\sin^2(\phi/2)}\cos(n\phi). \tag{2.20}$$

Taking into account the conjugate relationship between the phase difference ϕ and the number of Cooper pairs N that have been transferred across the junction, each term $\cos(n\phi)$ in this expansion corresponds to the transfer of n Cooper pairs. As shown in

---

[17] While the underlying system might contain various 3D modes that are mixed by disorder, the resulting eigenstates can generally still be treated as separate 1D systems [121].

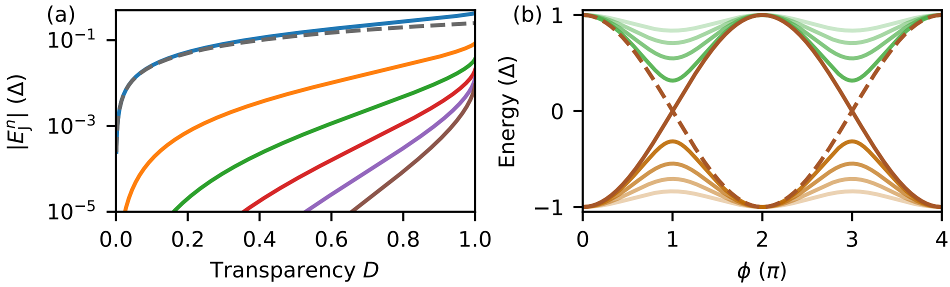

Figure 2.4: High transparency behaviour of Andreev bound states. (a) Absolute value of the Fourier coefficients of Eq. (2.20). The panel shows coefficients n from 1 to 6, for which the magnitude decreases monotonically with n, while the sign alternates with n. Dashed gray line shows the low transparency limit of a single channel $E_\mathrm{J} = |\Delta| D/4$. (b) ABS energy spectra for values of D from 0.2 to 1 in steps of 0.2, where the opacity of the line increases with D.

Fig. 2.4(a), the corrections from higher order terms $n > 1$ are small for low D, but this is not true when D approaches 1. In this regime substantial modifications with respect to Eq. (2.18) can be expected in the observables of the system, some potential applications of which are outlined in chapter 9.

While the Fourier decomposition is a useful tool for modeling the junction behaviour for moderate to large transparency, we note that it breaks down in the limiting case of $D = 1$, where one requires an infinite number of terms to produce the predicted $E_\mathrm{A} = \pm|\Delta| \cdot |\cos(\phi/2)|$. However, as discussed by Ivanov and Feigel'man, this expression is in any case not a valid description of the system [134]. To evaluate the behavior of the ABS in this regime, they show that one should instead obtain the energies $\pm E_\mathrm{A}$ as the eigenvalues of the Hamiltonian

$$H_\mathrm{qpc} = |\Delta| \begin{pmatrix} \cos\frac{\phi}{2} & \sqrt{1-D}\sin\frac{\phi}{2} \\ \sqrt{1-D}\sin\frac{\phi}{2} & -\cos\frac{\phi}{2}, \end{pmatrix} \tag{2.21}$$

which governs the two-dimensional subspace of the coupled left and right-moving Andreev bound states. For $D < 1$ its eigenvalues agree with those of Eq. 2.15, while for $D = 1$ one instead obtains the 4π-periodic relation $E_\mathrm{A} = \pm|\Delta|\cos(\phi/2)$; see Fig. 2.4(b).[18] We note, however, that the vast majority of experiments are performed for junction transparencies away $D = 1$, such that this 4π periodicity is not frequently discussed in the context of the (conventional) Josephson effect. Indeed, to the best of our knowledge the first proposal to reveal these nuances experimentally was put forth in Ref. [14] in 1999, and its verification had not been demonstrated up until the experiments reported in chapter 4, published simultaneously with the work of Kringhøj et al [169].

---

[18] The Hamiltonian of Eq. (2.21) is valid for $\pi \approx \pi$, where the relevant physics takes place away from the upper continuum of excitations. A more complete solution for $D = 1$ instead predicts the potential to be aperiodic rather than 4π periodic [14]. This can be understood from the fact that when the upper Andreev state touches the upper continuum, it will pass to the vacant levels of the continuum [134].

2.3. QUANTUM DOTS WITH SUPERCONDUCTING LEADS

In this section we turn to yet another kind of Josephson junction. It is of the type superconductor-quantum dot-superconductor, which we will refer to as a quantum dot with superconducting leads. In what follows we show that this junction gives rise to a plethora of phenomena (beyond those of SNS junctions) that are of fundamental interest, and we additionally motivate the implementation of novel qubits based on such junctions. For this we loosely rely on the reviews of Ref. [209, 215].

Before we can appreciate the combination of superconductivity and quantum dots, we should first briefly examine the quantum dot in isolation. The study of quantum dots encompasses an entire field of research, with a history spanning several decades. Semiconductor quantum dots in particular enable the construction of qubits out of both spin and charge degrees of freedom, and additionally allow for sensitive and rapid detection schemes of these quantities. A full overview is thus beyond the scope of this thesis; we refer the reader to the review of Ref. [116] and the recent PhD thesis of Lawrie [184] for works that discuss their properties at length.

For the purpose of this thesis, however, a quantum dot can essentially be considered as quantum confinement taken to its very limits. We take a quantum dot to be a box that can be filled with electrons (from a single one to many) for which all three spatial dimensions are of the order of the Fermi wavelength, such that it is effectively zero-dimensional. Since at this stage the details of the quantum dot eigenstates are not important, it suffices to say that the wave-functions are highly localized in space, and that the energy spectrum is discrete, with a level spacing that is large compared to all relevant energy scales. Its electronic structure is thus quantized into separate orbitals, each of which can each host up to two electrons of opposite spin. The latter is not yet dissimilar from the Andreev bound states hosted by the junctions discussed in the previous section. However, in contrast to the junctions discussed thus far, quantum dots also involve strong electrostatic interactions in the form of Coulomb repulsion. The energy cost of occupying a level with two spins is therefore not equal to the sum of the individual energy costs 2ϵ, but rather given by $2\epsilon + U_{ee}$, where U_{ee} is known the quantum dot's charging energy. As such the system is governed by the Hamiltonian

$$H_{\mathrm{QD}} = \sum_{\sigma} \epsilon_{\sigma} d_{\sigma}^{\dagger} d_{\sigma} + U_{ee} n_{\uparrow} n_{\downarrow}, \tag{2.22}$$

where σ indicates spin, and where for now we only consider only a single orbital; see Fig. 2.5(a) for an energy level diagram. Furthermore, $d_{\sigma}^{\dagger}$ (d_{σ}) creates (destroys) an electron with spin σ and energy $\epsilon_{\sigma} = \epsilon \mp E_{\mathrm{Z}}$, with E_{Z} a Zeeman energy term, and with $n_{\sigma} = d_{\sigma}^{\dagger} d_{\sigma}$. We note that the origin of U_{ee} is the same as the charging energy E_{c} of a superconducting island. However, we employ a distinct notation both for clarity and to convey that, in this thesis, these quantities are of a very different energy scale. Indeed, whereas we previously discussed that for the typical island studied in this thesis $|\Delta|/E_{\mathrm{c}} \geq 100$, we find that $|\Delta|/U_{ee} \sim 0.1$ for the quantum dots studied in chapter 5. It is thus not unexpected that U_{ee} is an important energy scale in the physics that follows.

Quantum dots can be constructed out of various different materials, but we choose to construct them out of semiconducting nanowires. This choice has the advantage that nearby electrostatic gate electrodes can be used to define the dot's confinement potential and to tune the number of occupied orbitals, both of which can be modified in-situ.

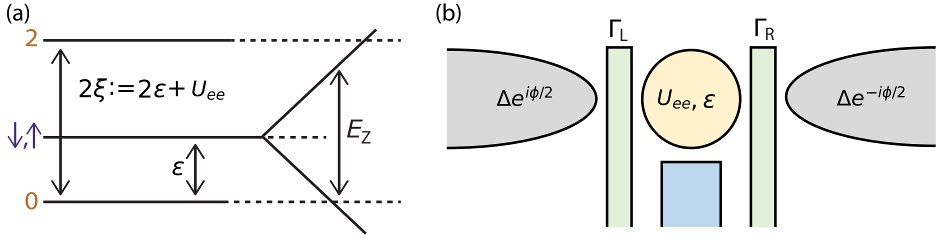

Figure 2.5: (a) Energy diagram of a single-level quantum dot, showing the energies of the different occupations and how they evolve in the presence of a Zeeman term E_Z. (b) Diagram showing a single-level quantum dot with superconducting leads. Nearby gate electrodes tune the tunnel rates $\Gamma_{L,R}$ and the relative level ϵ.

Yet this choice of material has another advantage: as discussed in Sec. 3.1, semiconducting nanowires are readily combined with superconductors, allowing for strongly coupled hybrid structures of the form superconductor-quantum dot-superconductor, illustrated in Fig. 2.5(b). The physics of this hybrid Josephson junction (for as we will see, it is also a Josephson junction) is once-more governed by the formation of Andreev bound states. However, in this section we discuss how the bound states can now be of a different character. In this junction superconductivity, which acts to pair up electrons into Cooper pairs, has to compete with the large Coulomb repulsion, which would favor having the junction empty or singly-occupied. When different parameters of the system are modified, this competition gives rise to a first-order quantum phase transition (at zero temperature), where the ground state of the junction changes from singlet (spin-zero) to doublet (spin-1/2) and vice-versa. Given that various quantum dot parameters are tuneable in-situ, thanks to the choice for a semiconducting platform, the finite-temperature remnants of this quantum phase transition can be experimentally investigated. This is the topic of chapter 5. Furthermore, we emphasize the difference between this tuneable ground state and the case of the non-interacting ABS in SNS junctions, where the doublet configuration is generally an excited state or at most degenerate with the singlet state [c.f. Fig. 2.3].[19] As encoding a qubit in low-energy states is generally preferable to an encoding that uses only excited states, this tunability motivates that a quantum dot with superconducting leads could be a suitable platform for a doublet-based qubit [234]. This is investigated in chapter 7.

RESONANT LEVELS

As we will discuss in more detail, a full theoretical description of the quantum dot with superconducting leads is not analytically tractable, instead requiring advanced numerical techniques. We therefore choose to build up our understanding in steps, first examining the case of a non-interacting quantum dot level: $U_{ee} = 0$. This system is described by a single spin-degenerate level with an energy ϵ with respect to the Fermi level of the superconducting leads, both of which are assumed to have an identical gap $|\Delta|$ and a phase difference ϕ between them. The level is then separated from those leads by two

---

[19] In non-interacting SNS junctions the doublet configuration can become the ground state in the presence of a magnetic field, but this is not considered in Sec. 2.2.

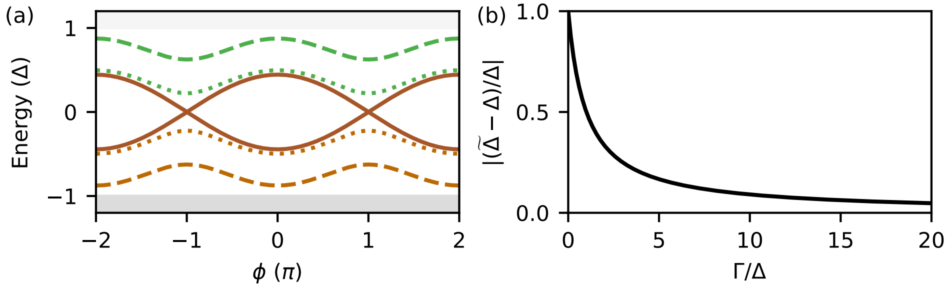

Figure 2.6: (a) Andreev bound state energies of the resonant level model in the single-particle picture. Solid lines show the case of $\epsilon = 0$, $\Gamma_L = \Gamma_R = 0.4$, dotted lines show $\epsilon = 0.4$ while keeping $\Gamma_L = \Gamma_R = 0.4$, and dashed lines show $\Gamma_L = 6\Gamma_R = 6$ while keeping $\epsilon = 0$, with all energies in units of $|\Delta|$. (b) Minimal energy gap between the ABS and the continuum as a function of $\Gamma = \Gamma_L + \Gamma_R$ for $\delta\Gamma, \epsilon = 0$.

tunnel barriers, the coupling across which is described by tunnel rates $\Gamma_{L,R}$. This system was first studied by Beenakker and van Houten [27], who derived a transcendental equation for the ABS energies of this system. More recently, Ref. [177] derived an approximate but convenient closed-form solution for the ABS energies[20]

$$E_A^{\mathrm{res}} = \pm \frac{|\Delta|}{|\Delta| + \Gamma} \sqrt{\epsilon^2 + |\gamma|^2}, \; \gamma = \Gamma \cos(\phi/2) + i\delta\Gamma \sin(\phi/2), \tag{2.23}$$

where $\Gamma = \Gamma_L + \Gamma_R$ and $\delta\Gamma = \Gamma_L - \Gamma_R$. As shown in Fig. 2.6(a), these energies essentially correspond to those of a short SNS junction, with only minor modifications. First, the effective transparency $\widetilde{D}$ is now a function of ϵ and $\delta\Gamma$, and is equal to one when these terms are zero, akin to a resonant tunneling processes. This implies that $\widetilde{D}$ can be fine-tuned towards one with nearby gate electrodes, an important tuning knob that enables the results of chapter 4. Second, in the resonant level model the ABS are generally detached from the continuum of states, such that they can lie deep inside the superconducting gap even for low transparencies and at $\phi = 0$. Indeed, as illustrated in Fig. 2.6(b), the ABS only approach the zero-phase energy of $\pm|\Delta|$ once Γ becomes much larger than $|\Delta|$. In essence this effect can be interpreted as the junction having a reduced local superconducting gap $E_A^{\mathrm{res}}(0) = \widetilde{\Delta}$, a result of induced superconductivity being obstructed by the tunnel barriers.[21]

ATOMIC LIMIT

To gain insight into the physics of $U_{ee} > 0$, we now first consider the limit of $|\Delta| \gg U_{ee}$. Specifically, we study the so-called atomic limit, for which $|\Delta| \to \infty$ [25, 217]. As discussed previously, this is not the limit realized in the systems studied in this thesis, for which $|\Delta| \sim 0.1 U_{ee}$. However, it allows for closed-form analytical solutions, from which

---

[20] During final editing we became aware of an even more recent work by Vakhtel and van Heck which revisits this model and includes also the imaginary-time Landau-Zener tunneling physics crucial to the physics of chapter 4 [314].

[21] An additional consequence of the detachment from the continuum of states is that for $\widetilde{D} = 1$ the ABS of the resonant level model are truly 4π periodic rather than aperiodic.

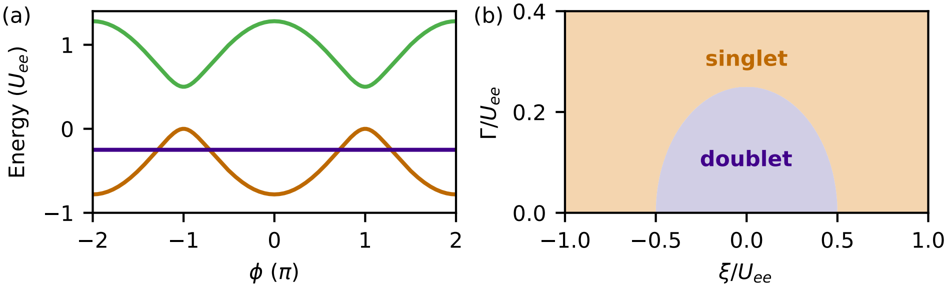

Figure 2.7: (a) Andreev bound state energies in the atomic limit and in the single-particle picture, shown for $\Gamma_L = \Gamma_R = U_{ee}/2$ and $\xi = U_{ee}/4$. We note that the levels are far sub-gap, as the model is evaluated for $|\Delta| \to \infty$. (b) Phase diagram in the atomic limit for $\phi = 0$.

much intuition can already be gained. Foregoing the details of the derivation, one finds that the spin-singlet ABS states are now governed by

$$E_A^{\text{atom}} = \xi \pm \sqrt{\xi^2 + 4\Gamma^2 \cos^2 \phi/2}, \tag{2.24}$$

where we introduce $\xi = \epsilon + U_{ee}/2$ and set E_Z, $\delta\Gamma = 0$ for simplicity. The energies are not unlike those of the ABS found for SNS junctions, and the states themselves are bonding and antibonding superpositions of zero and two electrons in the quantum dot, similar to what we encountered for the BCS ground state.

However, in contrast to the case of an SNS junction, a level crossing between the singlet and the spin-degenerate doublet states (which are at energy $\epsilon = \xi - U_{ee}/2$) can now be enacted by varying the model parameters; the doublet occupation can thus become the unique ground state of the junction.[22] Indeed, solving for $E_A = \xi - U_{ee}/2$, we obtain the boundary of the aforementioned quantum phase transition between singlet and doublet ground states

$$\xi^2 + 4\Gamma^2 \cos^2 \phi/2 = U_{ee}^2/4. \tag{2.25}$$

Fig. 2.7(a) shows how this level crossing can occur versus phase difference ϕ, with the doublet being the ground state around $\phi = \pi$. In turn, panel (b) shows a “phase diagram” for $\phi = 0$, depicting regions of singlet and doublet ground states separated by the phase transition boundary. While this boundary does not quantitatively match the numerically exact solution of the model (discussed further below), it still encompasses the relevant physics governing the phase transition. At $\Gamma = 0$, the quantum dot is fully decoupled from the leads, and the doublet region has the width of a typical Coulomb diamond: $\xi \in [-U_{ee}/2, U_{ee}/2]$. However, for increasing Γ, the coupling to the superconductors essentially induces superconductivity in the quantum dot, as was the case for the resonant level. This eventually overcomes the (weak) Coulomb repulsion, reducing the size of the diamond until the ground state is a singlet for all ξ.

---

[22] Taken at face value, a level crossing between singlet and doublet ABS appears to also be possible in the resonant level model for very negative values of ϵ. However, in this regime the approximations underlying Eq.(2.23) no longer hold; no crossing develops as long as $U_{ee} = 0$ [82].

YU-SHIBA-RUSINOV STATES

We now briefly consider the opposite limit of the system, that of $U_{ee} \gg |\Delta|$. In this case, BCS-like superpositions of zero and two electrons become prohibitively expensive to support, as the latter occupation comes at a significant energy penalty. However, this does not mean that the ground state of the junction is always an unpaired doublet. For appropriate parameters a different, non-BCS-like singlet ground state can still form. This is a Yu-Shiba-Rusinov-like (YSR) superposition between the spinful, singly occupied state of the quantum dot and a screening cloud of quasiparticles in the superconducting leads, see Fig. 2.8 [241]. These states are the superconducting counterparts of the well-known Kondo singlets, where the exchange interaction between quasiparticles in the leads and the spin on the dot can essentially outweigh the energy cost of having unpaired quasiparticles.

As the name implies, YSR states were first considered (independently) by Yu, Shiba, and Rusinov in the study of spinful impurities coupled to superconductors [269, 291, 292, 344]. As BCS superconductivity relies on the formation of Cooper pairs of opposite spin, scattering off of such impurities necessarily affects superconductivity, which they showed leads to the formation of bound states with energies located (potentially deep) inside the superconducting gap. However, as YSR considered bulk systems with embedded spin-1/2 impurities, the notion of a phase difference ϕ across the impurity had no meaning. Furthermore the quantum nature of the spins was initially neglected due to its complexity, so that Kondo screening also did not play a role. Approximate descriptions that take these concepts into account now do exist, such as e.g. mean-field slave-boson techniques [30] or so-called Kondo models [130, 158], where the latter reveals a striking universal behavior for the boundary between singlet and doublet ground states [144]. W choose not explicitly discuss these models here and refer to the reference material for further details. Instead, we reserve the rest of this section for the numerically exact solution of the model, which fully captures both the quantum nature of spin and charge.

Before we do so, we make a final remark. Recent work [352] highlights not only the formation of a modified singlet, but also of a modified doublet state in the $U_{ee}, \Gamma \gg |\Delta|$ regime of the quantum dot Josephson junction. In this case, one finds that the doublet state does not just correspond to an unpaired spin on the quantum dot (as was the case for the atomic limit), but is instead an over-screened spinful entity with coherent correlations to quasiparticles in both leads, also depicted in Fig. 2.8. Such states are a recent topic of interest [271], as they imply the formation of highly sought-after triplet correlations between the quasiparticles in the two leads, which can in principle be extended over long length scales. We hypothesize that this regime of over-screened doublets might be relevant inside the "chimney" of Fig. 5.5(b), although the experiments of that chapter did not allow for probing of the predicted correlations.

SINGLE IMPURITY ANDERSON MODEL WITH SUPERCONDUCTING LEADS

Having discussed the qualitative behavior of quantum dots with superconducting leads in different limits, we now turn to a numerically exact solution to the problem. So far, we have implicitly been considering what is known as the single impurity Anderson model (SIAM) with superconducting leads. It consists of a Hamiltonian of the form

$$H = H_{\mathrm{QD}} + H_{\mathrm{leads}} + H_{\mathrm{T}}, \tag{2.26}$$

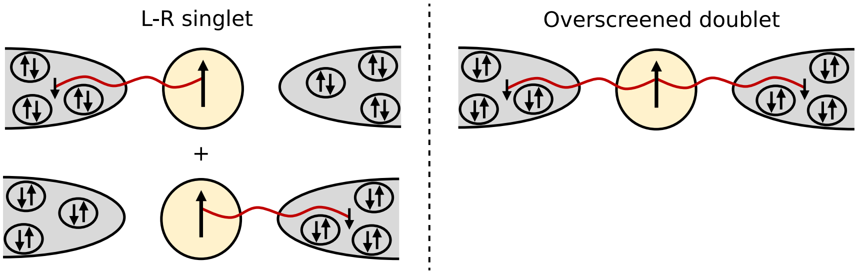

Figure 2.8: Schematic depictions of sub-gap states for large values of U_{ee}, Γ compared to $|\Delta|$. Left: Singlet state formed by an even superposition of two YSR-like singlets, where the local moment is distributed between the quantum dot and the left and right superonducting leads. Right: Overscreened doublet state in which an additional local moment is attached to the L-R singlet, forming a doublet state in which the spin on the quantum dot is strongly correlated with the spins in the superconducting leads. Image adapted from Ref. [271].

where H_{QD} is given by the single-level Hamiltonian of Eq. (2.22) and the second term describes two superconducting reservoirs, given by the BCS Hamiltonian of Eq. (2.4) (albeit typically written in the basis of plane waves). For simplicity we again assume both superconductors to have identical gaps $|\Delta|$ as well as a density of states ρ, and we oncemore take them to have a phase difference $\phi = \varphi_{\mathrm{L}} - \varphi_{\mathrm{R}}$ between them. The third term is then the tunneling Hamiltonian that couples the dot and the leads,

$$H_{\mathrm{T}} = \sum_{ik\sigma} \left(t_i c^{\dagger}_{ik\sigma} d_{\sigma} + \mathrm{h.c.} \right), \tag{2.27}$$

where $i = \mathrm{L,R}$ labels the left and right leads, k labels spin-degenerate single-particle states, and t_i are the dot-lead tunnel coupling strengths. For simplicity, we choose the latter to be independent of k and spin; the consequences of this choice are addressed in the next section. Within this approximation, the tunneling rate across each barrier takes on the simple form $\Gamma_i = \pi\rho|t_i|^2$.

As briefly mentioned to in the previous sections, the eigenvalues of this Hamiltonian are not analytically tractable for arbitrary parameter values. It can, however, be solved numerically using e.g. the numerical renormalization group (NRG) method. A thorough description of the NRG method is beyond the scope of this chapter; several details can be found in Sec. 5.8, and we recommend the review of Ref. [47] for an exhaustive introduction to the topic. In short, the NRG method is an iterative procedure for solving quantum impurity problems that involve one or several localized levels coupled to a continuum of electrons (which can possess some correlations, such as the case for a superconductor). The procedure consists of several steps: discretization of the continuum parts of the Hamiltonian in a way that emphasizes states near the Fermi level (the so-called logarithmic discretization), unitary transformation of the resulting discretized Hamiltonian to a linear tight-binding chain representation (the Wilson chain), and finally iterative diagonalization in which the Wilson chain sites are taken into account consecutively [47, 172, 274, 338, 343].

Although the growth of the Hilbert space is controlled by the truncation parameters that set the number of states retained after each step of the iteration, the NRG approach is computationally expensive and can generally not be performed on a personal

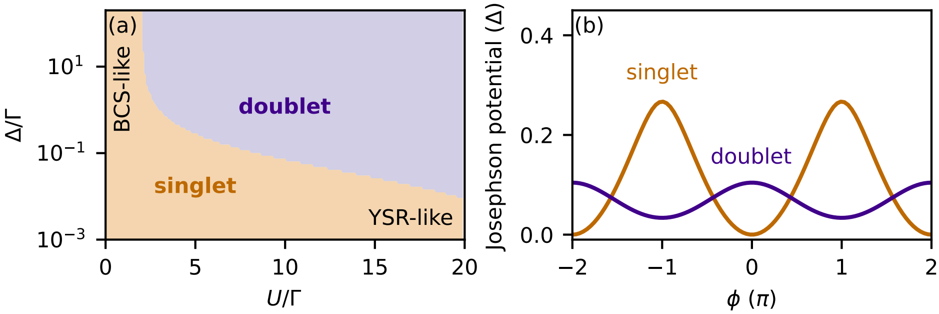

Figure 2.9: (a) Phase diagram of the SIAM with superconducting leads, computed via NRG for $\xi, \delta\Gamma, \phi = 0$ and adapted from Ref. [144]. (b) Phase dependence of the Josephson potential of the quantum dot junction in the singlet ($S = 0$, orange) and doublet ($S = 1/2$, purple) state, computed via NRG for $U_{ee} = 5$, $\xi = 0.25$, $\Gamma = 0.2$ and $\delta\Gamma, E_Z = 0$. Energies are given in units of $|\Delta|$ and the potentials are given relative to the minimum of the singlet state.

computer. However, during the work of chapter 5 our collaborator dr. Rok Žitko generated a vast amount of NRG data for various parameter regimes, freely available at DOI 10.5281/zenodo.5874832 [350]. Through interpolation one can use this to calculate the energies of the lowest-lying singlet and doublet states for virtually any combination of the model parameters. In turn, this allows us to construct highly accurate, multi-dimensional quantum phase transition diagrams that depend on the relative size of up to seven parameters: Γ, $\delta\Gamma$, ϕ, ξ, E_Z, $|\Delta|$, and U_{ee}. In chapter 5 we realize a device that is well-described by this model, and in which all but the latter two parameters are tuneable in-situ. We refer to that chapter for several phase transition diagrams and their physical interpretation; see e.g. Fig. 5.8.

However, not every regime is easily accessible experimentally. An example of such a difficult-to-measure phase diagram is shown in Fig. 2.9(a), which shows the boundary between singlet and doublet phases as the parameter hierarchy between Γ, Δ, and U_{ee} are varied, where in particular the latter two parameters are generally fixed in an experiment. Additionally, the approximate position of the BCS-like and the YSR-like singlet regimes considered in the previous subsections are also indicated, illustrating that there is a large cross-over between the two types of behavior. We invite the interested reader to use the publicly available NRG data for further investigation [350], and simultaneously point out Ref. [144], which contains approximate but insightful analytical boundaries that help build intuition.

PHASE DISPERSION OF THE DOUBLET STATE

Before we continue, we must address a crucial short-coming of the discussion thus far; in all the expressions that came before, spin-doublet occupation of the junction was always independent of phase, and therefore did not carry supercurrent. This is, however, generally not correct. By virtue of fourth-order co-tunneling processes, Cooper pairs can be transferred through the quantum dot even when it is occupied by a single spin, and the doublet state can therefore acquire a non-trivial energy-phase relation [104]. While not present in the resonant level and in the $|\Delta| \rightarrow \infty$ limit discussed above, this effect is readily captured in the NRG treatment of the model. This is shown in Fig. 2.9(b), where we implicitly assume that projection onto the lowest-energy states in each parity sector is sufficient to capture the salient features of the Josephson potential. Strikingly, one finds that the energy-phase relation of the doublet state is opposite to that of the singlet state; whereas the latter follows a sinusoidal potential with its energy minimum at $\phi = 0$, the former has an energy minimum at $\phi = \pi$.[23] Due to this distinctive feature the doublet state of the quantum dot with superconducting leads is often referred to as a π-junction, and the singlet-doublet quantum phase transition is also known as the $0-\pi$ transition.

The origin of the π shift can be understood on the basis of the allowed co-tunneling sequences for different dot occupations, which are restricted by the combination of Coulomb blockade and Pauli exclusion (see Fig. 2.10) [298, 316]. When a Cooper pair is transferred through a doublet configuration [panel (b)] the order in which the spins of a Cooper pair are annihilated in one lead is opposite to the order in which they are created in the other lead, which necessarily involves a permutation in the spin-ordering of a Cooper pair. As the constituent particles of a Cooper pair obey Fermi-Dirac statistics, this exchange implies that the wavefunction should acquire a minus sign, and in turn, moves the minimum of the 2π periodic energy-phase relation from $\phi = 0$ to π, producing the π-shift.

BEYOND THE SIAM

While the SIAM with superconducting leads is already of substantial complexity and is able to describe a multitude of experimental results, there are still various extensions that one can consider to make the model more realistic. Perhaps the primary candidate to address is the single-level nature of the quantum dot assumed thus far. In real devices, it is not always possible to take confinement to the extreme, and the quantum dot level spacing could thus be comparable to other relevant energy scales (such as $|\Delta|$ and U_{ee}). In this case co-tunneling can proceed through multiple quantum dot levels, each with their own ξ_n and $\Gamma^n_{\mathrm{L,R}}$. Clearly this leads to a rapid growth of the parameter space, which quickly makes the NRG approach unfeasible.[24] At the same time, the inclusion of additional levels can lead to important corrections: as discussed in Ref. [316], the Cooper-pair permutation argument that explains the π-junction behaviour is no longer the complete story when multiple quantum dot levels contribute to the co-tunneling sequence, as the parity of the orbital wavefunctions must also be taken into account. As a consequence, in a multi-level system the energy-phase relation of a singlet state can also have a π shift, while that of the doublets can be without one.

Additional effects are also expected when the leads can no longer be well-approximated by transitionally invariant and non-interacting BCS Hamiltonians, in which case they can acquire non-trivial level structures and complex dispersion relations. In this regime analytical solutions are even more sparse to come by, and NRG is no longer the appropriate language in which to express the problem. Here one instead has to rely on the

---

[23] While not discussed here, we note that a simplified model based on the Hartree-Fock approximation can also produce analytically tractable π-junction behavior for the doublet state, from which much intuition can be gained [321].

[24] In chapter 6 we instead consider a simplified extension in which off-resonant levels are summed up into a direct lead-lead tunneling term Γ_{LR}.

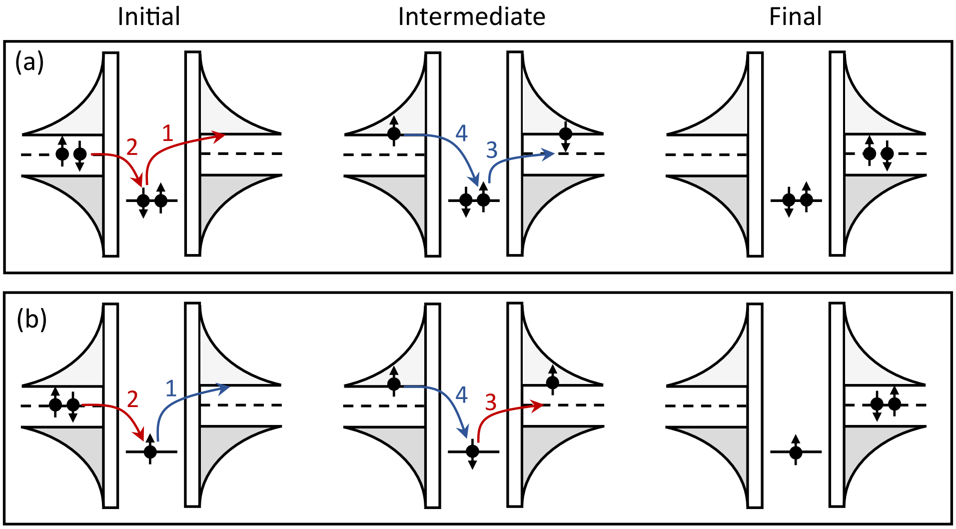

Figure 2.10: (a-b) Schematic depiction of two fourth-order co-tunneling sequences that transfer a Cooper pair through a doubly ($S = 0$, a) and singly ($S = 1/2$, b) occupied single-level quantum dot with superconducting leads. The first and last column show the initial and final states, while the middle columns show one of the possible intermediate virtual states. In panel (a), the order in which the spins of a Cooper pair are annihilated in the left superconductor is identical to the order in which they are created in the right superconductor. Note that the same holds for an empty dot level. However, in panel (b) the order of the spins is reversed during Cooper pair annihilation and creation. Panels adapted from Ref. [316].

density matrix renormalization group or dynamical mean-field theory methods, which are generally of even higher computational complexity [239]. While these scenarios are not explicitly encountered in this thesis, their largely unexplored physics should already be experimentally realizable, as briefly discussed in chapter 9.

In chapters 6 and 7 we furthermore encounter the need for modifying a different model assumption, namely that the dot-reservoir tunnel coupling strengths t_i are independent of k and spin. This is not a valid assumption in systems with strong spin-orbit interaction (SOI) (either in the leads or in the quantum dot), which essentially makes it so that spin does not have to be conserved during single electron tunneling events. The effect of SOI on the SIAM is typically incorporated by splitting the resulting tunneling rates into spin-conserving rates $\Gamma_{\mathrm{L,R}}$ and spin-flipping rates $\gamma_{\mathrm{L,R}}$ [234]. In and of itself this splitting of terms does not have strong consequences for the Josephson physics of the system; indeed, since the SOI does not break time reversal symmetry, one may expect that it will not affect the Josephson effect at all [77]. But when present in conjunction with multiple quantum dot orbitals, SOI can in fact give rise to profound interference effects. Ref. [234] proposes that even in the absence of a Zeeman term, the combination of these ingredients can lead to non-degenerate energy-phase relations for the doublet states $|\uparrow,\downarrow\rangle$, splitting the spins and thereby producing a spin-dependent supercurrent. Ref. [347] in turn shows that the combination of SOI and a Zeeman term can give rise to the anomalous Josephson effect, in which the minimum of the doublet state energy-phase relation is at $\phi_0 \neq 0, \pi$. Both of these effects are of fundamental interest, as well as promising for applications in the field of superconducting spintronics [196].

We experimentally study these predictions in chapter 6, and we refer to its Supplementary Materials in Sec. 6.7 for an extended SIAM that examines their origin, both using analytical and numerical methods. In practice, however, we find that the physics of this regime is well-described by a simple phenomenological model for the potential of the doublet state [234]:

$$U(\phi) = E_0 \cos(\phi) - E_{\mathrm{SO}}\, \vec{n}\cdot\vec{\sigma}\, \sin(\phi) + \frac{\vec{E}_{\mathrm{Z}}}{2}\cdot\vec{\sigma}\,. \tag{2.28}$$

Here $\vec{\sigma}$ is the spin operator, $\vec{n}$ is a unit vector along the polarization direction set by the SOI, and E_{SO} and E_0 are the spin-dependent and spin-independent contributions to Cooper pair tunneling across the quantum dot junction.[25] Note that the term proportional to E_0 has a minimum at $\phi = \pi$ by assumption, but we again emphasize that this does not have to be the case for a multi-level scenario.

The energy spectrum that results from diagonalizing this Hamiltonian at $\vec{E}_{\mathrm{Z}} = \vec{0}$ is shown in Fig. 2.11(a), which reveals two states of opposite energy-phase dispersion. These essentially correspond to the two (quasi)spin flavors of the quantum dot doublet states.[26] The zero-field Josephson potential of the doublet occupation is thus spin-dependent, a feature not found within the standard SIAM nor in the short junction limit of SNS devices. At $\vec{E}_{\mathrm{Z}} = \vec{0}$, this spin dependence is fully governed by the at-first-sight

---

[25] The product $E_{\mathrm{SO}}\, \vec{n}\cdot\vec{\sigma}\, \sin(\phi)$ is colloquially referred to as an effective magnetic field $\vec{B}_{\mathrm{SO}}$ due to its similarity to a Zeeman term.

[26] (The doublet is now technically a Kramer's doublet rather than a spin doublet due to the inclusion of the spin-orbit interaction.

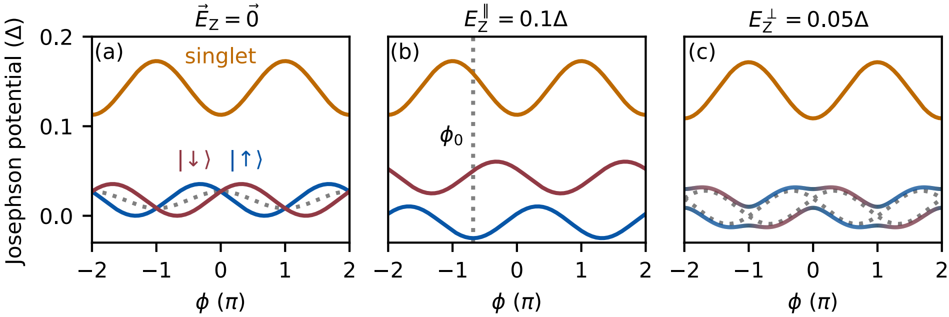

Figure 2.11: Phase dependence of the Josephson potential of the quantum dot junction in the extended SIAM, showing the singlet ($S = 0$) state (orange) and the two doublet ($S = 1/2$) states (blue, red). The potentials are computed via NRG for three different Zeeman fields, with $U_{ee} = 15$, $\xi = 0.1$, $\Gamma = 0.2$, $\gamma = 0.4$, $\Gamma_{\mathrm{LR}} = 0.1$ and $\delta\Gamma = 0$, given in units of $|\Delta|$. The potentials are plotted relative to the minimum of the doublet states at $E_Z = 0$. Details of the calculation can be found in Sec. 6.7.

peculiar sine term of Eq.(2.28). At the surface level, we emphasize that its inclusion is explicitly allowed by Kramer's theorem, for which the relation $U(\phi,\vec{\sigma}) = U(-\phi,-\vec{\sigma})$ should be obeyed. As discussed in detail in chapter 6, the microscopic origin of the term is an interference effect between co-tunneling trajectories that either include or do not include spin-flipping events, facilitated by the presence of multiple quantum dot orbitals and a finite phase difference.

We further note that at zero field the Josephson potential is on average governed by an equal weight of both spin occupations, given that there is no preferential spin direction; as such its time-averaged behavior is still like that of a π-junction. This changes in the presence of a Zeeman field $E_Z^{\parallel}$ applied parallel to the direction of the SOI. As shown in Fig. 2.11(b), in this regime one of the spin states becomes the unique ground state. As its minimum is displaced from $\phi = 0, \pi$ by the sine term, this directly realizes the anomalous Josephson effect, be it instantaneous or time-averaged. For completeness we also illustrate the effect of a Zeeman field $E_Z^{\perp}$ perpendicular to the SOI direction. As shown in panel (c), small values of $E_Z^{\perp}$ cause a hybridization between the spin states, opening up avoided crossings at $\phi = 0, \pi$ and producing multiple potential minima within a 2π-wide interval. This is not dissimilar from the physics of high transparency SNS junctions discussed in Sec. 2.2, where finite D results in a small avoided crossing between the ABS and produces multiple potential minima in a 4π-wide interval. The non-adiabatic phase evolution explored for high transparency SNS junctions in chapter 4 is therefore likely to be of relevance in this perpendicular field regime as well, although its consequences currently remain unexplored. Finally, we observe that at larger values of $E_Z^{\perp}$ the avoided crossings eventually out-compete the splitting governed by the SOI, lifting the anomalous Josephson effect.

2.4. TRANSMONS

In Sec. 2.1 we introduced isolated superconducting islands, which combine superconductivity with electrostatic interactions. We then discussed what occurs when two such islands are connected via a Josephson junction in Sec. 2.2, allowing for disipationless transfer of Cooper pairs between them. Here we emphasized the role of Andreev bound states, which underpin the energy-phase relations and thereby the observables of the junction. We explored how their exact nature depends on the type of junction involved, with extra emphasis on the quantum dot with superconducting leads in Sec. 2.3.

In these discussions, however, we have neglected the electrostatic interactions of the islands. Indeed, as the transfer of a Cooper pair implies the transfer of a charge of $2e$, it also creates a charge dipole. A proper description of coupled superconducting islands must include the electrostatic energy corresponding to this transfer process, given by

$$H_\mathrm{d} = 4E_\mathrm{c}\left(N - N_\mathrm{g}\right)^2 = 4E_\mathrm{c}\left(-i\frac{d}{d\phi} - N_\mathrm{g}\right)^2 \tag{2.29}$$

where we used the conjugate relation between the number of Cooper pairs N that have crossed the junction and the phase difference ϕ to write two equivalent expressions. We note that this equation is similar to, but different from, the single-island expression of Eq. (2.2). The factor of 4 accounts for the fact that we now deal with the transfer of *pairs* of electrons, and the charging energy $E_\mathrm{c} = \frac{e^2}{2C_\Sigma}$ encompasses all relevant capacitances of the system (e.g. an intrinsic capacitance across the junction). Furthermore, N_g is now a real-valued, generally time-fluctuating offset charge, which can be induced by for example a nearby gate electrode, background charges, or unpaired electrons. Combining this expression with that of a Josephson junction results in a generic Hamiltonian

$$H_\mathrm{tmon} = H_\mathrm{d} + U_\mathrm{J}(\phi), \tag{2.30}$$

where $U_\mathrm{J}(\phi)$ is the Josephson potential, which can take on the form of e.g. an SIS junction [Eq. (2.18)], an SNS junction [Eq. (2.21)] or even be governed by the physics of a quantum dot with superconducting lead [Sec. 2.3]. At the surface level, each of these choices gives rise to qualitatively comparable behaviour: the resulting energy spectrum is discrete by virtue of the compact variable ϕ, and it is generally non-equidistant by virtue of the non-linear Josephson term.[27] In a sense the energy spectrum thus appears qualitatively similar to the electronic states of e.g. the hydrogen atom, such that the system is often referred to as an artificial atom. As we will see, however, the details of this atom depend sensitively on $U_\mathrm{J}(\phi)$.

The Hamiltonian of Eq. (2.30) can be conveniently represented by the diagram of Fig. 2.12, and its description falls into the realm of circuit quantum electrodynamics (cQED): the study of light-matter interaction in superconducting circuits. In fact, the behaviour of this specific circuit has been studied for several decades already, most prominently for the case of an SIS junction. Depending on the parameter regime, it is known as the Cooper pair box [38], or as the transmon [162]. In what follows we present an overview of the circuits' properties, for which we make use of numerical techniques to diagonalize the Hamiltonian (c.f. Sec. 5.8). For further reading on both the specific circuit and cQED in general, we recommend the recent review by Blais et al. of Ref. [34].

For simplicity we will assume an SIS Josephson potential of the form $U_\mathrm{J}(\phi) = E_\mathrm{J}(1 - \cos\phi)$, such that behavior of the circuit is largely governed by the ratio of just two parameters: E_J and E_c. We then first examine the regime of small Josephson energy, $E_\mathrm{J}/E_\mathrm{c} = 1$,

---

[27] See Ref. [81] for a detailed discussion on the compact nature of ϕ.

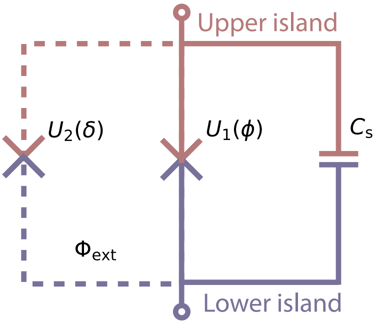

Figure 2.12: Circuit model of a floating transmon. Dashed lines denote the inclusion of an additional junction, forming a SQUID through which an external flux Φ_{ext} can be threaded.

known as the Cooper pair box regime. Here one recovers behavior somewhat comparable to that of the superconducting island; as shown in Fig. 2.13(a), the energy spectrum is indeed discrete, with levels that mostly follow the shapes of charge parabola's.[28] A major difference, however, is that the parabola's no longer cross: the Josephson effect allows the islands to exchange Cooper pairs, resulting in an avoided crossing $\sim E_J$ between states that differ by one Cooper pair (and a smaller avoided crossing between states that differ by two Cooper pairs). The position and relative spacing of the energy levels are thus strong functions of the offset charge N_g, which tunes the levels in and out of regions of avoided crossings. We refer to the variation of the level position with N_g as the charge dispersion $\delta E_n = |E_n(0.5) - E_n(0)|$, which is also a measure of how sensitive the system is to noise in the offset charge. The relative spacing between levels is instead captured by the so called anharmonicity $\alpha = E_{12} - E_{01}$, where E_{mn} denotes the difference $E_n - E_m$. This quantity essentially governs how close the energy level spacing of the circuit is to that of a harmonic oscillator, in which the non-linear Josephson junction is replaced by a linear inductor such that $\alpha = 0$. The anharmonicity is a crucial parameter for constructing a qubit out of e.g. the $n = 0$ and $n = 1$ levels, for which one needs to be able to selectively address the E_{01} transition with fast (and thus spectrally broad) control pulses.

The behaviour in the Cooper pair box regime can be further understood by examining the wavefunctions for a given offset charge. Shown in panel (d) is the case of $N_g = 0$, expressed in the so-called number basis of Cooper pairs. This reveals that the ground state is reasonably well-described by $N = 0$ Cooper pairs, given that the offset charge is set away from an avoided crossing. However, the excited states have significant weight among both $N = \pm 1$ Cooper pairs transferred across the junction. Indeed, the eigenstates of circuit are no longer states of a well-defined number of transferred Cooper pairs, but instead form superpositions. Albeit less intuitive in this regime, we can also examine the wavefunctions in the dual basis, the phase basis, shown in panel (g). This shows

---

[28] Note that a second, decoupled copy of the spectrum exists for islands that host an odd number of electrons, horizontally offset by $N_g = 0.5$. At $T = 0$ this is energy spectrum is vertically offset by an energy close to $|\Delta|$, however as discussed at the end of Sec. 2.1, in practice this energy gap is generally not present due to finite non-equilibrium quasiparticle densities. See e.g. Fig. 4.2 for such a doubled spectrum, which has an offset charge periodicity of $1e$ rather than $2e$.

that each level is distributed over a broad range of ϕ, and not particularly confined to the Josephson potential well. At the cost of some mathematical rigor (the Cooper pair box states are not minimum uncertainty states), this can essentially be understood from N and ϕ being conjugate variables, such that a narrow distribution in N implies a wide distribution in ϕ. In this parameter range it is therefore most intuitive to analyse the system in the number basis.

The behaviour of the system changes drastically when $E_\mathrm{J}/E_\mathrm{c} \gg 1$, for which one enters the transmon regime. Shown in panel (c) is the case of $E_\mathrm{J}/E_\mathrm{c} = 50$; here the remnants of the charge parabola's are no longer visible, having been replaced by energies that are nominally insensitive to the offset charge. The charge dispersion δE_n has thus been strongly suppressed, and the anharmonicity is now essentially constant as a function of N_g. This behaviour can once-more be understood from the wavefunctions. Examining their form in the number basis [panel (f)], the eigenstates of the system now all span several different Cooper pairs, rather than just one or two. In this regime the number basis is thus a less convenient framework for building intuition. Instead, analysis in the phase basis [panel (i)] reveals that the transmon eigenstates can be better understood from the perspective of a "phase particle", confined in the well set by the Josephson potential.

It is also from this basis that one can motivate the suppression of the charge dispersion, starting from Bloch's theorem. Given that one has a periodic potential $U_\mathrm{J}(\phi) = U_\mathrm{J}(\phi + 2\pi)$, a tight-binding treatment of the problem results in a state that is approximately a superposition of wavefunctions localized at $\phi = 0, \pm 2\pi, \pm 4\pi, \ldots$ As in crystalline solids this gives rise to "Bloch bands", where the amount of band bending (here the charge dispersion) depends on how much adjacent wavefunctions overlap. That this overlap decreases with $E_\mathrm{J}/E_\mathrm{c}$ is made intuitive by recasting the problem into that of a particle with mass $1/E_\mathrm{c}$ tunneling between potential minima separated by barriers of height E_J. In this case larger ratio's of $E_\mathrm{J}/E_\mathrm{c}$ exponentially reduce the tunneling probability, and thus the charge dispersion.

In Fig. 2.14 we further quantify the evolution of the eigenstates with the ratio $E_\mathrm{J}/E_\mathrm{c}$. Starting with the energy levels themselves, one finds that both E_n and the level spacing E_{mn} are an increasing function of E_J; see panel (a). In particular, one can show that $E_{01} \approx \sqrt{8E_\mathrm{J}E_\mathrm{c}} - E_\mathrm{c}$ in the limit of large $E_\mathrm{J}/E_\mathrm{c}$, while the spacing to the other levels is a function of the anharmonicity α, which we return to below. Panel (b) then depicts the evolution of the charge dispersion of the energy levels, which is indeed exponentially suppressed in $\sqrt{E_\mathrm{J}/E_\mathrm{c}}$. The panel also shows how higher lying levels retain more charge dispersion; being higher in energy, they are less confined by the potential well.[29] In turn, panel (c) shows the evolution of the anharmonicity α. As we remarked earlier, for low $E_\mathrm{J}/E_\mathrm{c}$ it starts off as a highly dependent function of N_g, but at higher ratio's it converges to a single value, approximately given by $\alpha \approx -E_\mathrm{c}$. The fact that the evolution of α is algebraic rather than exponential in $E_\mathrm{J}/E_\mathrm{c}$ is one of the central concepts that makes the transmon such a successful qubit platform; sensitivity to charge noise can be strongly suppressed while retaining the ability to address individual transitions. Nevertheless,

---

[29] The exponential suppression of the charge dispersion does not imply that the wavefunctions are exponentially spread out (localized) in the number (phase) basis. The standard deviation of these distributions rather proceeds (inversely) proportional to $\left(E_\mathrm{J}/E_\mathrm{c}\right)^{1/4}$, so that even in the transmon regimes the Cooper pair fluctuations are only of order one to two [162].

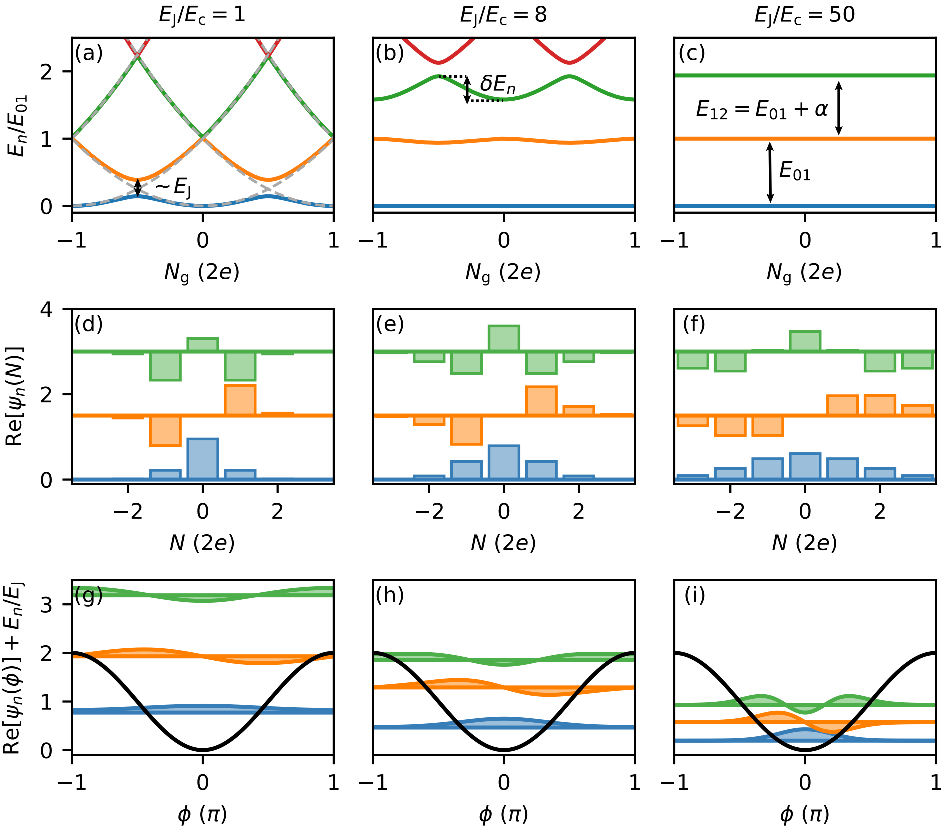

Figure 2.13: The transition from the Cooper pair box regime to the transmon regime. (a-c) Offset charge dependence of the energy levels E_n governed by Eq. (2.30) for the case of an SIS potential. Panel (a) shows the case of $E_J = 0$ in gray dashed lines. Energies are normalized by the energy difference $E_{01} = E_1 - E_0$ and given with respect to the lowest energy value of the ground state. (d-f) Real part of the wavefunction for the first three levels, expressed in the Cooper pair number basis. Levels are offset for clarity and evaluated for $N_g = 0$. (g-i) Same as (d-f) in the phase basis. The wavefunctions are now offset by their energy value with respect to the bottom of the Josephson potential, normalized by the Josephson energy. In addition, the normalized Josephson potential is plotted in black. In all panels, $E_c/h = 1\,\mathrm{GHz}$.

the smallness of α does limit the rate at which the transmon states can be manipulated without unwanted excitation of other states [332]. This has prompted investigation of alternative superconducting circuits for qubit applications, which we briefly return to in chapter 9. Finally, albeit not illustrated in the figures, another core feature of the transmon is that the transition matrix element connecting the ground and the first excited state via the charge operator does not decrease but instead increases in the ratio $E_\mathrm{J}/E_\mathrm{c}$ [162]. In other words, while the response to DC charge offsets is suppressed in the transmon regime, the response to AC oscillating electric fields is in fact enhanced. It is this important property that facilitates strong coupling to e.g. readout circuits.

Given that the charge dispersion is suppressed for large $E_\mathrm{J}/E_\mathrm{c}$, the resulting energy levels can no longer be conveniently tuned in-situ using N_g. To regain the ability to tune the energy levels, one can replace the single Josephson junction with two junctions in parallel, forming a superconducting quantum interference device (SQUID) [c.f. Fig. 2.12]. In a SQUID, the phase drop across the first junction (ϕ) and across the second junction (δ) are connected according to $\phi - \delta = \phi_\mathrm{ext}$ through the quantization of flux, where $\phi_\mathrm{ext} = (2e/\hbar)\Phi_\mathrm{ext}$ is the phase difference resulting from the externally applied magnetic flux through the SQUID loop, Φ_ext [76]. This results in an effectively flux-tunable Josephson energy, at the cost of introducing flux noise sensitivity [see Fig. 2.14(d)]. Crucially, the range of tunability depends strongly on the ratio of the Josephson energies. For identical junctions, the range is maximal, essentially from 0 to $E_\mathrm{J1}+E_\mathrm{J2}$, and the phase drop is divided across both junctions. In contrast, for $E_\mathrm{J1} \gg E_\mathrm{J2}$ the value of ϕ remains close to zero while δ is close to ϕ_ext. The large junction essentially provides a "reference" Josephson energy, on top of which the now flux-dependent potential of the other junction is added. This lies at the core of the spectroscopy performed in chapters 5 and 6, where it is employed to explicitly resolve the energy-phase relationship of quantum dots with superconducting leads.

BEYOND SIS JUNCTIONS

The discussion thus far focused on the case of an SIS junction. This is in part due to the simplicity of the description, which also captures many of the salient features of SNS junction based transmons, and because the SIS implementation makes up the vast majority of the transmon literature. Indeed, since its conception, almost every transmon has been modeled with a perfectly sinusoidal potential, and has been fabricated using well-studied junctions that accurately implement this potential. The decade-long collaboration between theory and experiment that followed has been hugely successful, enabling a wide range of highly advanced protocols and tools: transmon circuit parameters can now be engineered with percent-level accuracy, the transition frequency difference between levels can be readily probed below the MHz scale, and the state of the system can be manipulated and read out on nanosecond timescales [34, 99].

Nevertheless, one can create a transmon circuit out of virtually any Josephson junction, which is in fact the core methodology of this thesis. Rather than use the well-known properties of the SIS junction to build highly coherent and predictable qubits, we invert the construction and use the exhaustive toolbox available for transmon measurement to probe the behavior of the SNS and quantum dot Josephson junctions discussed in the preceding sections. Their properties are then revealed by the measurement of the

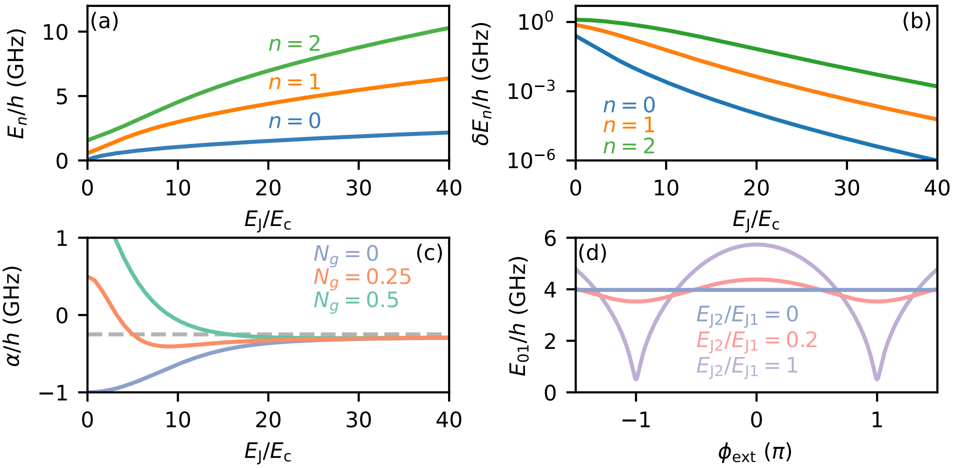

Figure 2.14: Evolution of circuit properties with increasing E_J/E_c. Panel (a) shows the evolution of the first three energy levels as evaluated at $N_g = 0.25$, while panel (b) shows the evolution of their charge dispersion. Panel (c) shows the evolution of the anharmonicity at three different values of offset charge. Panel (d) shows the evolution of the E_{01} transition energy versus the external flux in the presence of a second SIS junction with variable E_{J2}. In all panels $E_c/h = 0.25\,\text{GHz}$.

transmon circuit, for which any deviation from SIS-like behaviour can be readily quantified. Take for example the anharmonicity of a transmon with an SNS junction, which for $D \to 1$ approaches $-E_c/4$ rather than $-E_c$ [167]. Rather than illustrating how a transmon circuit can reveal the junction properties of interest through further calculations, however, we instead refer to the experimental results contained in the remainder of this thesis. As put forward in the outline of chapter 1, but now with the relevant theoretica concepts discussed, chapter 4 details work on an offset-charge sensitive transmon ($E_J/E_c \approx 5$) containing an SNS junction. Using this system we are able to probe the rapid suppression of charge dispersion when the junction transparency $D \to 1$, a consequence of the evolution from a 2π to a 4π periodic potential. In chapters 5 and 6 we use the aforementioned asymmetric SQUID construction to accurately probe the energy-phase relationship of quantum dots with superconducting leads, revealing the singlet-doublet transition, the spin-orbit induced spin-splitting of the doublet state, and ultimately the anomalous Josephson effect. In chapter 7 we then take the dependence of the circuit on its junction even further, creating a novel superconducting spin qubit out of the doublet state inside a quantum dot Josephson junction, while using the transmon to read out its state.

To conclude this section, we emphasize that the transmons studied in this thesis are essentially spectrometers, and not a direct attempt to build a better transmon qubit. Indeed, the qubit coherence properties are generally far from state of the art transmons. This does not mean that such devices are of no value to the general transmon community, however. In chapter 8 for example we again construct transmons based on SNS junctions, whose intrinsic magnetic field resilience (see Sec. 3.1) allows us to study quasiparticle mitigation methods in regimes not conveniently accessible using conventional

SIS junctions, while the results contained in this chapter are directly applicable to any type of transmon. Furthermore, several ideas and proposals exist that aim to leverage SNS and SQDS junctions to build better qubits [3], some of which are outlined in chapter 9.

3

EXPERIMENTAL METHODS

Of course it is exhausting, having to reason all the time in a universe which wasn't meant to be reasonable.

Kilgore Trout, Breakfast of Champions

The quality of our experiments relies on two equally important elements: the materials that constitute the device we measure, and the apparatus we use to do the measurements. In this chapter we provide an overview of those used throughout this thesis, and focus on the parts that received extra care.

3.1. INAS-AL NANOWIRES

In each of the following chapters we make use of the same material platform to host our Josephson junctions, both for semiconducting weak links (chapters 4 and 8) and for quantum dots with superconducting leads (chapters 5-7). This material platform is that of InAs-Al nanowires: quasi one-dimensional nanostructures consisting of a semiconducting core with a hexagonal cross-section, covered on several facets by a thin superconducting shell. The methods used to grow the wires are detailed in [173]; in short, the InAs cores are grown using molecular beam epitaxy, and the aluminium is grown epitaxially onto several of the cores' facets, without breaking vacuum. The aluminium is then also exposed to oxygen in-situ, in order to form a stable oxide with uniform coverage. Using this growth method, many tens of thousands of wires are grown simultaneously on a single growth chip, examples of which are shown in Fig. 3.1(a-b). Following growth these wires are generally stored in a vacuum environment to prevent further oxidation from occurring over longer periods of time.

In this thesis we make use of wires from two different growth chips, both sourced from the Niels Bohr Institute at the University of Copenhagen. The first batch we use, labeled "Qdev758", contains wires of nominal length $(7\pm2)\,\mu\text{m}$, diameter $(80\pm5)\,\text{nm}$, and a shell of thickness 6 nm, covering two facets of the hexagonal core.[1] These wires are used in chapter 4. In chapters 5 through 8 we make use of batch "Qdev1042", with wires of nominal length $(10\pm1)\,\mu\text{m}$, diameter $(111\pm5)\,\text{nm}$, and shell thickness 6 nm, again covering two facets. For our purposes these are rather similar wire-batches, with the main difference being that longer wires are easier to pick up and place using a micromanipulator (see Sec. 3.2). Additionally, the larger diameter of the second wire-batch could be of relevance for the multi-level effects underlying chapters 6 and 7, potentially a result of the reduced lateral confinement.

The choice for this specific material platform stems from several considerations. InAs nanowires are known to have a large spin-orbit coupling [90, 192] as well as a sizeable Landé g-factor [64, 283], essential for chapters 6 and 7. Combining the nanowires with a thin epitaxial Al shell [173] has furthermore been shown to produce large and hard induced superconducting gaps [53], persisting for magnetic fields above 1 T without undesirable in-gap states [78]. Crucially, Josephson junctions are readily patterned into the hybrid nanowires by selectively removing part of the Al shell using relatively straightforward wet-etching techniques; see Sec. 3.2.[2] This results in junctions with characteristics that are readily tunable through the field effect. The critical currents (and thus the Josephson energies) can be tuned-in situ with a nearby gate electrode, and can range from effectively zero to hundreds of nanoamperes [83, 296]. They can furthermore be described by just a single to several highly transparent Andreev bound states [118, 296], essential for the experiments in chapter 4. Thanks to these material properties, InAs-Al (as well as bare InAs) wires have an extensive history of successful integration into quantum dot experiments [54, 227, 316] and nanowire-based transmon qubits [182, 203], several of which underpin the experiments performed in this thesis.

---

[1] The quoted shell thickness is after in-situ oxidation.

[2] As shown in Fig. 3.1(d) the employed wet-etching recipe leaves behind oxide residuals, which can potentially deteriorate the electronic transport properties of the junction. Recently InAs-Al nanowire Josephson junctions were grown using in-situ shadow evaporation, through which one can circumvent this problem [157].

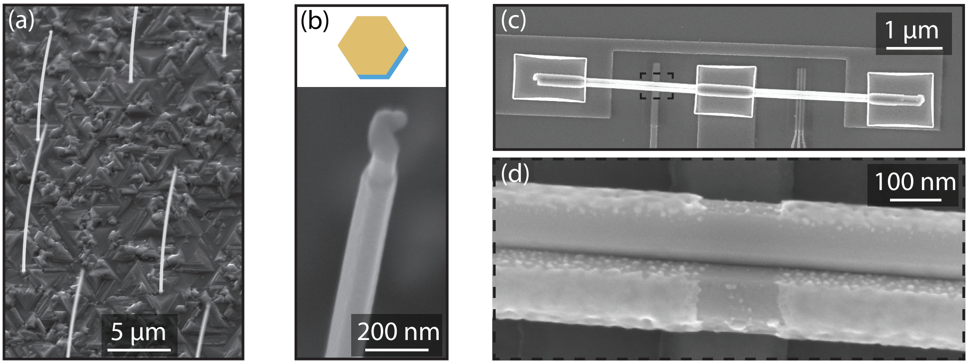

Figure 3.1: (a) Scanning electron micrograph (SEM) of an array of InAs-Al nanowires present on wirebatch Qdev1042. (b) SEM the top part of a nanowire taken from (a), revealing the boundary of the Al shell. (c) SEM of an etched and contacted nanowire placed on a device with the same layout as employed in chapter 5. (d) Zoom in of the junctions present in (c). This image further reveals that two wires were simultaneously placed down by accident.

The aforementioned qualities make InAs-Al nanowires an excellent platform. However, we would be remiss not to mention several viable alternative materials with comparable qualities. These are InSb-Al nanowires [37, 125], as well as InAs-Al and InSbAs-Al based two-dimensional electron gasses [160, 224, 288]. In recent years these have developed into mature hybrid material platforms, and for future experiments they could offer certain benefits, facilitating complex device layouts and improved junction characteristics. However, these materials require more advanced (and at times simply more involved) nanofabrication than InAs-Al based Josephson junctions, where the latter is the subject of the next section. Finally, we note that Josephson junctions based on materials that are not III-V semiconductors also hold promise for future experiments, among which candidates are isotopically purified germanium and lead telluride [128, 138, 277, 279, 311]

3.2. SAMPLE FABRICATION

The devices measured in this thesis are all fabricated in the cleanroom at the Kavli Nanolab Delft. While the general fabrication method is the same, each device differs slightly in its details, as over time parameters fluctuate and incremental optimizations are performed. We therefore do not provide an explicit recipe, but instead describe the procedure used to construct the device measured in chapters 6 and 7, which serves as a baseline for the development of similar devices. For brevity we furthermore do not include the various cleaning, spin-coating, baking and stripping steps, nor do we list the specific doses used in electron-beam lithography (EBL). A generic recipe is listed below, while a comparable but more exhaustive recipe is listed in appendix A of Ref. [68]:

1. Start with a commercially available 525 µm thick high-resistivity silicon wafer
2. Deposit a 100 nm layer of low-stress LPCVD SiN on both sides of the full wafer (performed at the Else Kooi Laboratory)

3. Sputter a 20 nm layer of NbTiN onto the front of the full wafer
4. Evaporate Pt/Pd EBL alignment markers, patterned with EBL
5. Dice wafer into coupons of 10 by 11.5 mm, proceeding with individual coupons
6. Define base-layer structures into NbTiN with SF_6/O_2 reactive ion etching, patterned with EBL
7. Deposit a 25–30 nm local PECVD SiN layer as gate dielectric, patterned with EBL and a buffered oxide etch
8. Deposit InAs-Al nanowires using a micromanipulator
9. Chemically etch away sections of Al shell with MF-321 developer (containing TMAH), patterned with EBL
10. Deposit 120 nm thick NbTiN to contact nanowires to base-layer, patterned with EBL and preceded by Ar milling
11. Dice coupons into 2 by 7 mm devices
12. Glue device to copper block and wire-bond to custom printed circuit board (PCB).

3.3. MEASUREMENT SETUP

CRYOGENIC SETUP

The devices studied in this thesis are measured at cryogenic temperatures. We do so in part to cool the devices far below their superconducting transition temperature T_c, where the superconductors are expected to be nominally quasi-particle free (see Sec. 2.1). As T_c is approximately 8–12 K for the NbTiN films and 1.2–1.6 K for the nanowires, this sets an initial requirement on the operating temperature. While the T_c of Al is already colder than outer space, such temperatures can be readily achieved through evaporative cooling using liquid ^{4}He or ^{3}He (down to around 1 K or 300 mK respectively, enabled by vacuum pumping). However, in order to maintain the coherence of our quantum devices we furthermore require thermal fluctuations of order $k_B T$ to be suppressed below the energy scales relevant in the experiment. As these can be as small as hundreds of MHz, corresponding to temperatures of tens of millikelvin, we require techniques beyond evaporative cooling. To this end we rely on commercially available, cryogen-free dilution refrigerators, capable of maintaining base temperatures of 10–20 mK over time-periods up to several years with substantial cooling power. In particular, all experiments performed in this thesis are measured in an Oxford Instruments Triton 200 system.

A detailed discussion of the workings of a modern dilution refrigerator are beyond the scope of this thesis; we refer to Ref. [354] for an elaborate review, and recommend the guide by Oxford Instruments for a concise introduction [24]. In short, a dilution refrigerator makes use of the unique properties of a ^{3}He – ^{4}He mixture. The ^{4}He atoms in the mixture are Bose particles, and they condense into a superfluid at cryogenic temperatures. The lighter ^{3}He atoms instead are fermions, which obey the Pauli exclusion principle and do not condense as easily (although, counter to intuition, superfluid ^{3}He does exist). The key working principle is that a mixture of these two substances cooled below 0.87 K undergoes a phase separation, separating into a concentrated ^{3}He phase floating on top of a more dense, dilute mixture, where a small percentage of the ^{3}He is dissolved in a superfluid ^{4}He background. This finite solubility persists to 0 K, which is key: it is the enhanced enthalpy of ^{3}He dissolved in ^{4}He compared to pure ^{3}He that makes the process of moving ^{3}He through the phase boundary endothermic. Enabled by distilling the ^{3}He from the mixture, this process endows the dilution refrigerator with its spectacular base temperature and cooling power.

PULSE TUBE NOISE

In the “dry” cryogen-free dilution refrigerator we use, no large baths of cryogens such as liquid nitrogen and helium are needed to cool down the system to the low-temperature regime where phase separation takes place. Instead, the system makes use of a pulse tube (PT) cooler: a sophisticated cryocooler capable of cooling down the lower stages of the refrigerator to 4 K by periodically compressing and expanding helium gas. While this strongly simplifies operation and automation compared to “wet” refrigerators, the usage of a PT comes at the cost of mechanical vibrations, which originate as follows (see Fig. 3.2). In our setup, the back-and-forth motion of gas inside the PT is driven by a helium compressor, whose high and low pressure lines are connected to the PT by a rotary valve. The valve has an internal disk that is incremented at a frequency of 140 Hz, with a full rotation frequency of 1.4 Hz, such that each half rotation switches the connection between the low and high pressure lines. While the helium compressor is located at a distance of several meters from the cryostat, the rotary valve itself is positioned on top of the frame of the cryostat, and its micro-stepping can be a tangible source of mechanical vibrations at 140 Hz. The dynamics of the helium gas inside the PT, propagating all the way down to the coldhead, instead result in acoustic vibrations at a frequency of 1.4 Hz. Note however that the latter should be interpreted as a pulse repetition frequency; it is the rate at which the aforementioned switches between compressor lines are repeated, while the actual frequency content generated by the dynamics of the gas can be at much higher frequencies. Indeed, the dominant spectral content of the acoustic vibrations was previously found to be in the 5–10 kHz range [147].

Care is taken by the manufacturer to dampen these noise channels inside the dilution refrigerator by using copper braids to decouple the PT from the experimental plates in addition to building a stiff support structure. However, our initial experiments using offset-charge sensitive transmons (such as those used in chapters 4 and 8) were still strongly hindered by these vibrations. As shown in Fig. 3.3(a), we found that the charge dispersion, that is, the offset-charge dependence of the transmon transition frequency, was fully smeared out during standard operation. Turning the pulse tube off for several seconds caused this effect to disappear, and the charge dispersion to be fully recovered.[3] This finding was further substantiated by the time dependence of the measured signal: estimating the power spectral density of the readout channel at a fixed frequency and gate point, we identify distinct peaks at multiples of 1.4 Hz, the rate at which the rotary disk makes a full rotation [see Fig. 3.3(b)]. These peaks completely disappear when the PT is turned off. As no peaks are found at 140 Hz, the vibrations originating from the rotary valve itself do not appear to be the source of the noise. This suggests that it is instead the acoustic vibrations resulting from the dynamics of the helium gas that couple into the sample, effectively modulating the qubit frequency by scrambling the offset

---

[3] The system remains at base temperature for at least 60 seconds with the PT turned off.

charge, and thereby obfuscating the intended charge-sensitive measurements.

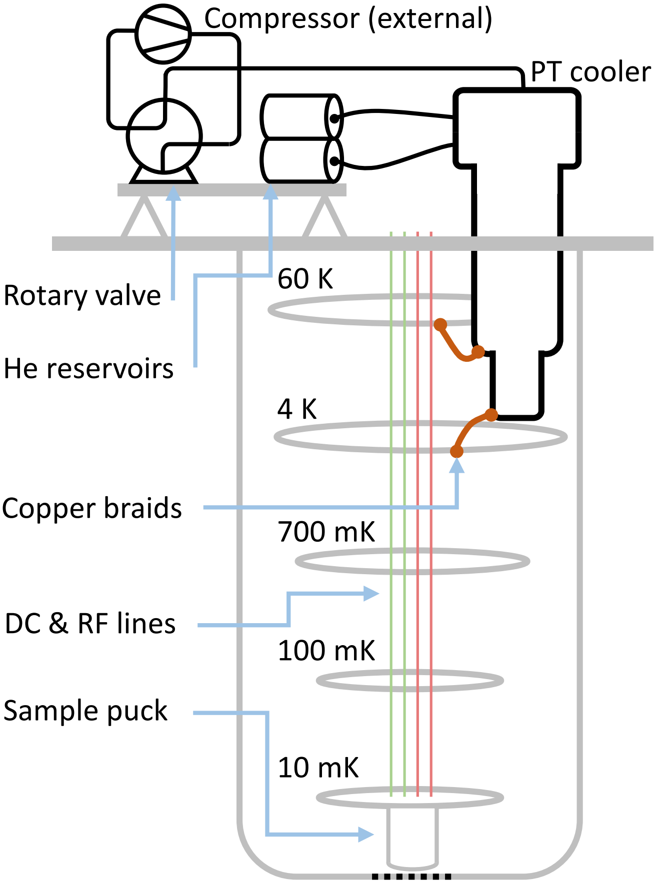

Figure 3.2: Schematic depiction of the connection between the cryogen-free dilution refrigerator and the relevant elements of the pulse tube (PT) cooler. Various other parts of the setup are omitted, including radiation shields, the superconducting magnet, and the entire dilution unit. Image adapted from Ref. [147].

Interestingly, we found that the PT noise was particularly strong in one specific setup. Cooling down the same device (together with its entire enclosure, see Sec. 3.3) in a second, nominally identical dilution refrigerator resulted in no measurable PT noise, while the noise reappeared upon returning the sample to the first setup. This indicated that it was not a fundamental limitation of the type of cryostat, but unique to the specific setup employed. We spent significant effort investigating how to mitigate the "pulse tube noise" in this setup, involving over 14 cooldowns of the device during a period of 7 months. While most attempts did not lead to improvement, we hope that a detailed account of the methods employed can be of use for future users encountering similar problems.

Before we detail our investigation, we note that to us it was not obvious how vibrations are converted to electrical noise affecting the induced charge on the transmon island. One candidate mechanism is through microphonics, where acoustic vibrations cause fluctuations in the (intended or spurious) capacitance of the various elements present in the setup, in turn resulting in time-fluctuating voltages. An alternative is the triboelectric effect, where electrostatic charges build up when materials are brought in and out of contact (such as encountered when rubbing balloons against your sweater), during which charges move from one material to the other and create a net charge imbalance. Yet another possibility is vibration-induced, spatially-varying oscillations of magnetic fields, which couple to electrical conductors through Faraday's law of induction.

Given no prior knowledge of the exact conversion mechanism taking place, our initial effort was focused on minimizing the vibrations. We began our modifications outside the cryostat, where changes can be made without requiring a full warm-up and cooldown of the system. We first verified that (with the PT turned off) similar degradation in charge dispersion could be achieved by gently and periodically perturbing the cryostat mounting frame with a hammer, showing that vibrations at the level of the frame are already problematic. This prompted us to weigh down the frame with an additional 200 kg. We then rerouted the room-temperature tubes and hoses connected to the PT, bending them into various shapes and angles. The tubes and helium gas reservoirs were also held in place with additional straps, as well as left fully floating. Finally, we replaced the driver that generates the 140 Hz electrical signal incrementing the rotary valve with a linear ramp driver from Precision Motion Controls, which is intended to result in smoother micro-stepping. While such measures led to improvements in previous experiments, we did not detect significant changes.

A second round of mechanical changes took place inside of the cryostat. We tried both strongly strapped down and fully (physically) floating DC lines, we made new brackets for tighter mounting of control line filters, and had a service engineer from Oxford Instruments re-fasten all relevant bolts and screws, making sure all elements were made out of molybdenum to avoid thermal contraction and expansion. Additionally, experiments were performed both with the large three-axis vector magnet inside and outside of the cryostat (see the next section). None of these efforts led to changes in the observed behaviour of the device, whose smeared out charge dispersion was the guiding metric.

After having exhausted these options of mechanical isolation, effort was taken to reduce electrical noise in the channels that could affect the transmon island. Considering only its capacitive coupling to various elements [see Fig. 3.3(c)], we speculated the noise had to originate from (i) the gate voltage used to control the offset charge, (ii) the ground potential, or (iii) spurious coupling to the feedline used to send signals in and out of the device. The latter appeared to be a likely candidate, as the coaxial line used to input RF signals had previously been identified as the main channel for PT noise in a spin qubit device [147]. They found that when coaxial lines are cooled down to cryogenic temperatures, thermal contraction of the dielectric causes it to be squeezed around the inner conductor, forming a gap between inner and outer conductor. Vibrations can then lead to both microphonic and triboelectric effects. While a plausible mechanism, placing high-pass filters with a cut-off frequency beyond tens of MHz on both the input and output ports of the device did not lead to appreciable changes, which should have effectively suppressed this noise channel. A thorough investigation and modification of the cryostat grounding was also fruitless, with no appreciable changes for various grounding

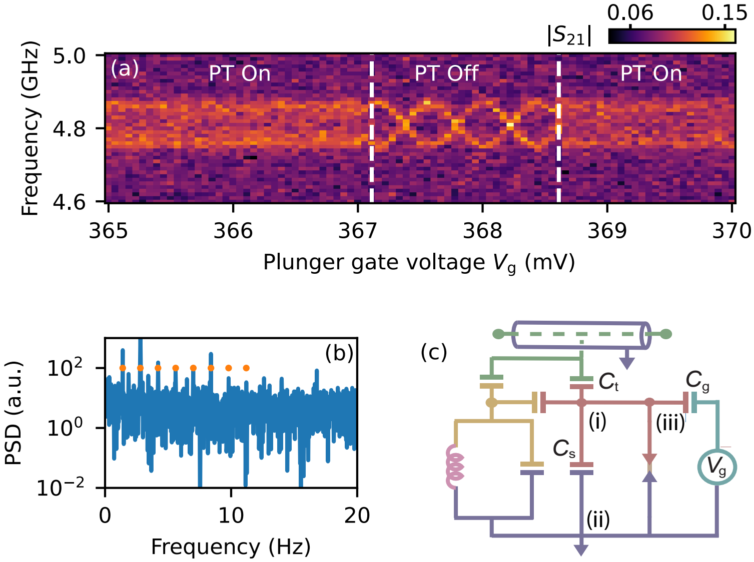

Figure 3.3: Pulse tube noise in an offset-charge-sensitive transmon qubit. (a) Two-tone spectroscopy measurement of the transmon qubit frequency versus the plunger gate voltage, which tunes the offset charge on the island. Data is shown both with the pulse tube (PT) cooler turned on and off. (b) Power spectral density of the readout resonator signal at a fixed readout frequency. The data is acquired over 120 seconds with a bandwidth of 100 Hz, with the PT turned on. Orange dots indicate multiples of 1.4 Hz. When the PT is turned off, the spectrum is featureless. (c) Circuit model of the offset-charge sensitive transmon and its readout and control elements.

schemes. This included a mode of operation in which gate voltages were applied with respect to the “cold” PCB ground in order to circumvent thermoelectric effects. The DC lines that are used to tune the offset charge of the island were the last candidate we investigated. We use cryogenic ribbon cables (“looms”) containing polyethurane-coated Cu (down to 4K) and NbTi wires (down to mK) to route the DC voltages from room temperature to the device. We tried incorporating second order RC filters with a cutoff frequency at 100 Hz (down from the 10 kHz filters typically employed throughout this thesis) into this signal path, in order to filter out the high frequency content produced by the gas dynamics. Again no changes were detected. We do note that we did not investigate filters with cut-off frequencies lower than the 1.4 Hz pulse repetition frequency. Although highly impractical for generic measurements, in hindsight this would have been a viable option for debugging. Nevertheless, the 1.4 Hz voltage noise that could be found on the DC lines using the techniques of Ref. [147] was below the single micro-volt level, which seemed too small to explain the detected smearing of the charge dispersion.

This left us with no remaining avenues of investigation. However, a potential advance was encountered by chance in preparation for chapter 8, where initial characterization experiments were performed with a metal layer deposited on the backside of the chip. In an attempt to ground the metal backside of the device, we chose not to secure the chip onto its copper mounting block using electrically insulating Apiezon N vacuum grease, as had been done in all previous experiments. Instead we used Electrolube silver conductive paint, an electrically conductive epoxy. This led to a device with stable, untarnished charge dispersion, and no signs of noise at 1.4 Hz. We initially attributed this to a change in the chip design; the device consisted of various modifications with respect to the chip that originally showed the PT noise. However, at a later stage the actual device used in chapter 8 was cooled down. Given that the metal layer was now on the front-side of the chip, we did not see the need for a conductive epoxy, such that we secured the chip using GE varnish, which is an insulating glue used for cryogenic anchoring. We found that the PT noise had returned, similar to our past experiments. Upon identifying this we re-glued the same device with silver epoxy, and the charge dispersion was once-more restored [See Fig. 8.7(b-c)]. While no definitive conclusions can be made from these correlations, we speculate that the source of the noise might have been due to charge buildup in the nominally insulating silicon substrate. Indeed, while we make use of high-resistivity silicon wafers (≥10 000 Ωcm), we later found out that this specific type is N-doped with phosphorous, suggesting that a small concentration of charge carriers might still be present. Future experiments with intrinsic silicon wafers could confirm these speculations. Nevertheless, the exact nature of the mechanism and why this problem would be particularly strong in one specific setup remains unknown.

RADIATIVE SHIELDING

The devices measured in this thesis make use of magnetic fields in the range of 1 mT to 1 T, enabled by a large, three-axis 6-1-1 vector magnet mounted at the 4 K stage of the dilution refrigerator. Compared to conventional dilution refrigerators, the mass of the magnet significantly adds to the overall cool down time of the system, extending it to several days. To overcome this disadvantage, the system is equipped with a bottom loading mechanism, through which a demountable “puck” that houses the device under test can be loaded though a series of baffles, attaching directly to the mixing chamber plate with a bolted contact. With this in place, an exchange between measurement devices operated at base temperature can be enacted within twelve hours and by a single user. However, the cost of this modification is a concession in radiative shielding: due to geometry constraints from the magnet and the loading mechanism, the coldest shield surrounding the device is thermalized at the still plate, with a temperature of approximately 700 mK. Given that the aluminium nanowire shells used in this thesis have a critical temperature that can be as low as 1.2 K, this shield forms a radiative environment that remains modestly capable of exciting non-equilibrium quasiparticles, detrimental for device performance. The baffles through which the puck is inserted are potentially also not fully light-tight, letting in radiation from even higher temperature stages. To combat this, we adopt a box-in-a-box approach to house our devices, designed with the help of dr. Olaf Benningshof and machined by Nico Alberts. It’s composition is detailed in the follow paragraph.

As discussed above and depicted in Fig. 3.4, the chips hosting the devices to be measured are first mounted onto a copper block and connected to a PCB via wirebonds, after which a first lid is placed onto the block. This block is then screwed into a larger enclosure, which is nominally light tight, with the exception of venting ports on its side that are included for achieving a good vacuum.[4] Although it is not shown in the figure, the outside of the enclosure is painted with a mixture of 1 mm large silicon carbide grains, Stycast 2850FT, and carbon black powder [23]. This mixture is specifically designed to absorb in the EHF and THF frequency ranges, at the lower end of which common IR absorbers are ineffective. The enclosure is then finally mounted inside the puck, which is filled with microwave absorbing Eccosorb foam to dampen spurious modes. We further note that the enclosure is designed such that the center of the chip aligns with the center of the fields produced by the magnet.

Performing measurements with and without the enclosure, we find a marked reduction in the density of non-equilibrium quasiparticles inside the device; following the method of Ref. [287] we estimate an effective device temperature of 90 mK with the lid in place, down from 190 mK [313] [c.f. Eq. (2.11)]. This resulted in a strong increase in the time between quasiparticle-induced parity switches measured in offset charge sensitive transmon devices, from tens of microseconds to several milliseconds, and likely helped facilitate the long parity lifetimes of the quantum dot devices measured in chapters 5 to 7. Further improvements at the level of the setup could potentially be made through more elaborate filtering of the RF lines used to send signals into and out of the device [286], which we did not explore in detail.

EXTENDED INFORMATION

Of course the quality of our experiments also relies on various other elements. At a global level, the wiring of the cryostat is done according to the philosophy of Ref. [171], while the microwave measurement techniques and calibration procedures are as detailed in the reviews of Refs.[34, 99]. Further details about the experimental methods are also given in the supplementary sections of the chapters that follow. This includes fabrication procedures, wiring diagrams, the measurement equipment used, and both scanning electron microscope and optical images of the devices studied.

---

[4] The ideal trade-off between an IR-free environment and high vacuum at the chip level remains to be investigated.

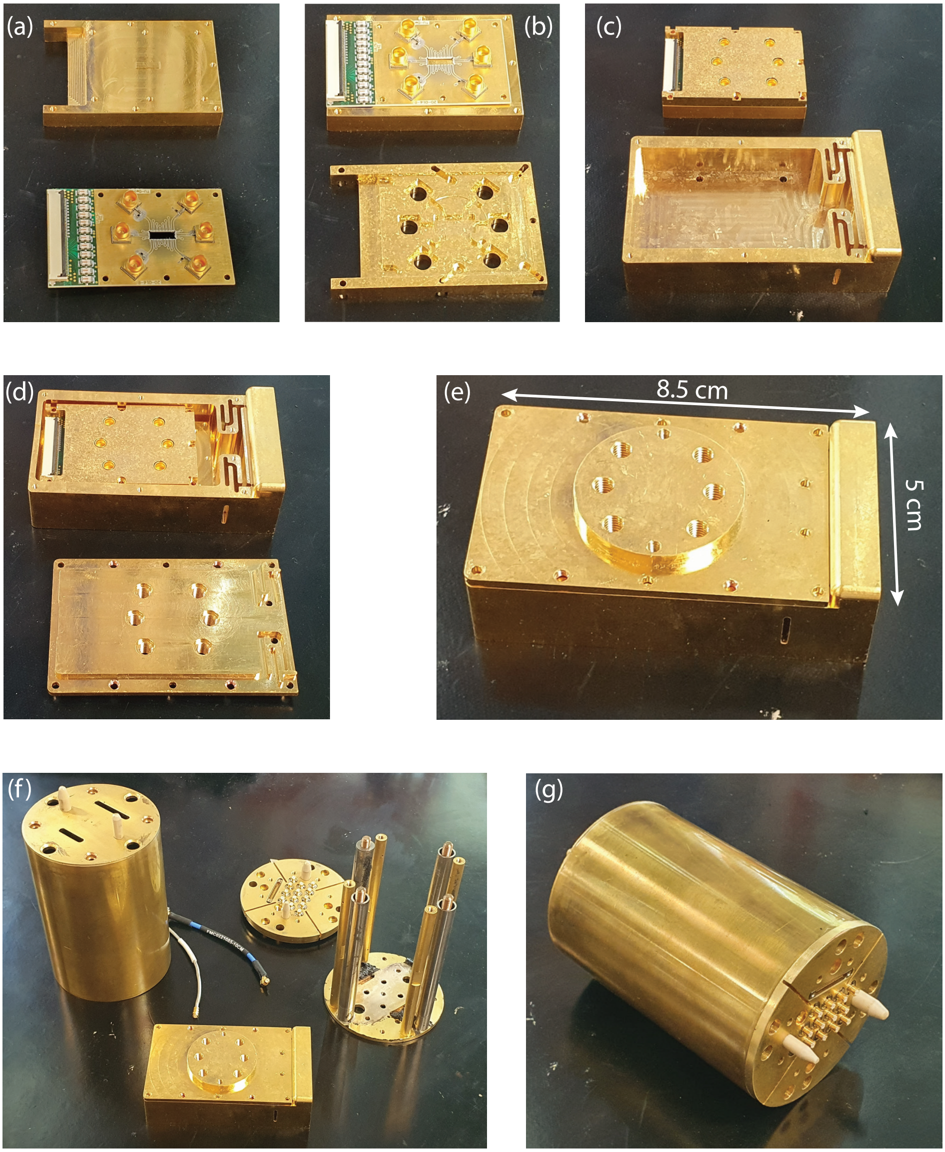

Figure 3.4: Overview of custom device shielding. (a) The chip (not shown) is glued onto a copper block and wirebonded to a custom designed printed circuit board, hosting 24 DC lines connected via an FFC connector and 6 RF lines connected via SMP connectors. (b-e) A lid is then placed onto the assembled block, which is screwed into a second, larger enclosure. (f-g) The enclosure is subsequently connected to flexible RF and DC lines, and embedded into the puck. Not shown are various SMP connectors, the flexible DC cable, and the infrared absorbing paint on the outside of the rectangular enclosure (see text). The components of the enclosure are made from gold-plated, high-purity, annealed copper.

4

OBSERVATION OF VANISHING CHARGE DISPERSION OF A NEARLY-OPEN SUPERCONDUCTING ISLAND

Isolation from the environment determines the extent to which charge is confined on an island, which manifests as Coulomb oscillations such as charge dispersion. We investigate the charge dispersion of a nanowire transmon hosting a quantum dot in the junction. We observe rapid suppression of the charge dispersion with increasing junction transparency, consistent with the predicted scaling law which incorporates two branches of the Josephson potential. We find improved qubit coherence times at the point of highest suppression, suggesting novel approaches for building charge-insensitive qubits.

The work in this chapter has been published as: A. Bargerbos, W. Uilhoorn, C. K. Yang, P. Krogstrup, L. P. Kouwenhoven, G. de Lange, B. van Heck, and A. Kou, Observation of vanishing charge dispersion of a nearly-open superconducting island, Physical Review Letters **124**, 246802 (2020).

4.1. INTRODUCTION

The manipulation of single charge carriers has been one of the most important advances in condensed matter physics, enabling a wide range of nanoelectronic technology in areas such as detection, thermometry, and metrology [163, 194, 201, 218, 243]. The control of single charge carriers is made possible by the quantization of charge on mesoscopic islands well-isolated from the environment. Charge quantization manifests as Coulomb oscillations: periodic dependence of the system's observables reflecting the energy cost of adding an additional charge to the system. As the coupling strength to the environment increases, quantum fluctuations progressively delocalize the charge, suppressing Coulomb oscillations. In normal state conductors, it is well-known that this suppression occurs through single-electron tunneling [5, 92, 137, 143, 166, 212, 225, 228, 345].

In the case of superconducting islands, the coupling to the environment instead occurs via coherent Cooper pair tunneling. In conventional tunnel junctions, the latter is mediated by a large number of weakly transmitting transport channels, characterized by the Josephson energy E_J. In this case, the size of the charge dispersion depends only on the ratio between the charging energy E_c and E_J, as illustrated by the Cooper pair box ($E_\mathrm{J}/E_\mathrm{c} \approx 1$) [38] and the transmon ($E_\mathrm{J}/E_\mathrm{c} \gg 1$) [162]. The Cooper pair box has large charge dispersion, whereas for the transmon charge dispersion is exponentially suppressed in the ratio $E_\mathrm{J}/E_\mathrm{c}$ [15, 162]. This behaviour originates from quantum tunneling of the superconducting phase difference ϕ below the Josephson potential barrier connecting two energy minima at $\phi = 0, 2\pi$.

The situation becomes more interesting if the Cooper pair tunneling is mediated by a single transport channel with high transparency [14]. In this limit, the energy spectrum of the Josephson junction is characterized by a narrowly avoided level crossing at $\phi = \pi$, and imaginary-time Landau-Zener (ITLZ) tunneling [14, 245] acts to prevent quantum tunneling trajectories from reaching the energy minimum at 2π. The charge dispersion of the superconducting island then vanishes completely as the transparency approaches unity. While some weak suppression of Coulomb oscillations has been observed in weak-links [199, 260], the effect of ITLZ tunneling on charging effects has eluded experimental verification because of the stringent requirements for ballistic Josephson junctions. However, recent advances in nanofabrication and nanowire growth [173] have enabled the development of superconductor-semiconductor-superconductor junctions with a small number of highly transmitting modes [106, 320]. Experiments in such devices have detected a single mode with nearly perfect transmission, attributed to resonant tunneling through an accidental quantum dot in the junction [118, 296]. Charge-sensitive devices connected to reservoirs via quantum-dot-based junctions are thus ideal for the investigation of near-ballistic Josephson junction behaviour.

In this Letter, we experimentally investigate the charge dispersion of a superconducting island connected to a reservoir via a semiconducting weak-link hosting a quantum dot. The device constitutes an offset-charge-sensitive (OCS) nanowire transmon, also known as a gatemon [70, 167, 182, 286]. By in-situ tuning of the transparency of the weak-link using an electrostatic gate, we observe its charge dispersion decrease by almost two decades in frequency at a rate far exceeding exponential suppression in $E_\mathrm{J}/E_\mathrm{c}$. The observed gate dependence of the charge dispersion is modeled by tunneling through a resonant level, incorporating the effect of ITLZ tunneling. This model agrees well with

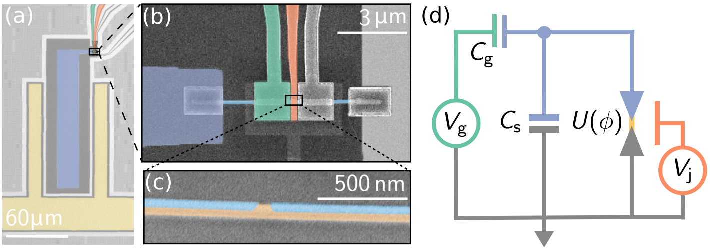

Figure 4.1: (a) False-color optical microscope image of the qubit. It consists of an island (purple) capacitively coupled to the ground plane (grey) and a CPW resonator (yellow). (b) Scanning electron micrograph (SEM) of the InAs-Al nanowire connecting the island (left) to the ground plane (right). Its weak-link is tuned by the junction gate (red), while the island gate (green) tunes n_g on the island. The unused gate is left uncolored. (c) False-color SEM of the nanowire before deposition of the top gates, showing the InAs core (orange) and the aluminum shell (blue). (d) Effective circuit diagram of the qubit. The weak-link with Josephson potential $U(\phi)$ is shunted by the island capacitance C_s, V_g tunes n_g, and V_j tunes the transparancy of the junction.

the measured suppression of charge dispersion, suggesting near-unity junction transparency. Finally, we observe improved qubit coherence times T_2^* and T_2^{echo} in regions of vanishing charge dispersion, which reflects the strong reduction in the charge sensitivity of the qubit.

4.2. EXPERIMENTAL SETUP & METHOD

The measured gatemon is shown in Fig. 4.1. The details of the device and experimental setup are provided in Ref. [313] so we highlight only the relevant features here. The device consists of a superconducting island coupled to ground via an Al/InAs/Al weak-link [70, 173, 182]. The weak-link (shown in Fig.4.1c) is defined by etching away ∼ 100 nm of the aluminum covering the InAs nanowire. A quantum dot is formed in the junction due to band-bending or disorder [53, 79]. The junction is shunted by the island capacitance C_s, which predominantly sets the charging energy $E_c \approx 750$ MHz. Electrostatic gates tune both the transparency of the junction and the dimensionless offset charge $n_g = C_g V_g / 2e$ on the island. The gatemon is capacitively coupled to a NbTiN $\lambda/2$ coplanar waveguide resonator [174] in order to excite and readout the system using standard dispersive readout techniques [32].

We measure the dependence of qubit's ground to first excited state transition frequency on the offset charge on the island $[f_{01}(n_g)]$ using two-tone spectroscopy as shown in Fig. 4.2a. Each measurement results in two sinusoidal curves shifted by half a period, belonging to qubit transitions for even and odd island parity. Their simultaneous detection is due to quasiparticle poisoning on timescales faster than the measurements[1] [282]. We define the qubit frequency f_{01} as the point of charge degeneracy between even and odd island parity and the charge dispersion δf_{01} as the maximal frequency difference between the two parity states, reflecting the maximal energy cost of charging the island with an additional electron.

Figure 4.2a also demonstrates the behavior of $\{f_{01}, \delta f_{01}\}$ at different V_j near full deple-

---

[1] Measurements are integrated for 50 ms while quasiparticle poisoning takes place on a timescale of ∼ 100 μs [313]

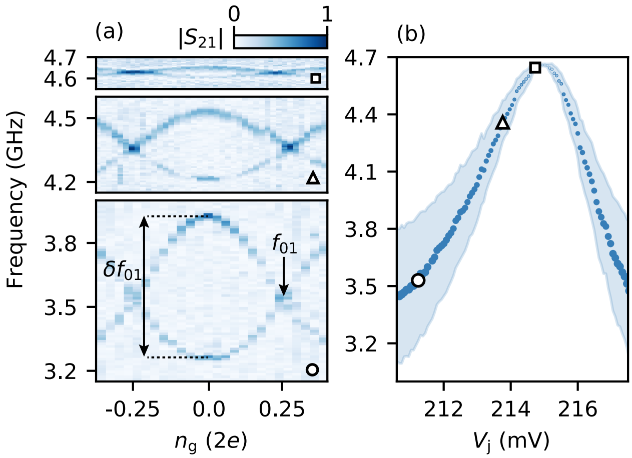

Figure 4.2: Evolution of the qubit frequency and charge dispersion as a function of V_j. (a) Normalized two-tone spectroscopy measurements of the $0 \rightarrow 1$ transition versus the offset charge tuned by V_g, measured at three successive values of V_j (bottom to top): 211.2, 213.8, and 214.7 mV. (b) Extracted f_{01} (markers) and δf_{01} (shading and marker size) versus V_j. Open markers indicate the positions of panel (a).

tion of the junction. In the lowest panel, we observe $f_{01} = 3.539$ GHz and $\delta f_{01} = 679$ MHz at $V_j = 211.2$ mV. As V_j is increased, in the middle and top panel of Fig. 4.2a, f_{01} increases to 4.629 GHz while δf_{01} decreases to 39 MHz. Figure 4.2b summarizes the dependence of f_{01} and δf_{01} as a function of V_j. We observe that the qubit frequency exhibits a peak, increasing by a factor of 1.35 before decreasing again. The rise in f_{01} is accompanied by a strong decrease in δf_{01}, suppressing by almost two orders of magnitude at the peak. This behaviour is consistent with the presence of a quantum dot in the junction, which has been linked to peaks in the critical current that coincide with transparencies close to unity [118, 296].

Due to finite stray capacitance, the transparency of the junction can also be tuned using the island gate. As shown in Fig. 4.3a, we observe suppression of the charge dispersion by tuning the island gate voltage V_g with V_j fixed at a value where the charge dispersion is already close to the qubit linewidth $\gamma_{01} \approx 10$ MHz[2] . We note that δf_{01} can no longer be discerned below γ_{01} since the two parity transitions start to overlap.

We can probe the suppression of Coulomb oscillations to below the limit set by γ_{01} by measuring the charge dispersion of higher-order qubit transitions, which have a rapidly increasing charge dispersion δf_{0n} [14, 162]. We repeat the measurement for increased driving powers in order to excite higher order qubit transitions. As shown in Fig. 4.3b-c, the $0 \rightarrow 2$ and $0 \rightarrow 3$ multi-photon transitions indeed exhibit larger charge dispersion than the $0 \rightarrow 1$ transition. Even these larger charge dispersions vanish down to the linewidth γ_{0n}, indicating a particularly strong suppression.

Beyond the remarkable suppression of the charge dispersion, we note that δf_{01} does not depend monotonically on f_{01}. The charge dispersion of the $0 \rightarrow 1$ transition is suppressed down to the linewidth over several periods, while the qubit frequency slowly in-

---

[2] These measurements are performed in a different cooldown of the same device.

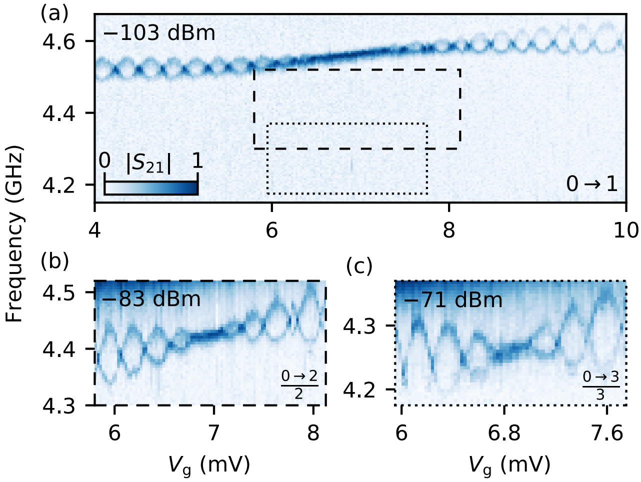

Figure 4.3: Island gate dependence of the charge dispersion. (a) Normalized two-tone spectroscopy measurement of the 0 → 1 transition over a range of V_g encompassing many periods in offset charge. The charge dispersion suppresses down to the linewidth and subsequently recovers, while the qubit frequency increases over the entire gate range. (b)-(c) Multi-photon transitions 0 → 2 and 0 → 3, excited with increased driving powers. The transitions follow the same trends as panel (a), exhibiting an increased charge dispersion that still suppresses down to the linewidth at its minimum. Powers listed are at the sample input.

creases over the entire range of V_g. Such a dependence cannot occur for superconducting tunnel junctions or a single mode superconducting quantum point contact (SQPC) [28], where larger larger qubit frequencies always result in lower charge dispersions [14, 162]. This behavior is the result of the quantum dot in the junction, in which case the charge dispersion need not be a monotonic function of the qubit frequency, as we explain below.

4.3. MODELING & RESULTS

We develop a quantitative understanding of the device using a simplified model of a quantum dot between two superconducting leads known as the resonant level model [27, 82, 104, 108]. As shown in Fig. 4.4a, we consider the presence of a single spin-degenerate level in the junction. The level has an energy ϵ_0 relative to the Fermi level, and is coupled to two identical superconductors with superconducting gap Δ via the (spin-degenerate) tunnel rates Γ_l and Γ_r. Our simple model does not include the electron-electron interactions of the quantum dot. The potential of the junction $U(\phi)$ is determined by the energies of a single pair of spin degenerate ABS (shown in Fig. 4.4b). Their energies have to be calculated numerically for general parameter values but can be expressed analytically in certain limits [82, 108]:

$$E_{\pm}(\phi) = \pm\widetilde{\Delta}\sqrt{1-\widetilde{D}\sin^2\phi/2}, \quad \widetilde{D} = \frac{4\Gamma_l\Gamma_r}{\epsilon_0^2+\Gamma^2},$$
$$\widetilde{\Delta} = \begin{cases} \Delta, & \text{if } \Gamma \gg \Delta, \epsilon_0 \\ \Gamma & \text{if } \Gamma \ll \Delta \text{ and } \epsilon_0 = 0, \end{cases} \tag{4.1}$$

where $\Gamma = \Gamma_l + \Gamma_r$. Here the ABS take on the same functional form as for an SQPC [26] but with an effective superconducting gap $\widetilde{\Delta} < \Delta$. The form of the effective junction transparency $\widetilde{D}$ also explicitly reflects a Breit-Wigner type resonant tunneling process, maximized for equal tunnel rates ($\delta\Gamma = |\Gamma_l - \Gamma_r| = 0$) and particle-hole symmetry ($\epsilon_0 = 0$).

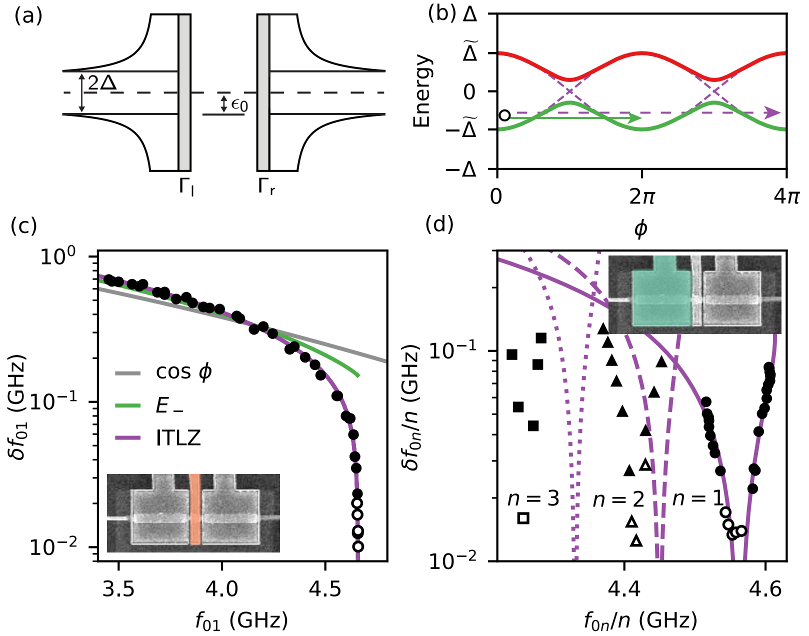

Figure 4.4: Suppression of charge dispersion mediated by a resonant level. (a) Schematic depiction of a resonant level coupled to two identical superconducting leads. (b) Calculated energy-phase dependence of the ABS in the resonant level model for $\widetilde{D} = 0.9$ (solid) and $\widetilde{D} = 1$ (dashed) with $\Gamma = \Delta$. Arrows indicate the available quantum tunneling trajectories for the two cases. (c) Extracted qubit frequency versus charge dispersion measured in Fig. 4.2 by varying V_j. Solid lines show fits using three models of $U(\phi)$: a sinusoidal potential, the negative energy ABS branch of the resonant level model, and a potential considering ITLZ tunneling between both ABS branches. (d) Extracted qubit frequency and charge dispersion of the first three transmon transitions measured as a function of V_g shown in Fig. 4.3. The solid line shows a fit of the 0 → 1 transition with the ITLZ model, and the dashed and dotted lines show the resulting 0 → 2 and 0 → 3 transitions respectively. Open markers denote an upper bound on the charge dispersion based on the linewidth when $\delta f_{0n} \leq \gamma_{0n}$ and are not included in the fits.

We now discuss the expected behavior of charge dispersion within this model. Under the typical assumptions of low to moderate values of $\widetilde{D}$ and $\widetilde{\Delta} \gg E_c, k_B T$, only the ground state of the junction is occupied so that charge transfer occurs through E_-. In this regime, charge dispersion is exponentially suppressed in $\widetilde{\Delta}\widetilde{D}/E_\mathrm{c}$, comparable to the case of tunnel junctions and governed by tunneling of the phase under the potential barrier of E_- [15, 162]. As $\widetilde{D} \to 1$, however, the energy gap between the ABS vanishes. Due to ITLZ tunneling, the probability amplitude for the quantum tunneling trajectory to stay in the lower ABS branch vanishes linearly with the reflection amplitude $\sqrt{1-\widetilde{D}}$ [14, 134]. As a consequence 2π-tunneling processes are suppressed, and so is the charge dispersion. When $\widetilde{D} = 1$, the charge dispersion eventually saturates to a small value set by tunneling through a 4π-wide potential barrier given by $\widetilde{\Delta}\cos\phi/2$.

Based on the discussion above, we fit the measured dependence of $\{f_{0n}, \delta f_{0n}\}$ using three junction models: a sinusoidal potential, a potential considering only the E_- ABS branch of the resonant level model, and a potential including ITLZ tunneling. The numerical details of the procedure are described in the supplementary information (see Sec. 4.5). In Fig. 4.4c, we plot the measured data for the dependence of δf_{01} on f_{01} while V_j is changed. In order to fit the data we assume that V_j tunes only ϵ_0 while $\Gamma_\mathrm{l} = \Gamma_\mathrm{r}$ are held constant. Furthermore, we fix $\Delta = 53$ GHz based on DC transport experiments on similar nanowires [79]. The model based on a sinusoidal potential, which describes a tunnel junction with many low-transmission channels, is completely inconsistent with our data. Including only the presence of E_- results in a fit that matches the initial decrease in δf_{01} but is unable to capture the rapid suppression of the charge dispersion at the peak in qubit frequency. The model including ITLZ tunneling accurately describes the full range of data, requiring transparencies close to unity as shown in Fig. 4.9. We find that $\Gamma = 23$ GHz, which gives an effective gap $\widetilde{\Delta} = 16$ GHz at the point of maximal suppression. The data and fit clearly demonstrate reaching the diabatic regime of ITLZ tunneling.

We additionally use the model including ITLZ tunneling to fit the V_g dependence of $\{f_{0n}, \delta f_{0n}\}$ in Fig. 4.4d. Based on the position of the island gate to the left of the junction as well as screening by the junction gate, we assume that V_g tunes only Γ_l with all other parameters held constant. The resulting fit matches the characteristic shape of the data, showing strong suppression when $\delta\Gamma = 0$ and reproducing the non-monotonic relationship between qubit frequency and dispersion. The measurements also show that the anharmonicity $\alpha = f_{12} - f_{01}$ remains finite for all $\widetilde{D}$, essential for operation as a qubit. While the fit is excellent for the $0 \to 1$ transition, it requires a significantly lower superconducting gap $\Delta = 18.6$ GHz. Additionally, the predicted qubit anharmonicities (indicated by the lines in Fig. 4.4d) are lower than the measured anharmonicities, while the shapes of the curves remain accurate. This systematic deviation indicates that the underlying junction potential might be shallower than captured by our model. We speculate that the discrepancies in Δ and the anharmonicities could be due to omitting the electron-electron interactions of the quantum dot, which has previously been found to suppress the critical current and alter the energy-phase dependence of the ABS [118, 195, 209, 321].

Finally, we investigate the qubit's relaxation and coherence times in the presence and absence of resonant tunneling. Shown in Fig. 4.5, we compare two cases: strong ITLZ tunneling with vanishing charge dispersion, and essentially adiabatic behaviour with $\delta f_{01} \approx 200$ MHz. We leverage the non-monotonic $\{f_{01}, \delta f_{01}\}$ dependence encoded by V_g to make this comparison at nominally equal transition frequency in the same device.

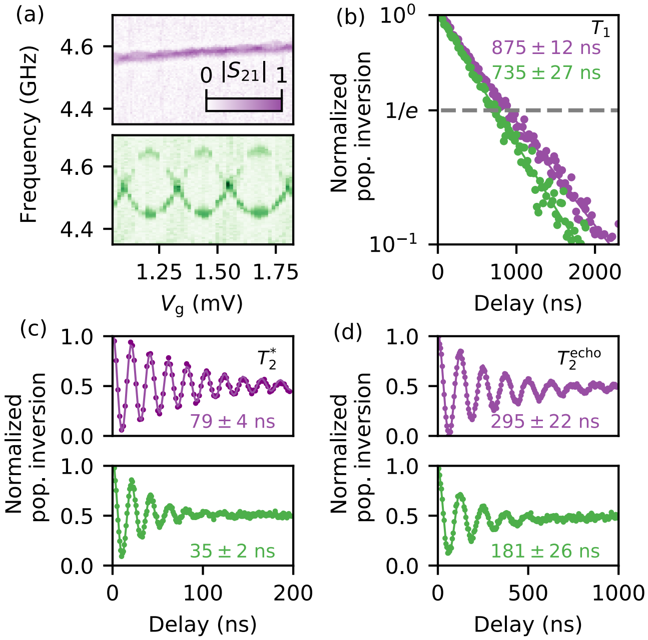

Figure 4.5: Time-resolved qubit measurements for $\widetilde{D} \to 1$ (purple) and $\widetilde{D} \approx 0.8$ (green) in the junction measured at equal qubit frequency. (a) Two-tone spectroscopy measurements for the two cases. The remaining panels show measurements of T_1 (b), T_2^* (c) and T_2^{echo} (d).

We find that the suppression leads to a moderately enhanced T_1. However, we do not expect charging effects to have a large effect on T_1 since the measurements are performed at $n_g = 0.5$ where relaxation processes should be mostly charge-insensitive. We find, however, that both T_2^* and T_2^{echo} improve considerably for the case of vanishing charge dispersion, reflecting the drastic reduction in sensitivity to charge noise. This is similar to the situation in conventional transmon qubits, where the exponential suppression of charge dispersion in E_J/E_c is also accompanied by a strong increase in coherence times [162]. However, in order to achieve the same level of δf_{01} suppression in a conventional transmon for the E_c of this device one would require $E_J/E_c \geq 30$, whereas we are operating at an effective $E_J/E_c \approx 5$. Even in the limit of full suppression, however, both relaxation and coherence times are short compared to results achieved in other gatemons [203]. We attribute these lower coherence times to ineffective radiation shielding and the quality of dielectrics used, which can be improved in future devices.

4.4. CONCLUSIONS

In summary, we measure the suppression of charge dispersion in an OCS gatemon with a highly transparent junction. We develop a model of tunneling through a resonant level in the junction that agrees with the dependence of the charge dispersion on both gates and indicates that, through tuning the parameters of our resonant level properly, we reach near-unity transparencies in our device. Furthermore, the observed rate of suppression of the charge dispersion obeys the scaling law dictated by ITLZ tunneling between ABS. Finally we demonstrate that the suppression improves the qubit's coherence, reflecting the strong decrease in charge sensitivity.

The vanishing of charging effects investigated here has implications for the design of hybrid circuits incorporating ballistic Josephson junctions [44, 55, 122, 242, 312, 327]. In particular, this vanishing may have positive implications for future gatemons [70, 167, 182, 203, 286]. The guaranteed vanishing of charge sensitivity for $\widetilde{D} \to 1$ while the anharmonicity remains finite places much less stringent requirements on E_c compared to other transmon implementations, allowing for faster qubit manipulation and strongly reducing the qubit's physical footprint. The natural magnetic field compatibility of S-QD-S transmons also sets the stage for detecting and manipulating Majorana zero modes [102, 120, 245]. Finally, independent research reports similar results on the charge dispersion of a full-shell nanowire gatemon with a DC transport lead [169].

4.5. SUPPLEMENTARY INFORMATION

DATA EXTRACTION

At each gate setting we measure the qubit transition frequency over at least one period in offset charge n_g. From this we extract the qubit frequency f_{0n} and charge dispersion δf_{0n} by applying a peak-finding algorithm to the raw two-tone spectroscopy data. The algorithm first smooths the data in frequency axis in order to combat noise, after which peaks are identified and fit with Lorentzian lineshapes in order to obtain their center frequency. For the gate voltage ranges in which two peaks are identified we take δf_{0n} to be the local maximum in peak separation. Conversely, f_{0n} is obtained from the regions where only a single peak is identified. In the regions of parameter space where δf_{0n} is smaller than the qubit linewidth γ_{0n} such that only a single peak can be discerned for any n_g (open markers in Fig. 4 of the main text), we take the center frequency to be f_{0n} and use the extracted linewidth of the Lorentzian lineshape as an upper bound for δf_{0n}.

MODELLING OF THE QUBIT

In order to model the measured data we study the Hamiltonian of a capacitively shunted junction given by

$$\hat{H} = 4E_\mathrm{c}\left(\hat{n} - n_\mathrm{g}\right)^2 + U(\hat{\phi}) \tag{4.2}$$

where $U(\hat{\phi})$ is the junction potential, E_c is the charging energy, $\hat{n}$ is the number of Cooper pairs that have traversed the junction, n_g is a dimensionless offset charge and $\hat{\phi}$ is the phase difference between the superconductors on either side of the junction. We obtain the qubit energy levels $E_n(n_g)$ and the corresponding qubit transitions $f_{ij}(n_g) = E_j(n_g) - E_i(n_g)$ through numerical diagonalization of the Hamiltonian, from which f_{0n} and δf_{0n} are calculated by evaluating the transitions at the appropriate offset charges.

We perform this procedure for three possible models for the junction potential: a sinusoidal potential as encountered in tunnel junctions, a potential considering only occupation of the E_- ABS branch of the resonant level model, and a potential including ITLZ tunneling between the ABS of the resonant level model. In the case of the sinusoidal

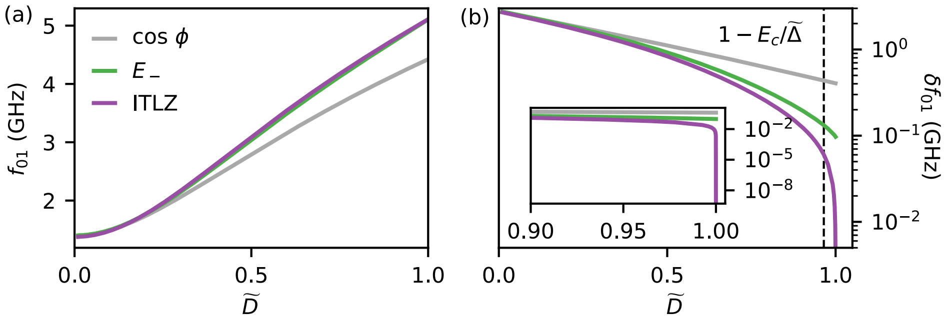

Figure 4.6: Qubit frequency (a) and charge dispersion (b) evaluated for three different models: a sinusoidal potential, the negative energy ABS branch of the resonant level model, and a potential considering ITLZ tunneling between both ABS branches. All models are evaluated for fixed parameter values $\widetilde{\Delta} = 14$ GHz and $E_c = 715$ MHz. The dashed line indicates the crossover value $1 - E_c/\widetilde{\Delta}$. Inset of (b): Zoom in of the behaviour near $D = 1$, where the ITLZ model exhibits rapid suppression in charge dispersion down to a small value set by tunneling through a potential barrier $\widetilde{\Delta}\cos\phi/2$.

model we take $U(\hat{\phi}) = -E_\mathrm{J}\cos\hat{\phi}$, where we define an effective $E_\mathrm{J} \equiv \widetilde{\Delta}\widetilde{D}/4$ in order to compare the models on equal footing. For the model including only the $E_-(\hat{\phi})$ ABS branch we use $U(\hat{\phi}) = -\widetilde{\Delta}\sqrt{1 - \widetilde{D}\sin^2\hat{\phi}/2}$, while in order to include ITLZ tunneling between the $E_\pm(\hat{\phi})$ branches we follow the work of Ivanov and Feigel'man [135] and approximate the many-body superconducting system by an effective two-level system. This results in a junction potential given by

$$U(\hat{\phi}) = \widetilde{\Delta}\begin{pmatrix} \cos\frac{\hat{\phi}}{2} & \sqrt{1-\widetilde{D}}\sin\frac{\hat{\phi}}{2} \\ \sqrt{1-\widetilde{D}}\sin\frac{\hat{\phi}}{2} & -\cos\frac{\hat{\phi}}{2} \end{pmatrix} \tag{4.3}$$

In the above $\widetilde{\Delta}$ and $\widetilde{D}$ are effective parameters resulting from the underlying quantum dot parameters discussed in section 4.5.

The results of this procedure are demonstrated in Fig. 4.6, which shows how f_{01} and δf_{01} depend on $\widetilde{D}$ for the three models. The sinusoidal model reproduces the expected results of the conventional tunnel junction transmon, exhibiting exponential suppression of δf_{01} for large values of $\widetilde{D}$ and thus $E_\mathrm{J}/E_\mathrm{c}$. The $E_-(\phi)$ model exhibits similar behaviour up to moderate values of $\widetilde{D}$, after which an enhanced suppression of δf_{01} takes place due to the increased height of the potential compared to the sinusoidal model. Finally, the model including ITLZ tunneling shows comparable behaviour to $E_-(\phi)$ up to large values of $\widetilde{D}$, after which a much more rapid decrease in charge dispersion takes place. This reproduces the scaling law predicted for ballistic Josephson junctions [14]. We note that the cross-over value of $\widetilde{D}$ between the adiabatic regime well-described by only E_- and the diabatic regime including ITLZ tunneling is approximately given by $\widetilde{D} = 1 - E_c/\widetilde{\Delta}$, where the rate of phase evolution becomes comparable to the energy gap between the ABS [135].

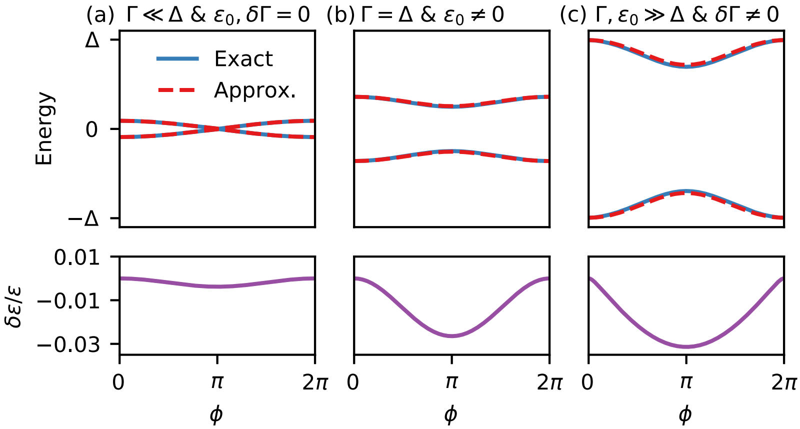

Figure 4.7: Comparison between the exact and approximate solutions for the ABS of the resonant level model. Top half shows the explicit energy levels for both solutions while the bottom half shows the relative error of the approximate model. (a) shows the comparison in the regime of weak coupling ($\Gamma \ll \Delta$) on resonance ($\epsilon_0 = 0$) with symmetric barriers ($\delta\Gamma = 0$). (b) shows the regime of moderate coupling in which $\Gamma_\mathrm{l} = \Gamma_\mathrm{r} = \Delta$ and where the level is off-resonant ($\epsilon_0 \neq 0$). (b) shows the regime of far off-resonant strong coupling with asymmetric tunneling rates, in which $\Gamma, \epsilon_0 \gg \Delta$ and $\delta\Gamma \neq 0$.

RESONANT LEVEL MODEL

In order to develop a quantitative understanding of our device we study a simplified model of a quantum dot between two superconducting leads known as the resonant level model [27]. Depicted in Fig. 4a of the main text, it considers the presence of a single spin-degenerate level in the junction with an energy ϵ_0 relative to the Fermi level, coupled to two identical superconductors with superconducting gap Δ via the spin-degenerate tunnel rates Γ_l and Γ_r. Its discrete energy spectrum follows from the solutions $\epsilon \in (0, \Delta)$ of the equation

$$\left(\Delta^2 - \epsilon^2\right)\left(\epsilon^2 - \epsilon_0^2 - \Gamma^2\right) + 4\Delta^2\Gamma_\mathrm{l}\Gamma_\mathrm{r}\sin^2(\phi/2) + 2\Gamma\epsilon^2(\Delta^2 - \epsilon^2)^{1/2} = 0 \tag{4.4}$$

where $\Gamma = \Gamma_\mathrm{l} + \Gamma_\mathrm{r}$. This equation can be solved numerically for general parameter values, resulting in a single pair of spin degenerate ABS $E_\pm(\phi)$. Furthermore, in certain limits its solution can be recovered analytically (given in Eq. 1 of the main text), which coincides with the eigenvalues of Eq. 4.3. However, we found these limits too constraining for the model to accurately describe our data. We therefore construct an approximate solution to Eq. 4.4 based on the ABS energies $E_\pm(\phi)$ and transparency $\widetilde{D}$ given by Eq. 1 of the main text, whereas for $\widetilde{\Delta}$ we do not use the limiting values but instead solve Eq. 4.4 for the bound state energy at $\phi = 0$. Shown in Fig. 4.7, we tested the validity of this approximation for a wide range of parameters by explicit comparison to the solutions of Eq. 4.4. The effective spectrum closely resembles the exact solutions over a wide range of parameters, with relative errors on the order of a few percent even in the regime $\Gamma \approx \Delta$. We therefore argue that the effective model of Eq. 4.3 should accurately describe the phenomenology of the resonant level junction. A more detailed description of the model and its derivation can be found in [169].

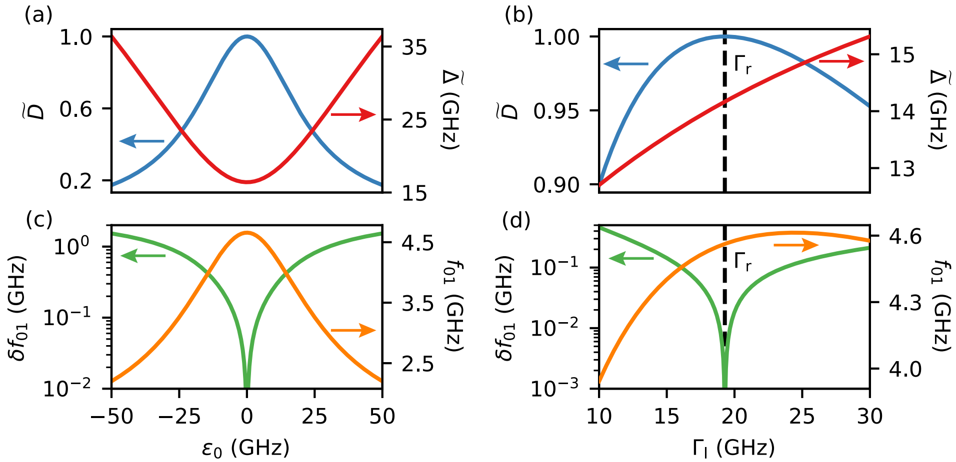

Figure 4.8: Effective junction and qubit parameters as a function of resonant level parameters. Panel a (b) shows how $\widetilde{D}$ and $\widetilde{\Delta}$ (f_{01} and δf_{01}) behave as a function of ϵ_0 for $\delta\Gamma = 0$, panel c (d) shows how these parameters behave as a function of Γ_l for $\epsilon_0 = 0$ and $\delta\Gamma \neq 0$.

Having constructed the effective parameters $\widetilde{D}$ and $\widetilde{\Delta}$, we now show how the ITLZ model introduced in section 4.5 behaves as a function of the underlying quantum dot parameters. We do this for the parameter values that resulted in the best fits to the measured data, shown in Fig. 4 of the main text. In Fig. 4.8 we study the effect of varying ϵ_0 at $\Gamma_l = \Gamma_r$. It results in a weak dependence of $\widetilde{\Delta}$, which is minimal when $\epsilon_0 = 0$. This coincides coincides with a maximum in $\widetilde{D}$, as given by Eq. 1 of the main text. Shown in (b) this translates into a qubit frequency that is maximal at $\epsilon_0 = 0$, coinciding with a minimum in charge dispersion. Panels (c-d) in turn show the dependence on Γ_l at fixed Γ_r with $\epsilon_0 = 0$. We find that $\widetilde{\Delta}$ is a monotonically increasing function of Γ_l, whereas $\widetilde{D}$ is maximal when the asymmetry $\delta\Gamma = |\Gamma_l - \Gamma_r|$ is minimized. Panel (d) shows that the relative rapidity at which $\widetilde{\Delta}$ and $\widetilde{D}$ change around $\delta\Gamma = 0$ can result in a situation where the maximal qubit frequency does not coincide with minimal charge dispersion. We believe this effect to be the origin of the non-monotonic dependence between the qubit frequency and the charge dispersion seen in figures 3 and 4d of the main text.

FITTING ROUTINE

We fit the measured relationships between $\{f_{0n}, \delta f_{0n}\}$ using the models developed in section 4.5. For the data measured as a function of V_j, shown in Fig. 4c of the main text, we assume that only ϵ_0 is varied. The remaining remaining parameters Δ, E_c, Γ_l, and Γ_r are taken to be independent. Additionally, we fix $\Delta = 53$ GHz based on DC transport experiments on similar nanowires [79] and we assume that $\Gamma_l = \Gamma_r$. We then apply a fitting routine in which for each set of parameter values a range of $\{\widetilde{\Delta}, \widetilde{D}\}$ is generated from the effective resonant level ABS potential for a large range of ϵ_0. These effective parameters are then used in the three different junction potentials of section 4.5, resulting in a set of calculated values for $\{f_{01}, \delta f_{01}\}$ that can be compared to the measured values. The best fit to the data for each model is obtained through the standard method of least-squares.

For the extracted relationships between $\{f_{0n}, \delta f_{0n}\}$ as a function of V_g, shown in Fig. 4d of the main text, this procedure is slightly modified. We now assume that only Γ_l is a function of V_g, with Δ, E_c, ϵ_0, and Γ_r taken to be independent. For simplicity we fix $\epsilon_0 = 0$. We note that, in order to obtain a good fit for the data versus V_g, Δ needed to enter as a free parameter. In addition, a good fit could not be found simultaneously for all three measured transitions with a single set of parameters. Instead we only fit the $\{f_{01}, \delta f_{01}\}$ data to the model, resulting in a qualitatively satisfying fit for the 01 transition. However, the fit suggests a value of superconducting gap $\Delta = 18.6$ GHz, much smaller than the value measured in DC experiments [79]. Moreover, the fit does not manage to capture the position of the higher order transitions. As discussed in the main text, we attribute this parameter discrepancy as well as the inability to fit all three transitions to possible modifications in the shape of the potential originating from the lack of electron-electron interactions in the model.

ESTIMATING TRANSPARENCIES

An estimate for the transparencies $\widetilde{D}$ realized the in the experiment can be obtained from the fits to the data. As illustrated in Fig. 4.8, each numerically calculated value of δf_{0n} corresponds to a value of $\widetilde{D}$, and one can therefore infer the values of $\widetilde{D}$ by matching the measured values of δf_{0n} to the numerical values. We emphasize that these values are model and parameter dependent, and are therefore only an estimate. Shown in Fig. 4.9a, we find that by varying V_j transparencies between 0.5 and 1 are attained, with the largest transparency based on a distinguishable charge dispersion (filled markers) being 0.998 and the largest value based on the qubit linewidth γ_{01} (open markers) being 0.9996. Finally in panel (b) we show the asymptotic probability p of the ABS remaining in the ground state as calculated from the extracted $\widetilde{D}$ and $\widetilde{\Delta}$ [14]. This illustrates that the suppression of charge dispersion coincides with the vanishing of p. Furthermore, it shows that sizeable ITLZ probabilities are obtained over a wide range of the measured values, robust to small changes in fit parameters. We do not repeat this procedure for the data obtained by varying V_g, given the unsatisfactory fit to the data.

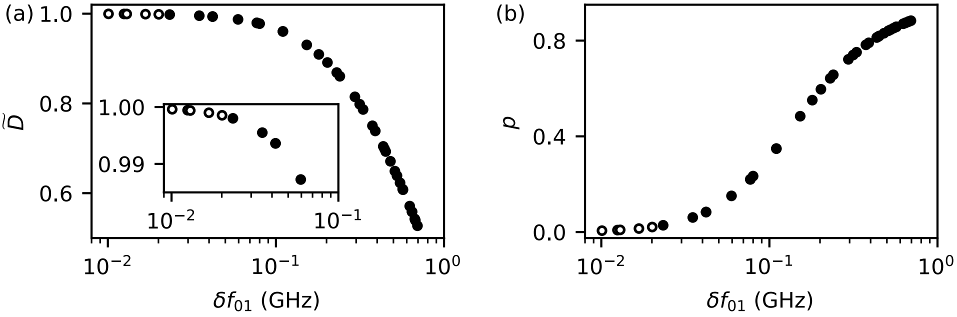

Figure 4.9: (a) Extracted $\widetilde{D}$ for the values of δf_{01} measured as a function of V_j, with the inset showing the behaviour near $\widetilde{D} = 1$. (b) Asymptotic probability for the ABS to remain in the E_- branch as calculated from the extracted $\widetilde{D}$ and $\widetilde{\Delta}$.

5

SINGLET-DOUBLET TRANSITIONS OF A QUANTUM DOT JOSEPHSON JUNCTION DETECTED IN A TRANSMON CIRCUIT

We realize a hybrid superconductor-semiconductor transmon device in which the Josephson effect is controlled by a gate-defined quantum dot in an InAs/Al nanowire. Microwave spectroscopy of the transmon's transition spectrum allows us to probe the ground state parity of the quantum dot as a function of gate voltages, external magnetic flux, and magnetic field applied parallel to the nanowire. The measured parity phase diagram is in agreement with that predicted by a single-impurity Anderson model with superconducting leads. Through continuous time monitoring of the circuit we furthermore resolve the quasiparticle dynamics of the quantum dot Josephson junction across the phase boundaries. Our results can facilitate the realization of semiconductor-based $0-\pi$ qubits and Andreev qubits.

The work in this chapter has been published as: A. Bargerbos*, M. Pita-Vidal*, R. Žitko, J. Ávila, L.J. Splitthoff, L. Grünhaupt, J.J. Wesdorp, C.K. Andersen, Y. Liu, P. Krogstrup, L.P. Kouwenhoven, R. Aguado, A. Kou, and B. van Heck, Singlet-doublet transitions of a quantum dot Josephson junction revealed in a transmon circuit, PRX Quantum **3**, 030311 (2022). The asterisk indicates authors that contributed equally to this work.

5.1. INTRODUCTION

Superconducting pairing and charging energy are two fundamental interactions that determine the behavior of mesoscopic devices. Notably, when a quantum dot (QD) is coupled to a superconductor, they compete to determine its ground state. A large charging energy favors single-electron doublet occupancy of the dot and thus a spin-1/2 ground state, while a strong coupling to the superconducting leads favors double occupancy in a singlet configuration with zero spin. A quantum phase transition between the singlet and doublet ground state can occur as system parameters such as the dot energy level and the coupling strength are varied. The latter also controls the nature of the singlet ground state, which can be either of the Bardeen-Cooper-Schrieffer (BCS) type or of the Kondo type. The rich phase diagram of the system, as well as its transport properties, are theoretically well captured by an Anderson model with superconducting leads [58, 104, 144, 153, 202, 209, 215, 232, 309, 343].

Quantum dots coupled to superconductors have been studied experimentally over the last two decades. Signatures of the singlet-doublet transition have been detected in tunneling spectroscopy measurements of N-QD-S devices (where N is a normal lead, and S is a superconducting one) via the observation of Fermi-level crossings [54, 73, 185, 187, 191, 249, 250, 315, 335]. Additionally, they have been detected in switching current measurements of S-QD-S devices via π-phase shifts in the current-phase relation of the resulting quantum dot Josephson junction [61, 74, 75, 86, 100, 140, 141, 176, 186, 213, 308, 316, 335].

Recent experiments [123, 124, 136] on Andreev pair and spin qubits [59, 234, 241, 348] have renewed the interest in quantum dot junctions due to the possibility of tuning the ground state of the system to be in addressable spin states. Knowledge of the phase diagram of the quantum dot junction is also beneficial for realizing proposals for a quantum-dot-based readout of topological qubits [155, 253, 294].

These developments have highlighted the need for a better fundamental understanding of the quantum dot junction and its dynamics, requiring tools which are not limited by the long integration times of low-frequency measurements nor by the invasiveness of transport probes. To address this need, we have embedded a fully controllable quantum dot in a microwave superconducting circuit. This experimental choice is motivated by the success of circuit quantum electrodynamics (QED) techniques in the investigation of mesoscopic effects in Josephson junctions [51, 70, 122–124, 136, 169, 182, 312, 313], which stems from its enhanced energy and time resolution compared to low-frequency transport techniques. In this context, the microwave response of a quantum dot junction has attracted recent theoretical [130, 177] and experimental [91] attention.

The core of our experiment is a transmon circuit formed by an island with charging energy E_c, coupled to ground via a superconducting quantum interference device (SQUID) formed by a parallel combination of a junction with a known Josephson energy E_J and a quantum dot junction (Fig. 5.1(a-c)). The energy-phase relation of the quantum dot junction depends on whether it is in a singlet or doublet state, with a characteristic π-phase shift between the two relations (Fig. 5.1(d)) [298]. The two energy-phase relations of the junctions add up together in the SQUID. Depending on whether the quantum dot junction is in the singlet or doublet state, as well as on the external flux, this results in a higher or lower curvature of the total potential around its minimum with respect to

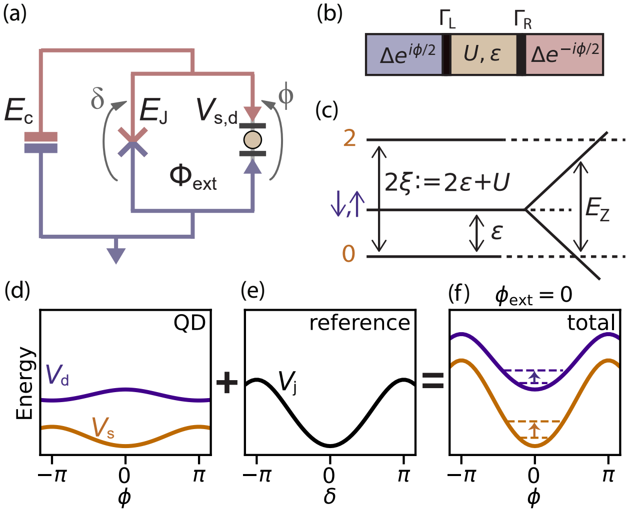

Figure 5.1: (a) Schematic diagram of a quantum dot junction incorporated into a transmon circuit. The transmon island with charging energy E_c is connected to ground by a SQUID formed by the parallel combination of a quantum dot junction and a reference junction. In this panel ϕ and δ denote the superconducting phase difference across the quantum dot and reference junctions respectively. Φ_{ext} is the externally applied magnetic flux through the SQUID loop. (b) Model diagram of the quantum dot junction in the excitation picture. Two s-wave superconductors are connected via tunnel barriers to a single level quantum dot. (c) Level diagram of the quantum dot hosting 0, 1, or 2 electrons when disconnected from the leads ($\Gamma_L = \Gamma_R = 0$). (d) Phase dependence of the Josephson potential of the quantum dot junction in the singlet (orange) and doublet (purple) state. (e) Josephson potential of the reference junction. (f) Josephson potential of the DC SQUID for $\phi_{ext} = (2e/\hbar)\Phi_{ext} = 0$, with the quantum dot junction in the singlet (orange) and doublet (purple) state. The dashed lines represented the two lowest transmon energy levels in each branch of the Josephson potential, with the arrow denoting the resulting transition frequency, which can differ for the two quantum dot junction states (orange and purple arrows for singlet and doublet, respectively).

that of the reference junction. Therefore, the two branches of the spectrum give rise to two distinct transition frequencies of the transmon circuit, which can be detected and distinguished via standard circuit QED techniques [35]. As a result, a transition from a singlet to a doublet state will appear as a discontinuous jump in a measurement of the transmon frequency spectrum.

Using this method, we have detected the singlet-doublet transition and reconstructed the phase diagram of a quantum dot junction as a function of all experimentally controlled parameters in a single device: the energy level of the dot, the tunnel couplings to the superconducting leads, the superconducting phase difference across the quantum dot junction, and also an external Zeeman field. The measured phase boundaries are in agreement with the single-impurity Anderson model with superconducting leads as calculated via the numerical renormalization group (NRG) [47, 274, 338, 343] methods, and include parameter regimes that have experimentally not been explored before. Finally, we have investigated the rates at which the quantum dot switches between doublet and singlet occupation via real-time monitoring of the transmon circuit, allowing us to determine the switching time-scales of the quantum dot junction parity across the phase transition.

5.2. DEVICE OVERVIEW

The quantum dot junction under investigation is formed in a 10 µm-long epitaxial superconductor-semiconductor nanowire with a 100 nm-wide hexagonal InAs core and a 6 nm-thick Al shell covering two of its facets [173]. The quantum dot junction is located in a 200 nm-long uncovered section of the nanowire where the Al has been etched away, where it is electrostatically defined by three bottom gate electrodes (Fig. 5.2(d)). As shown in the circuit of Fig. 5.2(a), this quantum dot junction is placed in parallel to a second Josephson junction, hereafter referred to as the “reference junction”, to form a SQUID. The reference junction consists of a second 110 nm-long uncovered segment of InAs on the same nanowire as the quantum dot junction. Its Josephson energy E_J can be tuned with a single gate electrode via the field effect.

The SQUID connects a superconducting island to ground, resulting in a transmon circuit [162] governed by the Hamiltonian

$$H = -4E_\mathrm{c}\partial_\phi^2 + V(\phi), \tag{5.1}$$

where $E_\mathrm{c} = e^2/2C_\Sigma$, with C_Σ the total capacitance of the island to ground. The Josephson potential $V(\phi)$ is determined by the phase-dependent energies of the reference junction, $V_\mathrm{j}(\delta) = E_\mathrm{J}(1-\cos\delta)$, and of the quantum dot junction, $V_\mathrm{s,d}(\phi)$:

$$V(\phi) = E_\mathrm{J}\left[1-\cos(\phi-\phi_\mathrm{ext})\right] + \begin{cases} V_\mathrm{s}(\phi) & \text{singlet} \\ V_\mathrm{d}(\phi) & \text{doublet}. \end{cases} \tag{5.2}$$

Here, the phase drops across the quantum dot junction (ϕ) and across the reference junction (δ) are connected according to $\phi-\delta = \phi_\mathrm{ext}$, where $\phi_\mathrm{ext} = (2e/\hbar)\Phi_\mathrm{ext}$ is the phase difference resulting from the externally applied magnetic flux through the SQUID loop, Φ_ext.

The presence of the reference junction serves several purposes. First, it allows us to tune the phase difference at the quantum dot junction by changing Φ_ext with the B_y component of the magnetic field [see Sec. 5.8]. We generally operate the device in a regime where the reference junction has a Josephson energy that is larger than that of the quantum dot by more than an order of magnitude. This ensures that δ is close to zero, while ϕ is close to ϕ_ext [76]. Second, the ability to tune E_J independently of the quantum dot junction ensures that the transition frequencies of the transmon circuit remain inside the measurement bandwidth for all parameter regimes of the quantum dot junction. Finally, the Josephson energy of the reference junction is such that $E_\mathrm{J}/E_\mathrm{c} > 25$, suppressing unwanted sensitivity to fluctuating charges in the environment and justifying the absence of an offset charge in the Hamiltonian of Eq. (5.1) [162].

In order to perform microwave spectroscopy measurements, the transmon is capacitively coupled to a readout resonator which is in turn coupled to a transmission line. This allows us to measure the circuit’s complex microwave transmission S_{21} through the transmission line’s input (1) and output (2) ports.

The experimental implementation of the circuit (Fig. 5.2(b-d)) differs from conventional circuit QED geometries in several ways [34], in order to allow the application of

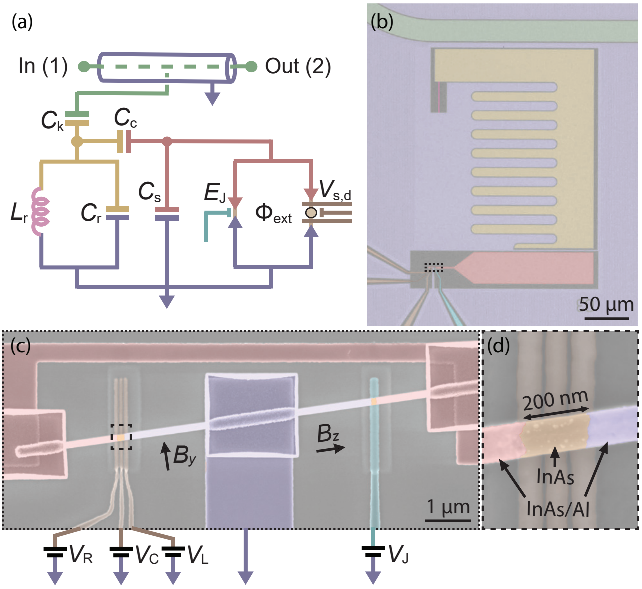

Figure 5.2: **Device overview.** (a) Diagram of the microwave circuit. A coplanar waveguide transmission line (green center conductor) is capacitively coupled to a grounded LC resonator. The resonator consists of an island (yellow) capacitively and inductively (pink) shunted to ground (blue). The resonator is in turn capacitively coupled to a transmon island (red), which is shunted to ground capacitively as well as via two parallel Josephson junctions. (b) False-colored optical microscope image of device A showing the qubit island, the resonator island, the resonator inductor, the transmission line, the electrostatic gates and ground. (c) False-colored scanning electron micrograph (SEM) of the transmon's Josephson junctions, showing the InAs/Al nanowire into which the junctions are defined. The B_y component of the magnetic field is used to tune Φ_{ext}. B_z is the magnetic field component parallel to the nanowire. (d) False-colored SEM of the quantum dot junction in which the quantum dot is gate defined. The three bottom gates have a width and spacing of 40 nm, although this is obfuscated by the dielectric layer placed on top.

magnetic fields in excess of 100 mT. Apart from the Josephson junctions, all circuit elements are made out of field compatible 20 nm-thick NbTiN films [203]. We additionally incorporate vortex pinning sites in the ground plane, the transmission line, the resonator island and the transmon island [174]. We use a lumped element readout resonator, which has previously been successfully utilized in flux-sensitive devices up to 1 T [252]. Its capacitance is formed by an interdigitated capacitor to ground, while its inductance is formed by a 200 nm wide NbTiN nanowire, which has a kinetic inductance of 15 pH/□. This design localizes the regions of high current density at the narrow inductor where vortices are less likely to nucleate due to its reduced width [272]. For the transmon circuit the SQUID loop area is chosen to be small, $\sim 5\,\mu\text{m}^2$, in order to suppress flux noise from misalignment in large parallel magnetic fields. Finally, InAs/Al nanowires, in which both junctions are defined, have been shown to support sizeable Josephson energies in fields in excess of 1 T [252, 313]. Further details about device fabrication as well as the cryogenic and room temperature measurement setup can be found in the Supplementary Information of Sec. 5.8.

5.3. ANDERSON MODEL FOR A QUANTUM DOT JUNCTION

As we will show, the quantum dot junction can be described by a single Anderson impurity tunnel-coupled to two superconducting leads. We review its most important properties to facilitate the discussion of the experimental results that follow. In particular, we discuss here the important parameters and concepts that are required to interpret the experimental results, deferring to the Supplementary Information of Sec. 5.8 for a technical description of the Hamiltonian and of the numerical methods used to produce the theoretical results.

The model contains a single-level quantum dot coupled to two superconducting leads via tunnel barriers, schematically depicted in Fig. 5.1(b). The superconducting leads have a pairing gap Δ and a phase difference ϕ, and the barriers are characterized by single-electron tunneling rates Γ_L and Γ_R. The energy diagram for the isolated quantum dot is shown in Fig. 5.1(c). The quantum dot is modeled as an Anderson impurity with single-occupancy energy ϵ, measured with respect to the Fermi level in the leads, and a repulsive Coulomb interaction U, which penalizes the double occupancy of the dot energy level.

The quantum dot is spin-degenerate at zero magnetic field. An external magnetic field B splits the degeneracy by a Zeeman energy $E_\mathrm{Z} = g\mu_\mathrm{B}B$, where g is the effective g-factor of the level and μ_B is the Bohr magneton. In the experiment we choose the B-field direction to be parallel to the nanowire, since this is the direction that suppresses the superconductivity in the Al nanowire shell the least.

The energy levels of Fig. 5.1(c) are divided in two sectors, corresponding to their fermion parity, or equivalently, to their total spin S. The singlet sector includes the states of even parity: the empty state $|0\rangle$ and the pair state $|2\rangle$. These states have $S = 0$ and are therefore insensitive to the magnetic field B. The doublet sector includes the states of odd parity, $|\uparrow\rangle$ and $|\downarrow\rangle$, which have $S = 1/2$. It is convenient to introduce the energy $\xi = \epsilon + U/2$, corresponding to half of the energy gap in the singlet sector, so that $\xi = 0$ corresponds to the electron-hole symmetry point, where $|0\rangle$ and $|2\rangle$ are degenerate in energy. The ground state of the isolated dot (that is, $\Gamma_\mathrm{L} = \Gamma_\mathrm{R} = 0$) belongs to the doublet sector for $|\xi| < \frac{1}{2}U$.

A salient feature of the model is that a quantum phase transition between doublet and singlet ground state can occur upon changing several experimentally-tunable parameters. The dot energy level ξ and the coupling strengths $\Gamma_\mathrm{L,R}$ (all experimentally tunable via the bottom electrostatic gates), as well as the superconducting phase difference ϕ and the magnetic field B, all act to shift the relative positions of the potentials V_s and V_d and to cause an energy crossing between the ground states of the two sectors. In the measurements reported in Sec. 5.4 and 5.5, we vary all these parameters and compare the extracted phase boundaries to theory.

For the theoretical comparison we use the NRG method [323, 338, 349] to compute the lowest-lying eigenvalues in the singlet and doublet spin sectors as a function of the phase difference ϕ [1]. This results in the Josephson potentials $V_\mathrm{s}(\phi)$ and $V_\mathrm{d}(\phi)$, which are then used as input to the model of Eq. (5.2) to calculate the transmon transition frequen-

---

[1] Note that the notion of singlet and doublet sectors, introduced for the isolated quantum dot, extends naturally to the coupled quantum dot, provided that the spin S is now regarded as the total spin of the system, including that of quasi-particles in the reservoirs

cies [see Sec. 5.8]. The projection onto the lowest-energy state of the Josephson junction in each sector is enough to capture the salient features of our experiment, although the inclusion of excited Andreev states of the quantum dot junction in the circuit model is theoretically possible [16, 17, 156, 177, 348].

Experimentally, the observation of the phase transition is facilitated by the presence of a π-phase shift between $V_s(\phi)$ and $V_d(\phi)$. The phase shift arises because the sequence of single-electron tunneling events that leads to the transport of a Cooper pair between the two leads depends on whether the quantum dot is initially in the singlet or the doublet sector. In particular, if the dot is initially in the doublet state, a permutation of spin-up and spin-down electrons is required in order to complete the tunneling sequence [298], leading to a π phase shift due to Fermi-Dirac statistics. Thus, while $V_s(\phi)$ has a minimum at $\phi = 0$, as encountered for conventional Josephson junctions, $V_d(\phi)$ has a minimum at $\phi = \pi$ (Fig. 5.1(d)). A quantum dot junction in a doublet state is often denominated as a π-junction, and the singlet-doublet transition is also referred to as the 0-π transition. In the following sections we will use the presence or absence of such a π-phase shift to identify regions with a singlet or a doublet ground state [2].

5.4. TRANSMON SPECTROSCOPY OF THE QUANTUM DOT

To perform spectroscopy of the resonator, we monitor the microwave transmission S_{21} across the transmission line while varying the frequency of a single continuous microwave tone, f_r. This results in a dip with Lorentzian lineshape around the resonance frequency of the lumped-element resonator. Two-tone spectroscopy is subsequently performed by fixing the frequency of this first tone, f_r, at the minimum of the transmission amplitude, $|S_{21}|$, while varying the frequency of a second tone, f_t, also sent through the transmission line. When the second tone matches the frequency of the ground to first excited transmon transition, $f_t = f_{01}$, a peak in $|S_{21}|$ is observed due to the transmon-state-dependent dispersive shift of the resonator [35]. This gives us access to the transmon transition frequency.

We are interested in the behavior of the device when a single level of the quantum dot provides the dominant contribution to the Josephson effect. To find such a regime, we search for an isolated resonance in the gate dependence of the frequency spectrum. Isolated resonances often occur when the gate voltages controlling the quantum dot are set close to their pinch-off values (see Ref. [169] and chapter 4), here operationally defined as the voltage values below which the quantum dot junction does not contribute appreciably to the transmon's transition frequency. In order to identify the right gate configuration, we perform the following sequence of calibration measurements. First, we characterize the reference junction with the quantum dot pinched-off; second, we explore the sizeable parameter space governed by the three quantum dot gates; third, we identify the relation between B_y and ϕ_{ext} through the transmon frequency's SQUID oscillations and find that 2.2 mT corresponds to one flux quantum through the loop; and

---

[2] Our assumption that regimes with 0-junction and π-junction behaviour correspond to the quantum dot junction being in a singlet or doublet state, respectively, is only valid in the single-level regime, where the level spacing of the quantum dot is significantly larger than Δ and U. In the multi-level regime, where excited states of the quantum dot are involved, the presence or absence of the π offset also depends on the character of the orbital wavefunctions in addition to the fermion parity [316].

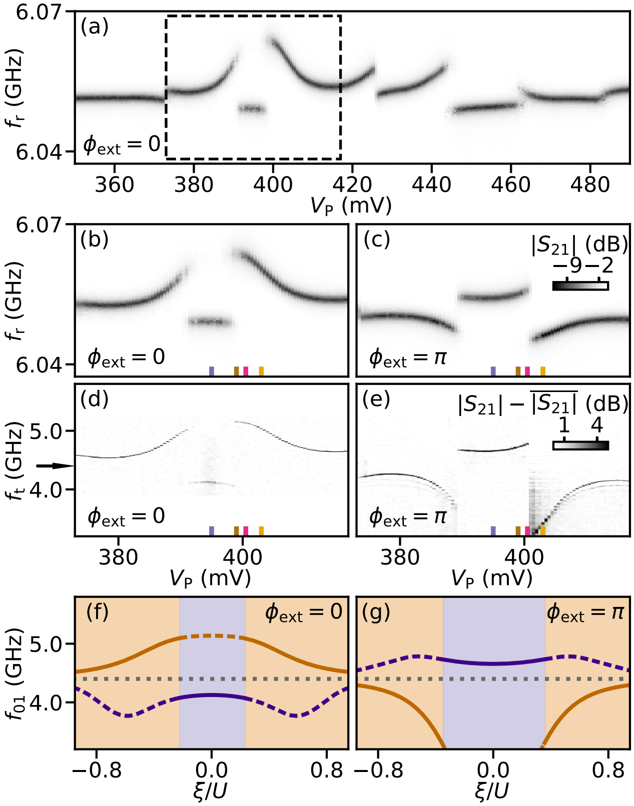

Figure 5.3: **Resonator and transmon spectroscopy.** (a) V_P dependence of single-tone spectroscopy for $\phi_{ext} = 0$, showing the resonator's transition frequency. V_P is a virtual gate voltage defined as a linear combination of V_C and V_R (see text). (b) Zoom-in of (a) in the plunger gate range indicated with dashed lines in (a). (c) Same as (b) but for $\phi_{ext} = \pi$. (d) V_P dependence of two-tone spectroscopy for $\phi_{ext} = 0$, showing the transmon's transition frequency. For each frequency trace, $|S_{21}| - |\bar{S}_{21}|$ is the magnitude of the transmission minus its average. The black arrow indicates f_{01}^0, the transmon frequency set by the reference junction when the quantum dot is pinched off. (e) Same as panel (d) but for $\phi_{ext} = \pi$. For panels (a-e) $V_T = 182$ mV and $V_L = 470$ mV. (f) Theoretical estimates of the singlet (orange), doublet (purple) and reference junction-only (dotted, grey) transmon frequencies as ξ is varied for $\phi_{ext} = 0$. Solid (dashed) lines indicate which quantum dot occupation corresponds to the ground (excited) state. (g) Same as panel (f) but for $\phi_{ext} = \pi$. For panels (f-g) $\Delta/h = 46\,\mathrm{GHz}$, $U/\Delta = 12.2$, $\Gamma_L/\Delta = 1.05$ and $\Gamma_R/\Delta = 1.12$. f_t and f_{01} denote, respectively, the frequency of the second tone in two-tone spectroscopy and the first transmon transition frequency (see text).

finally we define appropriate gate coordinates to account for cross-couplings. These calibration measurements are detailed in the Supplementary Material of Sec. 5.8. As a result of this procedure, the gate voltage of the reference junction V_J is fixed such that the transmon frequency when the quantum dot junction is pinched-off is $f_{01}^0 \approx 4.4\,\mathrm{GHz}$. Furthermore, we fix $V_L = 470$ mV and introduce virtual plunger (V_P) and right tunnel (V_T) gates as a linear combination of V_C and V_R, such that, in what follows, the single-particle energy level ξ is mostly independent of V_T.

We then move on to study the quantum dot junction. We first monitor the resonator frequency for $\phi_{\text{ext}} = 0$ while the plunger gate voltage V_{P} is varied (Fig. 5.3(a)). This reveals a resonant shape which is discontinuously interrupted near its peak at $V_{\text{P}} = 395$ mV, followed by other discontinuous jumps in the resonator frequency. A zoom into the resonance is shown in Fig. 5.3(b) and the corresponding transmon transition frequency, exhibiting the same discontinuity as the resonator, is shown in Fig. 5.3(d). We identify regions in V_{P} where the transmon frequency f_{01} is larger and smaller than the reference frequency f_{01}^{0}. This hierarchy is reversed upon changing the applied flux to $\phi_{\text{ext}} = \pi$, as shown in Figs. 5.3(c, e).

These observed discontinuities in frequency are a signature of a singlet-doublet transition. The change of the ground state of the quantum dot junction determines a sudden switch in the branch of the Josephson potential of Eq. (5.2) (from V_{s} to V_{d} or vice-versa) and, thus, a sudden change in the transmon frequency. This is illustrated numerically in Figs. 5.3(f-g), which show the expected evolution of the transmon frequencies as a function of the single-particle energy level ξ. Here, the transition occurs as ξ is tuned toward the electron-hole symmetry point $\xi = 0$, where the doublet ground state is energetically favorable.

The occurrence of the singlet-doublet transition requires a change of the fermion parity of the quantum dot junction. In the S-QD-S setup, this is possible in the presence of a population of excited quasiparticles in the superconducting leads, providing the required fermion parity reservoir. The presence of these quasiparticles should further result in a finite occupation of both the singlet and doublet states when their energy difference is small compared to the effective temperature of the quasiparticle bath, namely in the vicinity of the transition. Indeed, upon closer inspection of the data of Figs. 5.3(b-c), both branches of the spectrum are visible in a small frequency window surrounding each discontinuous jump. This is because these transition spectra are obtained by averaging over many subsequent frequency sweeps, thus reflecting the occupation statistics of the junction. This feature is further discussed in the next Section.

In Figs. 5.3(d-e), the fact that the frequency shift of the transmon has the opposite sign for the singlet and doublet sectors is a consequence of the π-phase shift in the Josephson potential between the two sectors. For the case $\phi_{\text{ext}} = 0$, the singlet potential interferes constructively with the reference junction potential, while the doublet potential interferes destructively, resulting in $f_{01} > f_{01}^{0}$ for the singlet and $f_{01} < f_{01}^{0}$ for the doublet. This behaviour is reversed when $\phi_{\text{ext}} = \pi$, and thus serves as a method for identifying the quantum dot junction state.

5.5. SINGLET-DOUBLET TRANSITION BOUNDARIES

Having established a method for identifying singlet and doublet states by transmon spectroscopy, we now experimentally investigate the phase diagrams of the quantum dot junction. We focus on the behaviour around $V_{\text{P}} = 395$ mV and monitor singlet-doublet transitions versus multiple different control parameters.

PLUNGER GATE AND FLUX

We first study the singlet-doublet phase map in V_{P} and ϕ_{ext} space. Fig. 5.4(a) shows the transmon frequency offset with respect to the frequency set by the reference junction,

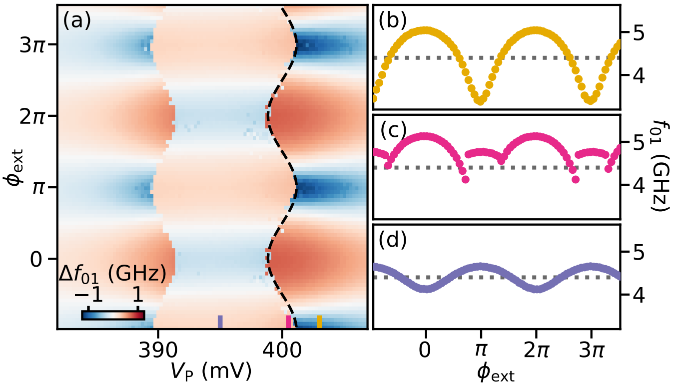

Figure 5.4: **Flux and plunger gate dependence.** (a) Transmon frequency shift with respect to the frequency set by the reference junction, $\Delta f_{01} = f_{01} - f_{01}^0$, versus $V_{\rm P}$ and $\phi_{\rm ext}$ as extracted from two-tone spectroscopy. The dashed line is a sinusoidal guide for the eye, denoting the transition boundary in line with the theoretical expectation. (b)-(d) Three linecuts of f_{01} versus $\phi_{\rm ext}$ at representative $V_{\rm P}$ values, indicated in panel (a) and Fig. 5.3(b-e). The dotted line indicates f_{01}^0. For all panels $V_{\rm T}$ = 182 mV.

$\Delta f_{01} = f_{01} - f_{01}^0$, as a function of $V_{\rm P}$ and $\phi_{\rm ext}$. As discussed in the previous Section, positive values of Δf_{01} result from constructive interference between the two junctions, while negative Δf_{01} values result from destructive interference. Going from left to right, three distinct plunger regions can be observed, with a sudden flux offset of exactly π between them (Fig. 5.4(b,d)). We identify the outer two regions as phases with a singlet ground state and the inner region as a doublet ground state. We note that the change in contrast between the two singlet regions suggests that $V_{\rm P}$ also weakly tunes $\Gamma_{\rm L,R}$ in addition to ξ.

For values of $V_{\rm P}$ close to the singlet-doublet transition we also observe a sinusoidal dependence of the transition boundary on the external flux, resulting in an enhanced region of doublet occupation around $\phi_{\rm ext} = \pi$ with respect to $\phi_{\rm ext} = 0$. This comes about from interference between tunneling processes involving the two superconducting leads of the quantum dot junction [74, 232], as further discussed in Sec. 5.5. At a value of $V_{\rm P}$ fixed near this boundary one thus also observes a singlet-doublet transition versus the external flux (Fig. 5.4(c)).

In Fig. 5.4 and subsequent figures, the transition boundary between the singlet and doublet phase appears to be sharp and not affected by the thermal broadening typical of transport experiments [61, 74, 75, 141, 308, 316]. The sharpness is a result of a selective spectroscopy technique. As shown in Fig. 5.23, in the vicinity of a transition two resonant dips appear in single-tone spectroscopy, one for the singlet and one for the doublet. In this circumstance, the center frequency of either dip can be chosen as the readout frequency for the subsequent two-tone spectroscopy measurement. This binary choice selects the transmon transition frequency belonging to the corresponding quantum dot junction state. It is reasonable to assume that the most prominent dip corresponds to the state of the quantum dot junction which is more prominently occupied, and thus lower in energy. If this is the case, the extracted phase boundaries are a close approximation of the zero-temperature phase diagram of the quantum dot junction. We note that when the occupations of singlet and doublet states are almost equally probable, the selective spectroscopy method is affected by selection errors, which leads to the pixelation effects visible in Fig. 5.4 near the phase boundaries. In Sec. 5.6, we will explicitly measure the lifetimes of the quantum dot in the singlet and doublet states, substantiating the latter statements.

TUNNEL GATE

Next, we explore the singlet-doublet transition in plunger and tunnel gate space, where the tunnel gate is expected to control the tunnel rates between the quantum dot and the leads, $\Gamma_{\mathrm{L,R}}$. Fig. 5.5(a) shows Δf_{01} versus plunger and tunnel gates at $\phi_{\mathrm{ext}} = 0$. The region of doublet occupancy ($\Delta f_{01} < 0$) takes the shape of a dome, similar to the one coarsely seen in flux-insensitive tunneling spectroscopy experiments [185, 187]. This shape is in accordance with theoretical expectations for the boundary in the $\xi - \Gamma$ plane. Its physical origin depends on the parameter regime [144]. For $U \ll \Delta$ it arises due to an increase in induced superconductivity on the dot with increasing values of Γ, favoring BCS-like singlet occupation. For $U \gg \Delta$ it instead comes about from increased anti-ferromagnetic Kondo exchange interactions between the spin on the dot and the quasiparticles in the leads, favoring a Yu-Shiba-Rusinov (YSR)-like singlet occupation. In both regimes the singlets compete with doublets, ultimately determining the transition to a singlet ground state at large enough $\Gamma = \Gamma_{\mathrm{L}} + \Gamma_{\mathrm{R}}$.

We investigate the same plunger and tunnel gate dependence at an external flux $\phi_{\mathrm{ext}} = \pi$, see Fig. 5.5(b). We find that the doublet phase is enhanced considerably compared to $\phi_{\mathrm{ext}} = 0$, due to the previously mentioned interference between tunneling processes to the superconducting leads. Notably, rather than a dome-like shape, the phase boundary takes a characteristic "chimney" shape that was theoretically predicted [232] but, to our knowledge, not yet confirmed experimentally before these measurements. Unlike the dome, the chimney does not close for any V_{T}. In an extended gate range, it is seen to connect to another doublet region of the parameter space which was disconnected from the dome of Fig. 5.5(a) at $\phi_{\mathrm{ext}} = 0$ [see Sec. 5.8].

The chimney at $\phi_{\mathrm{ext}} = \pi$ is much less thoroughly researched than the dome at $\phi_{\mathrm{ext}} = 0$. The open questions include that of the exact nature of the doublet states as a function of the U/Δ and Γ/U ratios, and the role of the flux bias [89, 145, 158, 346]. In particular, when $U \gg \Delta$, the doublet state for small Γ is a decoupled doublet state with a single local moment in the quantum dot. On the other hand, in the same limit but at large Γ (i.e. in the neck of the chimney), the strong exchange interaction with both superconductors is expected to lead to some mixing with the doublet states that involve one Bogoliubov quasiparticle from each lead [351], causing an overscreening of the local moment in the quantum dot. The role of the exchange interaction is more pronounced at $\phi_{\mathrm{ext}} = \pi$ also because the anomalous component of the hybridisation (describing the proximity effect) is suppressed due to the cancellation of contributions from the left and right leads [346], where the cancellation is exact when $\Gamma_{\mathrm{L}} = \Gamma_{\mathrm{R}}$. This further stabilizes the spin-doublet states. The experimental observation of the chimney calls for more thorough theoretical studies of this parameter regime of the model.

We compare the results at both values of external flux to the expected transition frequencies obtained from NRG calculations. We assume that $\xi = 0$ occurs at $V_{\mathrm{P}} = 395\,\mathrm{mV}$ since this is the symmetry point of the experimental data. At this point, by requiring

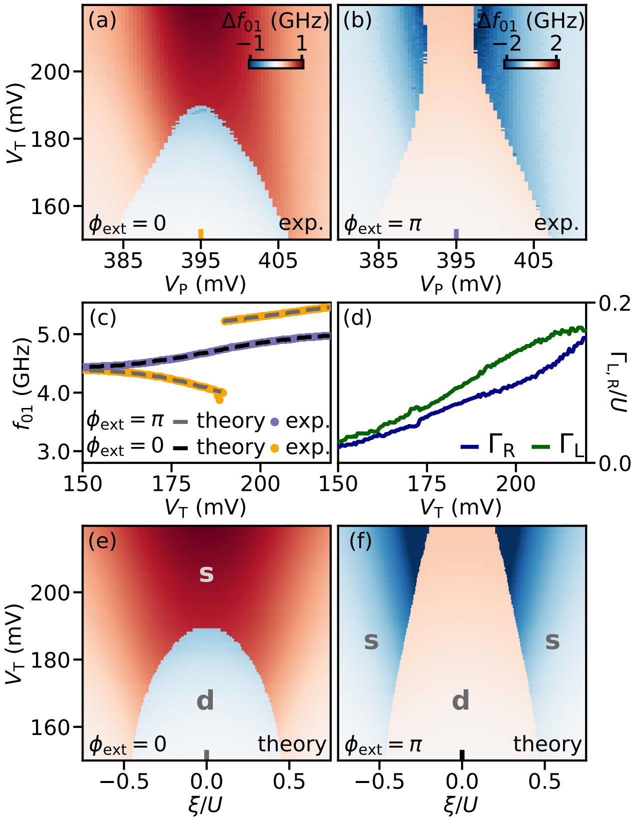

Figure 5.5: **Tunnel gate dependence.** (a) Δf_{01} versus V_P and V_T at $\phi_{ext} = 0$, where V_T is a virtual gate voltage defined as a linear combination of V_C and V_R (see text). The blue region corresponds to a negative supercurrent contribution from the quantum dot junction, while the red region corresponds to a positive contribution. (b) The same measurement as (a) repeated for $\phi_{ext} = \pi$. (c) Linecuts of (a) and (b) at $V_P = 395\,\mathrm{mV}$ overlayed with best-fits based on NRG calculations. (d) Extracted dependence of $\Gamma_{L,R}$ on V_T. (e) Calculated transmon frequencies based on NRG calculations at $\phi_{ext} = 0$ as matched to the measured data, with the V_T axis as given in figure (d). The color bar is shared with panel (a). (f) Same as (e) but for $\phi_{ext} = \pi$, with the same color bar as (b). For the NRG calculations in panels (c-f) we fix $\Delta/h = 46\,\mathrm{GHz}$ and $U/\Delta = 12.2$.

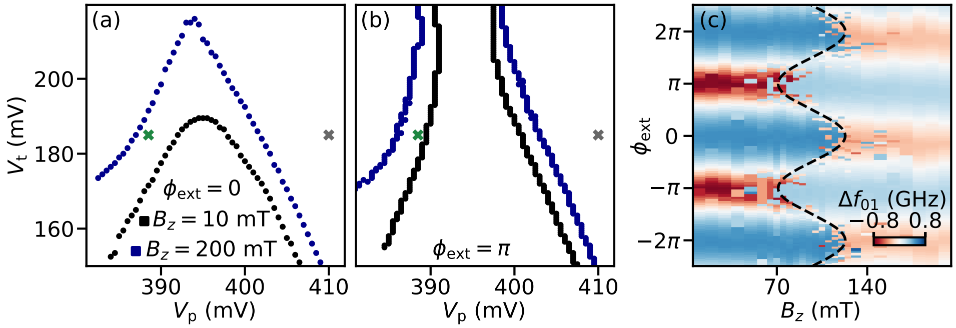

Figure 5.6: **Parallel magnetic field dependence.** (a) Borders between singlet and doublet regions for $B_z = 10$ mT (black) and $B_z = 200$ mT (blue). $\phi_{\text{ext}} = 0$ (b) Same as (a) but for $\phi_{\text{ext}} = \pi$. The grey marker denotes the gate point used to re-calibrate the flux axis after varying B_z [see Sec. 5.8]. (c) Δf_{01} versus B_z and ϕ_{ext}, measured at the gate point indicated in (a) and (b) with a green marker. The sinusoidal dashed line serves as a guide for the eye, in line with the transition boundary expect from theory.

simultaneous agreement between experiment and theory for both values of external flux (Fig. 5.5(c)), we are able to extract several of the model parameters. We find that $\Delta/h = 46$ GHz (190 μeV), close to the bulk value of Al. We furthermore extract $U/\Delta = 12.2$, corresponding to a sizeable charging energy of 2.3 meV. It places the nature of the singlets near $\xi = 0$ in the strongly correlated regime, with a YSR-like character rather than a BCS-like one. By matching values of $\Gamma_{\text{L,R}}$ to V_{T} we then find that Γ/U varies between 0.05 and 0.4, while $\Gamma_{\text{R}}/\Gamma_{\text{L}} \approx 0.75 - 1$ in the range of gates explored (Fig. 5.5(d)). The details of the numerical procedure as well as error estimation can be found in the Supplementary Information (Section I.C), including estimates based on an alternative potential shape for the reference junction [see Sec. 5.8].

The extracted set of parameters is consistent with the observed dome shape at $\phi_{\text{ext}} = 0$, as shown in Fig. 5.5(e). Additionally, as a result of the ratio $\Gamma_{\text{R}}/\Gamma_{\text{L}}$ remaining close to 1, the extracted parameters also match the observed diverging behaviour at $\phi_{\text{ext}} = \pi$ (Fig. 5.5(f)), which was not enforced in the parameter extraction. In these panels we did not map V_{P} to ξ beyond identifying $V_{\text{P}} = 395$ mV with $\xi = 0$ as a unique mapping could not be constructed due to the unintended dependence of Γ on V_{P}. We speculate that this causes the remaining discrepancies between the measured and calculated boundaries in the horizontal direction.

MAGNETIC FIELD PARALLEL TO THE NANOWIRE

Finally, we investigate the effect of a magnetic field applied parallel to the nanowire on the phase transition boundaries. Here, we expect a magnetic-field induced singlet-doublet transition to occur [185, 315, 335]. As B_z increases, the doublet sector separates into spin species that are aligned and anti-aligned with respect to the magnetic field, dispersing in opposite energy directions. The singlet ground state energy, on the other hand, is approximately independent of magnetic field. Given an appropriate zero-field energy level configuration, for some B_z value the energy of one of the two doublet states will thus become lower than that of the singlet, and become the ground state instead (see Fig. 5.1(c)).

Such a transition will only occur for specific configurations of V_P and V_T in the experimentally accessible range of magnetic fields. We therefore start by applying $B_z = 200\,\mathrm{mT}$ parallel to the nanowire axis, a sizeable magnetic field, yet one for which the E_J of the reference junction is not yet substantially suppressed [see Sec. 5.8]. At this field we investigate the effect on the V_P and V_T phase map. The result, shown in Figs. 5.6(a-b), reveals an expansion of the doublet region for both $\phi_\mathrm{ext} = 0$ and $\phi_\mathrm{ext} = \pi$. We can classify different regions in the parameter space by comparing the phase boundaries at $B_z = 10\,\mathrm{mT}$ and $B_z = 200\,\mathrm{mT}$. There are regions in which a singlet ground state remains a singlet ground state, independent of the flux and the magnetic field, as well as regions where a singlet-doublet transition occurs depending on the value of the flux. However there is also a region that starts off as a singlet ground state and ends up as a doublet ground state at high field, for all values of the flux. Thus, fixing V_P and V_T in this region, we expect to observe a transition with B_z for any value of ϕ_ext. A measurement of Δf_{01} versus ϕ_ext and B_z (Fig. 5.6(c)) indeed reveals such a transition, occurring at a different magnetic field depending on the external flux value. For details about the data analysis and identification of the flux axis we refer to the Supplementary Information of Sec. 5.8.

5.6. DYNAMICS OF THE SINGLET-DOUBLET TRANSITION

In the preceding sections we made use of selective spectroscopy to reconstruct the phase transition boundaries. We now turn to time-resolved spectroscopy techniques to study the parity dynamics of the quantum dot junction close to the transition, aiming to characterize the lifetimes of singlet (even parity) and doublet (odd parity) states. These methods have previously been used to study quasiparticle dynamics in superconducting qubits [286, 313], and recently also applied to a nanowire junction to study the poisoning of Andreev bound states [122, 124, 334].

To resolve individual switching events we use a second device (device B) with a larger signal-to-noise ratio (SNR) than the device used for the preceding sections (device A), enabling the use of short acquisition times. Device B is nearly identical to device A, except for two features meant to increase the SNR: (1) a stronger coupling between the resonator and the transmission line; (2) an additional capacitor at its input port, which increases the directionality of the outgoing signal [126]. On device B we perform measurements on microsecond timescales by directly monitoring changes in the outgoing signal at a fixed readout frequency. A continuous measurement of the outgoing microwave field then reveals a random telegraph signal between two different levels, a consequence of the switches in the quantum dot junction parity (Fig. 5.7(a-b)). Owing to the increased temporal resolution of the detection method, even short-lived excited state occupation can now be detected. The characteristic time scales of the telegraph signal reflect the underlying lifetimes of the singlet and doublet states, T_s and T_d, or equivalently their decay rates, $\Gamma_\mathrm{s} = 1/T_\mathrm{s}$ and $\Gamma_\mathrm{d} = 1/T_\mathrm{d}$. These quantities can be extracted via a spectral analysis of the time traces, as described in Sec. 5.8.

To investigate the switching dynamics we tune device B to a regime similar to that of Sec. 5.5 studied in device A. By measuring S_{21} with single-tone spectroscopy we oncemore find ground state transitions between singlet and doublet as a function of V_P (Fig. 5.7(c)). The discontinuous resonant shape, akin to that of Fig. 5.3(b), is symmetric around $V_\mathrm{P} = 546$

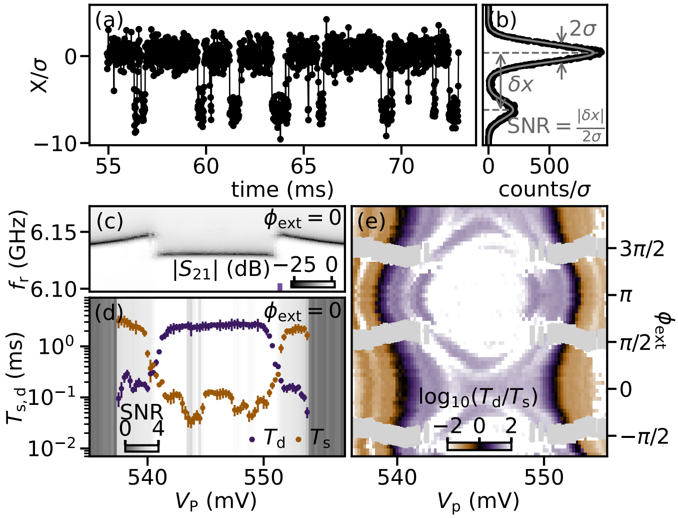

Figure 5.7: **Dependence of parity lifetimes on V_P and ϕ_{ext} for device B.** (a) A 18 ms cut of a continuously measured time trace integrated in time bins of $t_{\mathrm{int}} = 11.4\,\mu\mathrm{s}$, revealing jumps between two distinct states. X is the common axis onto which the quadratures of the outgoing microwave field are rotated to obtain the highest SNR, which takes a value of 3.3 in this panel. (b) 1D histogram of the response in (a) (black) and the best fit of a double Gaussian line-shape (gray). The separation of their centers δx and their width σ together define the SNR. The ratio of their amplitudes determines the ratio of the lifetimes. For panels (a-b) $V_P = 551.4$ mV and $\phi_{\mathrm{ext}} = 0$. (c) V_P dependence of $|S_{21}|$ at $\phi_{\mathrm{ext}} = 0$. (d) V_P dependence of the extracted lifetimes at $\phi_{\mathrm{ext}} = 0$. Markers indicate the mean while error bars indicate the maximum and minimum values of 10 consecutive 2 s time traces. The SNR is shown in greyscale in the background. For points where SNR < 1, the extracted lifetimes are discarded. (e) 2D map of $\log_{10}(T_d/T_s)$ versus V_P and ϕ_{ext}, extracted from a 2 s time trace for each pixel. White pixels indicate points at which SNR < 1, while grey regions indicate where the resonator frequencies of singlet and doublet states overlap and thus cannot be distinguished.

mV, which we identify with $\xi = 0$. The singlet and doublet resonant frequencies are simultaneously visible close to the discontinuity at the transition. The time-resolved measurements over the same gate voltage range reveal a smooth but strong evolution of the parity lifetimes with V_P (Fig. 5.7(d)). The hierarchy of lifetimes inverts as V_P is tuned across the phase transition, reflecting the change in the ground state parity. Away from the transition, in either the singlet or doublet phase, we observe the lifetime in the ground state sector to be on the order of several milliseconds, exceeding that of the excited state by more than an order of magnitude. These numbers are very favorable for the implementation of Andreev pair qubits [136] as well as Andreev spin qubits [122–124], whose control has so far been limited by microsecond parity lifetimes.

We further explore the evolution of the relative lifetimes versus V_P and ϕ_{ext}. Fig. 5.7(e) shows a two-dimensional map of $\log_{10}(T_d/T_s)$, which is a measure of the lifetime asymmetry. We find behaviour similar to that previously seen in Fig. 5.4, with a sinusoidal boundary of equal rates, indicative of the singlet-doublet transition. Furthermore, we observe a strong polarization of the junction parity inside the doublet phase ($T_d \gg T_s$), where the signal-to-noise ratio (SNR) eventually becomes limited by our ability to resolve the rare and short-lived switches out of the ground state. Additionally, we find a modulation of T_d with flux, with longer lifetimes at $\phi_\mathrm{ext} = \pi$ [see Sec. 5.8]. This flux dependence likely originates from the oscillation of the singlet-doublet energy gap with flux, but might also be indicative of a coherent suppression of the tunneling rates.The polarization of the junction parity also occurs inside the singlet phase, where $T_\mathrm{s} \gg T_\mathrm{d}$ for V_P values away from the transition (Fig. 5.7(d)).

Strong parity polarization may not be surprising for a system in thermal equilibrium at temperatures below 100 mK, typical of these experiments, corresponding to a thermal energy small compared to the singlet-doublet energy difference away from the transition. However, parity lifetimes in superconducting circuits are seldom determined by thermal fluctuations, but rather by highly energetic non-equilibrium quasiparticles [105]. While such non-equilibrium quasiparticles are most likely also present in our device, we believe that their influence is suppressed by the large charging energy of the quantum dot junction.

Finally, we observe a non-monotonic variation of the rate asymmetry inside both the singlet and doublet phase, forming apparent contours of fixed lifetimes (Fig. 5.7(e)). We hypothesize two possible reasons behind this structure in the data: it could be caused by parity pumping mechanisms where the readout tone is resonant with the energy difference between singlet and doublet [334], as well as by the spectral density of the non-equilibrium quasiparticles present in the environment [287]. Further investigation of the tunnel gate, power, and temperature dependence of the rate asymmetry can be found at the end of 5.8; we leave a more detailed study for future work.

5.7. CONCLUSIONS

We have demonstrated the use of a transmon circuit to sensitively detect the ground state parity of a quantum dot Josephson junction. The transition frequency of the transmon exhibits a discontinuity if the ground state of the device changes from a singlet to a doublet, due to the presence of a π-phase shift in the Josephson potential of the junction. This allowed us to accurately reconstruct the occurrence of the singlet-doublet transition as a function of all control parameters available in a single device, matching them to those expected from NRG calculations of an Anderson impurity model. In particular, we have observed the flux-induced enhancement of the doublet phase, in the form of the striking transformation of a dome-shaped phase boundary at $\phi_\mathrm{ext} = 0$ into a chimney-shaped phase boundary at $\phi_\mathrm{ext} = \pi$ (Fig. 5.5).

In future research, this singlet-doublet tuning capability could become beneficial for several applications. First, it can be used to define and control Andreev pair and spin qubits, and to couple them to conventional superconducting qubits. Second, tuning the dot to the doublet phase is a robust way to induce a π phase shift, which could be exploited to define a hybrid $0-\pi$ qubit that does not rely on the fine-tuning of the applied flux [181]. Third, it can facilitate the bottom-up realization of a topological superconductor from a chain of proximitized quantum dots [97, 275, 302]. Finally, fast gate or flux-based switching between the 0 and π shift of the dot can also be of interest for applications in Josephson magnetic random access memory (JMRAM) technologies [67].

We have subsequently used continuous time-domain monitoring of the transmon resonant frequency to determine the lifetimes of singlet and doublet states. We find that the time between switching events is strongly enhanced when the quantum dot is tuned away from the phase transition. Since our estimates indicate that $U \gg \Delta$ in our devices, we attribute this effect to the large energy difference associated with charging the quantum dot. These findings are encouraging for Andreev qubits, which benefit from long parity lifetimes, and suggest that large-U quantum dots could be effective as filters for high-energy quasiparticles. However, further work is required to understand the full dependence of parity lifetimes on U.

In this work we have focused on the study of a single-level quantum dot by tuning our junction very close to pinch-off. Looking forward, there is much left to explore in the parameter space of such a device. To begin with, it would be interesting to understand whether the crossover from the BCS-like to the YSR-like singlet has any signature in the microwave response of the system. Second, opening the junction further brings the quantum dot into a multi-level regime, not captured by the single impurity Anderson model, and still largely unexplored. Finally, while we have primarily studied the ground state properties of the quantum dot junction, microwave spectroscopy should allow one to study its excitations, as e.g. recently demonstrated in Refs. [51, 91], particularly at $\phi_{\text{ext}} = \pi$.

Further work will also aim at elucidating the role of spin-orbit coupling in the quantum dot junction. It is well known that, when time-reversal invariance is broken, spin-orbit coupling can induce a spin-splitting of energy levels in the doublet sector [59, 234, 312], essential for Andreev spin qubits. While this effect could have been expected to occur in the measurements presented here, it was not detected; we speculate that the level spacing in the dot was too large to result in a significant splitting [234].

Important extensions of our work could arise if the hybrid nanowire in our microwave circuit was driven into the Majorana topological phase [16, 17, 102, 156], which is currently challenging because of a large parameter space [246] and because of demanding disorder requirements [4]. Including a quantum dot in a Josephson junction between two topological superconductors could be beneficial for the detection of the 4π Josephson effect: as we have seen, it mitigates quasiparticle poisoning, although it would not resolve [284] the problem of distinguishing Majorana zero modes from trivial zero-energy Andreev bound states [256]. Finally, the manipulation of quantum dots coupled to superconducting leads is an essential ingredient of scalable proposals for topological quantum computation [155].

5.8. SUPPLEMENTARY INFORMATION

NUMERICAL MODELING

ANDERSON MODEL WITH SUPERCONDUCTING LEADS

As discussed in the main text, we model the quantum dot junction as a single Anderson impurity coupled to two superconducting leads. The Hamiltonian of the model takes the form

$$H = H_{\text{dot}} + H_{\text{leads}} + H_{\text{T}}. \tag{5.3}$$

The first term describes a single-level quantum dot,

$$H_{\text{dot}} = \sum_{\sigma=\uparrow,\downarrow} \epsilon_\sigma d_\sigma^\dagger d_\sigma + U n_\uparrow n_\downarrow\,. \tag{5.4}$$

Here, $\epsilon_{\uparrow,\downarrow} = \epsilon \pm E_Z/2$ gives the single-particle energies: ϵ is the dot energy level measured with respect to the Fermi level in the leads, and $E_Z = g\mu_B B$ is the Zeeman energy. In the latter, g is the effective g-factor of the level, μ_B is the Bohr magneton, and B is the magnetic field strength. Finally, $U > 0$ is the repulsive Coulomb interaction between the electrons, which disfavors the double occupancy of the impurity, while $n_\sigma = d_\sigma^\dagger d_\sigma$ are number operators for the dot level, with d_σ ($d_\sigma^\dagger$) the electron annihilation (creation) operators.

The many-particle energy levels of Eq. (5.4) are divided in two sectors, corresponding to their fermion parity, or equivalently, to their total spin S. The singlet sector includes the states of even parity, which have $S = 0$: the empty state $|0\rangle$ and the pair state $|2\rangle = d_\uparrow^\dagger d_\downarrow^\dagger |0\rangle$. The doublet sector includes the states of odd parity, which have $S = 1/2$: $|\uparrow\rangle = d_\uparrow^\dagger |0\rangle$ and $|\downarrow\rangle = d_\downarrow^\dagger |0\rangle$. It is convenient to introduce the energy $\xi = \epsilon + U/2$, corresponding to half of the energy gap in the singlet sector, so that $\xi = 0$ corresponds to the electron-hole symmetry point, where $|0\rangle$ and $|2\rangle$ are degenerate in energy. The ground state of H_dot belongs to the doublet sector for $|\xi/U| < 1/2$.

The second term in Eq. (5.3) describes two superconducting reservoirs,

$$H_\text{leads} = \sum_{i,k} \epsilon_k n_{i,k} + \sum_{i,k} \left(\Delta e^{-i\phi_i} c_{i,k\uparrow}^\dagger c_{i,k\downarrow}^\dagger + \text{h.c.} \right) \tag{5.5}$$

where $i = \text{L}, \text{R}$ labels the left and right leads, k labels spin-degenerate single-particle states, $\Delta e^{-i\phi_i}$ is the s-wave pairing potential in each reservoir, and $c_{i,k\sigma}$ ($c_{i,k\sigma}^\dagger$) are the electron annihilation (creation) operators in the leads. The gauge-invariant phase difference between them is $\phi = \phi_L - \phi_R$. We assume the reservoirs to have identical gap Δ and density of states ρ; this assumption should be reasonable since in the experiment the two leads are made out of a single hybrid nanowire. We further take the g-factor of the reservoirs to be zero, capturing the magnetic field dependence of the combined system in the effective quantum dot g-factor of Eq. (5.4).

Finally, the third term is the tunneling Hamiltonian coupling the dot and the reservoirs,

$$H_T = \sum_{i,k,\sigma} \left(t_i c_{i,k,\sigma}^\dagger d_\sigma + \text{h.c.} \right), \tag{5.6}$$

where t_i are the dot-reservoir tunnel coupling strengths, which, for simplicity, we choose to be independent of k and spin. The tunneling rate across each barrier is given by $\Gamma_i = \pi\rho|t_i|^2$. The tunneling terms in H_T break the conservation of the parity and spin in the quantum dot. Nevertheless, the notion of singlet and doublet sectors introduced for the dot Hamiltonian of Eq. (5.4) is inherited by the total Hamiltonian of Eq. (5.3), provided that the spin S is now regarded as the total spin of the system, including that of quasiparticles in the reservoirs. The same holds for parity, which must be redefined as the parity of the total number of electrons in the system.

Over the years, the model of Eq. (5.3) (or immediate extensions of it) has become paradigmatic to describe quantum dots coupled to superconducting leads. It has been studied in different limits and using a variety of numerical methods, often requiring advanced many-body methods such as the numerical renormalization group (NRG) and quantum Monte Carlo for full quantitative descriptions [215]. In the present work, we used NRG methods to extract the energies of the singlet and doublet states for any combination of the model parameters. These energies are then incorporated in a DC SQUID transmon Hamiltonian which is used to match the experimental data and extract estimates of the model parameters. These procedures are detailed in the remainder of this Section.

NRG CALCULATION

The NRG method is an iterative procedure for solving quantum impurity problems involving a localized few-level system coupled to a continuum of itinerant electrons (fermionic bath, normal-state or mean-field BCS superconductor). It consists of several steps: 1) discretization of the continuum parts of the Hamiltonian using a geometric-progression mesh with an accumulation point at the Fermi level (the so-called logarithmic discretization), 2) unitary transformation of the resulting discretized Hamiltonian from the star-geometry (impurity coupling to each representative mesh point) to a linear tight-binding chain representation (the so-called Wilson chain), 3) iterative diagonalization in which the Wilson chain sites are taken into account consecutively [47, 172, 274, 338, 343]. The discretization is controlled by the discretization parameter $\Lambda > 1$ which controls the coarseness of the grid. When the discretization is coarse, the results can be improved by twist averaging, which consists of performing the same calculation for several different discretization grids and averaging the results [47, 323]. The growth of the Hilbert space is controlled by the truncation parameters which control the number of states retained after each step of the iteration.

The calculations in this work have been performed with the NRG Ljubljana code [349]. Since the main quantities of interest are the ground state energies in each spin sector, very high quality results can be obtained even with coarse discretization ($\Lambda = 8$) and keeping no more than 3000 states (spin multiplets) in the truncation. We have verified that the twist averaging is not required. The BCS gap was chosen to be $\Delta = 0.1D$, where D is the half-bandwidth. The calculations were performed for a problem with symmetric hybridisations, $\Gamma_\mathrm{L} = \Gamma_\mathrm{R}$. This is sufficient, because the results for an arbitrary coupling asymmetry can be obtained from the following mapping [145]:

$$\phi_S(\phi, a) = 2\arccos\sqrt{1 - \frac{4a}{(a+1)^2}\sin^2(\phi/2)}, \tag{5.7}$$

where $a = \Gamma_\mathrm{L}/\Gamma_\mathrm{R}$ is the asymmetry, ϕ is the BCS phase difference in the asymmetric problem, and ϕ_S is the effective BCS phase difference in the effective symmetric problem.

Such calculations were performed for a set of values of the interaction strength U (from very low values $U = 0.1\Delta$ that correspond to ABS-like subgap states, up to $U = 30\Delta$ that correspond to YSR-like subgap states). In every value of U, a grid of ξ and Γ parameters was set up, and a sweep of ϕ between 0 and π (50 points) has been performed for each (ξ, Γ) pair. The ground state energies are obtained as the sum of all energy shifts [172] performed during the NRG evolution, which has been shown to produce extremely accurate results [323]. Some calculations have also been performed in the presence of a small Zeeman splitting. The results have been collected, documented, and made available on a public repository [349]. The full set of input files and scripts is provided for running the calculations for different parameters or for different Hamiltonians.

Having developed the NRG calculation, we can gain insight into the expected boundaries between singlet and doublet occupation. In Fig. 5.8(a), we show the phase diagram for the symmetric configuration $\Gamma_L = \Gamma_R$ at fixed $\phi = 0$ and $U/\Delta = 5$. In the (ξ, Γ) plane, the phase diagram takes a dome-like shape with the transition value of Γ being the highest at the electron-hole symmetry point $\xi = 0$. At this point, the transition value of Γ diverges if the phase difference between the reservoirs is changed to $\phi = \pi$, because in this case a destructive interference between tunneling events to the left or right occurs. This causes the "dome" in the (ξ, Γ) plane to turn into the "chimney" shown in Fig. 5.8(b).

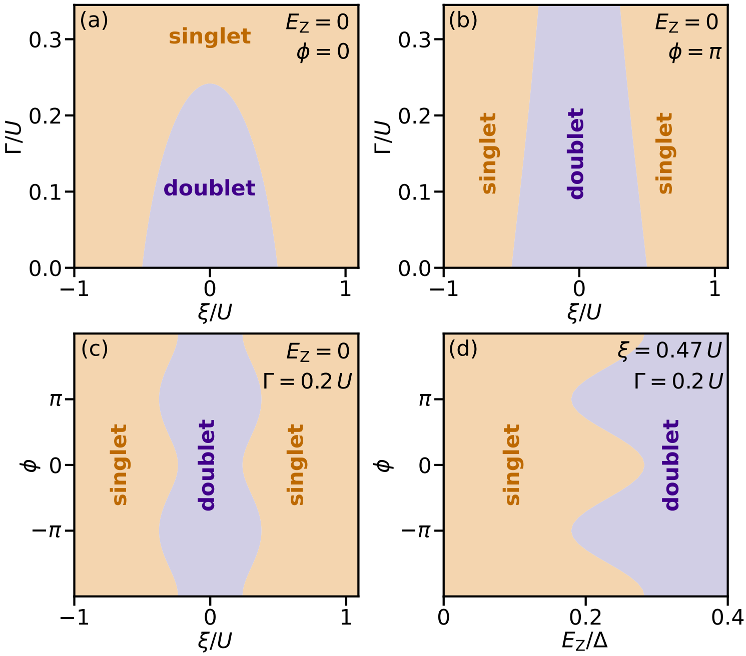

Figure 5.8: **Boundaries between singlet and doublet ground states extracted from NRG calculations.** (a) Boundary in the $\xi - \Gamma$ plane at $\phi = 0$ for $\Gamma_L = \Gamma_R$. (b) Same as (a) for $\phi = \pi$. (c) Boundary in the $\xi - \phi$ plane at $\Gamma = 0.2\,U$. (d) Boundary in the $E_Z - \phi$ plane for $\xi = 0.47\,U$. All panels are for $U/\Delta = 5$.

As mentioned above, at $\Gamma = 0$ the ground state is in the doublet sector for $|\xi/U| < 1/2$. Upon increasing Γ, the Kondo coupling favours the binding of a Bogoliubov quasiparticle in the superconductor to the impurity local moment ("Yu-Shiba-Rusinov" screening), ultimately determining the transition to a singlet ground state at a value Γ_c. The value of Γ_c depends on ξ, ϕ, U and Δ, as well as on the asymmetry between Γ_L and Γ_R. This implies that the singlet-doublet transition can be observed varying any of these parameters individually. Since in the experiment the values of U and Δ are fixed, being determined by the materials and the geometry of the physical device, we focus here on variations in ξ, ϕ, Γ_L and Γ_R.

In Fig. 5.8(c), we show the singlet-doublet transition boundary in the $\xi - \phi$ plane. The interference effect is modulated continuously by the value of the phase difference ϕ, resulting in periodic oscillations of the boundary. The average position of the oscillating boundary is determined by Γ. In Fig. 5.8(d), we show the effect of a Zeeman energy E_Z in the case when the ground state is singlet at $B = 0$. As mentioned in the main text, a singlet-doublet transition is induced at finite E_Z due to the spin-splitting of energy levels in the doublet sector.

TRANSMON DIAGONALIZATION

Having established how to calculate singlet and doublet potentials using the NRG method, we now turn to their inclusion in the Hamiltonian of the transmon circuit [main text Eq. (5.1)]. To numerically solve the Hamiltonian for an arbitrary potential term $V(\phi)$ we make use of the Fourier decomposition (note that the potential can include an external flux ϕ_{ext}):

$$V(\phi) = E_{\text{J},0} + \sum_n E^{\cos}_{\text{J},n} \cos\left(n\phi\right) + \sum_n E^{\sin}_{\text{J},n} \sin\left(n\phi\right) \tag{5.8}$$

with the components

$$E_{\text{J},0} = \frac{1}{2\pi}\int_{-\pi}^{\pi} V(\phi)\, d\phi \tag{5.9a}$$

$$E^{\cos}_{\text{J},n} = \frac{1}{\pi}\int_{-\pi}^{\pi} V(\phi)\cos\left(n\phi\right) d\phi \tag{5.9b}$$

$$E^{\sin}_{\text{J},n} = \frac{1}{\pi}\int_{-\pi}^{\pi} V(\phi)\sin\left(n\phi\right) d\phi \tag{5.9c}$$

where we assume the potential to be a real-valued 2π-periodic function. We can then express the full Hamiltonian in the charge basis as

$$H = 4E_c\hat{N}^2 + E_{\text{J},0} + \sum_n \tfrac{1}{2}\, E_{\text{J},n}\hat{N}^n_+ + \text{h.c.} \tag{5.10}$$

with $E_{\text{J},n} = E^{\cos}_{\text{J},n} - iE^{\sin}_{\text{J},n}$, $\hat{N}$ the charge operator and $\hat{N}^n_+ |N\rangle = |N+n\rangle$.

Upon substituting the potential of main text Eq. (5.2) into Eq. (5.10) and diagonalizing the Hamiltonian, we find the eigenvalues and obtain the energy levels of the combined reference junction and quantum dot junction system. Their difference then results in the transmon's transition frequencies. To numerically compute the eigenvalues we truncate the number of charge states and Fourier coefficients to $N = 35$ for all calculations [162]. We verify that this leads to good convergence for the eigenvalues. We further note that while the presence of the potential offset $E_{\text{J},0}$ does not affect the transmon transition frequencies, its inclusion is crucial: it plays a large role in determining whether the ground state of the combined system corresponds to singlet or doublet occupation for a given set of quantum dot junction parameters.

PARAMETER MATCHING ROUTINE

To match the numerical model to the experimental data we have to overcome several complications. First, the mapping between experimental control parameters and those present in the model is not always trivial. As discussed in the main text, V_p appears to not only tune ξ but also $\Gamma_{\text{L,R}}$. In turn V_t is constructed in such a way that (to first approximation) it does not tune ξ, but it does act on both tunnel rates simultaneously

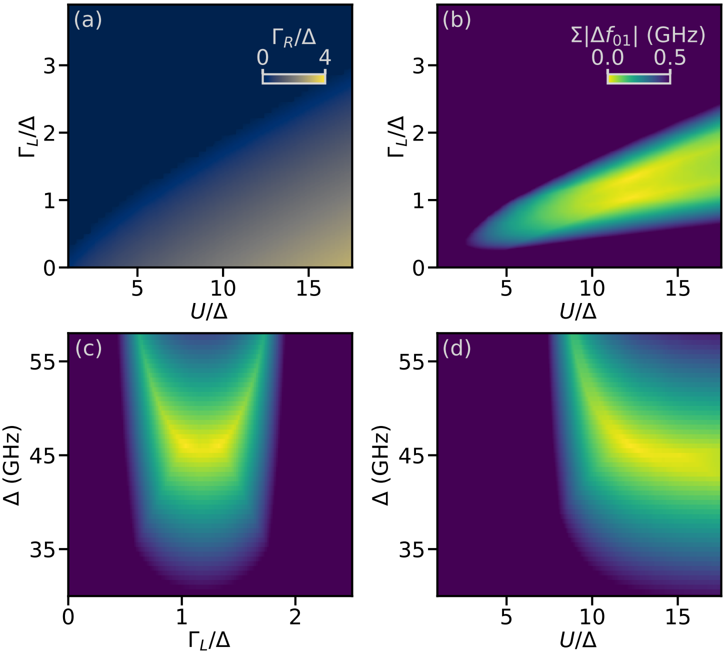

Figure 5.9: **Numerical matching of model parameters** (a) Calculation of the value of Γ_R that leads to a singlet-doublet transition with other model parameters held fixed. Here we fix $\phi_{ext} = 0$ and $\xi = 0$. A value of zero indicates that no such transition occurs. (b) Calculation Eq. (5.11) in the $U - \Gamma_L$ plane evaluated at $\Delta = 46\,\text{GHz}$. (c) Same as (b) in the $\Delta - \Gamma_L$ plane for $U/\Delta = 12.2$. (d) Same as (b) in the $U - \Delta$ plane for $\Gamma_L/\Delta = 1.19$.

with different, unknown lever arms. For mapping the magnetic field axis to the Zeeman energy the challenge lies in determination of the effective g-factor of the quantum dot, known to be a strongly gate and angle-dependent quantity [283]. Only the flux axis allows for a simpler identification, in particular if one assumes that in the singlet configuration the combined DC SQUID Josephson potential takes its minimal (maximal) values at 0 (π), which should hold for even modest SQUID asymmetry. A separate challenge comes from the large number of parameters of the model: Δ, U, ξ, Γ_L, Γ_R, and ϕ_{ext}. With 6 potentially correlated parameters to match one has to carefully assess whether the fit is under-determined.

Given these considerations, we identify a specific gate point in the experimental data that could result in a well-constrained situation: the top of the dome shape of Fig. 5.5(a) in the main text. Here we have access to three measured quantities at a known flux ϕ_{ext}: the singlet and doublet qubit frequencies $f_{01}^{s}(0)$ and $f_{01}^{d}(0)$ measured at the boundary of the transition, and also the doublet qubit frequency $f_{01}^{d}(\pi)$. We furthermore know that here $E_s \approx E_d$ for $\phi_{ext} = 0$, since the data lies on the boundary of a singlet-doublet transition versus tunnel gate. Finally, based on the symmetry of the dome shape we identify that this V_P should correspond to $\xi \approx 0$. We can therefore eliminate two of the model parameters (ξ and ϕ_{ext}) and are left to determine Δ, U, Γ_L and Γ_R.

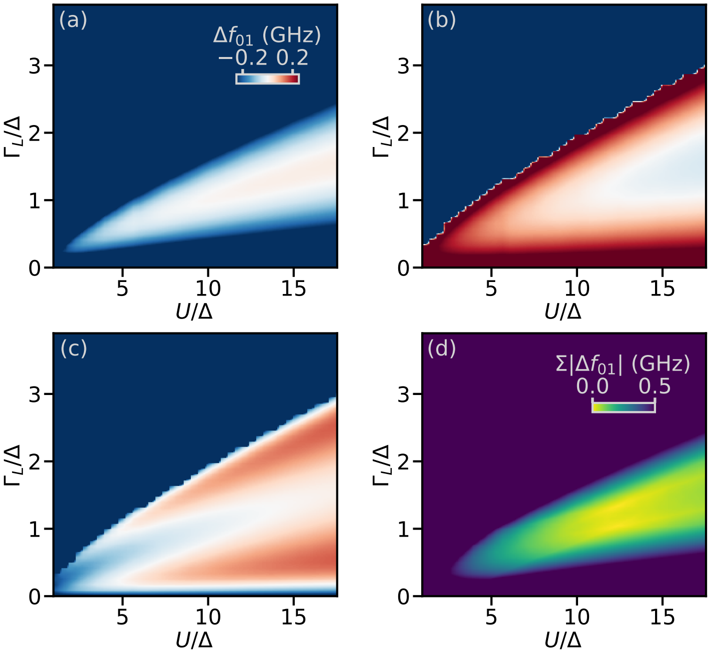

Figure 5.10: **Numerical matching in $\Gamma_\mathrm{L} - U$ plane** (a) Difference in the calculated and measured singlet qubit frequency at $\phi_\mathrm{ext} = 0$ evaluated at $\Delta = 46\,\mathrm{GHz}$. (b) Same as (a) for the doublet qubit frequency at $\phi_\mathrm{ext} = 0$. (c) Same as (a) for the doublet qubit frequency at $\phi_\mathrm{ext} = \pi$. (d) The absolute sum of the differences in panels (a-c).

In a first step we tackle the condition of a singlet-doublet transition occurring versus tunnel gate. For each value of Δ, U and Γ_L we numerically diagonalize the Hamiltonian of Eq. (5.10) to determine the lowest energy level of the total circuit for both the singlet and doublet states and find the value of Γ_R for which these energies are equal. For this we use a reference junction potential $V_\mathrm{j} = E_\mathrm{J}(1-\cos\phi)$ with $E_\mathrm{J} = 12.8$ GHz and $E_\mathrm{c}/h = 210\,\mathrm{MHz}$ as determined later in this section. Shown in Fig. 5.9(a), this results in a U-dependent range of Γ_L for which there is indeed a value of Γ_R that leads to a singlet-doublet transition. Outside of this range Γ_L is so large that the ground state is always a singlet.

Having determined these possible values of Γ_R we calculate the three relevant transmon frequencies $f_{01}^\mathrm{s}(0)$, $f_{01}^\mathrm{d}(0)$, and $f_{01}^\mathrm{d}(\pi)$. These are then compared to the measured values, and an optimal solution is sought that minimizes the sum of the absolute difference between calculation and measurement of all three quantities

$$\Sigma|\Delta f_{01}| = |f_{01}^\mathrm{s,exp.}(0) - f_{01}^\mathrm{s,calc.}(0)| + |f_{01}^\mathrm{d,exp.}(0) - f_{01}^\mathrm{d,calc.}(0)| + |f_{01}^\mathrm{d,exp.}(\pi) - f_{01}^\mathrm{d,calc.}(\pi)|. \quad (5.11)$$

In Figs. 5.9(b-d) we plot a sample of this three-dimensional optimization, while Fig. 5.10 shows how each panel is constructed from the individual singlet and doublet qubit frequencies. Other than the trivial symmetry between $\Gamma_\mathrm{L,R}$, it appears that there is indeed a single region of parameters matching our data. At its global minimum we find $\Delta/h = 46\,\mathrm{GHz}$ ($190\,\mu\mathrm{eV}$), $U = 12.2\Delta$, $\Gamma_\mathrm{L} = 1.19\Delta$ and $\Gamma_\mathrm{R} = 1.47\Delta$, which results in a precise match to the measured qubit frequencies.

Having determined Δ, U, Γ_L, and Γ_R at this single point in gate space, we attempt to match the model to the V_T axis of the data. To do so we fix Δ and U to the determined values and for each value of V_T find the best set of $\Gamma_\mathrm{L,R}$ to match the data. To determine these two parameters we have two measured quantities: up to the transition we have $f_{01}^\mathrm{d}(0)$ and $f_{01}^\mathrm{d}(\pi)$, and after the transition we have $f_{01}^\mathrm{s}(0)$ and $f_{01}^\mathrm{d}(\pi)$. This procedure results in good correspondence to the experimental results, as shown in main text Fig. 5.5(c,d). We note that by construction this captures all the granularity and measurement uncertainty of the experimental data, even though the underlying quantities might have been more smooth. A subsequent procedure that attempts to match V_P to ξ did not turn out to be unique, as V_P appears to also act on $\Gamma_\mathrm{L,R}$. We therefore leave this mapping undetermined.

The uncertainty in the extracted quantities is affected by several factors. The first is the measurement accuracy; we measure the qubit frequency with MHz-scale precision. Based on numerical evaluation of the model, this precision in qubit frequency should limit the extracted parameter accuracy to several GHz. A more substantial uncertainty comes from the determination of the transmon island charging energy E_c, which is typically determined from the transmon transition anharmonicity $\alpha = f_{12} - f_{01}$. While the anharmonicity can be measured to high precision, a complication arises from the usage of a nanowire based Josephson junction as the reference junction. Up to now we have assumed its potential to take the form $V(\delta) = E_\mathrm{J}(1-\cos\delta)$; that of a conventional superconductor-insulator-superconductor (SIS) tunnel junction governed by many weakly transparent channels. In this case we find that $E_\mathrm{c}/h = 210\,\mathrm{MHz}$, resulting in the parameter estimates given above. However, previous work has found that nanowire-based Josephson junctions are better described by several or even a single transport channel, such that $V(\delta) = -\sum_n \Delta\sqrt{1 - T_n \sin^2 \delta/2}$. This change in potential shape can lead to a strong reduction in the anharmonicity, and thus an underestimation of E_c when using the SIS potential [167]. We therefore also match our reference junction dependence to a single transport channel, which is the most extreme case for a reduction in the anharmonicity, finding good agreement with a single transport channel of $T = 0.58$. This in turn leads to an extracted $E_c/h = 306\,\mathrm{MHz}$, resulting in a different set of extracted quantum dot parameters. In particular, we now find $\Delta = 30.5\,\mathrm{GHz}$ and $U = 17.3\Delta$. This value of the induced gap in the InAs-Al nanowire is on the low end of what is typically found in DC transport experiments, which might hint at a reduced proximity effect in the ungated leads [12, 339].

Capacitance simulations of the full circuit do not provide an unambiguous answer for which of the two limits is more appropriate, as the circuit was designed to target $E_c/h = 250\,\mathrm{MHz}$ which falls in the center of the estimated range. As it stands we therefore do not have to uniquely determine the experimentally realized E_c and thereby resolve the uncertainty in the extracted quantities. However, future works could make use of additional circuit QED compatible quantum dot probes such as direct DC access [168] or dispersive gate-sensing techniques [69] to independently characterize several model parameters and further constrain the matching.

CALCULATED 2D MAPS

Having established how to match the model parameters to the data, we now turn to the reconstruction of the full 2D dependencies measured in the experiment (Fig. 5.11). For the plunger versus tunnel gate dependence, we calculate both the singlet and doublet qubit frequencies for all values of $\Gamma_{\mathrm{L,R}}$ encoded by V_{T} for a range of ξ at both $\phi_{\mathrm{ext}} = 0$ and π. We subsequently mask the data according to the ground state of the combined transmon Hamiltonian, and obtain a result that closely approximates the measured data (main text Fig. 5.5). Using the same set of quantum dot junction parameters, we also perform a similar procedure for the 2D map of plunger gate and external flux, resulting good correspondence with main text Fig. 5.4.

STATE POPULATION

We now turn to the singlet and doublet lifetimes determined in device B. For this device we could not identify a measurement point where a unique set of parameters matched the measured data, and can therefore not make a quantitative comparison to the numerics. Instead, we attempt to gain some intuition about the obtained results based on the parameters of device A.

In main text Fig. 5.7 we extract $\log_{10}(T_{\mathrm{d}}/T_{\mathrm{s}})$, the ratio of the lifetimes of singlet and doublet occupation. If the system was in thermal equilibrium with a bath of temperature T, one would naively expect that the relative lifetimes should follow the state populations $P_{\mathrm{s,d}}$ as described by a Maxwell-Boltzmann distribution:

$$P_i = \frac{1}{Z} g_i \exp\left(-E_i/k_{\mathrm{B}}T\right) \tag{5.12}$$

where g_i is the degeneracy of the state, $E_{\mathrm{s,d}}$ are the singlet and doublet energies, and k_{B} is the Boltzmann constant. We take $Z = 2\exp\left(-E_{\mathrm{d}}/k_{\mathrm{B}}T\right) + \exp\left(-E_{\mathrm{s}}/k_{\mathrm{B}}T\right)$, where we

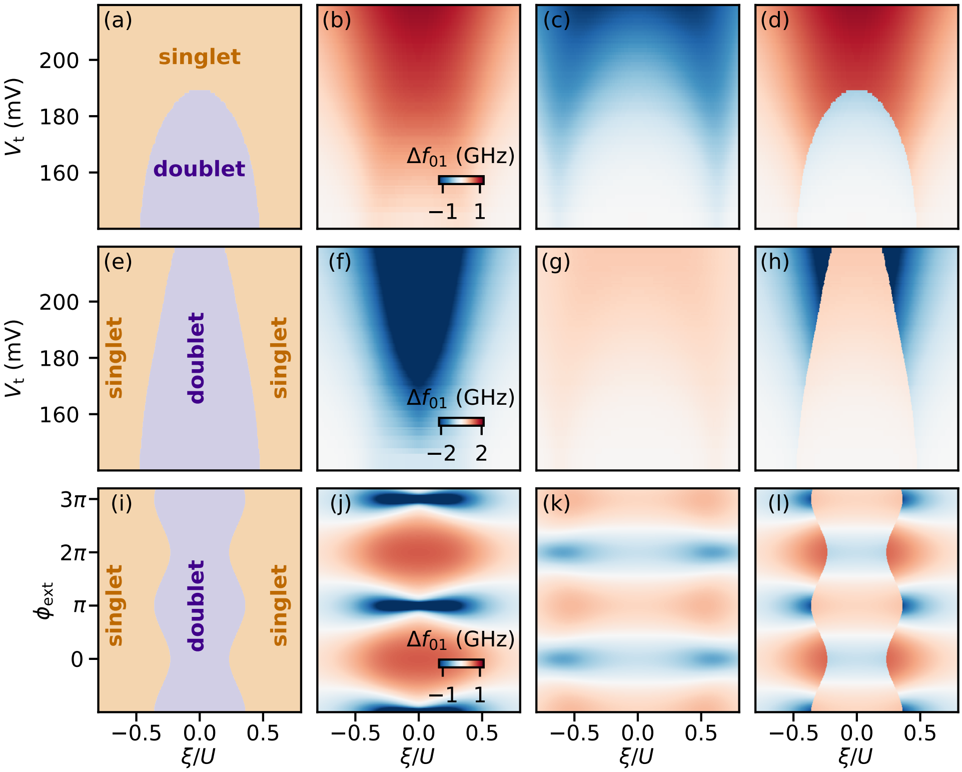

Figure 5.11: **Numerically calculated transmon frequency maps** (a,e,i) Boundaries between singlet and doublet ground states extracted from NRG calculations for $\phi_{\text{ext}} = 0$, $\phi_{\text{ext}} = \pi$, and $\Gamma_R = 1.23\Gamma_L$ respectively. Panels (b-d), (f-h), (j-l) show how the singlet qubit frequency, the doublet qubit frequency, and the combined result conditioned on the ground state of panels (a,e,i) respectively depend on the parameters. Each row shares the same color map. This leads to saturation of the color map in the panels corresponding to the unconditioned singlet and doublet qubit frequencies, but facilitates comparison to the experimental results. For all panels $U/\Delta = 12.2$ and $\Delta = 46\,\text{GHz}$.

neglect potential other many-body states which should be unoccupied at the experimentally relevant temperatures. In Fig. 5.12(a) we then plot $\log_{10}(P_d/P_s)$, choosing a bath temperature of 400 mK. Qualitatively this follows the same trend as observed experimentally, with a sharp boundary at the phase transition and a saturated population imbalance away from that. We stress once-more that this is not a quantitative comparison. However, the need for a temperature far in excess of the refrigerator's base temperature of 20 mK could hint at a non-thermal origin such as non-equilibrium quasiparticles [105].

In the main text we also speculate that non-thermal effects lie at the origin of the experimentally observed contours of fixed lifetime ratio's. We corroborate this in Fig. 5.12(b), where we plot the energy difference between singlet and doublet occupation of the quantum dot junction. This quantity exhibits distinct contours of equal energy difference that qualitatively match those found in the experiment. If the environment has spectral components resonant with these specific energies, one could expect these to modify the dynamics.

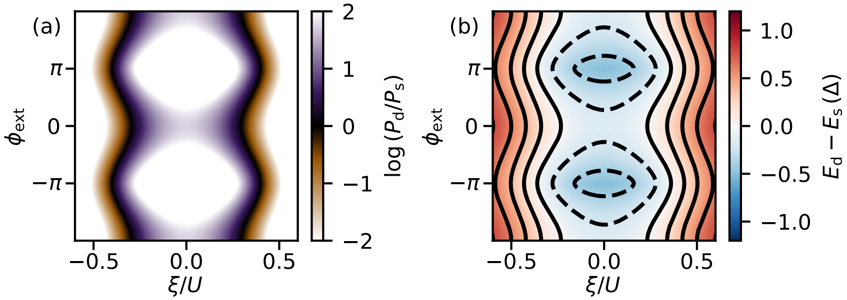

Figure 5.12: **State population versus ξ and ϕ_{ext}** (a) Ratio of the expected state population as calculated from Eq. (5.12) for a temperature of 400 mK. The colormap is saturated to facilitate comparison to main text Fig. 5.7. (b) Difference between doublet and singlet energy. Each contour indicates a boundary of equal energy difference. Parameters are the same as that of Fig. 5.11.

DEVICE AND EXPERIMENTAL SETUP

NANOFABRICATION DETAILS

The device fabrication occurs in several steps using standard nanofabrication techniques, and it is identical for device A and B. The substrate consists of 525 µm-thick high-resistivity silicon, covered in 100 nm of low pressure chemical vapor deposited Si_3N_4. On top of this a 20 nm thick NbTiN film is sputtered, into which the gate electrodes and circuit elements are patterned using an electron-beam lithography mask and SF_6/O_2 reactive ion etching. Subsequently, 30 nm of Si_3N_4 dielectric is deposited on top of the gate electrodes using plasma enhanced chemical vapor deposition and then etched with buffered oxide etchant. The nanowire is then deterministically placed on top of the dielectric using a nanomanipulator and an optical microscope. For this we use an approximately 10 um-long vapour-liquid-solid (VLS) hexagonal InAs nanowire with a diameter of 100 nm and a 6 nm-thick epitaxial Al shell covering two facets [173]. After placement, two sections of the aluminium shell are removed by wet etching with MF-321 developer. These sections form the quantum dot junction and the reference junction, with lengths 200 nm and 110 nm respectively. A zoom-in of the the quantum dot junction is shown in Fig. 5.2(d) of the main text. The reference junction is controlled by a single 110 nm-wide electrostatic gate, set at a DC voltage V_J. The quantum dot junction is defined by three 40 nm-wide gates separated from each other by 40 nm, set at DC voltages V_L, V_C and V_R. Note that in Fig. 5.2(d) the gates appear wider (and the gaps between gates appear smaller) than stated due to distortion by the Si_3N_4 layer; the given dimensions are therefore determined from a scanning electron microscopy image taken before the deposition of the dielectric. After the junction etch the nanowire is contacted to the transmon island and to ground by an argon milling step followed by the deposition of 150 nm-thick sputtered NbTiN. Finally, the chip is diced into 2 by 7 millimeters, glued onto a solid copper block with silver epoxy, and connected to a custom-made printed circuit board using aluminium wirebonds.

GENERAL CHIP OVERVIEW

Optical microscope images of the chips containing devices A and B are shown in Figs. 5.13(a) and (b), respectively. Each chip, 7 mm long and 2 mm wide, consists of four devices coupled to the same transmission line. For the chip containing device A, only one device was functional. Out of the other three, one did not have a nanowire, another contained three nanowires stuck together, and for the third device a gate electrode showed no response. The chip of device B includes an on-chip capacitor on the input port of the transmission line to increase the signal-to-noise ratio. For this chip only two of the devices were bonded: device B, which was functional, and another device that did not show any response to the electrostatic gates. The two unbonded devices were dismissed based on prior optical inspection, containing two and no nanowires respectively.

FLUX CONTROL WITH IN-PLANE MAGNETIC FIELD

In all measurements we control the external flux ϕ_{ext} with the in-plane component of the magnetic field perpendicular to the nanowire, B_y, as illustrated in Fig. 5.14 [334], for which one flux quantum corresponds to 2.2 mT. This is done since flux tuning with the out-of-plane magnetic field B_x led to strong hysteric behaviour in the resonator as well as

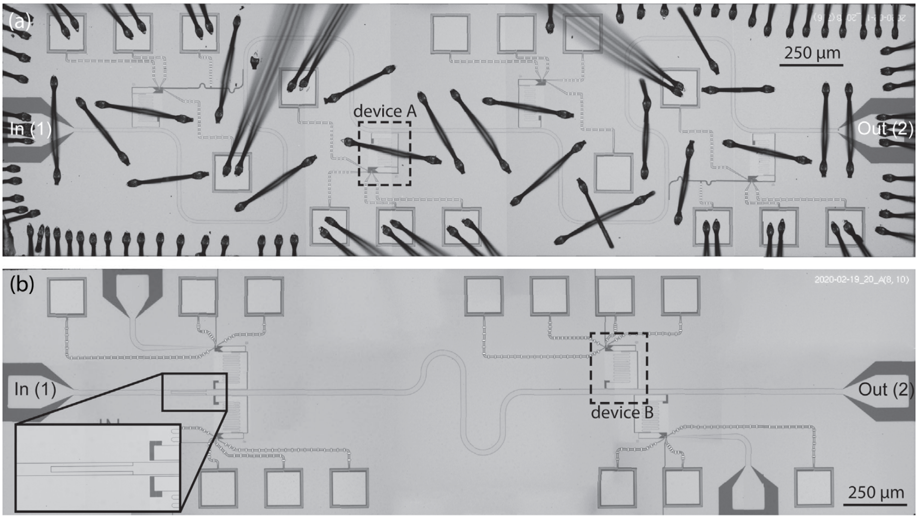

Figure 5.13: **Chip design.** (a) The chip of device A, containing four nearly identical devices coupled to the same transmission line. The image is taken after wire-bonding onto a PCB. (b) The chip of device B, incorporating an input capacitor in the transmission line (enlarged in inset). The image is taken before wire-bonding onto a PCB.

flux jumps in the SQUID loop. We attribute these effects to Abrikosov vortex generation and the presence of superconducting loops on the chip, causing screening currents.

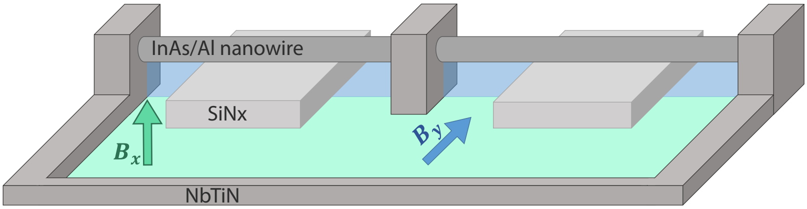

Figure 5.14: **Flux control with $\mathbf{B_y}$.** The nanowire is elevated with respect to the NbTiN plane due to the gate dielectric. This defines a loop area perpendicular to B_y. B_y can therefore be used to control the flux through the SQUID loop while keeping the out-of-plane field component (B_x) fixed, reducing the occurance of external flux jumps.

FLUX JUMPS IN DEVICE A WHEN $|B| < 9\,\mathrm{mT}$

For all measurements of device A, the value of the applied magnetic field is kept above 10 mT to prevent flux jumps observed when $|B| < 9\,\mathrm{mT}$. In particular, for Figs. 5.3 to 5.5 in the main text, $B_z = 10\,\mathrm{mT}$. The reason for this is purely technical. Device A contains various on-chip aluminium wire-bonds connecting separate sections of the ground plane together. Below the critical magnetic field of aluminium (~10 mT [203]) these wire bonds create superconducting loops close to the device region, and have a significant cross-section perpendicular to the chip plane. In this regime, the application of an in-plane magnetic field B_y generates unwanted currents across these superconducting loops, which in turn result in multiple jumps observed in the flux through the SQUID loop (Fig. 5.15), making it impossible to reliably control ϕ_{ext}. Applying a field $|B| > 9\,\text{mT}$ turns the aluminium wire bonds normal and prevents the unwanted flux jumps, as shown in Fig. 5.15(a). As this magnetic field is small compared to other energy scales involved, it should not affect the physics under study. We further note that the absence of superconducting loops containing wire-bonds in device B made it possible to measure this device at $B_z = 0$ mT without suffering from similar flux jumps.

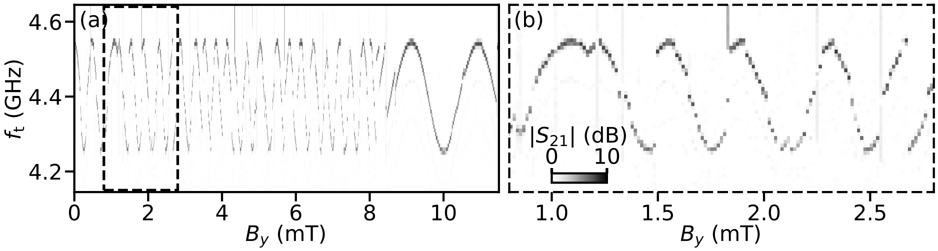

Figure 5.15: **Flux jumps under |B| = 9 mT for device A.** Multiple flux jumps and a distorted periodicity observed at low magnetic fields disappear when $|B| > 9\,\text{mT}$. Here, $B_z = B_x = 0$

Cryogenic and room temperature measurement setup

Both devices are measured in the same Triton dilution refrigerator with a base temperature of 20 mK. As shown in Fig. 5.16, it contains an input RF line, an output RF line and multiple DC gate lines. The DC gate lines are filtered at base temperature with multiple low-pass filters connected in series. The input RF line contains attenuators and low-pass filters at different temperature stages, as indicated. The output RF line contains a travelling wave parametric amplifier (TWPA) at the 20 mK temperature stage, a high-electron-mobility transistor (HEMT) amplifier at the 4 K stage, and an additional amplifier at room temperature. A three-axis vector magnet (x-axis not shown) is thermally anchored to the 4 K temperature stage, with the device under study mounted at its center. The B_z component of the magnetic field is controlled with a MercuryiPS current source while the B_x and B_y axes are controlled with Yokogawa GS200 and GS610 current sources respectively. At room temperature a vector network analyzer (VNA) is connected to the input and output RF lines for spectroscopy at frequency f_r. On the input line, this signal is then combined with the qubit drive tone at frequency f_t for two-tone spectroscopy. A separate tone at f_r only used for time-domain measurements is also combined onto this line. For time-domain measurements the output signal is additionally split off into a separate branch and down-converted to 25 MHz to be measured with a Zurich Instruments ultra-high frequency lock-in amplifier.

Basic characterization and tune up of device A

Reference junction characterization

In this section we investigate the basic behaviour of the reference junction versus junction gate voltage V_J and magnetic field B_z when the quantum dot junction is completely closed. This information is used to choose a V_J set-point, $V_\mathrm{J} = 640\,\mathrm{mV}$, which maintains a good SQUID asymmetry in all regimes of interest. Figs. 5.17(a) and (b) show the V_J dependencies of the resonator and transmon frequencies, respectively. As V_J is varied, different junction channels open sequentially [118, 296], with transparencies that increase non-monotonically due to mesoscopic fluctuations at the junction. This in turn affects the transmon's E_J and results in the observed fluctuations of its frequency.

The B_z dependencies of f_{01} and $f_{02}/2$ at $V_\mathrm{J} = 640\,\mathrm{mV}$ are shown in Fig. 5.17(e). From this we estimate both the transmon island charging energy E_c (not to be confused with U, the charging energy of the quantum dot junction) and the parameters of reference junction potential used in this section to match the measurements to the numerical calculations. Illustrated in this figure is a fit of the data with a Josephson potential governed by a single Andreev level at the junction $V(B,\delta) = -\Delta(B)\sqrt{1 - T\sin^2\frac{\delta}{2}}$. Here $\Delta(B) = \Delta\sqrt{1-(B/B_\mathrm{c})^2}$ is the field dependent superconducting gap [203], Δ is the superconducting gap at zero field, B_c is the critical magnetic field and T is the transparency of the junction. As the fit is not constrained well enough to provide a unique solution, we fix $\Delta/h = 60$ GHz based on recent experiments on the same nanowires [299]. We obtain $E_\mathrm{c}/h = 306$ MHz, $T = 0.58$, and $B_\mathrm{c} = 413$ mT, resulting in an effective $E_\mathrm{J} \sim \Delta T/4 = 8.7$ GHz. A similar procedure is then performed for $V_\mathrm{j} = E_\mathrm{J}(1-\cos\delta)$, resulting in $E_\mathrm{c}/h = 210\,\mathrm{MHz}$ and $E_\mathrm{J}/h = 12.8$ GHz.

We can use these parameters to estimate the experimentally-realized SQUID asymmetry $\alpha_S = E_J/E_{J,QD}$ where $E_{J,QD}$ denotes the effective quantum dot junction Josephson energy. To do so we estimate $E_{J,QD}$ from the calculated qubit frequencies of the singlet and doublet obtained through the relation $\hbar\omega_{01} \approx \sqrt{8E_{J,QD}E_c} - E_c$ [162]. We find that $\alpha_S > 10$ for almost all of the parameter range, exceeding 30 for low values of V_t. The asymmetry is at its smallest for the upper values of V_t in the vicinity of $\xi = 0$, where we find a minimum asymmetry $\alpha_S = 4$. We note that the effects of these variations in asymmetry are fully captured by the numerical model; its effects are predominantly on the modulation of the qubit transition frequency with flux and not on the position of the singlet-doublet transition boundaries.

QUANTUM DOT JUNCTION CHARACTERIZATION

In this section we show the basic behaviour of the quantum dot gates when the reference junction is closed. Fig. 5.18 shows effective pinch-off curves for all three quantum dot gates ramped together (a) and for each of them separately, when the other two are kept at 1250 mV (b-d). This shows that each of the three quantum dot gates can independently pinch off the quantum dot junction even if the other gates are in the open regime, signifying strong lever arms and good gate alignment. We note that these are not pinch-off curves as encountered in conventional tunnel spectroscopy. They reflect the voltages at which there is no longer a measurable transmon transition frequency mediated by the quantum dot junction, which could either be due to low tunneling rates or a full depletion of the quantum dot.

We further note that the gate setpoint chosen for the measurements shown in the main text should not be directly compared to the individual pinch-off curves shown here. In panels (b-d) the non-varying quantum dot gates are kept fully open at 1250 mV which, due to cross coupling between gates, results in lower pinch-off values than those at the gate setpoint used for the measurements in the main text.

DEVICE TUNE UP

This section describes the process of tuning up the quantum dot gates to the setpoint used for the main text figures. We start by closing the reference junction ($V_J = -200$ mV) and going to a point in quantum dot gate voltages near pinchoff ($V_C = 100$ mV, $V_L = 250$ mV and $V_R = 400$ mV, see Fig. 5.18). Monitoring the frequency of the resonator while varying one of the gates reveals small shifts away from its bare frequency which resemble the shape expected for quantum dot resonances (Fig. 5.19(a)). Fixing the readout frequency f_r at the bare frequency of the resonator, one can map out the regions where these shifts happen on a two-dimensional map versus the left and right gates (Fig. 5.19(b)). In such maps, a pixel with a dark color indicates the resonator is not shifted from its bare frequency while a bright pixel indicates a shift of the resonator frequency, which we can use to identify potential regions of interest.

After identifying such a region in V_L-V_R space, we open the reference junction to its set-point $V_J = 640$ mV, which lifts the reference transmon frequency to $f^0_{01} = 4.4$ GHz, closer to the bare resonator frequency. This magnifies the dispersive shift of the resonator and, furthermore, brings the external flux into the picture. As shown in Fig. 5.19(e), the asymmetric SQUID behaves as expected for different quantum dot gate setpoints. The reference junction sets the reference value for the transmon frequency, f^0_{01}, and the quantum dot contributes with small variations above or below this setpoint due to constructive or destructive interference, respectively.

Fixing $\phi_{\text{ext}} = 0$ and repeating the initial measurement versus V_{R} with the reference junction open reveals much stronger deviations of the resonant frequency than before (Fig. 5.19(c)). Importantly, the observed resonant frequency is now discontinuous, which, as detailed in the main text, is a signature of a singlet-doublet transition of the quantum dot junction. We tentatively identify the regions for which the resonator frequency is shifted to lower values as doublet regions and perform single frequency readout versus V_{R} and V_{L}, now with f_{r} fixed at the resonator frequency corresponding to doublet regions (Fig. 5.19(d)). The resulting two-dimensional map reveals regions for which the transmission amplitude signal is low (dark regions in Fig. 5.19(d)) which we identify as potential regions with a doublet ground state.

The next step for tuning up is identifying an isolated region where the quantum dot is in a doublet ground state and exploring the behaviour versus the central quantum dot gate. This is shown in Fig. 5.20. As V_{C} is varied at $\phi_{\text{ext}} = 0$ (Fig. 5.20(c)), the resonator first shows a displacement towards higher frequencies to then abruptly drop to a lower frequency, to then finally go back to the higher frequencies once-more. As detailed in the main text, we identify this behaviour with a singlet-doublet transition as the relative level of the quantum dot ξ is being varied. Figs. 5.20(a) and (b) show how this central doublet ground state region varies with each of the two lateral quantum dot gates. In both cases we observe a dome shape, resembling the behaviour we would expect when varying the tunnel coupling between quantum dot and leads. However, these dome shapes are rotated in V_{C}-V_{R} and V_{C}-V_{L} space. This is understood as the result of cross coupling between the different quantum dot gates.

After identifying the cross coupling effect between different quantum dot gates, we define a new set of virtual gates in an attempt to tune the model parameters independently. We fix V_{L} =470 mV (set-point kept for all results shown in the main text) and focus on V_{R}-V_{C} space. Fig. 5.21(b) shows the dome shape previously identified in V_{R}-V_{C} space. We identify a line along the dome (indicated with a dashed line) for which the quantum dot level appears to be fixed and define new plunger virtual gate (V_{P}, perpendicular to this line) and right tunnel virtual gate (V_{T}, along this line) (see Fig. 5.21(d)). This rotated gate frame is the one used for the main text. Note that this routine does not guarantee that V_{P} does not affect the tunneling rates. It rather ensures that V_{T} does not (strongly) affect the quantum dot level ξ.

LARGER TUNNEL VOLTAGE RANGE

In Fig. 5.22 we show the behaviour of the singlet and doublet regions beyond the V_{T} range investigated in Fig. 5.5 of the main text. At $\phi_{\text{ext}} = \pi$ we do not observe the doublet phase boundary fully closing for any V_{T}. According to theory, this should only occur if $\xi \approx 0$ and $\Gamma_{\text{L}} \approx \Gamma_{\text{R}}$ are maintained at each gate setting in the experiment. That this condition would remain satisfied for any V_{T} is implausible given the cross-coupling present in the system. We instead speculate that at higher gate voltages the tunnel rates cease to be a monotonically increasing function, which is substantiated by the tunnel gate dependence at $\phi_{\text{ext}} = 0$. Here we observe a temporary recovery of the doublet region at higher V_{T}, which should not occur for increasing values of Γ. We further speculate that in this regime of increasingly large Γ/U the dot can eventually be tuned to a different charge configuration, involving energy levels not captured by the single-level model.

We note that for these measurements only single tone spectroscopy was performed. We therefore plot $\Delta f_\mathrm{r} = f_\mathrm{res} - f^0_\mathrm{res}$, where f^0_res denotes the resonator frequency with the quantum dot junction pinched off. Its qualitative interpretation is the same as that of Δf_{01} used in the main text.

State selective spectroscopy

For the measurements performed close to singlet-doublet transitions, single-tone spectroscopy simultaneously shows two resonances whose relative depth varies with the distance from the transition. This is once more illustrated in Fig. 5.23, which shows single-tone spectroscopy at several different V_P regions while ϕ_ext is varied. It corresponds to the measurements of Fig. 5.4 of the main text. In panels (a) and (d) we observe only a single resonance; at these plunger gate values the quantum dot junction is sufficiently deep in the singlet and doublet parity sector respectively that only one state is occupied. However, at the plunger gate values between these two regimes (panels (c-d)) the behaviour is more complex. We simultaneously observe two resonances and their depth becomes a function of flux.

For the two-tone spectroscopy measurements in the main text we make use of the averaged occupation of the states captured in the single-tone spectroscopy measurement to identify most occupied state. This can be inferred from the relative depth of the resonances: for example in Fig. 5.23(e) the most occupied state is the singlet, albeit by a small margin. This in turn allows us to do state selective two-tone spectroscopy, revealing the transmon transition that corresponds to the most occupied state of the system. To do so we fix the frequency of the first tone f_r at the bottom of the deepest resonance, corresponding to the most populated sector of the system. We illustrate this in Figs. 5.23(f) and (g), where by fixing f_r at the bottom of the resonance corresponding to the singlet (doublet) state we observe a peak only when f_t is equal to the transmon frequency corresponding to the singlet (doublet) state. It is this peak position that we report as f_{01}.

Magnetic field dependence of device A

In this section we elaborate on the analysis of the data shown in Fig. 5.6(c) in the main text. When varying both ϕ_ext and B_z in a measurement, one has to consider the possibility of an unwanted misalignment of the magnetic field with respect to the nanowire axis. This, in combination with the multiple orders of magnitude difference between the applied B_z (hundreds of mT) and the B_x (less than 1 µT) or B_y (several mT) needed to thread a flux quantum through the SQUID loop, can result in big changes of the $\phi_\mathrm{ext} = 0$ point for different values of B_z. Therefore, one has to re-calibrate the value of B_y that corresponds to $\phi_\mathrm{ext} = 0$ for each B_z value. To do so, we use the flux dependence of f_{01} at a gate point for which the quantum dot junction ground state remains a singlet for the whole B_z range as a reference for identifying $\phi_\mathrm{ext} = 0$. This gate point is indicated with a grey cross in Fig. 5.24(a).

The measurement shown in Fig. 6(c) is therefore performed as follows:

```
for each $B_z$ value do
    apply $B_z$
```

```
    for each $B_y$ value do
        apply $B_y$
        measure $f_{01}$ at the grey gate point
        measure $f_{01}$ at the green gate point
    end for
end for
```

For each B_z value we then reconstruct the B_y dependence of ϕ_{ext} through the dependence of the reference gate point (grey). Furthermore, we use this method to identify points in B_y where flux jumps happen and correct for them. While they almost never occur for small magnetic fields, and none of the other data required such a correction, we found that at increasing B_z jumps would occur more often. We believe this is due to a small misalignment between B_z and the plane of the chip. The resulting corrected ϕ_{ext} reference is shown in Fig. 5.24(b), while Fig. 5.24(d) shows several linecuts.

PARITY LIFETIME EXTRACTION PROCEDURE

In this section we elaborate on the analysis method for extracting the characteristic lifetimes of the singlet and doublet states, T_{s} and T_{d}. We start with a continuous measurement at a fixed readout frequency where we monitor the demodulated output signal integrated in time bins of $t_{\text{int}} = 2.3\,\mu\text{s}$. This reveals a complex random telegraph signal jumping between two states in the (I,Q)-plane. The histogram of the acquired (I,Q) points shows two states (Fig. 5.25(a)) whose centers define an axis X. A segment of the measured telegraph signal, projected onto this X axis, is shown in Fig. 5.25(c). Taking the histogram along this axis results in a double Gaussian distribution (Fig. 5.25(d)) that is well-described by

$$g(x) = \frac{A_1}{\sqrt{2\pi\sigma^2}} e^{\frac{-(x-x_1)^2}{2\sigma^2}} + \frac{A_2}{\sqrt{2\pi\sigma^2}} e^{\frac{-(x-x_2)^2}{2\sigma^2}} \tag{5.13}$$

Here, $A_{1,2}$ are the relative populations of singlet and doublet occupation, $x_{1,2}$ are the centers of each Gaussian and σ is their standard deviation. For the data shown in Fig. 5.25, the fit results in $A_1 = 2169\sigma$, $A_2 = 506\sigma$, $x_1 = 0.37\sigma$ and $x_2 = -6.19\sigma$, from which we determine the SNR $= |x_1 - x_2|/2\sigma = 3.28$.

From the time domain information of the signal we construct its power spectral density (PSD), which is its squared discrete Fourier transform (Fig. 5.25(b))

$$S_X(f) = \frac{\Delta t}{N\pi} \left| \sum_{n=1}^{N} X(n\Delta t) e^{-i2\pi f n\Delta t} \right|^2 \tag{5.14}$$

where $X(t)$ is the measured signal (as projected onto the previously defined X-axis), $\Delta t = 2.3\,\mu\text{s}$ is the discrete time bin in which the data is measured, $N = \frac{T}{\Delta t}$ is the number of points and T is the total signal length. In practice we use Welch's method with a Hanning window [328] to calculate the power spectral density, dividing the trace into 50 sections of length 40 ms that overlap by 20 ms and averaging the power spectral density of all segments. This results in a spectrum that is well fit by a single Lorentzian of the form

$$S(f) = A\frac{4\Gamma}{(2\Gamma)^2 + (2\pi f)^2} + B, \tag{5.15}$$

from which we obtain $1/\Gamma = 0.337$ ms, $A = 5.75 \cdot 10^{-5}$ and $B = 1.65 \cdot 10^{-10}$ Hz^{-1}.

Combining the amplitude ratio $R = A_1/A_2$ obtained from the Gaussian fit of the two quadratures and the Γ value obtained from the Lorentzian fit of the PSD, we calculate

$$T_\mathrm{s} = 1/\Gamma_\mathrm{s} = \frac{1+R}{2\Gamma R} \tag{5.16}$$

$$T_\mathrm{d} = 1/\Gamma_\mathrm{d} = \frac{1+R}{2\Gamma} \tag{5.17}$$

to obtain $T_\mathrm{s} = 0.89$ ms, $T_\mathrm{d} = 0.21$ ms.

EXTENDED PARITY LIFETIME DATA

PARITY LIFETIMES LINECUT VERSUS FLUX

Fig. 5.26 shows the flux dependence of the lifetimes of the singlet and doublet states at $V_\mathrm{P} = 554.4$ mV, which accompanies main text Fig. 5.7. We find that both singlet and doublet lifetimes show an approximate sinusoidal dependence on the applied flux. As discussed in the main text, this flux dependence most likely originates from the oscillation of the singlet-doublet energy gap with flux. However it could also be indicative of a coherent suppression of the tunneling rates [255]. We further note that the sudden drops in SNR are due to crossings of the transmon frequencies of the singlet and doublet states. At these points both resonator frequencies become indistinguishable and their lifetimes can not be measured.

POWER AND TEMPERATURE DEPENDENCE OF PARITY LIFETIMES

Here we present additional data on the readout power and temperature dependence of the parity lifetimes shown in Fig. 5.7 of the main text. The power dependence at four selected points across a phase boundary is shown in Figs. 5.27(c-f). Away from the transition (purple) and right on top of the transition (green) the readout power does not have a strong effect on the extracted lifetimes in the investigated range. For plunger gate values V_P closer to the transition, however, the asymmetry of the lifetimes decreases with power (blue). Although the origin of this dependence is not clear, we conjecture it is related to parity pumping effects [334].

Temperature dependencies at the same gate points, measured at a readout power of -22 dBm at the fridge input, are shown in Figs. 5.27(g-j). Here the mixing chamber temperature of the dilution refrigerator is measured with a ruthenium oxide resistance thermometer and increased in a controlled step-wise fashion with a variable-output heater mounted on the mixing chamber plate. We observe different effects of temperature for each of the gate points. In general, there is a temperature independent regime at low temperatures, followed by a temperature dependent drop above a certain characteristic temperature, which varies over tens of mK for different gate points. For some of the gate points, however, the temperature independent contribution is absent and the effect of increased mixing chamber temperature starts immediately at base temperature (Fig. 5.27(i)). These results are indicative of non-equilibrium effects playing a role in the physics of the devices under study, their exact behaviour dependent on the energy level configuration of the quantum dot junction.

PARITY LIFETIMES VERSUS TUNNEL GATE

To complement the data shown in Fig. 5.7 of the main text, taken at $V_T = -60$ mV, we also show the V_T dependence of the parity lifetimes at $\phi_{ext} = 0$ in Fig. 5.28. As for device A, the doublet ground state region exhibits a dome shape in V_P and V_T space, and at the transition between singlet and doublet ground states the lifetimes for both states become equal. Away from the transition, the lifetime asymmetry increases and the lifetimes differ by more than one order of magnitude. We note that the gate compensation of device B was not ideal, resulting in a small tilt of the dome.

Similarly to the behaviour shown in the main text for ϕ_{ext} and V_P, in this case we also observe contours of equal ratio where the lifetime asymmetry abruptly increases or decreases. For higher readout power these contours become accentuated, as shown in Fig. 5.28(c). Furthermore, for higher power the region with similar lifetimes around the ground state transition becomes wider. This is due to the parity lifetimes having a different dependence on power for different regions in gate space. For most regions in gate space there is again almost no dependence on readout power in the range explored (Fig. 5.28(e,f)). However, on special gate regions, such as close to ground state transitions (Fig. 5.28(g)) and on top of the observed contours (Fig. 5.28(d)), the lifetime asymmetry decreases rapidly with power, similar to the effect shown in Fig. 5.27.

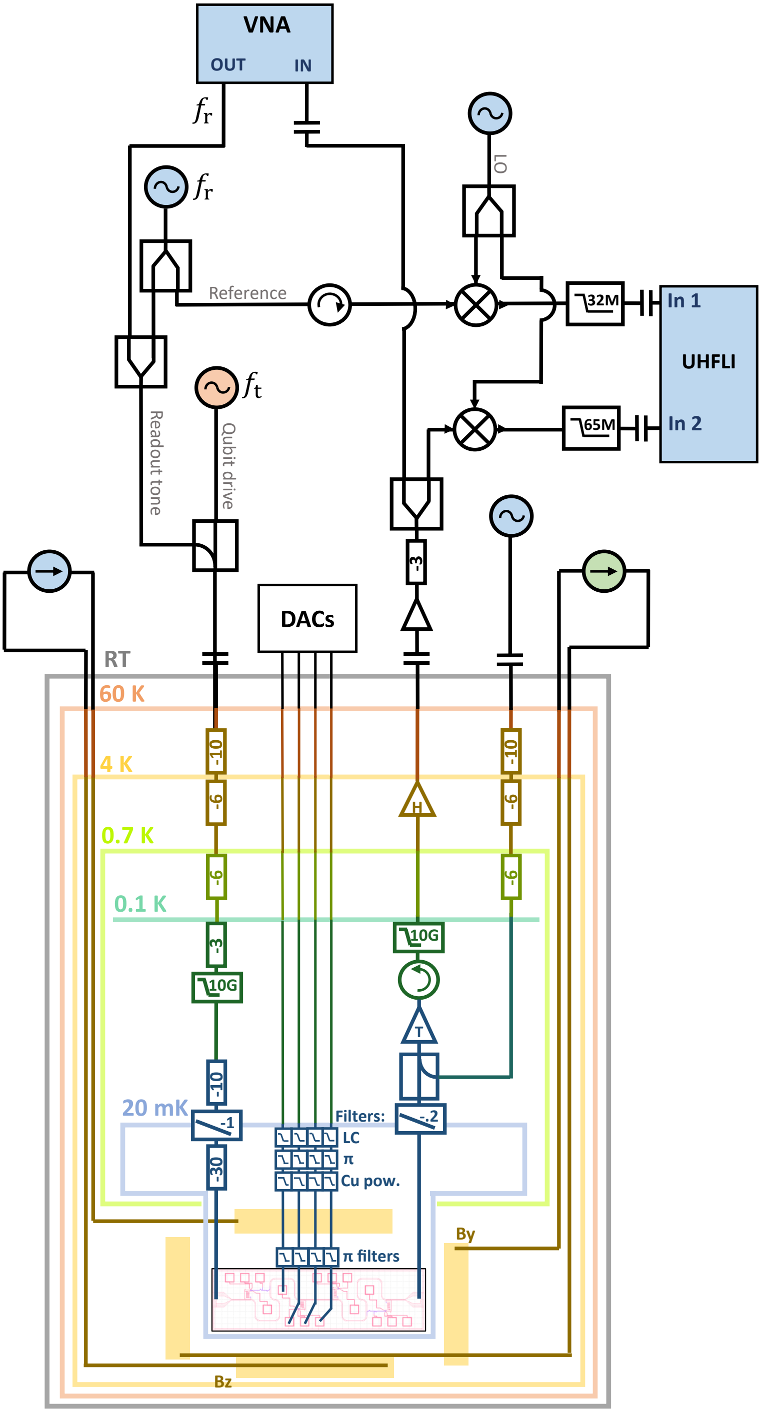

Figure 5.16: **Measurement setup at cryogenic and room temperatures.**

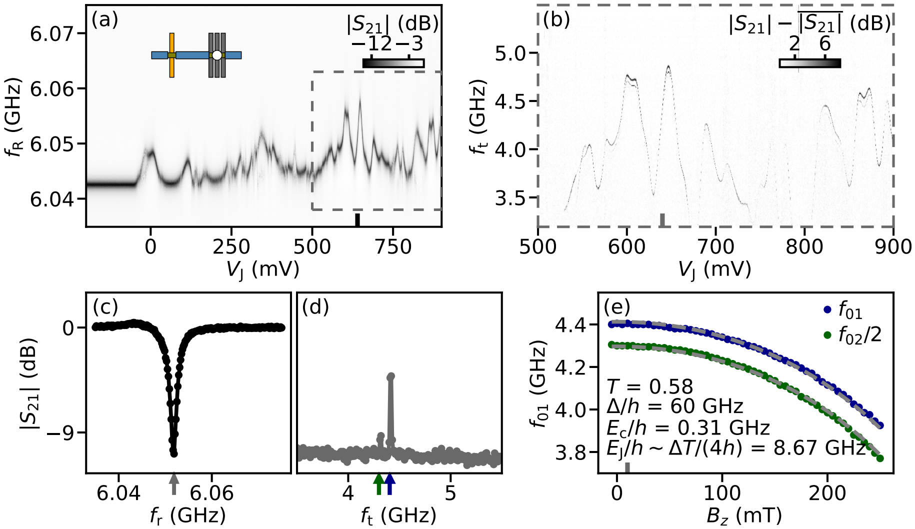

Figure 5.17: **Reference junction characterization for device A.** (a) V_J dependence of single-tone spectroscopy when the quantum dot junction is pinched-off ($V_C = 52.4$ mV, $V_L = 470$ mV, $V_R = 373$ mV). At low V_J values the reference junction is pinched-off and $E_J \sim 0$, thus the resonator is at its bare resonance frequency. As V_J increases, the resonator frequency increases non-monotonically due to mesoscopic fluctuations of the overall increasing transmission of different junction channels. (b) V_J-dependence of two-tone spectroscopy for the V_J range indicated in (a) with a dashed line rectangle. The black lines in (a) and (b) indicate the $V_J = 640$ mV set-point which sets the transmon frequency to its set-point used for the main text figures, $f_{01} = f_{01}^0 = 4.4$ GHz. (c) Line-cut of (a) at the V_J set-point, showing a resonance. (d) Line-cut of (b) at the V_J set-point, showing two peaks. The highest peak, at higher frequency, appears when the second tone frequency matches the transmon frequency ($f_t = f_{01}^0$). The lower peak corresponds to $f_{02}/2$ and shows the anharmonicity of the transmon. For (d), the first tone frequency f_r is fixed at the bottom of the resonance, indicated with a grey arrow in (c). (e) B_z evolution of f_{01}^0 and $f_{02}/2$ at $V_J = 640$ mV.

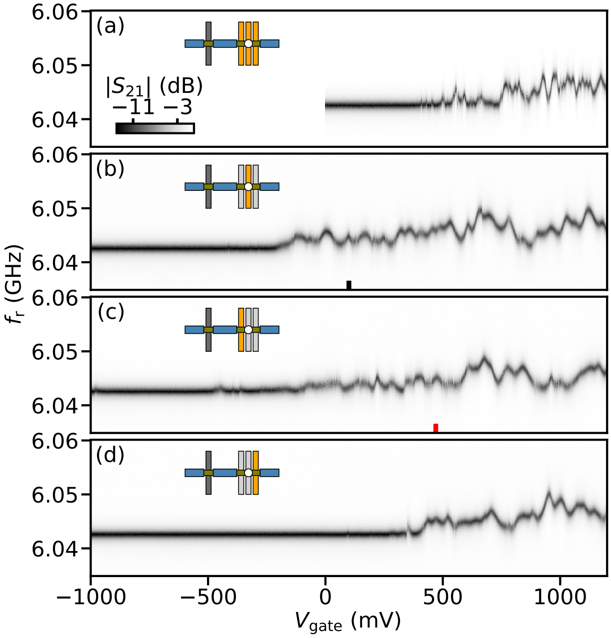

Figure 5.18: **Quantum dot gates characterization for device A.** (a) Gate voltage dependence ($V_L = V_C = V_R = V_{gate}$) of single-tone spectroscopy, showing how the quantum dot junction is pinched off at V_{gate} values lower than 300 mV. (b-d) V_C, V_L and V_R dependence, respectively of single-tone spectroscopy. In each panel, the two unused gates are kept at 1250 mV. This shows how each of the three quantum dot gates can independently pinch off the quantum dot junction. For all panels, the reference junction is closed ($V_J = -200$ mV). The black line in (b) indicates the value of $V_C = 100$ mV at which Fig. 5.19 is taken. The red line in (c) indicates the fixed value of $V_L = 470$ mV at which all main text figures are taken.

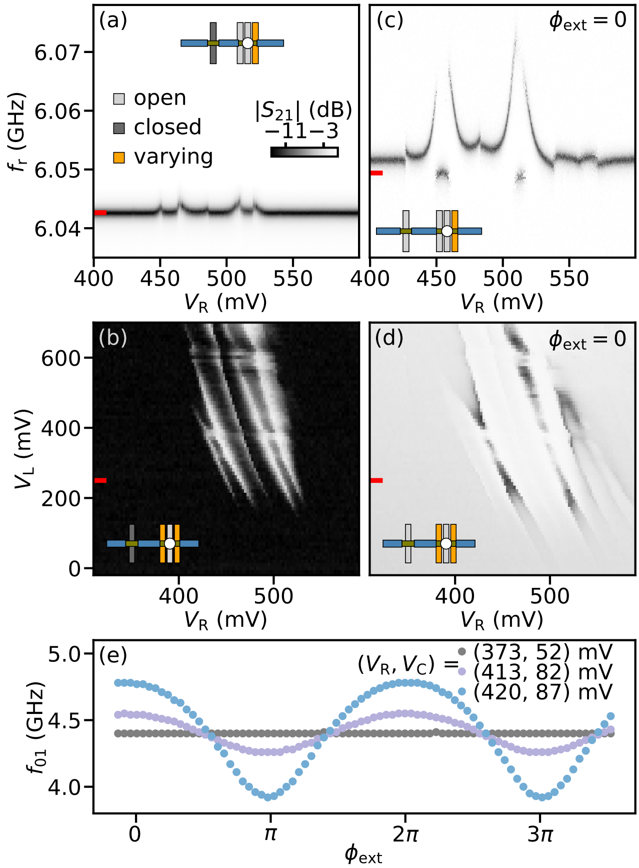

Figure 5.19: **Quantum dot tune up for device A.** (a) Single-tone spectroscopy measured at V_L = 250 mV, exhibiting two small resonances. Here the reference junction is fully closed (V_J = -200 mV). The red line indicates the readout frequency used in panel (b). (b) Single frequency readout of the resonator. Bright colors indicate a shift in the resonance frequency, marking the onset of supercurrent through the dot. The red line indicates the V_L value of panel (a). (c) Same as panel (a) but with the reference junction opened to the V_J = 640 mV setpoint used throughout the manuscript. The two junctions in parallel form a SQUID, increasing the qubit frequency and in turn the resonance frequency. Measured at $\phi_{ext} = 0$. (d) Same as panel (b) but with the reference junction set to V_J = 640 mV and $\phi_{ext} = 0$, measured at the frequency indicated with a red line in (c). For (a-d), V_C = 100 mV (close to pinchoff), indicated with a black line in Fig. 5.18. (e) f_{01} versus ϕ_{ext} at fixed V_J = 640 mV, for three quantum dot gates setpoints corresponding to a quantum dot junction which is fully closed (grey), slightly open (violet) or very open (blue) showing the DC SQUID behaviour of the two parallel Josephson junctions.

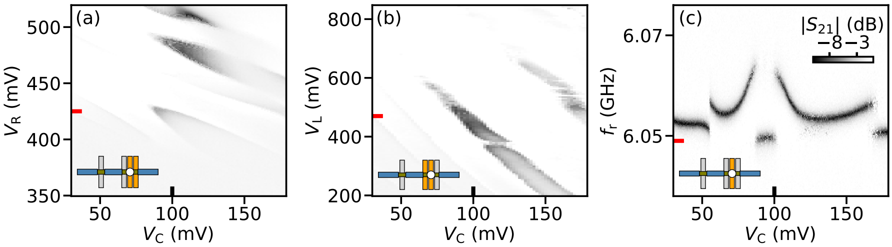

Figure 5.20: **Quantum dot gate dependence for device A.** (a) Single frequency readout of the resonator at the frequency indicated in Fig. 5.19(c) with a red line, performed versus V_C and V_R for fixed $V_L = 470$ mV. (b) Same as (a) but versus V_C and V_L and for fixed $V_R = 425$ mV. (c) Single-tone spectroscopy versus V_C, measured at $V_L = 470$ mV and $V_R = 425$ mV, revealing a quantum dot resonance. For all panels $\phi_{\text{ext}} = 0$.

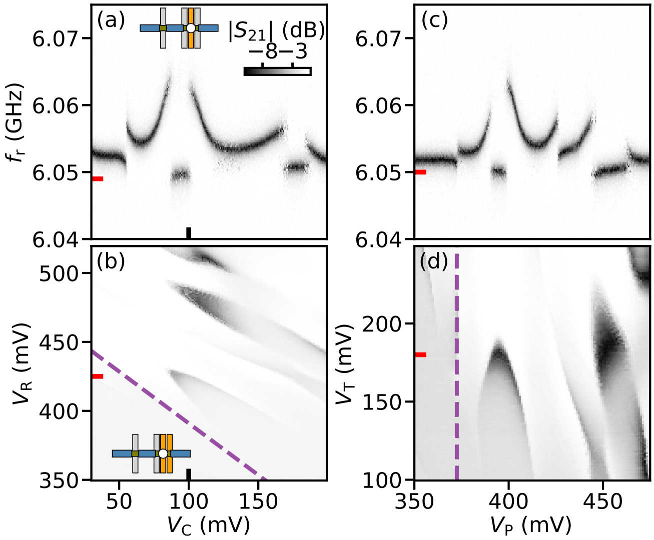

Figure 5.21: **Gate compensation for device A.** (a) Single-tone spectroscopy versus $V_C$at $V_R = 427$ mV. (b) Single frequency readout of the resonator measured versus the central (V_C) and right (V_R) quantum dot gate voltages, performed at a at fixed V_L 470 mV. The red line indicates the V_R value of panel (a). (c) Resonator spectroscopy versus V_P at $V_T = 180$ mV. (d) Same as (b) but in the transformed coordinate frame, measured vs. the virtual plunger (V_P) and right tunnel (V_T) gate voltages. In (a) and (c), the red lines indicate the readout frequencies used in panels (b) and (d), respectively. For all panels $\phi_{\text{ext}} = 0$.

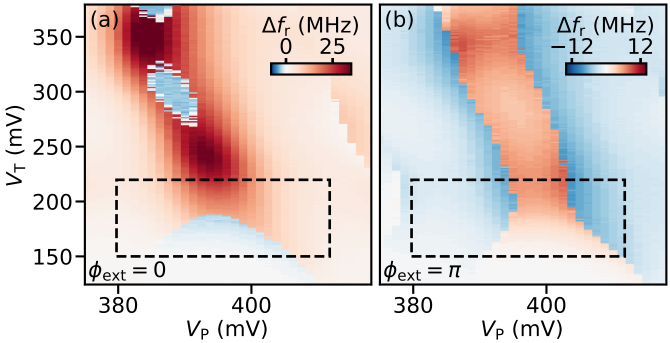

Figure 5.22: **Extended V_T dependence.** (a) Δf_r versus V_P and V_T at $\phi_{ext} = 0$, revealing singlet (red) and doublet (blue) ground state regions separated by sharp transitions. (b) Same as (a) but for $\phi_{ext} = \pi$. We note that the plunger gate axis is shifted by about 5 mV with respect to (a) and the data shown in the main text, which we speculate is due to an irreproducible gate jump. Dashed rectangles indicate the gate ranges in which the measurements of Fig. 5.5 of the main text are taken.

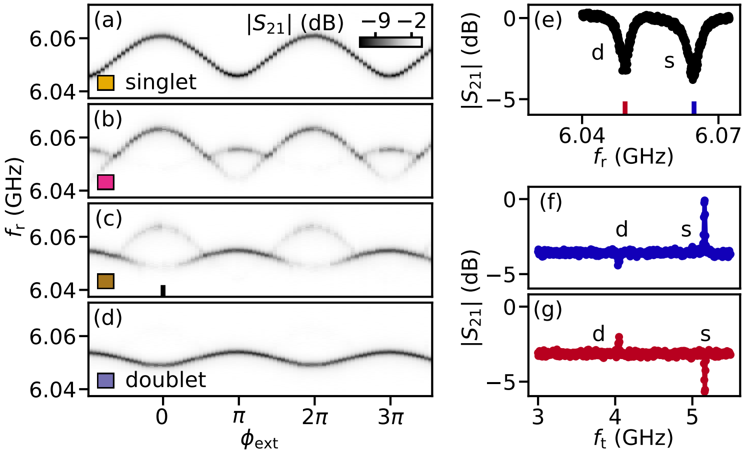

Figure 5.23: **State selective spectroscopy.** (a-d) ϕ_{ext} dependence of single-tone spectroscopy at four representative V_P values, indicated in Fig. 5.3 in the main text. Traces at intermediate V_P values show two resonances simultaneously due to switches on timescales faster than the integration time. (e) Linecut of (c) at $\phi_{ext} = 0$, indicated by a black line in (c). (f) Two-tone spectroscopy at the same settings as in (e), with the first tone at the frequency of the singlet resonance. The measurement shows a peak at the transmon frequency of the singlet state. (g) Same as (f) but with the readout frequency corresponding to the doublet resonance, which shows a peak at the transmon frequency of the doublet state.

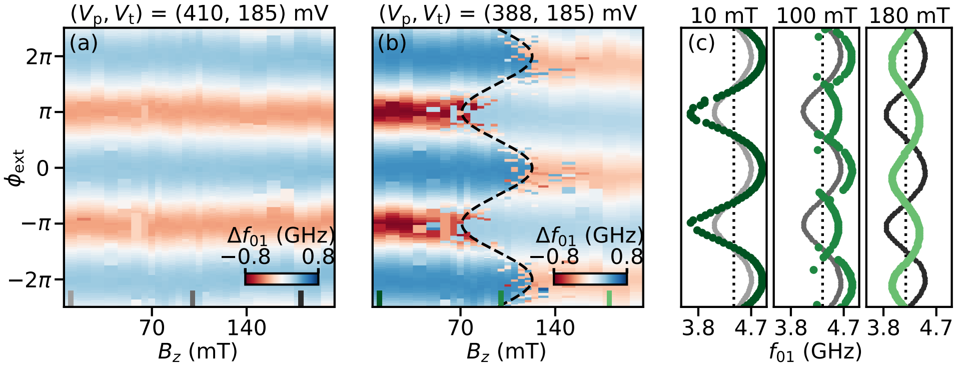

Figure 5.24: **Data analysis for magnetic field dependence of device A.** (a) and (b) show Δf_{01} versus B_z and ϕ_{ext}, measured the two gate points indicated in Fig. 5.6 with grey and green markers, respectively. In (a), the singlet is the ground state for all B_z. This gate point is used to identify a flux reference for each B_z. For (b), there is a singlet-doublet ground state transition with B_z, where the sinusoidal dashed line serves as a guide for the eye. (c) f_{01} versus ϕ_{ext} for the three B_z values indicated in (a) and (b). The dotted line indicates f_{01}^0, which decreases with B_z as shown in Fig. 5.17(e).

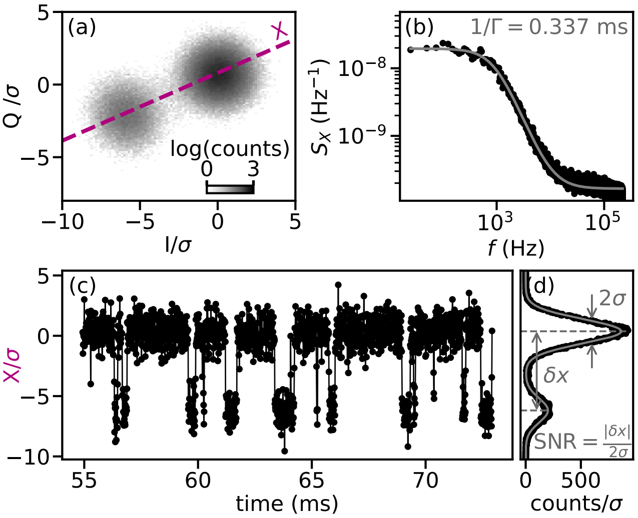

Figure 5.25: **Parity lifetime analysis.** (a) Logarithmic-scale histogram of the resonator response in the (I,Q)-plane after integrating a 2 s time trace with time bins of $t_{\text{int}} = 11.4\,\mu\text{s}$. It exhibits two separate Gaussian distributions whose centers define an axis, X, indicated with a dashed line. (b) Power spectral density (black) of an unintegrated 2 s time trace projected onto the X axis. In grey, best fit of a Lorentzian lineshape with a white noise background (Eq. (5.14)). (c) 18 ms cut of the integrated response projected onto the X axis, revealing jumps between two distinct states. (d) 1D histogram of the response in (a) projected onto the X axis (black) and the best fit of a double Gaussian line-shape (grey, Eq. (5.13)). For all panels $V_L = 325\,\text{mV}$, $V_T = -60\,\text{mV}$, $V_P = 551.4\,\text{mV}$, $B_z = 0$ and $\phi_{\text{ext}} = 0$.

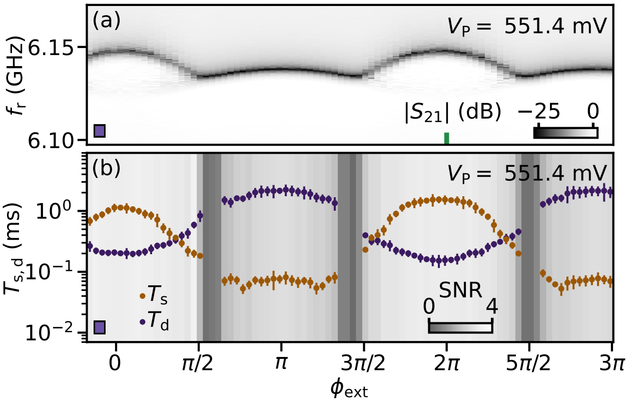

Figure 5.26: **Flux dependence of parity lifetimes** (a) ϕ_{ext} dependence of single-tone spectroscopy at V_P = 551.4 mV. (b) ϕ_{ext} dependence of the parity lifetimes extracted following the analysis in Fig. 5.25 at V_P = 551.4 mV. Markers indicate the mean and error bars indicate the maximum and minimum values of 10 consecutive 2 s time traces. SNR = $\frac{|\delta x|}{2\sigma}$ is shown in greyscale in the background. For points where SNR < 1, the extracted parity lifetimes are not shown as we do not consider them reliable. Measured at the same V_T , V_L and B_z as for Fig. 5.25.

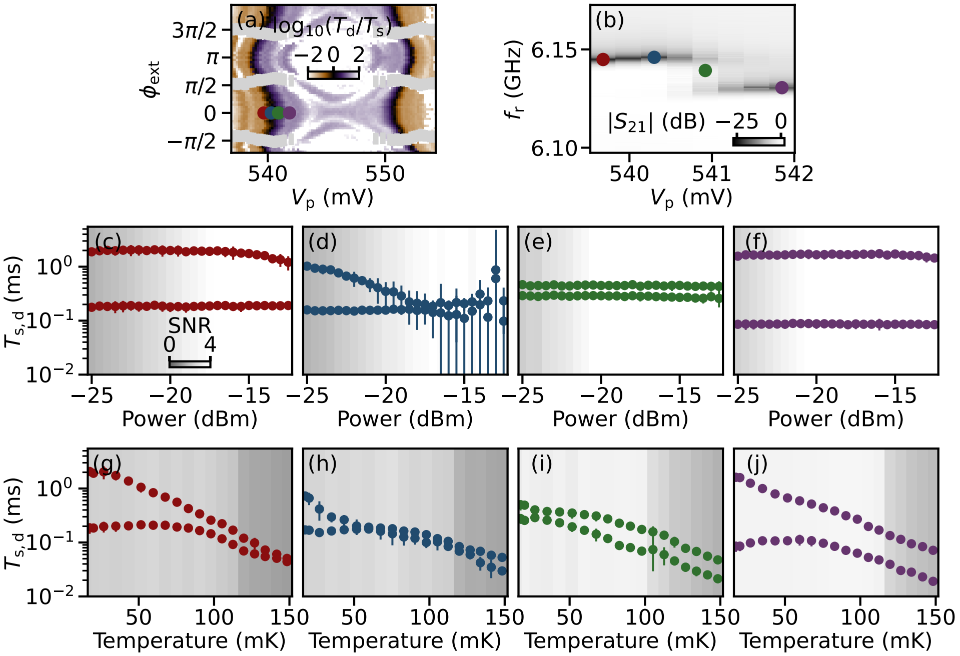

Figure 5.27: **Power and temperature dependence of parity lifetimes across the singlet-doublet transition** (a) 2D map of $\log_{10}(T_d/T_s)$ versus V_P and ϕ_{ext}, extracted from a 2 s time trace for each pixel. This is the same panel as Fig. 5.7(e) in the main text. (b) V_P dependence of single-tone spectroscopy at $\phi_{ext} = 0$, across a singlet/doublet transition. For (a) and (b), the mixing chamber temperature is 18 mK and the readout power is −22 dBm. (c-f) Readout power dependence at 18 mK of the extracted parity lifetimes at the plunger points indicated in (a) and (b). Markers indicate the mean and error bars indicate the maximum and minimum values of 10 consecutive 2 s time traces. The SNR is shown in greyscale in the background. For points where SNR < 1, the extracted parity lifetimes are discarded. (g-j) Same as (c-d) but versus temperature and at a power of −22 dBm. All powers are given at the fridge input.

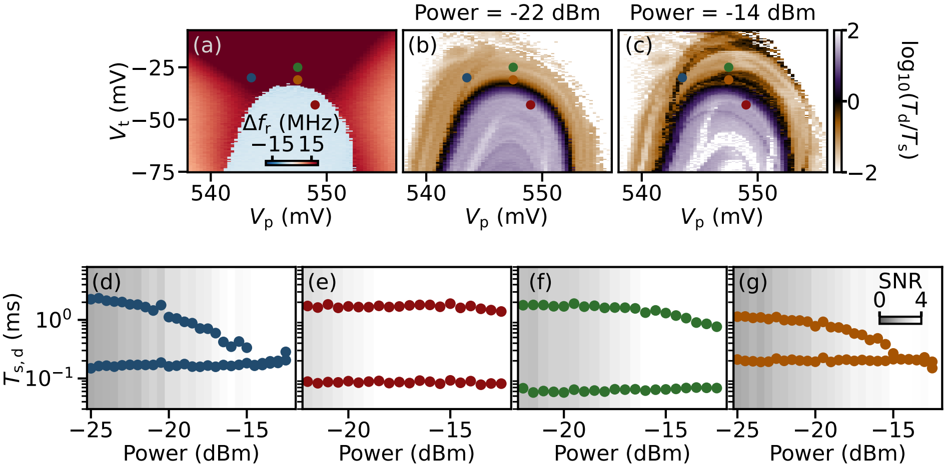

Figure 5.28: **Tunnel, plunger and power dependence of parity lifetimes** (a) $\Delta f_r = f_{res} - f^0_{res}$ versus V_P and V_T measured at $\phi_{ext} = 0$. It shows a regions of constructive and destructive interference, separated by sharp dome-like boundary. (b) Two-dimensional map of $\log_{10}(T_d/T_s)$ versus V_P and V_T, measured at a power of −22 dBm. (c) Same as (b) but for a power of −14 dBm. (d-e) Power dependence of the extracted parity lifetimes at the gate points indicated in (a-c). All powers are given at the fridge input.

6

SPECTROSCOPY OF SPIN-SPLIT ANDREEV LEVELS IN A QUANTUM DOT WITH SUPERCONDUCTING LEADS

We use a hybrid superconductor-semiconductor transmon device to perform spectroscopy of a quantum dot Josephson junction tuned to be in a spin-1/2 ground state with an unpaired quasiparticle. Due to spin-orbit coupling, we resolve two flux-sensitive branches in the transmon spectrum, depending on the spin of the quasi-particle. A finite magnetic field shifts the two branches in energy, favoring one spin state and resulting in the anomalous Josephson effect. We demonstrate the excitation of the direct spin-flip transition using all-electrical control. Manipulation and control of the spin-flip transition enable the future implementation of charging energy protected Andreev spin qubits.

The work in this chapter has been published as: A. Bargerbos*, M. Pita-Vidal*, R. Žitko, L.J. Splitthoff, L. Grünhaupt, J.J. Wesdorp, Y. Liu, L.P. Kouwenhoven, R. Aguado, C.K. Andersen, A. Kou, and B. van Heck, Spectroscopy of spin-split Andreev levels in a quantum dot with superconducting leads, arXiv e-prints 2208.09314 (2022). The asterisk indicates authors that contributed equally to this work.

6.1. INTRODUCTION

In the confined geometry of a Josephson junction, the Andreev reflection of an electron into a hole at a normal-superconducting interface results in discrete Andreev bound states (ABS) [18, 26, 44, 98, 175, 276]. ABS are of fundamental importance from the perspective of mesoscopic superconductivity and are also at the basis of several qubit proposals [59, 80, 234, 348]. In particular, when an ABS is populated by a single quasi-particle, the trapped quasi-particle can serve as the superconducting version of a spin qubit. In the presence of spin-orbit coupling, the Josephson phase difference ϕ may break the spin degeneracy, coupling the spin degree of freedom to the supercurrent across the junction [31, 59] and allowing for direct integration of spin qubits into superconducting circuits for remote communication, transduction, or hybrid qubit platforms [3, 183, 297].

Experimental work on InAs/Al nanowire Josephson junctions has shown the presence of the predicted spin-split ABS [124, 221, 312], culminating in the first demonstration of coherent Andreev spin qubit manipulation [123]. These remarkable experiments were operated in a regime in which the spin-1/2 junction states were an excited manifold and were thus susceptible to qubit leakage via quasiparticle escape or recombination, bringing the junction back into its spin-zero ground state. Furthermore, the direct manipulation of the spin states proved unfeasible, likely due to the smallness of relevant matrix elements [237], requiring complex excitation schemes involving auxiliary levels [52, 123].

In chapter 5 we showed that embedding a gate-controlled quantum dot in the InAs/Al Josephson junction makes it possible to tune its ground state to be an odd-parity spin-1/2 state. In this doublet phase, the lifetime of the trapped quasi-particle can exceed 1 ms, likely benefiting from the large charging energy of the quantum dot suppressing quasiparticle poisoning events.

In this Letter, employing the same transmon techniques as in chapter 5, we report the detection of the spin-orbit-induced spin-splitting of the doublet states of a quantum dot Josephson junction. The energy difference between spin states is smaller than the electron temperature, which would make it difficult to detect in transport measurements. We also demonstrate that the spin-split states populations, as well as the spin-selective transmon frequencies, can be controlled via external magnetic fields smaller than 40 mT. In the presence of magnetic field, we furthermore observe the anomalous Josephson effect: a shift of the minimum of the energy-phase relation to a value ϕ_0 which is neither 0 nor π or, equivalently, the presence of a non-zero equilibrium supercurrent at $\phi = 0$ [46, 308, 342, 347]. Finally, we show that the spin states can be directly manipulated by applying microwaves to a bottom gate, via the electric dipole spin resonance (EDSR) [94, 107, 227, 231, 263, 317]. Our experiment is directly comparable to, and inspired by, the theoretical proposal of Ref. [234], which we use to model the data, combined with further understanding based on a modified single-impurity Anderson model (SIAM).

6.2. DEVICE & CONCEPTUAL OVERVIEW

At the core of our experiment lies the quantum dot Josephson junction, which is hosted in a nominally 10 μm-long InAs/Al superconductor-semiconductor nanowire with a 110 nm-

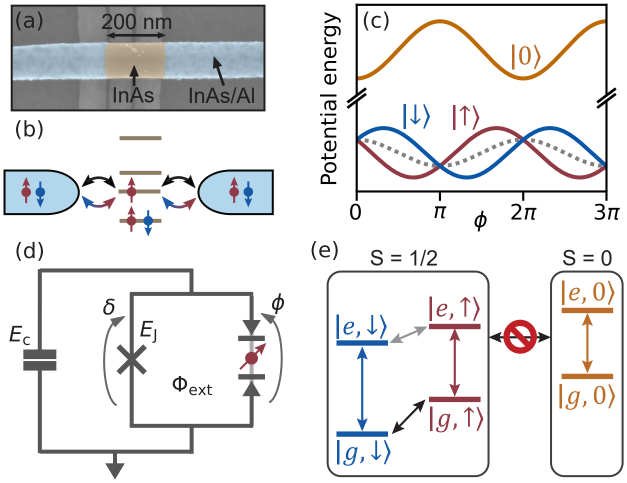

Figure 6.1: (a) False-colored scanning electron micrograph of the quantum dot junction. (b) Conceptual diagram of the quantum dot junction with multiple energy levels. Black and blue-to-red arrows denote the spin-conserving and spin-flipping tunnel couplings, respectively. (c) Josephson potential U versus the superconducting phase difference between the leads ϕ, shown for different quantum dot junction states: the singlet state in orange, and the two doublet states in red and blue. The dotted gray line indicates the potential of the doublet states in the absence of the E_{SO} term. (d) Circuit model for a transmon with charging energy E_{c} and a grounded SQUID formed by the parallel combination of a quantum dot junction and a reference Josephson junction with Josephson energy E_{J}. δ denotes the phase difference across the reference junction, and Φ_{ext} is the external magnetic flux through the SQUID loop. (e) Level diagram of the joint transmon-quantum dot junction system. The transmon transition frequencies $|g\rangle \leftrightarrow |e\rangle$ (vertical arrows) depend on the quantum dot junction state. Coherent microwave transitions between singlet and doublet are forbidden. However, intra-doublet spin-flip transitions are possible (diagonal arrows).

wide hexagonal core and a 6 nm-thick shell covering two facets [173]. The quantum dot is electrostatically defined in a 200 nm-long wet-etched InAs section using three bottom gate electrodes with voltages V_L, V_C and V_R, and its superconducting leads are formed by the flanking InAs/Al sections [Fig. 6.1(a)]. The bottom gates can be used to control the occupation of the quantum dot and its coupling to the superconducting electrodes. This results in two possible ground states of the quantum dot junction: either a spin-zero or a spin-1/2 state. We are particularly interested in the latter case [Fig. 6.1(b)], where the ground state manifold is spanned by the two components, $|{\downarrow}\rangle$ and $|{\uparrow}\rangle$, of a Kramers doublet, and a minimal model for the potential energy of the quantum dot junction is given by [234]

$$U(\phi) = E_0 \cos(\phi) - E_{SO}\, \vec{\sigma} \cdot \vec{n} \sin(\phi) + \frac{1}{2} \vec{E}_Z \cdot \vec{\sigma} \,. \tag{6.1}$$

Here, $\vec{\sigma}$ is the spin operator, $\vec{n}$ is a unit vector along the spin-polarization direction set by the spin-orbit interaction, and E_{SO} and E_0 are the spin-dependent and spin-independent Cooper pair tunneling rates across the quantum dot junction. Note that the term proportional to E_0 has a minimum at $\phi = \pi$. This π-shift originates from the odd occupancy of the junction [104, 298] and distinguishes the Josephson energy from that of a conventional tunnel junction. Finally, $\vec{E}_Z$ is a Zeeman field arising in the presence of an external magnetic field.

The energy scales E_0 and E_{SO} can be understood as follows [234]: Cooper pair tunneling occurs via a sequence of single-electron co-tunneling processes through the quantum dot energy levels. The spin-independent component E_0 arises from those sequences in which both electrons co-tunnel through the same energy level. The amplitude for these sequences is the same whether the initial state of the quantum dot junction is $|{\downarrow}\rangle$ or $|{\uparrow}\rangle$. On the other hand, E_{SO} arises from tunneling processes in which one electron co-tunnels through the singly-occupied level, involving a spin rotation, while the second one co-tunnels through a different level. Since in the presence of spin-orbit coupling the single-electron tunneling amplitudes can be spin-dependent, for these processes the *pair* tunneling amplitude may depend on the spin of the initial state.

The two potential energy branches of the doublet states at $\vec{E}_Z = \vec{0}$, $E_{\downarrow,\uparrow} = E_0 \cos\phi \pm E_{SO} \sin\phi$, are sinusoidals with an amplitude of $\sqrt{E_0^2 + E_{SO}^2}$ and minima at a phase ϕ_0 of $\pi \pm \arctan(E_{SO}/E_0)$, see Fig. 6.1(c). If $E_{SO} = 0$, the potential energy reduces to the well-known π-junction behavior without spin-splitting. At non-zero E_{SO}, the shift of the minima away from $\phi = 0, \pi$ is a precursor [234] to the anomalous Josephson effect [46, 347]; while at $\phi = 0$ there will be instantaneous supercurrents on timescales short compared to the spin lifetime, the time-averaged current will be zero due to thermal fluctuations. For completeness, in Fig. 6.1(c) we also show the potential energy E_s of the lowest-energy singlet state $|0\rangle$, with a minimum at $\phi = 0$, as expected for a conventional Josephson junction.

We can derive the occurrence of both E_0 and E_{SO} within a minimally-extended SIAM with superconducting leads. The SIAM is a simple model widely used to understand quantum dot junctions, containing a single energy level coupled to the leads via spin-conserving tunneling events [58, 104, 144, 153, 202, 209, 215, 232, 309, 343]. Only two extensions to the SIAM are required to generate the spin-splitting term E_{SO}: (i) spin-flipping single-electron tunneling between the leads and the energy level [19, 66, 234,

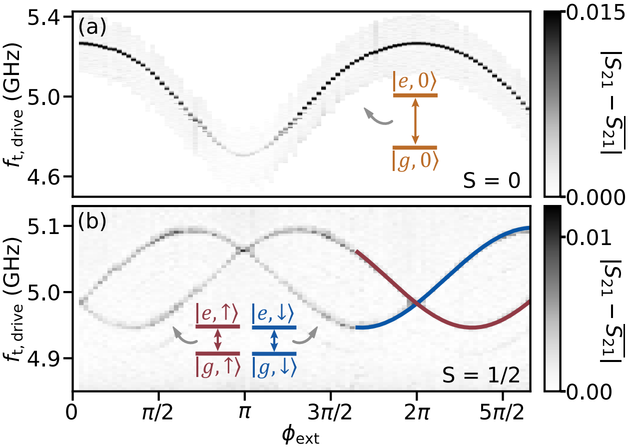

Figure 6.2: Comparison of singlet and spin-split doublet ground states in transmon two-tone spectroscopy. (a) Transmitted microwave signal versus external flux, ϕ_{ext}, and transmon drive frequency $f_{\mathrm{t,drive}}$ for the quantum dot junction in the singlet state. (b) Same as (a) for the doublet state, at gate setpoint A, revealing the spin-splitting of the doublet state. The two ground states occur for two different gate voltage settings, as detailed in chapter 5 and Sec. 6.7. Solid lines show fits to a transmon circuit model containing Eq. (6.1).

297] and (ii) inter-lead tunneling, resulting from integrating out the additional quantum dot energy levels. These results are derived in Sec. 6.7 of the Supplementary Material, together with a validation based on numerical renormalization group calculations (See Sec. 6.7). In view of the strong spin-orbit coupling in InAs [90, 192] and the confinement on the order of 100 nm [54, 316, 318], we expect both spin-flipping and spin-conserving tunneling, as well as additional quantum dot levels, to be present in our device. Note that within this model, the energy E_0 in Eq. (6.1) may have either sign depending on the relative strength of the two terms. While both situations may occur at different gate settings in the same device, the tuning procedure to find a doublet ground state relies on the detection of a π-shift (see chapter 5). Thus, our experiment naturally selects the case $E_0 > 0$, justifying the sign choice in Eq. (6.1).

To resolve the predicted spin-splitting we follow the method introduced in chapter 5 and incorporate the quantum dot junction into the superconducting quantum interference device (SQUID) of a transmon circuit [Fig. 6.1(d)] [162]. The different potential energies corresponding to the states $|0\rangle$, $|\downarrow\rangle$, or $|\uparrow\rangle$ give rise to distinct transition frequencies of the transmon circuit [Fig. 6.1(e)], which can be detected and distinguished via standard circuit quantum electrodynamics techniques [34, 35]. We refer to the Supplementary Materials for further details on the device implementation (Sec. 6.7).

6.3. TRANSMON BASED SPIN SPECTROSCOPY

To study the system in the regime of interest, we tune the quantum dot junction to a spin-1/2 ground state, as detailed in Sec. 6.7, where we refer to this setpoint as gate setpoint A [1]. This is followed by a two-tone spectroscopy measurement for which we apply both tones through the feedline and detect the transmon transition frequency as a function of the applied flux $\Phi_{\rm ext}$. The flux is tuned with a small in-plane external magnetic field applied perpendicular to the wire [333], requiring a 1.8 mT field for adding one flux quantum through the SQUID. We note that, since the reference junction is tuned to have a Josephson energy $E_{\rm J}/h = 12.5$ GHz, much higher than that of the quantum dot junction, the phase difference across the latter is well approximated by $\phi_{\rm ext} = 2e\Phi_{\rm ext}/\hbar$.

In Fig. 6.2(a), we show the typical flux dispersion observed in two-tone spectroscopy when the gate voltages are such that the ground state is a singlet, with the maximum frequency occurring at $\phi_{\rm ext} = 0$. In fact, this measurement serves as a calibration of the applied flux, which is assumed to be an integer multiple of the flux quantum when the transmon frequency is maximal. In contrast, when the ground state is electrostatically set to be a doublet, the transition spectrum displays two shifted frequency branches, with maxima at $\phi_{\rm ext} = \phi_0 \neq 0, \pi$ [Fig. 6.2(b)]. The measured spectrum is in good agreement with that predicted by a transmon circuit model with the potential energy of Eq. (6.1), with $E_0/h = 190\,$MHz and $E_{\rm SO}/h = 300\,$MHz. The latter corresponds to a temperature scale of 14 mK, indicating that transmon-based spectroscopy can experimentally resolve the spin-orbit splitting of the doublet state well below the thermal broadening that typically limits tunneling spectroscopy experiments. Furthermore, the simultaneous observation of both transmon branches is indicative of a large thermal occupation of the excited spin state, which prevents the splitting from being observable in switching current measurements as the two contributions to the current cancel out.

We note that tuning the junction to a spin-1/2 ground state is not a sufficient condition to observe the spin-splitting in the transition spectrum. By tuning the quantum dot to different resonances, corresponding to a quasi-particle trapped to different levels of the quantum dot, we frequently find instances of doublets without the predicted splitting, such as the one studied in detail in chapter 5. There are also doublet states that show a small, MHz-size spin-splitting comparable to the transmon linewidth, as well as doublet states with larger splittings than shown in Fig. 6.2(b). This range of behaviours is shown in the Supplementary Materials . We attribute this variability to mesoscopic fluctuations [234], due to factors outside of our experimental control, such as disorder and confinement effects on the quantum dot wave functions.

6.4. MAGNETIC FIELD DEPENDENCE

The transition spectrum is affected by magnetic field through the Zeeman interaction and depends sensitively on the field direction with respect to the spin-orbit direction $\vec{n}$. This is shown in Fig. 6.3, which shows the behaviour for two limiting cases: $B_\parallel$, the direction along $\vec{n}$, and $B_\perp$, the direction perpendicular to $\vec{n}$ and in the chip plane. The evolution for intermediate directions and the procedure used to infer $\vec{n}$ are discussed in Supplementary Materials. The flux dispersion of the transition frequencies is only weakly affected by increasing $B_\parallel$ [2]. Moreover, one of the two spin branches gradually

---

[1] Precise gate voltage values for different gate configurations are reported in the Supplementary Materials of Sec. 6.7.

[2] We attribute the field-dependent change in flux dispersion to the renormalization of the impurity g-factor by coupling to the leads, known as the impurity Knight shift [240].

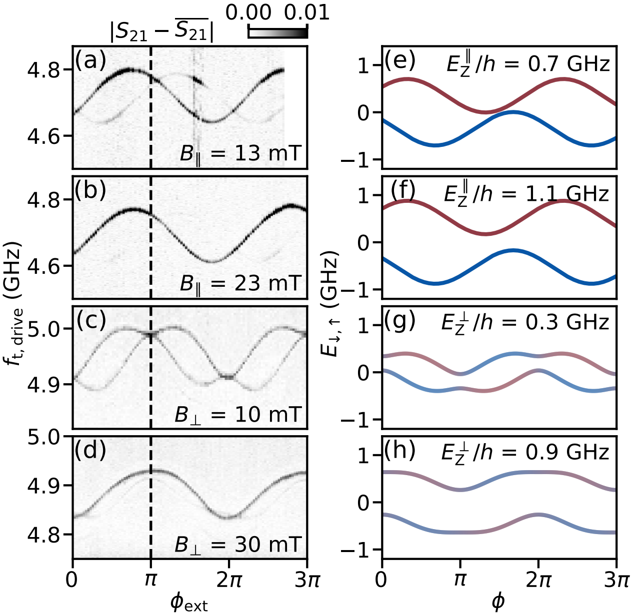

Figure 6.3: Magnetic field dependence of the doublet states for gate setpoint A. (a-d) Transmon spectroscopy versus ϕ_{ext} for a magnetic field applied either parallel (a,b) or perpendicular (c,d) to the inferred spin-orbit direction $\vec{n}$. The vertical dashed lines indicate $\phi_{\mathrm{ext}} = \pi$. (e-f) Numerically calculated ϕ-dependence of the Josephson potential for the two doublet states, obtained by diagonalizing the model in Eq. (6.1), in the presence of parallel (e-f) and perpendicular (g-h) Zeeman field. Blue and red colors denote $|\downarrow\rangle$ and $|\uparrow\rangle$ spin polarization, respectively, with a blend of the two indicating mixing of the states. Panels (e-h) are not fits to the data of (a-d). Instead, together with the contribution from the reference junction, constitute the potentials that determine the transmon energy levels and serve to build a qualitative understanding (see text).

disappears [Fig. 6.3(a)] until at $B_\parallel \gtrsim 23$ mT only a single spectroscopic line remains visible [Fig. 6.3(b)]. In this regime, the minimum transmon transition frequency of the single-valued dispersion is shifted by ϕ_0 away from $\phi_{\mathrm{ext}} = 0$. This is a consequence of a ϕ_0-shift of the maximum of the energy-phase relation away from $\phi = 0$, as the transmon transition frequency is given by the Josephson inductance, the second derivative of the energy-phase relationship. This observation therefore demonstrates the presence of the anomalous Josephson effect [46, 290, 308, 342, 347]. In contrast, increasing the magnetic field along the $B_\perp$ direction appears to couple the two spectroscopic lines, leading to branches with two minima per flux period [Fig. 6.3(c)]. At even higher fields this behaviour is lifted, and once-more only one of the two transmon branches persists [Fig. 6.3(d)]. In this case, however, the ϕ_0-offset has strongly decreased.

The observed behaviour can be qualitatively understood from Eq. (6.1) by considering the cases in which the Zeeman field is respectively parallel or perpendicular to the spin-orbit direction. A parallel field $E_Z^\parallel$ separates the doublet potentials in energy without distorting their phase dependence [Fig. 6.3(e-f)]. As the energy separation increases, the thermal population of the higher-energy state decreases and, with it, so does the visibility of the corresponding transmon frequency branch. As the transmon

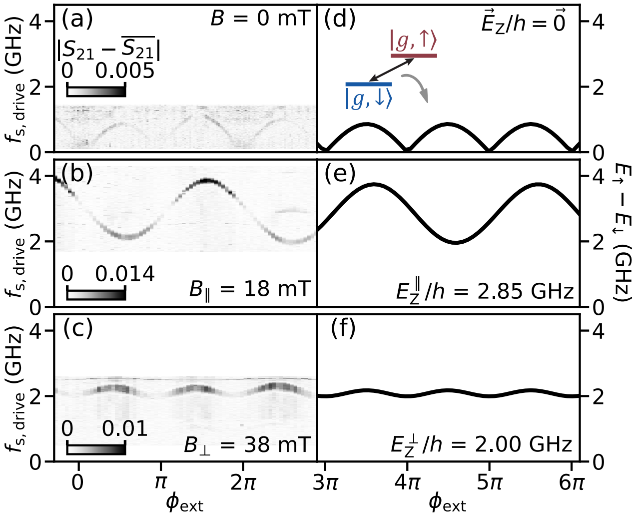

Figure 6.4: Direct spin-flip spectroscopy for gate setpoint B. (a-c) Measured flux dependence of the direct $|g,\downarrow\rangle \leftrightarrow |g,\uparrow\rangle$ transition frequency for no (a), parallel (b), and perpendicular (c) magnetic field relative to $\vec{n}$. (d-f) Numerically calculated flux dependence of the $|g,\downarrow\rangle \leftrightarrow |g,\uparrow\rangle$ transition frequency for no (d), parallel (e), and perpendicular (f) Zeeman fields relative to $\vec{n}$.

frequency is insensitive to overall shifts in the energy-phase relation, it remains largely unaffected by the ϕ-independent field-induced energy shift. A Zeeman term $E_Z^\perp$ perpendicular to the spin-orbit direction instead couples the two states and opens up an avoided crossing in the Josephson potential [Fig. 6.3(g)]. This results in the peculiar flux dependence seen in spectroscopy for moderate fields [Fig. 6.3(c)]. Finally, when $E_Z^\perp$ becomes much larger than E_{SO}, the doublet states instead polarize along the applied field direction [Fig. 6.3(h)], suppressing the ϕ_0-offset [308, 347].

We note that, at this gate setpoint, the $\vec{n}$ direction does not appear to be directly related to the orientation of the nanowire, as it points 13 degrees away from the nanowire axis. Moreover, this direction is found to be unique to each region in gate space, as discussed in the Supplementary Materials. This behavior differs from that of long single-gated semiconducting Josephson junctions, where the $\vec{n}$ direction is perpendicular to the nanowire axis [304, 312]. We attribute this variability to mesoscopic fluctuations of the junction wavefunctions and of the direction of the electrostatic field when the gate setpoint is changed [115].

6.5. Direct driving of spin flip transitions

In order to use the doublet states as a superconducting spin qubit [59, 234], the ability to drive transitions between the doublet states is crucial. Encouragingly, a recent work by our group indicates that spin-flip transitions of ABS are possible in the presence of an external magnetic field [333]. Further motivated by all-electrical microwave excitation of spins in quantum dots via EDSR [227, 231], we apply a microwave tone directly to the central gate to excite the doublet states. For this, we tune the transmon frequency close to the resonator frequency, enhancing its dispersive shift. In addition, we tune away from the gate setpoint investigated so far (gate setpoint A) to a parameter regime with a larger spin-splitting $E_{\mathrm{SO}}/h = 560\,\mathrm{MHz}$ (gate setpoint B) to maximize the visibility of the doublet splitting (See Supplementary Materials).

Applying a microwave drive to the central gate electrode, we find that a low-frequency transition of up to 1 GHz can be detected for a vanishing applied magnetic field [3], as also shown in Ref. [221] [Fig. 6.4(a)]. Its poor visibility is potentially due to the lack of magnetic field, which reduces the efficacy of EDSR [94, 107], as well as to the large thermal population of the excited state, which reduces the achievable change in dispersive shift. This large thermal population can be expected from the fact that the spin-flip transition energy corresponds to an effective temperature range of 0 to 50 mK, below the typical electron temperatures found in transport and transmon [139] experiments, 35–100 mK. At elevated $B_{\parallel}$ the transition frequency rises and becomes well-resolved [Fig. 6.4(b)]. For an applied perpendicular field the transition frequency increases more slowly, and its flux periodicity is half that of the transition in the parallel field direction [Fig. 6.4(c)]. Note that the $\vec{n}$ direction found for gate setpoint B (72 degrees away from the nanowire axis) differs from that of gate setpoint A, and that therefore $B_{\parallel}$ and $B_{\perp}$ in Fig. 6.4 point in different directions than in Fig. 6.3.

The observed behaviour is consistent with the expected transitions between the doublet states [Fig. 6.4(d-f)], with the period-halving in perpendicular field being a result of the avoided crossings between the spin branches [c.f. Fig. 6.3(g)]. The comparison to the model furthermore allows us to estimate the effective Landé g-factors in the parallel and perpendicular directions, $g_{\parallel} = 11$ and $g_{\perp} = 3.8$ respectively. We note that the value and the anisotropy of the g-factor depend strongly on the gate voltages (see Supplementar Materials), likely tied to an interplay of spin-orbit coupling and confinement, beyond the scope of the model considered here [64, 159, 283, 340].

6.6. CONCLUSIONS

To conclude, our microwave measurements have revealed the rich spin structure of energy levels in a quantum dot Josephson junction and the occurrence of the anomalous Josephson effect. These findings are promising for applications in superconducting spintronics [196, 293]. The ability to directly drive spin-flip transitions between the doublet states has strong implications for the nascent field of Andreev spin qubits [59, 234], since so far their coherent manipulation relied on fine-tuned Raman transitions through auxiliary levels [52, 123]. Having direct, all-electrical access to these transitions promises simpler and faster qubit manipulation [227, 317]. Furthermore, the polarization of the doublet states at elevated magnetic fields eliminates the unwanted excited state population observed in previous investigations [123, 124]. Finally, the demonstrated tunability of the transition frequency, enabled by both flux and magnetic field, is a necessary ingredient for scalable networks of such qubits [297].

---

[3] The tuning of the external flux requires a small magnetic field, which for the data in Fig. 6.4(a) ranges from $-1.5\,\mathrm{mT}$ to $0.7\,\mathrm{mT}$.

6.7. SUPPLEMENTARY INFORMATION

THEORY

To solidify our understanding of the results and of the mechanisms that govern the size of the spin splitting, we set up a minimal model that is able to reproduce the qualitative features observed experimentally. Our starting point is an extension of the single-impurity Anderson model (SIAM) for a quantum dot (QD) attached to two superconducting leads [215], see Fig. 6.5. Compared to the standard SIAM, our model also contains spin-flip tunneling between the impurity and the leads due to the presence of spin-orbit coupling, as well as an additional direct tunneling term between the leads. The non-interacting part of the Hamiltonian is

$$\begin{aligned} H_0 = &\sum_{\sigma} \epsilon d^\dagger_\sigma d_\sigma + E_x S_x + E_y S_y + E_z S_z \\ &+ \sum_{i,k\sigma} \epsilon_k c^\dagger_{i,k\sigma} c_{i,k\sigma} + \sum_{i,k} \Delta_i \left(e^{i\phi_i} c^\dagger_{i,k\uparrow} c^\dagger_{i,k\downarrow} + \text{H.c.} \right) \\ &+ \sum_{i,k\sigma} \left(V_{i,k} c^\dagger_{i,k\sigma} d_\sigma + \text{H.c.} \right) + \sum_{i,k\sigma} \left(i W_{i,k} c^\dagger_{i,k\sigma} d_{\bar{\sigma}} + \text{H.c.} \right) \\ &+ \sum_{k,k',\sigma} \left(t c^\dagger_{\mathrm{L},k\sigma} c_{\mathrm{R},k'\sigma} + \text{H.c.} \right). \end{aligned} \tag{6.2}$$

The first line describes the QD level ϵ closest to the Fermi level (the “resonant” level), subject to an external magnetic field $\vec{E}_Z$ with the components E_x, E_y and E_z expressed in units of energy (i.e., as Zeeman energy contributions). The operator $d^\dagger_\sigma$ is the creation operator for an electron in the resonant level, and S_x, S_y, S_z are impurity spin operators. The second line describes two superconductors with the dispersion relation ϵ_k and order parameters $\Delta_i \exp(i\phi_i)$. The operator $c^\dagger_{i,k\sigma}$ is the creation operator for an electron in the left ($i = \mathrm{L}$) or right ($i = \mathrm{R}$) superconductor, in level k and with spin σ. The third line describes the QD-superconductor hybridisation; we include both spin-preserving and spin-flipping processes with amplitudes $V_{i,k}$ and $W_{i,k}$, respectively. The notation $\bar{\sigma}$ denotes spin inversion, $\bar{\uparrow} = \downarrow$, $\bar{\downarrow} = \uparrow$. Alternatively, we may characterize the tunnel barriers via tunneling rates $\Gamma_\mathrm{L} = \pi\rho|V_{\mathrm{L},k_F}|^2$ or $\Gamma_\mathrm{R} = \pi\rho|V_{\mathrm{R},k_F}|^2$ for spin-preserving processes, and $\gamma_\mathrm{L} = \pi\rho|W_{\mathrm{L},k_F}|^2$ or $\gamma_\mathrm{R} = \pi\rho|W_{\mathrm{R},k_F}|^2$ for spin-flip tunneling. Here ρ is the normal-state density of states and we took the matrix elements at the Fermi level, hence at $k = k_F$. Finally, the last line accounts for the presence of all other (“non-resonant”) levels in the QD: the electron can also cotunnel through the QD via those high-lying levels, which provides another conduction pathway through the dot. Formally, we may consider this term to arise from integrating out all other levels in the QD, so that

$$t = \sum_{l,k,k'} \frac{V^*_{\mathrm{L},k;l} V_{\mathrm{R},k';l}}{\Delta\epsilon_l}, \tag{6.3}$$

where we sum over all “non-resonant” levels, $V_{\mathrm{L/R},k;l}$ are the corresponding tunneling amplitude, while $\Delta\epsilon_l$ are the energy levels. (For simplicity, we are disregarding interactions and spin-flip processes.) The inter-lead hopping term makes the model resemble those for a QD embedded in a nanoscopic Aharonov-Bohm ring [152]. The model breaks

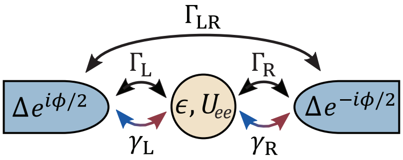

Figure 6.5: Model diagram of the quantum dot junction. Two s-wave superconductors are connected via tunnelling rates to a single level quantum dot. $\Gamma_{\rm L,R}$ and $\gamma_{\rm L,R}$ denote, respectively, the spin-conserving and spin-flipping tunneling rates between the superconducting leads and quantum dot. $\Gamma_{\rm LR}$ denotes a spin-conserving effective tunneling rate between the superconducting leads via all remaining energy levels, with $\Gamma_{\rm LR} = \pi\rho|t|^2$.

down if the level spacing is too small (less than the scale of $\Gamma_{\rm L/R}$): in that case one should use a multi-orbital Anderson impurity model instead.

In addition to this last term, we could also include the spin-flip tunneling through high-lying levels, however this brings about no new qualitative effect. As we will show, for what follows, the important element is that the ratio of spin-flip to spin-preserving tunneling rate is different for the resonant level and for the aggregate tunneling rate through all remaining non-resonant levels. This generic situation is expected to hold in most circumstances due to mesoscopic variability of tunneling matrix elements for different QD levels. The hopping elements, $V_{i,k}$, $W_{i,k}$ and t, are in general complex-valued ("directional"): if we reverse the electron flow direction, the amplitude needs to be complex conjugated.

The interacting part of the Hamiltonian is standard:

$$H_{\rm int} = U_{ee} n_\uparrow n_\downarrow, \tag{6.4}$$

where U_{ee} is the electron-electron repulsion on the QD and $n_\sigma = d_\sigma^\dagger d_\sigma$ is the occupancy operator.

The model is analytically tractable in the regime $\Delta_{\rm L}, \Delta_{\rm R} \gg U_{ee}$ (the "superconducting atomic limit"[2, 153, 217, 232, 268, 309, 321]) and in the regime $\Gamma_{\rm L}, \Gamma_{\rm R} \ll U_{ee}$ (the perturbative limit). We find that it is particularly instructive to integrate out the superconducting electrons and compute the hybridization matrix for this Hamiltonian. This leads to relatively simple closed-form expressions that can be used to construct a highly simplified model. Such a model nevertheless seems to be sufficient to account for the full range of the observed behaviors. The analytic calculations may be verified with explicit calculations using the numerical renormalization group (NRG) techniques, probing their validity over a wide range of parameters.

ANALYTICS

We work in the 4×4 Nambu representation with

$$d_a^\dagger = \begin{pmatrix} d_\uparrow^\dagger & d_\downarrow & d_\downarrow^\dagger & d_\uparrow \end{pmatrix}. \tag{6.5}$$

Similar notation is used for the c_k operators in the superconducting leads. We will use indexes from the beginning of the alphabet, $a, b, \ldots$, to denote the Nambu-space index $1,2,3,4$. We define the Green's function (GF) matrices $G_{ab}(z) = \langle\langle d_a; d_b^\dagger \rangle\rangle_z$ and $F_{ab,ik}(z) =$

$\langle\langle d_a; c^\dagger_{ik,b}\rangle\rangle_z$; here $\langle\langle A;B\rangle\rangle_z$ denotes the Laplace transform of the Green's function, $\langle\langle A;B\rangle\rangle_z = \int_0^\infty e^{izt}\langle\langle A;B\rangle\rangle_t \mathrm{d}t$, where $\langle\langle A;B\rangle\rangle_t = -i\Theta(t)\langle\{A(t),B(0)\}\rangle$ is the retarded GF. In this notation, the equations of motion (EOMs) take the form $z\langle\langle A;B\rangle\rangle_z = \langle\{A,B\}\rangle + \langle\langle A;[H,B]\rangle\rangle_z$. The EOM for the QD take the form

$$z\mathbf{G}(z) = \mathscr{I} + \mathbf{G}(z)\mathbf{H}_0 + \sum_{i,k}\mathbf{F}_{ik}(z)\mathbf{V}_{ik} + \mathbf{U}(z). \tag{6.6}$$

Here the argument $z = \omega + i\delta$ is complex frequency, $\mathscr{I}$ is the identity matrix, $\mathbf{H}_0$ corresponds to the Nambu matrix representation of the non-interacting part of the impurity Hamiltonian:

$$\mathbf{H}_0 = \begin{pmatrix} \epsilon + E_z/2 & 0 & (E_x - iE_y)/2 & 0 \\ 0 & -\epsilon + E_z/2 & 0 & -(E_x - iE_y)/2 \\ (E_x + iE_y)/2 & 0 & \epsilon - E_z/2 & 0 \\ 0 & -(E_x + iE_y)/2 & 0 & -\epsilon - E_z/2 \end{pmatrix}, \tag{6.7}$$

$\mathbf{V}_{ik}$ contains the hopping matrix elements:

$$\mathbf{V}_{ik} = \begin{pmatrix} V_{i,k} & 0 & iW_{i,k} & 0 \\ 0 & -V^*_{i,k} & 0 & iW^*_{i,k} \\ iW_{i,k} & 0 & V_{i,k} & 0 \\ 0 & iW^*_{i,k} & 0 & -V^*_{i,k} \end{pmatrix}, \tag{6.8}$$

and $\mathbf{U}(z)$ contains the contributions of the interacting part of the Hamiltonian, H_{int}. The EOMs for mixed GFs F_{ik} (dropping the frequency argument z in GFs for clarity) may be written as

$$\begin{aligned} \mathbf{F}_{\mathrm{L}k}\,[z\mathscr{I} - \mathbf{H}_{\mathrm{L}k}] &= \mathbf{G}\mathbf{V}^\dagger_{\mathrm{L}k} + \mathscr{F}_{\mathrm{R}}\mathbf{T}^*, \\ \mathbf{F}_{\mathrm{R}k}\,[z\mathscr{I} - \mathbf{H}_{\mathrm{R}k}] &= \mathbf{G}\mathbf{V}^\dagger_{\mathrm{L}k} + \mathscr{F}_{\mathrm{L}}\mathbf{T}, \end{aligned} \tag{6.9}$$

with

$$\mathbf{H}_{ik} = \begin{pmatrix} \epsilon_k & e^{+i\phi_i}\Delta_i & 0 & 0 \\ e^{-i\phi_i}\Delta_i & -\epsilon_k & 0 & 0 \\ 0 & 0 & \epsilon_k & -e^{i\phi_1}\Delta_1 \\ 0 & 0 & -e^{-i\phi_1}\Delta_1 & -\epsilon_k \end{pmatrix}, \tag{6.10}$$

$$\mathbf{T} = \begin{pmatrix} t & 0 & 0 & 0 \\ 0 & -t^* & 0 & 0 \\ 0 & 0 & t & 0 \\ 0 & 0 & 0 & -t^* \end{pmatrix}, \tag{6.11}$$

and

$$\mathscr{F}_i = \sum_k \mathbf{F}_{ik}. \tag{6.12}$$

Using the lead propagator $\mathbf{G}_{ik} = [z\mathscr{I} - \mathbf{H}_{ik}]^{-1}$, this may be rewritten as

$$\begin{aligned} \mathbf{F}_{\mathrm{L}k} &= \mathbf{G}\mathbf{V}^\dagger_{\mathrm{L}k}\mathbf{G}_{\mathrm{L}k} + \mathscr{F}_{\mathrm{R}}\mathbf{T}^*\mathbf{G}_{\mathrm{L}k}, \\ \mathbf{F}_{\mathrm{R}k} &= \mathbf{G}\mathbf{V}^\dagger_{\mathrm{R}k}\mathbf{G}_{\mathrm{R}k} + \mathscr{F}_{\mathrm{L}}\mathbf{T}\mathbf{G}_{\mathrm{R}k}. \end{aligned} \tag{6.13}$$

We now assume that V_{ik} and W_{ik} do not depend on k, i.e., $V_{ik} \equiv V_i$ and $W_{ik} \equiv W_i$; this is a reasonable approximation for the relevant bath levels in the vicinity of the Fermi level. We define $\mathbf{G}_i = \sum_k \mathbf{G}_{ik}$ and we sum the EOMs over k:

$$\begin{aligned} \mathscr{F}_{\mathrm{L}} &= \mathbf{G}\mathbf{V}_{\mathrm{L}}^{\dagger}\mathbf{G}_{\mathrm{L}} + \mathscr{F}_{\mathrm{R}}\mathbf{T}^{*}\mathbf{G}_{\mathrm{L}}, \\ \mathscr{F}_{\mathrm{R}} &= \mathbf{G}\mathbf{V}_{\mathrm{R}}^{\dagger}\mathbf{G}_{\mathrm{R}} + \mathscr{F}_{\mathrm{L}}\mathbf{T}\mathbf{G}_{\mathrm{R}}. \end{aligned} \tag{6.14}$$

or

$$\begin{pmatrix} \mathscr{F}_{\mathrm{L}} & \mathscr{F}_{\mathrm{R}} \end{pmatrix} \begin{pmatrix} \mathscr{I} & -\mathbf{T}\mathbf{G}_{\mathrm{R}} \\ -\mathbf{T}^{*}\mathbf{G}_{\mathrm{L}} & \mathscr{I} \end{pmatrix} = \mathbf{G}\begin{pmatrix} \mathbf{V}_{\mathrm{L}}^{\dagger}\mathbf{G}_{\mathrm{L}} & \mathbf{V}_{\mathrm{R}}^{\dagger}\mathbf{G}_{\mathrm{R}} \end{pmatrix}. \tag{6.15}$$

The important observation here is that $\mathscr{F}_i$ are proportional to $\mathbf{G}$. This means that the third term in the EOM (6.6) can be written as

$$\sum_{ik} \mathbf{F}_{ik}(z)\mathbf{V}_{ik} = \mathbf{G}(z)\boldsymbol{\Delta}(z), \tag{6.16}$$

where $\boldsymbol{\Delta}(z)$ is the hybridization matrix which describes the renormalization of the QD level due to electron excursions in the superconducting leads. Eq. (6.15) can be solved for each $\mathscr{F}_i$ individually, but the expressions are very lengthy and not very informative. Instead, we proceed with calculating the hybridization matrix $\boldsymbol{\Delta}(z) = [\mathbf{G}(z)]^{-1}\sum_i \mathscr{F}_i\mathbf{V}_i$. We furthermore assume that t is real and introduce the dimensionless quantity $\tilde{t} = \pi\rho t$. We also set $\phi_{\mathrm{L}} = \phi/2$ and $\phi_{\mathrm{R}} = -\phi/2$. Finally, we take the large-Δ limit of the lead propagator

$$\mathbf{G}_{ik} = \frac{1}{z^2 - (\Delta_i^2 + \epsilon_k^2)} \begin{pmatrix} z+\epsilon_k & e^{i\phi_1}\Delta_i & 0 & 0 \\ e^{-i\phi_i}\Delta_i & z-\epsilon_k & 0 & 0 \\ 0 & 0 & z+\epsilon_k & -e^{i\phi_i}\Delta_i \\ 0 & 0 & -e^{-i\phi_i}\Delta_i & z-\epsilon_k \end{pmatrix} \tag{6.17}$$

to obtain

$$\mathbf{G}_i = \sum_k \mathbf{G}_{ik} = -\pi\rho \begin{pmatrix} 0 & e^{i\phi_i} & 0 & 0 \\ e^{-i\phi_i} & 0 & 0 & 0 \\ 0 & 0 & 0 & -e^{i\phi_i} \\ 0 & 0 & -e^{-i\phi_i} & 0 \end{pmatrix}. \tag{6.18}$$

With these assumptions and simplifications in place, the hybridisation matrix can be written as

$$\boldsymbol{\Delta}(z) = \frac{\pi\rho}{1 + 2\tilde{t}^2\cos\phi + \tilde{t}^4} \begin{pmatrix} -2a & b & -2c & 0 \\ b^* & 2a & 0 & 2c \\ -2c & 0 & -2a & -b \\ 0 & 2c & -b^* & 2a \end{pmatrix}, \tag{6.19}$$

where we introduced the following notation

$$\begin{aligned} a &= (V_{\mathrm{L}}V_{\mathrm{R}} + W_{\mathrm{L}}W_{\mathrm{R}})\tilde{t}(\tilde{t}^2 + \cos\phi), \\ b_i &= V_i^2 + W_i^2, \\ b &= e^{-i\phi/2}(b_{\mathrm{R}} + \tilde{t}^2 b_{\mathrm{L}}) + e^{+i\phi/2}(b_{\mathrm{L}} + b_{\mathrm{R}}\tilde{t}^2), \\ c &= (V_{\mathrm{R}}W_{\mathrm{L}} - V_{\mathrm{L}}W_{\mathrm{R}})\tilde{t}\sin\phi. \end{aligned} \tag{6.20}$$

The key feature of this expression is that this matrix includes terms in the out-of-diagonal 2×2 blocks. These correspond to the presence of an effective magnetic field in the x direction that induces the spin polarization along this same direction. The particular direction (x) results from the assumed form of the spin-orbit-coupling terms in Eq. (6.2) and from assuming real $V_{\mathrm{L,R}}$, $W_{\mathrm{L,R}}$ and t. In terms of second quantization operators, the hybridisation matrix corresponds to the following form:

$$\Delta_{\mathrm{hyb}} = \frac{\pi\rho}{1+2\tilde{t}^2\cos\phi+\tilde{t}^4}\left(-2a\sum_{\sigma} d^\dagger_\sigma d_\sigma - 4cS_x + b d^\dagger_\uparrow d^\dagger_\downarrow + b^* d_\downarrow d_\uparrow + \text{const.}\right). \tag{6.21}$$

Not all terms contribute in both spin sectors. The pairing terms proportional to b are only relevant in the spin-singlet sector, while the effective spin-splitting terms proportional to c are only relevant in the spin-doublet sector. The potential term proportional to a contributes in both subspaces. Since we are interested only in the $S = 1/2$ subspace, in the following we concentrate on this particular 2×2 subspace. We find that the effective Hamiltonian of the doublet sector in the $\uparrow, \downarrow$-basis is given by

$$H_{\mathrm{eff}} = \begin{pmatrix} \epsilon + E_z/2 & \left(E_x - iE_y\right)/2 \\ \left(E_x + iE_y\right)/2 & \epsilon - E_z/2 \end{pmatrix} - \frac{2\pi\rho}{1+2\tilde{t}^2\cos\phi+\tilde{t}^4}\begin{pmatrix} a & c \\ c & a \end{pmatrix}. \tag{6.22}$$

This model is exact in the double limit $U_{ee} \to 0$, $\Delta_{\mathrm{L,R}} \to \infty$. In general, one expects correction factors to parameters that depend on both $\Delta_{\mathrm{L,R}}$ and U_{ee}, which control the energy cost of charge fluctuations from the doublet state. These corrections can be accurately computed using the NRG method. Nevertheless, the general form remains the same, as confirmed by numerical calculations, see below. Most importantly, the conditions for the matrix element c to be non-zero, as revealed in this calculation, hold fully generally, and are the following: a) the presence of additional QD levels (i.e., nonzero parameter t in the generalized SIAM), b) the presence of both spin-preserving and spin-flip tunneling (so that the combination $V_{\mathrm{R}}W_{\mathrm{L}} - V_{\mathrm{L}}W_{\mathrm{R}}$ is non-zero, which is expected to be generally true except in cases of accidental cancellation), c) finite phase bias ϕ.

We need to note that in the superconducting atomic limit the doublet state in the standard superconducting-SIAM model does not depend on the phase bias ϕ, as can be checked by taking the limit $W_{\mathrm{L,R}} \to 0$ and $t \to 0$ in Eq. (6.22). However, away from the superconducting atomic limit an additional diagonal term $E_D \cos(\phi)$ arises, with $E_D > 0$. This term is generated by fourth-order processing in hopping (second order in hybridisation) and has a minimum at $\phi = \pi$ [298], as typical for Josephson junctions with an odd-parity ground state.

Assuming $V_{\mathrm{L}} = V_{\mathrm{R}} \equiv V$, $W_{\mathrm{L}} = -W_{\mathrm{R}} \equiv W$ (note that this sign for W_i choice merely reflects the sign convention in the Hamiltonian and actually corresponds to the symmetric situation with the same amplitude for the left SC to QD and for the QD to right SC spin-flip tunneling), and defining

$$\Gamma_V = \pi\rho V^2, \quad \Gamma_W = \pi\rho W^2,$$

the second term of Eq. (6.22) can be written as

$$\frac{2\tilde{t}}{1+2\tilde{t}^2\cos\phi+\tilde{t}^4}\begin{pmatrix} (\Gamma_V - \Gamma_W)\left(\tilde{t}^2+\cos\phi\right) & 2\sqrt{\Gamma_V\Gamma_W}\sin\phi \\ 2\sqrt{\Gamma_V\Gamma_W}\sin\phi & (\Gamma_V - \Gamma_W)\left(\tilde{t}^2+\cos\phi\right) \end{pmatrix}. \tag{6.23}$$

Assuming that $\tilde{t} \ll 1$, we can simplify the model further by performing a series expansion to obtain

$$2\tilde{t}\begin{pmatrix} (\Gamma_V - \Gamma_W)\cos\phi & 2\sqrt{\Gamma_V\Gamma_W}\sin\phi \\ 2\sqrt{\Gamma_V\Gamma_W}\sin\phi & (\Gamma_V - \Gamma_W)\cos\phi \end{pmatrix}. \tag{6.24}$$

Defining

$$E_t = 2\tilde{t}(\Gamma_V - \Gamma_W), \quad E_{\mathrm{SO}} = 4\tilde{t}\sqrt{\Gamma_V\Gamma_W}, \tag{6.25}$$

we find the approximate small $\tilde{t}$ Hamiltonian given by (up to a constant):

$$H_{\mathrm{eff}} = \begin{pmatrix} E_z/2 & \left(E_x - iE_y\right)/2 \\ \left(E_x + iE_y\right)/2 & -E_z/2 \end{pmatrix} - \begin{pmatrix} E_t\cos\phi & E_{\mathrm{SO}}\sin\phi \\ E_{\mathrm{SO}}\sin\phi & E_t\cos\phi \end{pmatrix}. \tag{6.26}$$

This expression takes the form of the phenomenological potential for the transmon circuit given by main text Eq. (6.1). Given that there is a potential cancellation of the E_t term, it is prudent to include in the model an addition term of the form $E_D\cos(\phi)$ from processes that are higher-order in hybridisation. This term will combine with $-E_t\cos(\phi)$ to produce the $+E_0\cos(\phi)$ potential with $E_0 = E_D - E_t$ in Eq. (6.1). Note that E_0 can take either a positive or negative sign.

Within the limit considered here, we find that E_{SO} depends on each of the three types of coupling in the model: spin-conserving, spin-flipping, and direct lead-lead tunneling. All three have to be present for the spin-splitting to occur. Furthermore, it may happen that the cosine term drops out if the prefactors of all contributions add up to zero, resulting in a Josephson potential shifted by $\pi/2$ compared to the singlet state. This fine-tuned situation is indeed encountered in the experiment as discussed later in the Supplementary Materials.

It is instructive to evaluate the eigenvalues of the isolated quantum dot junction. In the simplified model of Eq. (6.1) these are given by

$$E_{\uparrow,\downarrow} = E_0\cos\phi \pm \frac{1}{2}\sqrt{E_y^2 + E_z^2 + \left(E_x - 2E_{\mathrm{SO}}\sin\phi\right)^2}. \tag{6.27}$$

For $E_y = E_z = 0$, this simplifies to

$$E_{\uparrow,\downarrow} = E_0\cos\phi \pm \left(E_x/2 - E_{\mathrm{SO}}\sin\phi\right) \tag{6.28}$$

The Zeeman field parallel to E_{SO} enters as a constant offset, which does not change the curvature of the potential and does not affect the transmon frequency. Furthermore, this results in the spin-flip transition frequency given by

$$E_\uparrow - E_\downarrow = E_x - 2E_{\mathrm{SO}}\sin\phi \tag{6.29}$$

which is linear in the applied Zeeman field. Setting $E_x = E_y = 0$ instead, we find

$$E_{\uparrow,\downarrow} = E_0\cos\phi \pm \frac{1}{2}\sqrt{E_z^2 + 4E_{\mathrm{SO}}^2\sin^2\phi} \tag{6.30}$$

Here the E_z term does enter the curvature of the potential, thus affecting the transmon frequency. Furthermore, the resulting in the spin-flip qubit transition frequency is given by

$$E_\uparrow - E_\downarrow = \sqrt{E_z^2 + 4E_{\mathrm{SO}}^2\sin^2\phi} \tag{6.31}$$

The presence of the $\sin^2\phi$ term results in the doubling in periodicity we observe in the perpendicular field dependence of main text Fig. 6.4(c) compared to the parallel field dependence of Fig. 6.4(b).

NRG CALCULATIONS

The proposed model has very little symmetry: the spin-orbit coupling fully breaks the rotational SU(2) spin symmetry, and the BCS mean-field approximation breaks the U(1) charge conservation. The only remaining symmetry is Z_2 fermionic number parity (even or odd total number of electrons in the system). Furthermore, the Hamiltonian has complex-valued matrix elements. Nevertheless, the quantum impurity problem can still be solved using the conventional impurity solver, the numerical renormalization group (NRG), albeit at quite significant computational cost. The NRG method consists of discretizing the continua (two superconducting baths), their transformation into Wilson tight-binding chains, and an iterative diagonalization of the resulting chain/ladder Hamiltonian. We performed a very coarse discretization with the discretization parameter $\Lambda = 8$; nonetheless, for the purposes of computing energy splitting, this remains a surprisingly good approximation. We retain up to 3000 states in each NRG step. On 8 cores of an AMD EPYC 7452 processor, such NRG calculations take approximately 15 minutes for each parameter set. The band is assumed to have a constant density of states in the interval $[-D:D]$. In the following, all model parameters will be given in units of half-bandwidth D.

We first verify the findings from the analytics, specifically the spin splitting induced by the combination of the spin-flip scattering, the presence of multiple levels in the QD (represented by the interdot tunneling term t), and finite superconducting phase difference between the two SC contacts, as described by the $E_{\rm SO}\sin\phi$ terms in the effective Hamilotinian with $E_{\rm SO} = 4\tilde{t}\sqrt{\Gamma_V\Gamma_W} = 4\tilde{t}\Gamma_V\sqrt{\Gamma_W/\Gamma_V}$, see Eqs. (6.25) and (6.25). In Fig. 6.6 we plot the dependence of the splitting $E_\uparrow - E_\downarrow$ as a function of key parameters. We indeed observe that the splitting is linear in the hybridisation Γ for fixed Γ_W/Γ_V ratio, in the ratio $W/V = \sqrt{\Gamma_W/\Gamma_V}$ and in the hopping t. Finally, we also ascertain the $\sin(\phi)$ dependence of the splitting. We have thus confirmed that the splitting is linear in t, Γ, W/V, and ϕ for small parameter values.

The dependence on other model parameters, in particular U_{ee} and Δ, is not simple. The parameters U_{ee} and Δ control the energy cost of charge fluctuations, and the behavior depends not only on their ratio, but also on their values compared to the hybridisation Γ as well as the bandwidth D. The simplest case is the linear regime of small parameter Γ, where the splitting is simply inversely proportional to $1/(U_{ee}/2+\Delta)$ to a good approximation, see Fig. 6.7(a). For larger Γ, we observe deviations from this simple form, see Fig. 6.7(b). It is also instructive to consider the dependence on Δ at fixed U_{ee}. The limit of small U_{ee} is merely of academic interest, because the doublet state is then a (highly) excited state: we find a roughly linear dependence on Δ, see Fig. 6.7(c). For large U_{ee}, however, we find a complex dependence that furthermore depends on the value of Γ, showing a cross-over from quadratic dependence for $\Delta \ll \Gamma$ to a roughly linear dependence for $\Delta \gtrsim \Gamma$, see Fig. 6.7(d). From these plots we conclude that the dependence on U_{ee}, Δ and Γ (when Γ is not small) is highly non-trivial and should in general be computed numerically (e.g. using the NRG method).

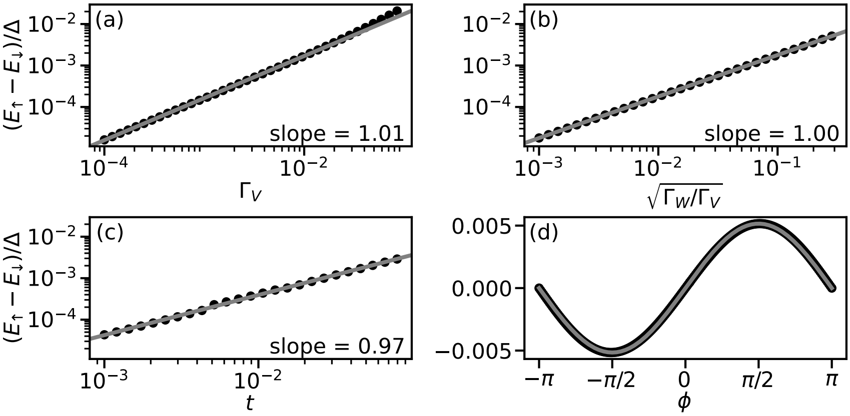

Figure 6.6: Scaling of the induced spin splitting in the doublet state with parameters Γ_V, Γ_W, and t, as well as the ϕ-dependence. Unless stated otherwise, the parameter set is $U_{ee} = 1$, $\epsilon = -U_{ee}/2$, $\Gamma_V = 0.02$, $\Gamma_W = \Gamma_V/5$, $t = 0.1$, $\Delta = 0.01$, $\phi = \pi/4$. (a) Γ_V-dependence, demonstrating the linearity of splitting as a function of the hybridisation strength, with small non-linear corrections for large Γ_V. (b) Γ_W/Γ_V-dependence, demonstrating the linearity of splitting as a function of the ratio of spin-flip over spin-preserving tunneling processes to the impurity orbital in resonance. (c) t-dependence, demonstrating the linearity of splitting as a function of cotunneling through non-resonant impurity levels. (d) ϕ-dependence, showing a very clean $\sin(\phi)$ behavior of the spin-splitting, as predicted by the reduced analytical model.

In Fig. 6.8 we explore the three contributions to the doublet potential: the conventional doublet $E_D\cos(\phi)$ potential with the minima at $\phi = \pm\pi$, the $E_{\text{SO}}\sin(\phi)$ potential due to spin-flip scattering with minima at $\phi = \pm\pi/2$, as well as the $-E_t\cos(\phi)$ potential due to cotunneling though the multiple levels of the QD with minimum at $\phi = 0$, see Fig. 6.8. We plot the results for a range of t starting from zero; this case serves as a reference from which we extract the standard E_D part. With increasing t, both E_{SO} as well as E_t increase. This displaces the minima in the effective potential from $\phi = \pm\pi$ towards $\phi = \pm\pi/2$. When E_t becomes equal to E_D, the $\cos(\phi)$ part of the potential cancels out. For $E_t > E_D$, the minima move past $\phi = \pm\pi/2$ and tend toward $\phi = 0$.

A major time-saving procedure is to incorporate the effects of the external magnetic field as a perturbation to the results of an NRG calculation for a Hamiltonian without any field terms. This ploy rests on the observation that the impurity spin operators are exactly marginal (in the renormalization-group sense): their matrix elements remain of the same order of magnitude throughout the NRG iteration, i.e., they neither blow up nor decay to zero. The method may hence be dubbed the “marginal-operator trick”. The idea is to perform the NRG iteration of spin operators S_x, S_y, S_z through unitary transformations to find the effective spin operators in the NRG eigenbasis in the low-energy sector. These are then added to the effective Hamiltonian with bare Zeeman energies E_x, E_y, E_z:

$$H_{\text{eff}} = \sum_w E(w)\,|w\rangle\langle w| + E_x\tilde{S}_x + E_y\tilde{S}_y + E_z\tilde{S}_z. \tag{6.32}$$

Here w indexes the eigenstates $|w\rangle$ with eigenenergies $E(w)$, while $\tilde{S}_i$ are the trans-

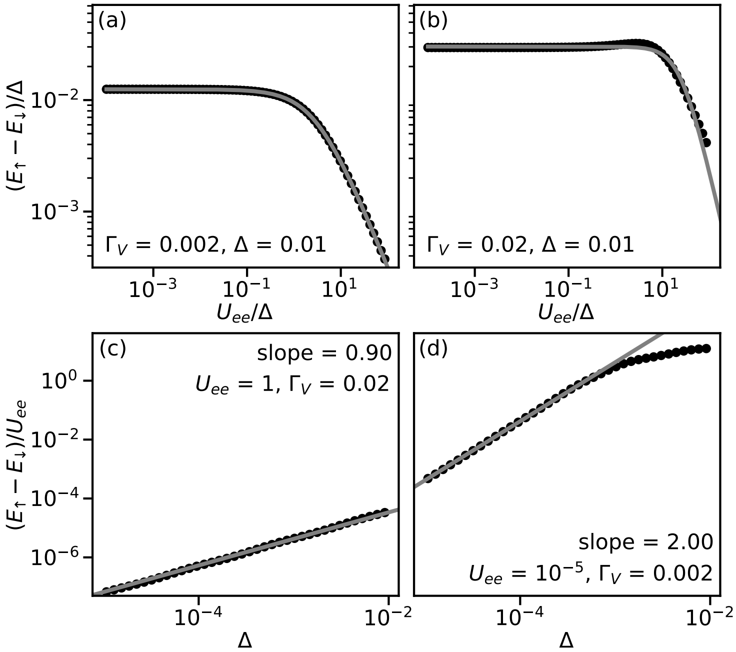

Figure 6.7: Scaling of the induced spin splitting in the doublet state with parameters U_{ee} and Δ. Other parameters as in Fig. 6.6. (a) U_{ee}-dependence at $\Gamma_V = 0.002$ showing the cross-over from the $U_{ee} \ll \Delta$ regime to the $U_{ee} \gg \Delta$ regime. (b) Same as a, but for stronger hybridisation $\Gamma_V = 0.02$, showing the more complex behavior away from the low-Γ_V limit. (c) Δ-dependence at $\Gamma_V = 0.02$, showing that the splitting is roughly proportional to Δ in the $U_{ee} \gg \Gamma, \Delta$ regime. (d) Same as (c), but for $\Gamma_V = 0.002$ and much smaller $U_{ee} = 10^{-5}$ (non-interacting limit), showing quadratic scaling for $\Delta \ll \Gamma$ that crosses over into linear scaling for $\Delta \gg \Gamma$.

formed spin matrices in this same basis. The basis can be truncated to a small number of levels; in many cases it is sufficient to retain solely the subgap states. This effective Hamiltonian may then be diagonalized at negligible numerical cost for arbitrary values of E_x, E_y and E_z. In case where only two (subgap) states are retained one can even write down closed-form expressions for eigenenergies and eigenstates. The marginal-operator trick is a good approximation up to Zeeman energies comparable to the BCS energy gap Δ, as it has been ascertained by comparisons with the NRG calculations with the Zeeman terms included from the outset, see Fig. 6.9. This method is clearly very generally applicable to any problem involving marginal operators in the Hamiltonian, obviating the need for costly parameter sweeps in multidimensional spaces.

TRANSMON DIAGONALIZATION

Having established how to calculate an effective potential in the doublet sector, we now turn to its inclusion in the Hamiltonian of the encompassing transmon circuit [162]:

$$H = -4E_\mathrm{c}\partial_\phi^2 + E_\mathrm{J}(1-\cos\delta) + U(\phi), \tag{6.33}$$

where E_c and E_J denote the charging energy of the transmon island and the Josephson energy of the reference junction, respectively, and $U(\phi)$ denotes the effective doublet

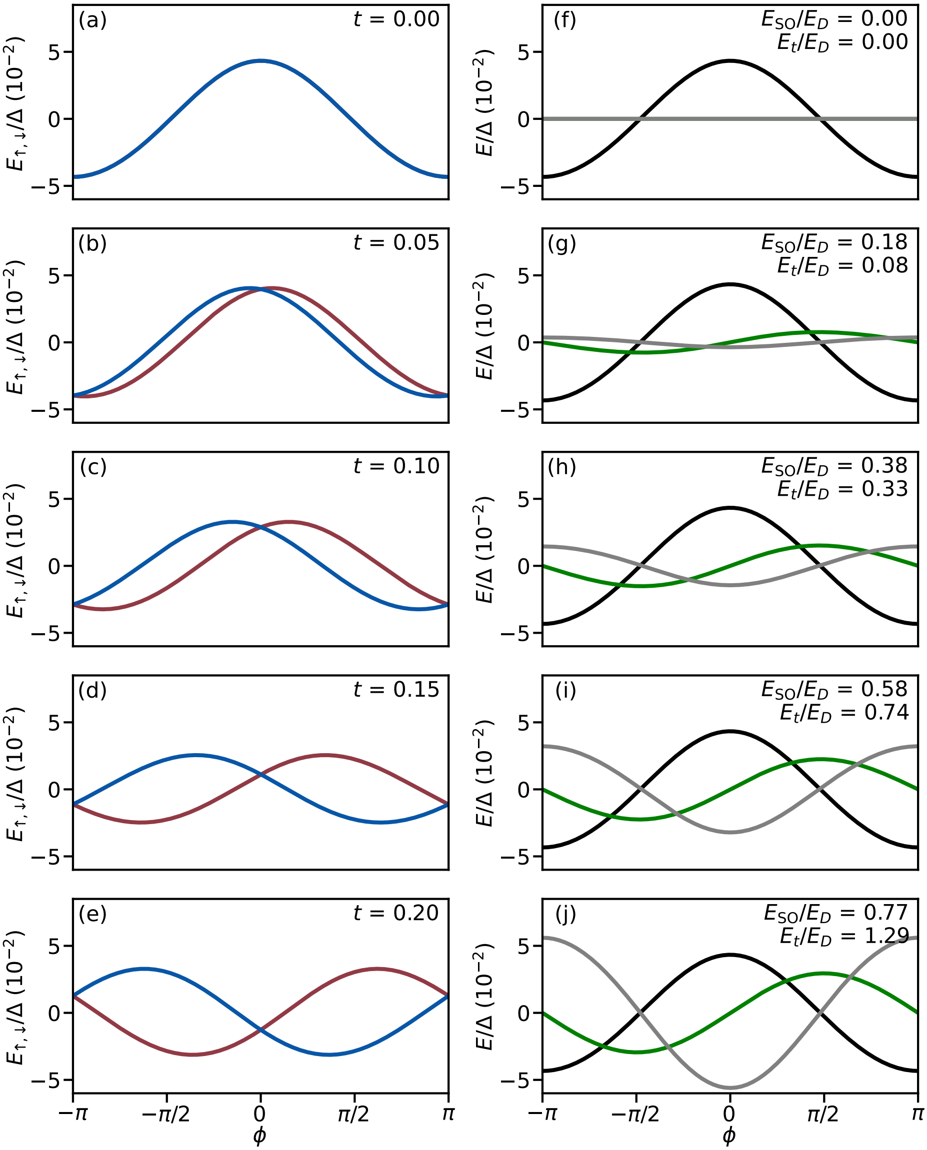

Figure 6.8: Decomposition of the doublet potential energy into its components. We show the results for various values of t, as indicated for each panel. All plots have the same axis ranges in order to permit direct comparison of magnitudes. (a-e) Total potential for the two spin states. (f-g) $E_D \cos(\phi)$ potential, common to all cases (black), $-E_t \cos(\phi)$ (green) and $E_{\text{SO}} \sin(\phi)$ (grey) contributions. We find $E_D = 4.33\,10^{-3}$ (same for all t) and the E_t/E_D and E_{SO}/E_D ratios indicated for each panel. Other model parameters are $U_{ee} = 1$, $\epsilon = -U_{ee}/2$, $\Delta = 0.1$, $\Gamma_V = 0.2$, $\Gamma_W/\Gamma_V = 1/5$.

potential of main text Eq. (6.1). The two phase drops across the quantum dot junction (ϕ) and across the reference junction (δ) are connected according to $\phi - \delta = \phi_{\text{ext}}$, where

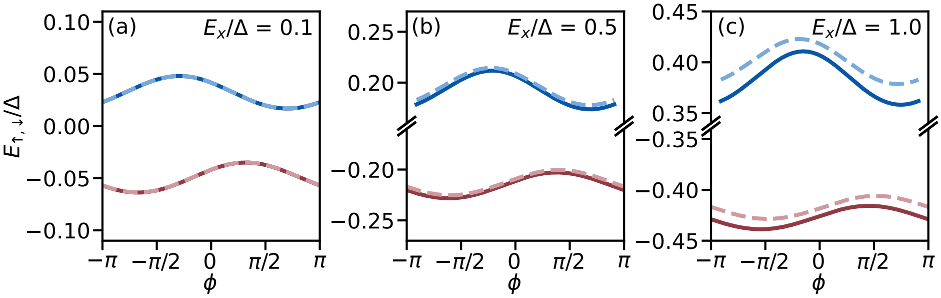

Figure 6.9: Comparison of the energies of the doublet subgap states as a function of the phase bias computed using the standard NRG procedure (solid lines) and using the "marginal-operator trick" approximation (discontinuous lines). Vertical scale is the same for all panels. Model parameters are $U_{ee} = 1.5$, $\Gamma_\mathrm{L} = \Gamma_\mathrm{R} \equiv \Gamma = 0.2$, $\gamma_\mathrm{L} = \gamma_\mathrm{R} = 0.2\Gamma$, $t = 0.1$, $\epsilon = 0.1 - U_{ee}/2$, $\Delta = 0.1$.

$\phi_\mathrm{ext} = (2e/\hbar)\Phi_\mathrm{ext}$ is the phase difference resulting from the externally applied magnetic flux through the SQUID loop, Φ_ext [Fig. 6.1(d)].

Following Ref. [169] and chapter 4, we numerically diagonalize (6.33) in the phase basis. This results in the energy levels E_n as well as the associated transition frequencies $f_{nm} = (E_m - E_n)/h$, capturing both the transmon and the spin-flip transitions. Having calculated the transition frequencies, fits can be made to the data. This is done to obtain the estimates for the effective model parameters found in the main text and in the next sections, using $E_\mathrm{c}/h = 284\,\mathrm{MHz}$ and $E_\mathrm{J}/h = 12.4 - -12.7\,\mathrm{GHz}$ as reference junction parameters. Note that the reference junction gate voltage is generally held fixed in the experiment, and that the range in E_J is the result of cross-coupling between the quantum dot and reference junction gate lines.

Here we note that the sinusoidal reference junction potential used in Eq. (6.33) is that of a conventional superconductor-insulator-superconductor (SIS) tunnel junction, governed by many weakly transparent channels. Previous work has found that nanowire-based Josephson junctions are more accurately described by several or even a single transport channel, leading to a more skewed potential shape [167]. This can result in a reduction of the the qubit anharmonicity, and thus an underestimation of E_c when using the SIS potential. However, the inclusion of a more involved potential introduces additional fitting parameters, and obtaining unique solutions is not guaranteed. This holds in particular because the reference junction is operated far from its pinchoff voltage, such that several channels are expected to contribute to the potential. We therefore choose to use the SIS potential throughout the Letter. In practice, this choice affects the value of E_c that is extracted from the fit, which in turn rescales the extracted values of E_0 and E_SO.

DEVICE AND EXPERIMENTAL SETUP

DEVICE OVERVIEW

The physical implementation of the device studied is shown in Fig. 5.2. It is analogous to that of chapter 5, repeated here for convenience. The chip, 7 mm long and 2 mm wide, consists of four devices coupled to a single transmission line with an input capacitor to increase the directionality of the outgoing signal [Fig. 5.2(b)]. For the experiments performed in this Letter only two of the devices were wire-bonded: the device measured in the main text, and a second device, which was not functional.

For each device, a lumped element readout resonator is capacitively coupled to the feedline [Fig. 6.10(c)]. The resonator is additionally capacitively coupled to the transmon island, which is connected to ground via a SQUID loop formed by the reference and quantum dot junctions [Fig. 6.10(d)]. Both junctions are implemented on a single 10 um-long epitaxial superconductor-semiconductor nanowire with a 110 nm-wide hexagonal InAs core and a 6 nm-thick Al shell covering two of its facets, in turn covered by a thin layer of aluminium oxide. The growth conditions were almost identical to those detailed in Ref. [173], with the only two differences being that this time the As/In ratio is 12, smaller than in Ref. [173], and that the oxidation of the Al shell is now performed in-situ, for better control, reproducibility and homogeneity of the oxide layer covering the shell. Inspection of the nanowire batch, performed under a scanning electron microscope directly after growth, indicated an average wire length of 9.93± 0.92 µm and an average wire diameter of 111 ± 5 nm. For the device investigated here, the two facets of the aluminum shell are situated on the top part of the nanowire. The two junctions are defined in two uncovered nanowire sections (110 nm-long for the reference junction and 200 nm-long for the quantum dot junction). A zoom-in of the the quantum dot junction is shown in Fig. 6.10(e). The reference junction is controlled by a single 110 nm-wide electrostatic gate, set at a DC voltage V_J. The quantum dot junction is defined by three 40 nm-wide gates separated from each other by 40 nm. We note that in Fig. 6.1(e) the gates appear wider (and the gaps between gates appear smaller) than stated due to distortion by the gate dielectric layer. The outer two gates are set at DC voltages V_L and V_R. The central gate is connected to a bias-tee formed by a 100 kΩ resistor and a 100 pF capacitor. This permits the simultaneous application of a DC signal V_C to control the level of the quantum dot junction and a microwave tone $f_{s,\text{drive}}$ to drive the spin-flip transition.

NANOFABRICATION DETAILS

The device fabrication occurs in several steps using standard nanofabrication techniques. It is identical to that described in chapter 5, and repeated here for the sake of completeness. The substrate consists of 525 µm-thick high-resistivity silicon, covered in 100 nm of low pressure chemical vapor deposited Si_3N_4. On top of this, a 20 nm thick NbTiN film is sputtered, into which the gate electrodes and circuit elements are patterned using an electron-beam lithography mask and SF_6/O_2 reactive ion etching. Subsequently, 30 nm of Si_3N_4 dielectric is deposited on top of the gate electrodes using plasma enhanced chemical vapor deposition and then etched with a buffered oxide etchant. The nanowire is then deterministically placed on top of the dielectric using a nanomanipulator and an optical microscope. After placement, two sections of the aluminium shell

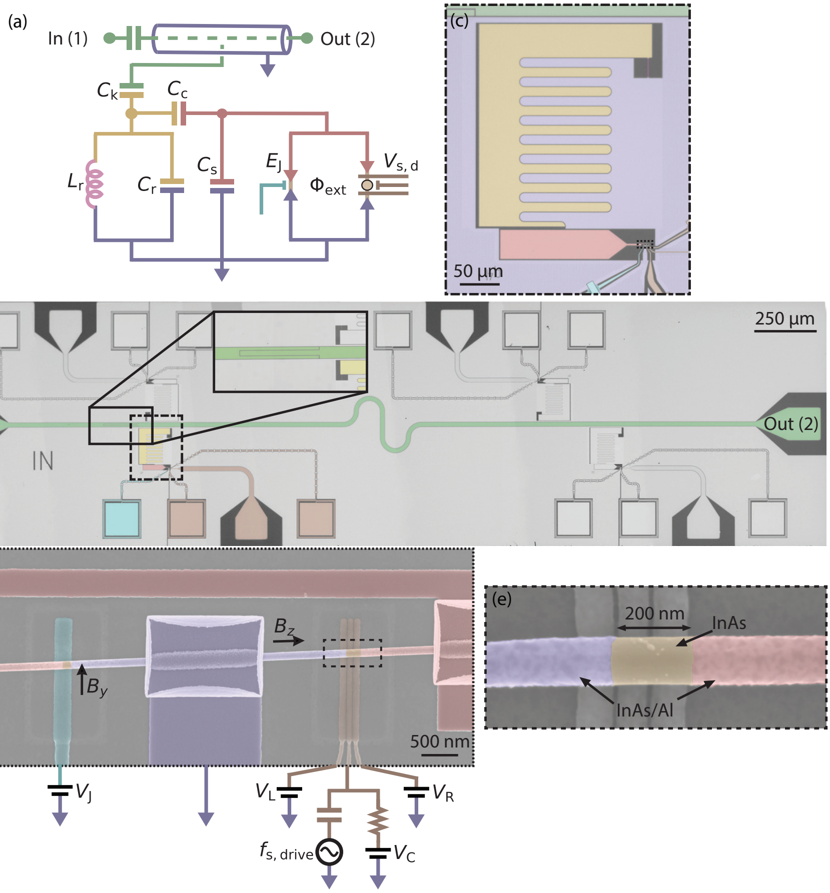

Figure 6.10: **Device overview.** (a) Diagram of the microwave circuit. A coplanar waveguide transmission line with an input capacitor (green center conductor) is capacitively coupled to a grounded LC resonator. The resonator consists of an island (yellow) capacitively and inductively (pink) shunted to ground (blue). The resonator is in turn capacitively coupled to a transmon island (red), which is shunted to ground capacitively as well as via two parallel Josephson junctions. (b) Chip containing four nearly identical devices coupled to the same transmission line, which has an input capacitor, enlarged in inset. (c) False-colored optical microscope image of the device showing the qubit island, the resonator island, the resonator inductor, the transmission line, the electrostatic gates and ground. (d) False-colored scanning electron micrograph (SEM) of the measured device, showing the InAs/Al nanowire into which the junctions are defined. The B_y component of the magnetic field is used to tune Φ_{ext} [334]. B_z is the magnetic field component parallel to the nanowire. (e) False-colored SEM of the measured device, showing the quantum dot junction in which the quantum dot is gate defined. The three bottom gates have a width and spacing of 40 nm, although this is obfuscated by the dielectric layer placed on top.

are selectively removed by wet etching with MF-321 developer. These sections form the quantum dot junction and the reference junction, with lengths 200 nm and 110 nm respectively. After the junction etch, the nanowire is contacted to the transmon island and to ground by an argon milling step followed by the deposition of 150 nm-thick sputtered NbTiN. Finally, the chip is diced into 2 by 7 millimeters, glued onto a solid copper block with silver epoxy, and connected to a custom-made printed circuit board using aluminium wirebonds.

CRYOGENIC AND ROOM TEMPERATURE MEASUREMENT SETUP

The device was measured in a Triton dilution refrigerator with a base temperature of 20 mK. As shown in Fig. 6.11, the setup contains an input RF line, an output RF line, an additional RF line for driving the spin-flip transition, and multiple DC gate lines. The DC gate lines are filtered at base temperature with multiple low-pass filters connected in series. The input and drive RF lines contain attenuators and low-pass filters at different temperature stages, as indicated. The output RF line contains a traveling wave parametric amplifier (TWPA) at the 20 mK temperature stage, a high-electron-mobility transistor (HEMT) amplifier at the 4 K stage, and an additional amplifier at room temperature. A three-axis vector magnet (x-axis not shown) is thermally anchored to the 4 K temperature stage, with the device under study mounted at its center. The three magnet coils are controlled with Yokogawa GS610 current sources. At room temperature, a vector network analyzer (VNA) is connected to the input and output RF lines for spectroscopy at frequency f_r. On the input line, this signal is then combined with the transmon drive tone at frequency $f_\mathrm{t,drive}$, for two-tone spectroscopy. The spin-flip drive tone at frequency $f_\mathrm{s,drive}$ is sent through the additional RF line.

BASIC CHARACTERIZATION AND TUNE UP

This section describes how the device is tuned to its gate setpoints.

We start by characterizing the effect of the electrostatic gates, which control each of the two Josephson junctions. Fig. 6.12(a) shows the basic behaviour of the reference junction versus junction gate voltage V_J when the quantum dot junction is completely closed. As V_J is varied, different junction channels open sequentially [118, 296], with transparencies that increase non-monotonically due to mesoscopic fluctuations. This in turn affects the E_J of the transmon, allowing for in-situ tunability of its frequency, and the transmon then affects the resonator through its dispersive shift [35], resulting in the observed change in resonator frequency. We use this to choose a V_J set-point which maintains a good SQUID asymmetry in all regimes of interest. The black line in Fig. 6.12(a) indicates $V_\mathrm{J} = 3860\,\mathrm{mV}$, the setpoint used in Figs. 6.3(a-b) in the main text. After a small non-reproducible gate jump in the reference junction the setpoint was retuned to $V_\mathrm{J} = 4064.5\,\mathrm{mV}$, which was used for all other data shown in the main text. For all resonances explored, we maintained $E_\mathrm{J}/E_\mathrm{c} > 40$.

We start by characterizing the effect of the electrostatic gates, which control each of the two Josephson junctions. Fig. 6.12(a) shows the basic behaviour of the reference junction versus junction gate voltage V_J when the quantum dot junction is completely closed. As V_J is varied, different junction channels open sequentially [118, 296], with transparencies that increase non-monotonically due to mesoscopic fluctuations. This in turn affects the E_J of the transmon, allowing for in-situ tunability of its frequency, and the transmon then affects the resonator through its dispersive shift [35], resulting in the observed change in resonator frequency. We use this to choose a V_J set-point which maintains a good SQUID asymmetry in all regimes of interest. The black line in Fig. 6.12(a) indicates $V_\mathrm{J} = 3860\,\mathrm{mV}$, the setpoint used in Figs. 6.3(a-b) in the main text, which fixes the transmon frequency at $f_\mathrm{t} = 4.7\,\mathrm{GHz}$. After changing the quantum dot junction from gate setpoint A to gate setpoint B and due to cross-coupling between the quantum dot and reference gates, the reference junction started exhibiting poisoning

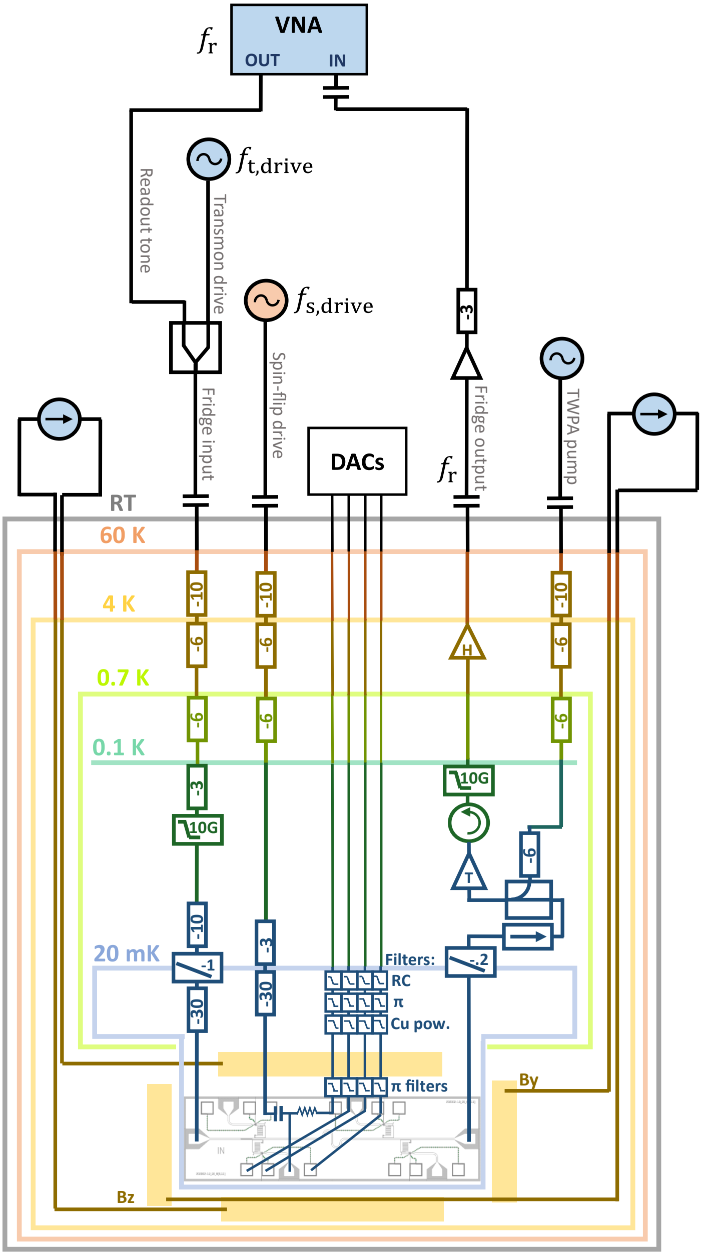

Figure 6.11: **Measurement setup at cryogenic and room temperatures.**

behavior. Therefore, its setpoint was then set to $V_J = 4064.5\,\text{mV}$, fixing the transmon frequency at $f_t = 4.95\,\text{GHz}$, which was used for all other data shown in the main text. Fig. 6.12(b) shows a measurement taken at the moment when the V_J value was changed from its $V_\mathrm{J} = 3860\,\mathrm{mV}$ to its $V_\mathrm{J} = 4064.5\,\mathrm{mV}$ setpoint, both indicated with black lines. For all resonances explored, we maintained $E_\mathrm{J}/E_\mathrm{c} > 40$.

In Figs. 6.12(c-f) we show analogous measurements where we vary the quantum dot gate voltages when the reference junction is closed. We first measure an effective pinch-off curve for all three quantum dot gates ramped together [Fig. 6.12(c)], before sweeping each gate separately, with the other two quantum dot gates kept at 2000 mV [Figs. 6.12(d-f)]. This shows that each of the three quantum dot gates can independently pinch off the quantum dot junction, even if the other gates are in the open regime, signifying strong lever arms and good gate alignment. Note that these are not pinch-off curves as encountered in conventional tunnel spectroscopy; they reflect the voltages at which there is no longer a measurable transmon transition frequency mediated by the quantum dot junction, which could either be due to low tunneling rates or a full depletion of the quantum dot.

The subsequent tuning procedure for finding an isolated quantum dot resonance is discussed in detail in chapter 5, summarized here for the specific resonances used in the main text. First we close the reference junction and go to a point in quantum dot gate voltages near pinchoff. Fixing the readout frequency f_r at the bare frequency of the resonator, one can then map out the regions where dispersive shifts occur on a two-dimensional map versus the left and right quantum dot gates, with the central gate held fixed. This signifies regions in which there is a supercurrent flowing through the quantum dot junction. After identifying such a region in V_L-V_R space, we subsequently open the reference junction, which lifts the reference transmon frequency closer to the bare resonator frequency. This magnifies the dispersive shift of the resonator and, furthermore, brings the external flux into the picture. Fixing $\phi_\mathrm{ext} = 0$ and repeating the initial measurement then reveals much stronger deviations of the resonant frequency due to the enhanced dispersive shift.

Using this approach we identify isolated quantum dot resonances, and subsequently explore their evolution versus the central quantum dot gate. This is shown in Fig. 6.13, where we furthermore account for cross coupling between the different quantum dot gates by defining a new set of virtual gates. For simplicity we fix V_L and focus on the rotated V_R-V_C space, denoted as the V_P-V_T-space. Note that this compensation scheme is unique for each isolated region we explore. Fixing $\phi_\mathrm{ext} = 0$ and varying the central dot gate, the resonator first shows a displacement towards higher frequencies to then abruptly drop to a lower frequency, to then finally go back to the higher frequencies once-more [Fig. 6.13(a,c)]. This behaviour is reversed for $\phi_\mathrm{ext} = \pi$ [Fig. 6.13(b,d)], and can be identified as a singlet-doublet transition resulting from the relative level of the quantum dot is being varied by V_P. We note that in the V_T direction we do not always find the expected dome shape characteristic of singlet-doublet transitions; while such a shape does develop for resonance B [Fig. 6.13(c-d)], the doublet phase of resonance A [Fig. 6.13(a-b)] remains open even at elevated tunnel gate voltages. This is potentially a result of a non-monotonic dependence of tunnel rates on the gate voltage.

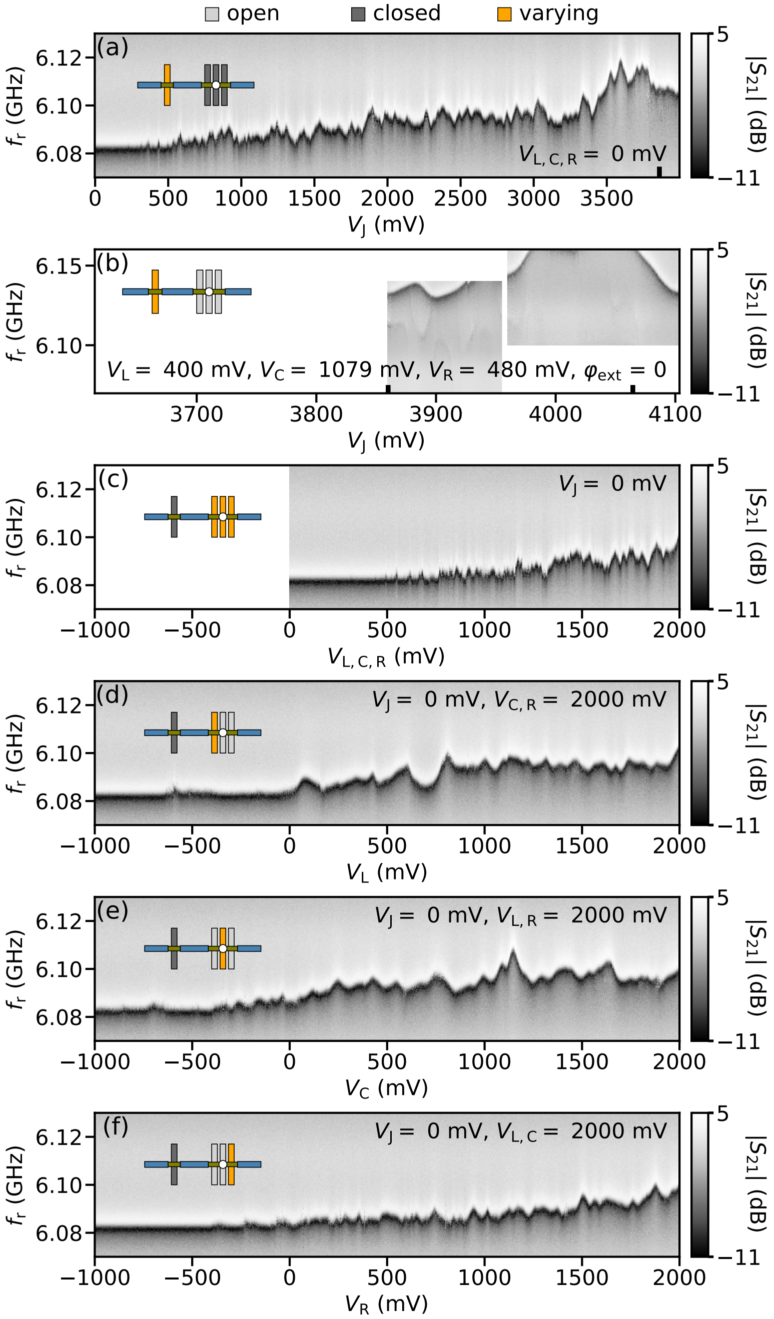

Figure 6.12: **Electrostatic gates characterization.** Transmission amplitude as a function of frequency of a single tone f_r and gate voltage. For each panel, the inset indicates which gate is being varied (orange) and which ones are set to a value above (light grey) or below (dark grey) their pinch-off value.

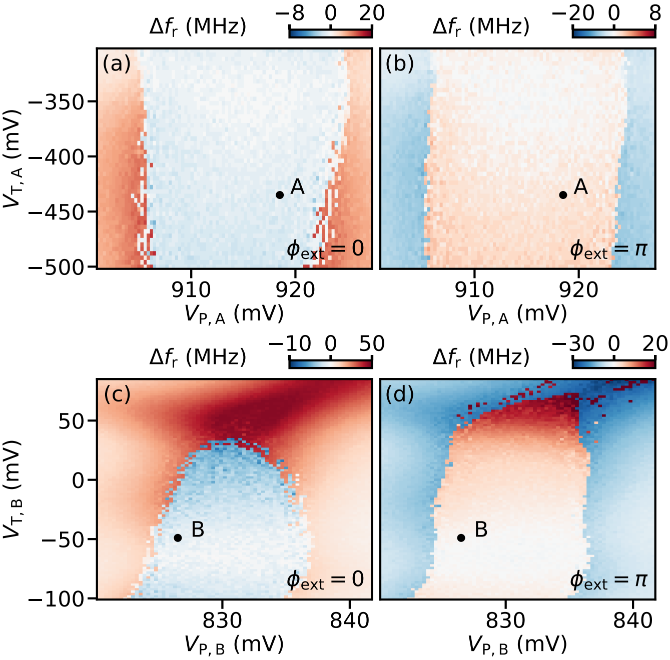

Figure 6.13: (a,c) Shift of the resonator resonance frequency with respect to its value when the quantum dot junction is fully closed, Δf_r, versus V_P and V_T at $\phi_{ext} = 0$, revealing singlet (red) and doublet (blue) ground state regions separated by sharp transitions for resonance A (a) and resonance B (c). (b,d) Same as (a,c) but for $\phi_{ext} = \pi$.

EXTENDED DATA

SPIN-ORBIT SPLITTING AT DIFFERENT RESONANCES

As discussed in the main text, we find a wide variety of phase-dependent splittings depending on the quantum dot resonance studied. This is shown in Fig. 6.14, portraying a range of resonances all the way from an even phase dependence with no splitting (panel d) to resonances that have a fully odd phase dependence (panel b). By Fitting the potentials with the transmon Hamiltonian, we extract a set of effective parameters for each resonance, tabulated in Table 6.1.

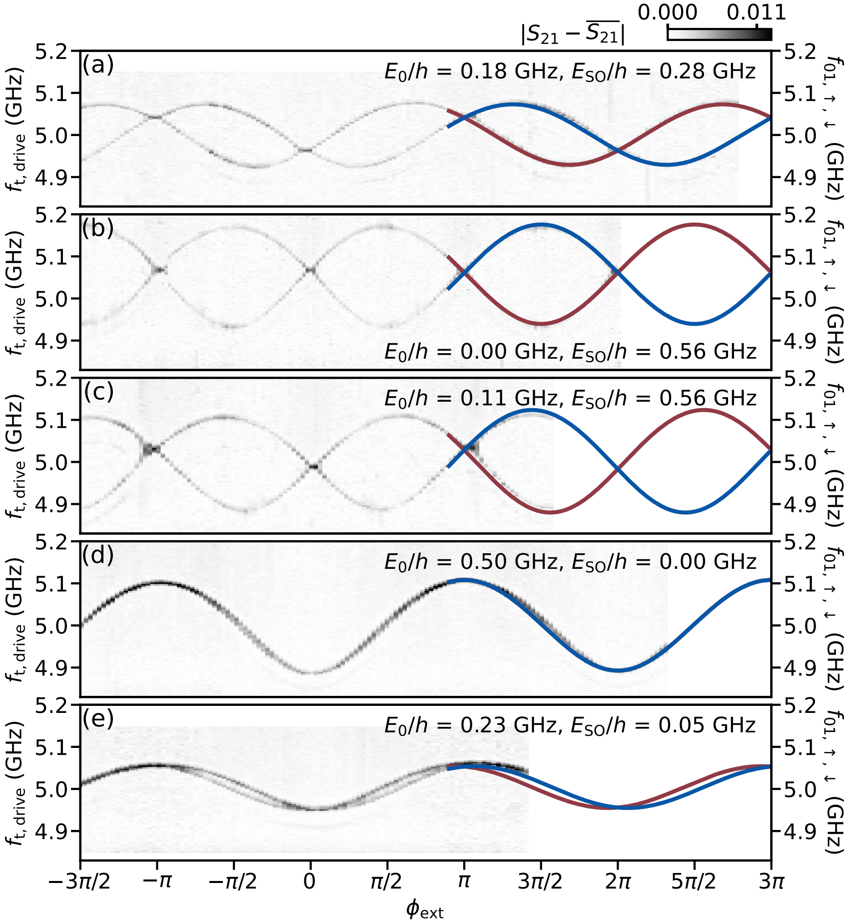

Figure 6.14: **Spin-splitting energies at different resonances.** Flux dependence of transmon spectroscopy taken at different points in quantum dot gate space, indicated in Table 6.1. In all cases, the quantum dot junction is in a doublet state. Different panels show different spin-splitting energies. (a) and (b) are gate setpoints A and B of the main text, respectively.

Table 6.1: Quantum dot junction gate voltage set points and extracted model parameters for the five panels in Fig. 6.14.

	V_L (mV)	V_C (mV)	V_R (mV)	E_0/h (GHz)	E_SO/h (GHz)
A	79.0	1020.0	363.0	0.18	0.28
B	430.0	531.0	635.2	0.00	0.56
C	430.0	520.0	652.0	0.11	0.56
D	430.0	614.8	335.0	0.50	0.00
E	430.0	655.2	305.2	0.23	0.05

SPIN-ORBIT SPLITTING WITHIN THE SAME RESONANCE

Within the extended SIAM model, E_SO and E_0 are expected to depend on Γ_V, Γ_W, and $\tilde{t}$ (see Sec. 6.7). One would therefore expect that these quantities can also vary within a single resonance, as the gate voltages tune the relative energy levels as well as the tunnel barriers of the quantum dot. This is indeed observed in the experiment: as shown in Fig. 6.15(a,b) for resonance A, we find that both effective doublet parameters vary with the rotated plunger and tunnel gates. In particular, both E_0 and E_SO show an increase towards the boundary of the singlet doublet transition, i.e. towards the edges of the Coulomb diamond. This is in line with the predictions of Ref. [234], as in the middle of the Coulomb diamond the energy cost of adding an electron to the quantum dot is maximal and the high energy of the intermediate states reduces the probability of Cooper pair tunneling. Additionally, contrary to initial expectation, the magnitude of the effective parameters appears to decrease for larger tunnel gate values. While the tunnel gate is expected to increase the tunnel rates, and thus the effective parameters, we note that in practice the situation is highly complex; there are up to three gate voltages that control five model parameters ($\Gamma^{\mathrm{L,R}}_{V,W}$, $\tilde{t}$), with potentially non-monotonic dependencies as well as cross-coupling. A full understanding of such a system will require a more detailed study of such dependencies, which we leave for future work. At this stage we instead emphasize the gate-tunability of these quantities, allowing for in-situ fine-tuning of the model parameters

Furthermore, we also find that the effective Landé g-factor g^* depends on gate voltage [Fig. 6.15(c)], in line with previous results on quantum dots in InAs nanowires, demonstrating its electric gate tunability [64]. This could be of relevance for qubit applications, as the tunability can be used to rapidly drive spin states in and out of resonance with a static magnetic field induced electron spin resonance condition. Finally, we note that the observed gate dependence of g^* is distinct from that of E_SO and E_0, supporting the assertion that its origin is tied to a complex interplay of spin-orbit coupling and confinement, beyond the model considered here [159, 283, 340].

MAGNETIC FIELD ANGLE DEPENDENCE AND DETERMINATION OF THE SPIN-SPLITTING DIRECTION

In this Section we detail the method used to determine the direction of the spin-orbit interaction at a fixed gate point. This is done by comparing the angle dependence of transmon and spin-flip spectroscopy to the predictions of the model discussed in Sec. 6.7. For this it is useful to define a coordinate space determined by the nanowire direction, Z, the

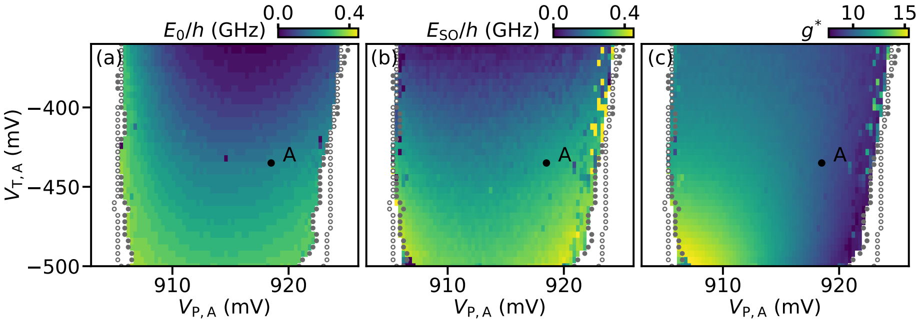

Figure 6.15: **Gate dependence within resonance A.** (a) Magnitude of E_0 extracted from transmon qubit spectroscopy at $\phi_{\text{ext}} = 0, \pi$ versus rotated plunger and tunnel gate voltages, at a magnetic field of 18 mT applied parallel to the nanowire. (b) Same as (a) for E_{SO}, extracted from spin-flip spectroscopy at $\phi_{\text{ext}} = \pi/2, 3\pi/2$. (c) Same as (b) for g^*, extracted from the same measurement as (b).

on-chip direction perpendicular to the nanowire, Y, and the direction perpendicular to the chip, X. We then define $\theta \in [0, 180)$ as the polar angle with respect to the Z direction and $\phi \in [0, 360)$ as the azimuthal angle [see Fig. 6.16], such that $B_x = B_r \cos(\phi)\sin(\theta)$, $B_y = B_r \sin(\phi)\sin(\theta)$ and $B_z = B_r \cos(\theta)$. Note that the cartesian field directions B_x, B_y and B_x set a frame of reference and should not be confused with the directions $B_\parallel$ and $B_\perp$ presented in the main text, which are specific for each gate setpoint. With this convention, $\phi = 90$ is the plane of the chip, while $\phi = 0$ is the plane perpendicular to the chip containing the nanowire. In each of these two planes, we first fix the magnitude of the applied magnetic field, B_r, and measure the evolution of transmon and spin-flip spectroscopy while varying θ in steps of two degrees. For each plane we determine the angle for which the applied field is perpendicular to the spin-splitting direction, $\theta_{\perp,0}$ and $\theta_{\perp,90}$, by comparison to the theory model. The cross product of these two directions determines the direction parallel to the spin-splitting term.

Representative data of such a measurement for resonance A is shown in Fig. 6.16(a-b), where we fix $\phi = 90$ and find $\theta_{\perp,90} = 78$. Performing an analogous measurement in the $\phi = 0$ plane, we determine $\theta_{\perp,0} = 86$. From these two, we obtain $(\theta_{\text{s}}, \phi_{\text{s}}) = (167, 72)$ as the spin-splitting direction of resonance A. This is 13 degrees away from the nanowire axis. Furthermore, we generally find that the measured spin-split direction varies depending on which quantum dot resonance is studied; for resonance B of the main text we obtain a spin-splitting direction of $(\theta_{\text{s}}, \phi_{\text{s}}) = (72, 45)$, which is 84 degrees away from the spin-splitting direction of resonance A.

We can furthermore estimate the effective Landé g-factor from the evolution of the spin-flip transition frequency versus the angle of the magnetic field. Shown in Fig. 6.16(c) for resonance A, the effective g-factor varies from 3 to 11 depending on the angle, minimal for magnetic fields perpendicular to the spin-orbit direction. The measured behaviour is well-described by a simple cosine, in line with previous results on quantum dots in InAs nanowires [283].

SPIN-FLIP SPECTROSCOPY ENABLED BY SPIN-ORBIT SPLITTING

As discussed in the main text, we do not rely on driving transitions of the transmon circuit to perform spectroscopy of the junction's excitation spectrum. While in principle possible by using three microwave tones, this could result in limitations due to the finite transmon lifetime as well as undesired mixing processes between the different tones. Instead, we use the dispersive shift from the transmon's ground state to induce a doublet-state-dependent shift on the resonator, similar to how the island parity of offset-charge sensitive transmon qubits can be distinguished [286, 313]. As the difference between the transmon frequencies of both doublet states is small, inducing a sizeable dispersive shift larger than the resonator's linewidth requires us to tune the spin-dependent transmon qubit frequency close to that of the resonator [Fig. 6.10(a-b)]. Having done so, we can observe the spin-flip transition directly with conventional two-tone spectroscopy, where the first tone is applied at the frequency of the readout resonator, and the second tone at the spin-flip frequency [Fig. 6.10(c)]. The transmon, off-resonant from both tones, remains in its ground state during the measurement.

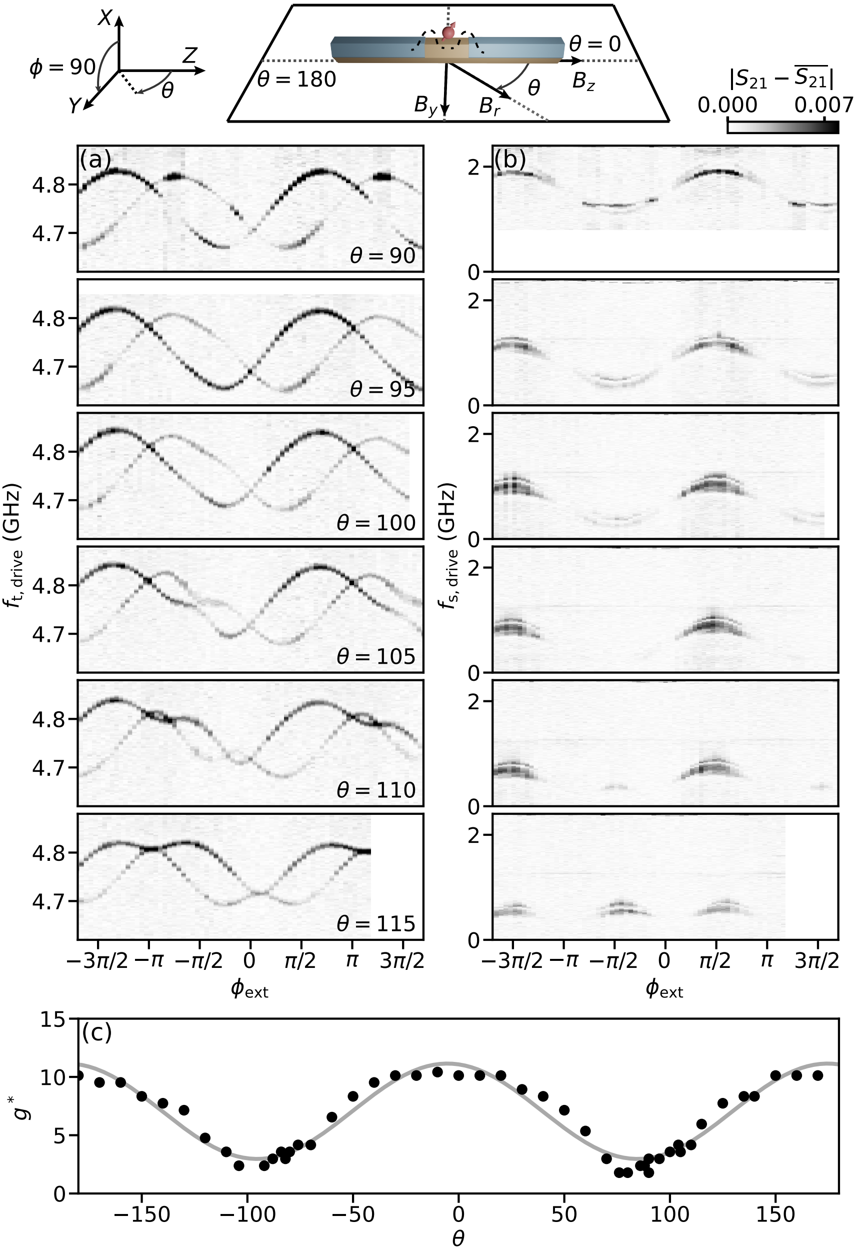

Figure 6.16: **Magnetic field angle dependence of resonance A.** (a-b) Flux dependence of transmon (left column) and spin-flip (right column) transitions for different magnetic field directions, for a fixed total magnetic field $B_r = 12\,\mathrm{mT}$. Each row corresponds to a different magnetic field orientation on the chip plane, $\phi = 90$, determined by the angle θ with respect to the nanowire direction (see diagram at the top). All panels share the same color bar. (c) Effective Landé g-factor g^* versus θ. Markers show data extracted from spin-flip spectroscopy at 12 mT, and the solid line shows a fit with a cosine.

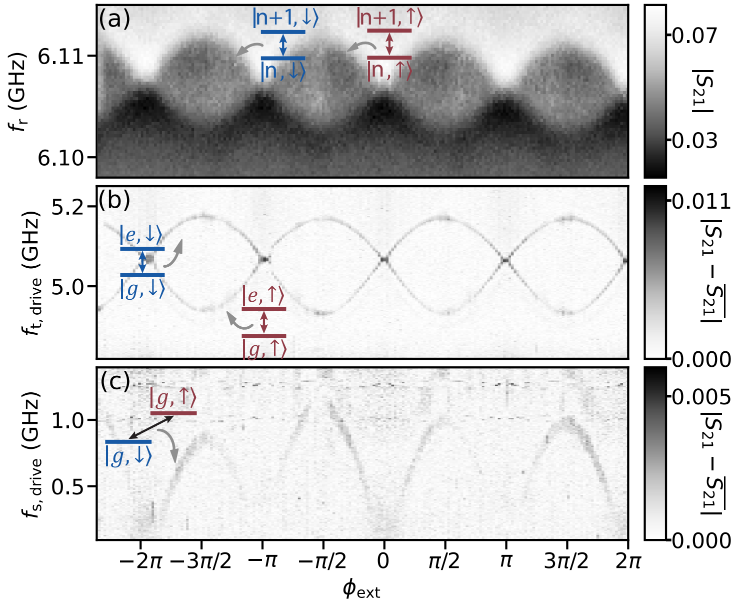

Figure 6.17: **Spin-flip two-tone spectroscopy.** (a) Flux dependence of single-tone spectroscopy showing the resonator frequency. Each of the two visible branches corresponds to a different spin state of the quantum dot junction. (b) Flux dependence of two-tone spectroscopy showing the transmon frequency. The continuous lines denote the two transmon branches corresponding to the two possible spin states of the quantum dot junction. They are the result from the same fit as in Fig. 6.14. (c) Flux dependence of two-tone spectroscopy showing the spin-flip frequency. The continuous line denotes the spin-flip transition frequency obtained from the same fit as in Fig. 6.14.

7

DIRECT MANIPULATION OF A SUPERCONDUCTING SPIN QUBIT STRONGLY COUPLED TO A TRANSMON QUBIT

Spin qubits in semiconductors are currently one of the most promising architectures for quantum computing. However, they face challenges in realizing multi-qubit interactions over extended distances. Superconducting spin qubits provide a promising alternative by encoding a qubit in the spin degree of freedom of an Andreev level. Such an Andreev spin qubit could leverage the advantages of circuit quantum electrodynamics, enabled by an intrinsic spin-supercurrent coupling. The first realization of an Andreev spin qubit encoded the qubit in the excited states of a semiconducting weak-link, leading to frequent decay out of the computational subspace. Additionally, rapid qubit manipulation was hindered by the need for indirect Raman transitions. Here, we exploit an electrostatically-defined quantum dot Josephson junction with large charging energy, which leads to a spin-split doublet ground state. Additionally, we use a magnetic field to tune the qubit frequency over a frequency range of 10 GHz and to investigate the qubit performance using direct spin manipulation. Using an all-electric microwave drive we achieve Rabi frequencies exceeding 200 MHz. We furthermore embed the Andreev spin qubit in a superconducting transmon qubit, demonstrating strong coherent qubit-qubit coupling. These results are a crucial step towards a hybrid architecture that combines the beneficial aspects of both superconducting and semiconductor qubits.

The work in this chapter has been published as: M. Pita-Vidal*, A. Bargerbos*, R. Žitko, L.J. Splitthoff, L. Grünhaupt, J.J. Wesdorp, Y. Liu, L.P. Kouwenhoven, R. Aguado, B. van Heck, A. Kou, and C.K. Andersen, Direct manipulation of a superconducting spin qubit strongly coupled to a transmon qubit, arXiv e-prints 2208.10094 (2022). The asterisk indicates authors that contributed equally to this work.

7.1. INTRODUCTION

Spin qubits in semiconductors [116, 200] and transmon qubits in superconducting circuits [162] are currently two of the most promising platforms for quantum computing. Spin qubits are promising from a scalability standpoint due to their small footprint and compatibility with industrial semiconductor processing [356]. However, despite encouraging progress in recent years [36, 119, 179, 222, 273], spin qubit architectures face challenges in realizing multi-qubit interactions over extended distances. Transmon-based circuits currently boast some of the largest numbers of qubits on a single device [13, 133], and are readily controlled, read out, and coupled over long distances due to the use of circuit quantum electrodynamics (QED) techniques [33, 35, 324]. However, transmon qubits have a small anharmonicity, limiting the speed of qubit operations, and they are relatively large (typically 0.01 to 1 mm^2 per qubit), which leads to large chip sizes and makes transmons susceptible to cross-coupling with distant control elements.

A potential route to leverage the benefits of both superconducting qubits and spin qubits is to encode a qubit in the spin degree of freedom of a quasi-particle occupying an Andreev bound state in a Josephson junction [59, 234]. These states are confined by Andreev reflections at the superconducting interfaces and, thus, are localized in a small and well-defined region, similarly to conventional spin qubits. Furthermore, in the presence of spin-orbit interaction (SOI), the supercurrent across the Josephson junction becomes spin-dependent [31, 59], which allows for interfacing with superconducting circuit elements. Such a superconducting spin qubit has recently been realized in the weak link of a superconductor-semiconductor hybrid nanowire [123], where it was named the Andreev spin qubit (ASQ). This first implementation showed that an ASQ can be efficiently read out using standard circuit QED techniques. However, qubit control was hindered by frequent leakage out of the computational subspace of the qubit, formed by higher energy Andreev levels of the junction. Additionally, due to the selection rules of the system in the absence of a magnetic field [237], direct driving of the ASQ is partly suppressed [221] and qubit manipulation may require virtual driving of auxiliary states to induce qubit transitions [123].

In this work, we utilize previous insights from semiconducting spin-orbit qubits (SOQ) [227, 231] to construct an ASQ using a quantum dot within a Josephson junction, building on the work of chapters 5 and 6. To enhance the confinement of the quantum dot, we implement it in a Josephson junction shorter than that from Ref. [123] and we use three electrostatic bottom gates. These two features lead to an enhanced charging energy of the dot compared to that in previous implementations of Andreev spin qubits, such that it can be exploited to deterministically prepare the quantum dot into a doublet phase with well-defined spin-split states; see chapter 6. As a consequence, the computational subspace of the qubit is now formed by the lowest energy states of the junction in the doublet phase. Moreover, this charging energy enhances the parity lifetime of the doublet subspace to the millisecond regime, therefore providing protection against leakage resulting from parity switches of the junction [234]. Furthermore, this design allows for fast and direct qubit control through spin-orbit mediated electric dipole spin resonance (EDSR) [107, 227, 231, 317]. We additionally demonstrate the magnetic field tunability of the qubit transition frequency over a frequency range of more than 10 GHz, pushing the device into a parameter regime inaccessible to previous experiments, which allows us to investigate the origin of dephasing. At elevated qubit frequencies, this moreover results in a suppression of the population of the excited state, facilitating qubit manipulation and readout without any additional steps needed for initialization of the qubit beyond the qubit relaxation. Finally, the intrinsic coupling between the spin degree of freedom and the supercurrent facilitates strong coherent coupling between the ASQ and a transmon qubit.

7.2. ANDREEV SPIN QUBIT

We implement the ASQ in a quantum dot Josephson junction formed in a hybrid InAs/Al semiconducting-superconducting nanowire, see Fig. 7.1(a). The quantum dot is electrostatically defined by three gate electrodes under an uncovered InAs section of the nanowire and tunnel-coupled to the superconducting segments (see chapter 5). In the limit of weak coupling between the superconducting part of the nanowire and the quantum dot, and in the presence of a magnetic field, the ASQ can be described by the effective Hamiltonian

$$H_s = E_0 \cos(\phi) - E_{SO}\, \vec{\sigma} \cdot \vec{n} \sin(\phi) + \frac{1}{2} \vec{E}_Z \cdot \vec{\sigma}, \tag{7.1}$$

where ϕ is the phase difference across the junction, $\vec{\sigma}$ is the spin operator, $\vec{n}$ is a unit vector along the zero-field spin-polarization direction, set by the SOI, and $\vec{E}_Z$ is a Zeeman field arising in the presence of an external magnetic field. E_0 denotes the effective Josephson energy of the quantum dot junction, common for both spin states. We note that the the term proportional to E_0 has a minimum at $\phi = \pi$, originating from the odd occupancy of the junction. In turn, E_{SO} denotes the spin-dependent contribution to the energy of the junction. It originates from the occurrence of electron co-tunneling accompanied by a spin flip, and it is finite only if SOI is present and multiple levels of the quantum dot are involved in the co-tunneling sequence [234]. The difference between the energies of the $|\downarrow\rangle$ and $|\uparrow\rangle$ eigenstates of Eq. (7.1) determines the ASQ qubit frequency $f_s = E_\uparrow - E_\downarrow$, as depicted in Fig. 7.1(b). For readout and control, we embed the ASQ into a superconducting transmon circuit, as illustrated in Fig. 7.1(c). The transmon circuit consists of a capacitor, with charging energy E_c, shunting a superconducting quantum interference device (SQUID) formed by the parallel combination of a gate-tunable Josephson junction with Josephson energy E_J, and the quantum dot Josephson junction hosting the ASQ. We operate in the regime $E_J/\sqrt{E_0^2 + E_{SO}^2} > 20$ so that the phase difference ϕ across the quantum dot Josephson junction can be controlled through the magnetic flux through the SQUID loop $\Phi_{ext} = \phi_{ext}\Phi_0/(2\pi)$, where $\Phi_0 = h/2e$ is the magnetic flux quantum. Due to the presence of the E_{SO} term, the transmon frequency f_t becomes spin-dependent. We exploit this fact to readout the ASQ state by capacitively coupling the transmon circuit to a readout resonator. Due to the transmon-resonator dispersive coupling, the resonator frequency in turn becomes spin-dependent and probing the readout resonator therefore leads to a spin-dependent response. Spectroscopy of the spinful Andreev levels can, thus, be performed using standard two-tone circuit QED techniques (see Fig. 6.17). Finally, the spin-flipping qubit transition can be directly driven, while maintaining the transmon in its ground state, by applying a microwave tone on the central quantum dot gate [221, 333]. Such microwave drive allows for all-electrical manipulation through EDSR [227, 231]. For further details about the device

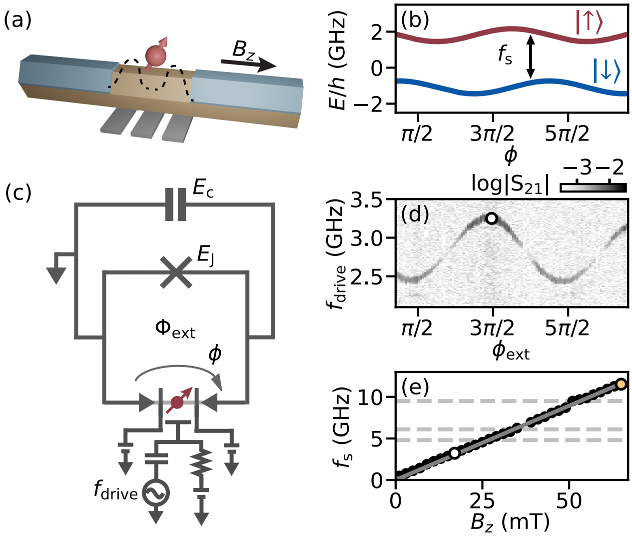

Figure 7.1: (a) Schematic depiction of an Andreev spin qubit in a hybrid superconductor-semiconductor nanowire. The qubit is formed in a gate-defined quantum dot with an odd number of electrons and is coupled to superconducting leads. The dashed line is a sketch of the potential landscape created by the gates. (b) Eigenenergies of the Andreev spin qubit levels as a function of the phase difference ϕ, as described by the effective model of Eq. 7.1. The frequency of the qubit spin-flip transition $|\downarrow\rangle \leftrightarrow |\uparrow\rangle$ is denoted by f_s. In this panel the component of the Zeeman energy parallel to the zero-field spin-polarization direction is $E_Z^{\parallel} = 2.9\,\text{GHz}$. (c) Circuit model of the Andreev spin qubit embedded in a transmon circuit. The spin state is manipulated by a microwave drive, at frequency f_{drive}, applied to the central gate electrode. The transmon island, with charging energy E_c, is connected to ground by a SQUID formed by the parallel combination of the ASQ and a reference Josephson junction. Here, ϕ denotes the superconducting phase difference across the quantum dot junction, while Φ_{ext} is the externally applied magnetic flux through the SQUID loop. (d) Transmission through the readout circuit as a function of the external flux and the applied drive frequency, measured at a magnetic field $B_z = 17\,\text{mT}$ parallel to the nanowire (see Fig. 7.5). (e) Extracted qubit frequency f_s versus B_z (markers), measured at $\phi_{ext} = 3\pi/2$. The data is fitted with a linear dependence (solid line), resulting in an effective Landé g-factor of $g^* = 12.7 \pm 0.2$. Horizontal dashed lines denote the first and second transmon frequencies, as well as the readout resonator frequency.

implementation and setup, see the Supplementary Information in Sec. 7.6.

Following the gate-tuning strategy described in chapter 5, we prepare the quantum dot junction in a regime where it is occupied by an odd number of electrons, with $E_0/h = 211\,\text{MHz}$ and $E_{SO}/h = 305\,\text{MHz}$ and with a parity lifetime of 2.8 ms. In this regime, the qubit states $|\uparrow\rangle$ and $|\downarrow\rangle$ are the lowest energy levels of the system, and the qubit subspace is separated from higher lying states by a frequency gap of at least 20 GHz (see Supplementary Materials). After fixing the gate voltages of the quantum dot, we investigate the tunability of the spin-flip transition f_s by applying a microwave tone at frequency f_{drive} and performing dispersive readout of the transmon qubit. As shown in Fig. 6.1(d), we can finely control f_s by applying a magnetic flux through the SQUID loop [1], although

---

[1] We attribute the shift of the minima and maxima of the spin-flip frequency away from $\pi/2$ and $3\pi/2$ to the phase-dependent renormalization of the impurity g-factor by coupling to the leads, known as the impurity Knight shift [240].

the visibility of the measurement signal is reduced around $\phi_{\text{ext}} = 0, \pi$, where the spin-dependent transmon frequencies are degenerate. By applying an external magnetic field along the nanowire B_z of up to 65 mT, the qubit frequency can be varied from 250 MHz to 12 GHz, see Fig. 6.1(e). The magnetic field direction is chosen to maximize the magnetic field compatibility of the Al shell of the nanowire and is generally not aligned with the spin-orbit direction $\vec{n}$ [115].

7.3. QUBIT COHERENCE

To perform coherent manipulation of the spin states we fix $B_z = 65$ mT and $\phi_{\text{ext}} = 3\pi/2$, setting $f_s = 11.5$ GHz, where the residual population of the excited state is suppressed to less than 5 %, facilitating qubit manipulation and readout (see Fig. 7.10). We observe Rabi oscillations between the qubit states $|\uparrow\rangle$ and $|\downarrow\rangle$ by applying a Gaussian microwave pulse with a carrier frequency at the spin-flip transition frequency $f_{\text{drive}} = f_s$, see Fig. 7.2. Here, the Gaussian pulses are truncated so that the total pulse length is 2.5 times the Gaussian full width at half maximum (FWHM). As shown in Fig. 7.2(a), we resolve up to 10 oscillations by varying the amplitude and duration of the pulse envelope. The population transfer between the spin states, as measured by the dispersive readout scheme, follows the expected time-dependence of a standard Rabi oscillation, as shown in Fig. 7.2(b), from which we extract the Rabi frequency for each pulse amplitude. For a fixed Rabi frequency, we calibrate the FWHM needed for π and $\pi/2$ pulses for single qubit manipulation.

In contrast to previous approaches to implementing Andreev spin qubits, we drive the qubit transition directly and do not rely on auxiliary energy levels in the junction [52, 123]. This is motivated by recent work by our group, indicating that spin-flip transitions of Andreev bound states can be activated by a magnetic field; see Ref. [333] and chapter 6.

As expected for a two-level system, the Rabi frequency is linear over a wide range of pulse amplitudes. It only starts to deviate from this linear dependence for strong drive amplitudes, see Fig. 7.2(c). This deviation is due to saturation of the maximum power provided by the room-temperature electronics. We measure Rabi frequencies larger than 200 MHz, exceeding the largest Rabi frequencies achieved in SOQ [317] and more than an order of magnitude faster than previous results for the ASQ [123]. We observe that the Rabi frequency is approaching the anharmonicity of typical transmon qubits, with no indications of higher order levels being driven. The two-level nature of the ASQ thus intrinsically supports faster single qubit gates than standard transmon qubits [332].

Next, we characterize the lifetime of the ASQ by applying a π pulse and reading out the qubit state after a delay time τ. We obtain an exponential decay with a characteristic time $T_1 = 24.4 \pm 0.5\,\mu$s at $B_z = 65$ mT, see Fig. 7.3(a). As a function of magnetic field, T_1 varies between 10 and 40 μs for qubit frequencies above the transmon frequency. We conjecture that the observed lifetime is limited by Purcell-like decay from coupling to the transmon, given the short transmon lifetime of around 250 ns. For B_z closer to zero, T_1 drops down to around 1 μs (see Fig. 7.13). This is in contrast to the near-zero-field lifetimes found in previous ASQ experiments [123, 124], which were in the range of 10 – −50 μs. The cause of this discrepancy is unknown, but a potential reason is an enhanced resonant exchange with the nuclear spins in InAs due to stronger strain in the nanowire,

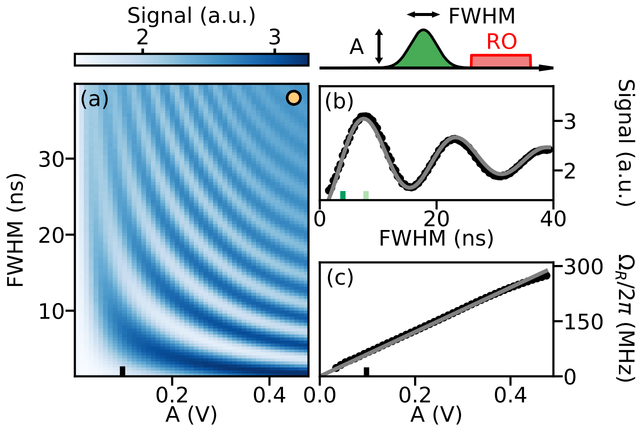

Figure 7.2: Coherent manipulation of the Andreev spin qubit for $f_\mathrm{S} = 11.5\,\mathrm{GHz}$ at $B_z = 65\,\mathrm{mT}$. (a) Rabi oscillations for a range of Gaussian pulses characterized by their amplitude A at the waveform generator output and their full width at half maximum (FWHM), see pulse sequence. As also indicated in the pulse sequence, the Rabi pulse is immediately followed by a readout (RO) pulse (red, not to scale). (b) Rabi oscillation corresponding to $A = 0.1\,\mathrm{V}$, fit with $a\cos(t\Omega_R)\exp(\mathrm{t}/\mathrm{t_d})$ (solid line). The fit yields a decay time $t_\mathrm{d} = 27\,\mathrm{ns}$. (c) Extracted Rabi frequencies versus pulse amplitude, fit with a linear equation (solid line).

which may vary for different nanowires depending on the exact growth conditions [303].

To characterize the coherence time of the qubit, we apply two $\pi/2$ pulses separated by a delay time, after which we read out the qubit state. From this experiment we extract a Ramsey coherence time of $T_{2\mathrm{R}} = 11 \pm 1\,\mathrm{ns}$, see Fig. 7.3(b), much smaller than T_1, and thus indicative of strong dephasing. Dephasing that originates from slow noise compared to the spin dynamics can be partially cancelled using a Hahn-echo sequence [114], which introduces a π pulse halfway between the two $\pi/2$ pulses. This echo sequence increases the measured coherence time by more than three times, to $T_{2\mathrm{E}} = 37 \pm 4\,\mathrm{ns}$, see Fig. 7.3(c).

The coherence time of the qubit can be further enhanced by using dynamical-decoupling pulse sequences, which serve to filter out faster environmental fluctuations. We apply Carr–Purcell (CP) sequences [22, 48, 50], interleaving a varying number of equidistant π pulses, n_π, in between two $\pi/2$ pulses. As n_π increases, higher frequency noise is cancelled out, extending the decoherence times. We reach T_2 times up to more than 90 ns for $n_\pi = 7$, at which stage we are most likely limited by decoherence during the π pulses, see Fig. 7.3(d). We subsequently fit the n_π dependence of T_2 with a power law $T_2(n_\pi) \propto n_\pi^\gamma$. Assuming a noise power spectral density of the form $f^{1/\beta}$, we expect the relation $\beta = \gamma/(1-\gamma)$ [48, 65, 216]. The observed scaling with $\gamma = 0.47 \pm 0.1$ therefore suggests that the decoherence is governed by noise with a $1/f$ spectral density in the frequency range 25 to 100 MHz.

There are several potential sources of dephasing that are compatible with a $1/f$ noise spectral density, such as flux noise through the SQUID loop and charge noise [41, 282]. We exclude the former, as we do not observe an increase of coherence times at the flux sweet spots (see Fig. 7.15). Similarly, no consistent trend is observed when varying the gate voltages, nor when increasing the magnetic field strength. The latter indi-

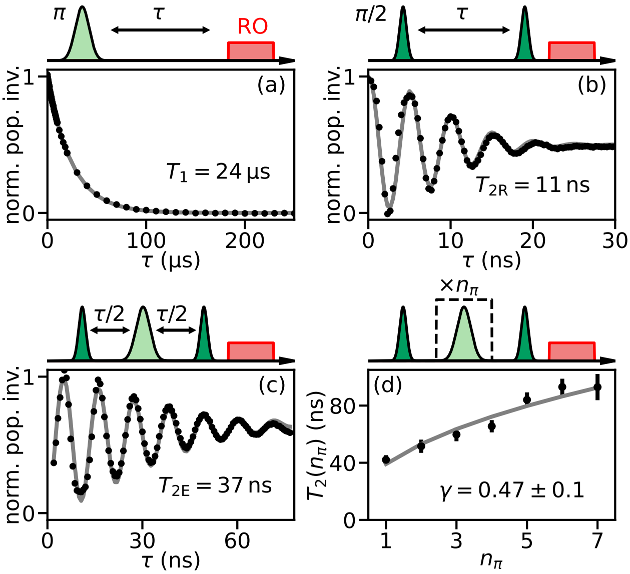

Figure 7.3: Coherence of the Andreev spin qubit at the same setpoint as Fig. 7.2. (a) Qubit lifetime, (b) Ramsey, (c) Hahn-echo and (d) CPMG experiments. Solid lines indicate fits to the data. For (b-d) oscillations are introduced into the decay by adding a phase proportional to the delay time for the final $\pi/2$-pulse. The data of (a-c) is obtained using a π-pulse ($\pi/2$-pulse) of FWHM = 8 ns (4 ns), while for (d) this is 4 ns (2 ns). For (a-c) we plot the normalized population inversion, where each sub-panel is individually normalized to the resulting fit.

cates that charge noise is likely not the dominant contributor to dephasing, given that EDSR becomes more effective at coupling charge noise to the qubit at elevated fields [107, 227, 231, 317]. Additionally, based on the evolution of the Rabi decay time with increasing pulse amplitudes [205], the size of the charge fluctuations required to cause the observed amount of dephasing is estimated to be 0.25 mV, significantly larger than what is expected to originate from the gate lines (see Fig. 7.17). However, the contribution of charge fluctuations originating elsewhere, such as in the dielectric material on the device, could still be contributing to the dephasing. Given that the sensitivity to fluctuations in environmental offset charge on the transmon island is suppressed by the large $E_J/E_c > 30$ ratio, it is furthermore unlikely that the ASQ dephasing originates from offset-charge-dependent fluctuations of the transmon frequency qubit [162].

Another potential source of dephasing originates from the dynamics of the spinful nuclei in the nanowire, which may couple to the ASQ as a result of the hyperfine interaction. It has previously been shown that these dynamics can lead to longitudinal Overhauser field fluctuations with a $1/f$ spectral density [204]. Moreover, this effect is expected to be particularly strong in InAs due to the large nuclear spin of indium ($I = 9/2$) and should not be strongly affected by magnetic field in the B_z range investigated here, which is not enough to polarize the nuclear spins. Corroborated by the fact that the extracted T_{2R} and T_{2E} times are strikingly similar to those found for the weak-link InAs ASQ [123], the InAs SOQ [227] and the InSb SOQ [317], we conjecture that the nuclear environment provides a significant contribution to the decoherence of the ASQ.

7.4. ASQ-TRANSMON COUPLING

One of the main characteristics of the ASQ is the intrinsic coupling between the spin degree of freedom and the supercurrent across the quantum dot Josephson junction. We have so far only exploited this coupling for read-out of the qubit state using circuit QED techniques. Now, we demonstrate the observation of coherent coupling of the ASQ with the transmon qubit.

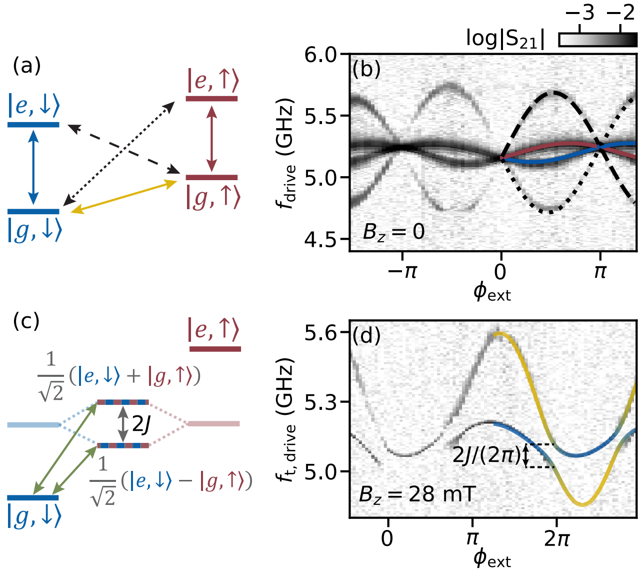

Figure 7.4: Coherent ASQ-transmon coupling. (a) Frequency diagram of the joint ASQ-transmon circuit of Fig. 7.1(c) at large detuning between ASQ and transmon qubit energy levels. In addition to the two spin-conserving transmon transitions (solid red and blue) and the transmon-conserving spin qubit transition (solid yellow), two additional transitions involving both qubits can take place in the presence of coherent coupling between them (dashed and dotted black). (b) Two-tone spectroscopy of the joint two-qubit system at $B_z = 0$. In addition to the two spin-dependent branches of the transmon qubit frequency, two additional transitions appear. Overlaid are transition frequencies obtained from the model of Eq 7.2. (c) Frequency diagram of the joint ASQ-transmon circuit for $|e,\downarrow\rangle = |g,\uparrow\rangle$. In the presence of coherent coupling, the two qubits hybridize into states with a frequency splitting of $2J$. Green arrows denote the transitions from ground to the two hybridized states. (d) Two-tone spectroscopy versus external flux at $B_z = 28\,\mathrm{mT}$, where $f_\mathrm{s} \approx f_\mathrm{t}$. This results in avoided crossings between the two qubit frequencies. Overlaid are the transition frequencies obtained from the model of Eq. 7.2. Their colors denote the expectation value of the spin degree of freedom of the excited state and go from $|\downarrow\rangle$ (blue) for the transmon transition to $|\uparrow\rangle$ (yellow) for the spin-flip transition. $f_\mathrm{t,drive}$ denotes the frequency of the second tone, sent through the readout resonator.

A first signature of a coherent coupling is the presence of transitions that involve both qubits, in addition to the single-qubit transitions, see Fig. 7.4(a). At zero applied magnetic field, we spectroscopically detect two of such transitions at $f_\mathrm{t} + f_\mathrm{s}$ and $f_\mathrm{t} - f_\mathrm{s}$, where f_t is the transmon frequency, see Fig. 7.4(b). We classify them based on a fit with the joint Hamiltonian of the total ASQ-transmon circuit of Fig. 7.1(c), given by

$$H_\mathrm{tot} = -4E_\mathrm{c}\partial_\phi^2 - E_\mathrm{J}\cos\left(\phi - \phi_\mathrm{ext}\right) + H_\mathrm{s}(\phi). \tag{7.2}$$

We identify the additional observed resonances as the double excitation $|g\downarrow\rangle \leftrightarrow |e\uparrow\rangle$ and the $|g\uparrow\rangle \leftrightarrow |e\downarrow\rangle$ SWAP transitions, where $|g\rangle$ and $|e\rangle$ denote the ground and first excited transmon states, respectively. These transitions could be used to construct entanglement and two qubit gates between the two different qubit platforms, provided the transitions can be driven at a faster rate than the decoherence rates of either qubit.

Additionally, one of the hallmarks of strong coherent coupling is the appearance of an avoided level crossing when both qubit frequencies are made equal, $f_\mathrm{t} \approx f_\mathrm{s}$. In this case the $|e,\downarrow\rangle$ and $|g,\uparrow\rangle$ states are expected to hybridize into superposition states with a frequency splitting of $2J$, see Fig. 7.4(c). At $B_z = 28\,\mathrm{mT}$ this splitting can be readily observed in the experiment. By varying the external flux ϕ_ext such that the ASQ frequency f_s crosses the transmon frequency f_t, we find avoided crossings with a minimum frequency splitting $2J/(2\pi) = 2\times 52$ MHz, as shown in Fig. 7.4(d). As J is four times larger than the decoherence rate of the ASQ, $1/T_{2\mathrm{R}} \approx 14\times 2\pi\,\mathrm{MHz}$ and one order of magnitude larger than the decoherence rate of the transmon, $\approx 1.2\times 2\pi\,\mathrm{MHz}$, the coupling between the two qubits falls into the strong coupling regime. This result establishes the first realization of a direct strong coupling between a spin qubit and a superconducting qubit, in contrast to the results of Ref. [180], where a high-impedance bus resonator was required to mediate the coupling between spin and transmon qubit through virtual photons.

Analytical estimates predict that the coupling $J \propto E_\mathrm{SO}\phi_\mathrm{zpf}\sin(\theta)$, where ϕ_zpf is the magnitude of zero-point fluctuation of the transmon phase, and θ is the angle between the Zeeman field and the spin-orbit direction; see Sec. 7.6. This suggests that by choosing a resonance with a larger E_SO and by aligning the magnetic field perpendicular to the spin-orbit direction, coupling rates of hundreds of MHz can be achieved, which would enable rapid two-qubit gates between the transmon and the ASQ and potentially allow for the study of light-matter interactions in the ultrastrong coupling regime [95, 278].

7.5. TOWARDS NEW PLATFORMS AND MULTIPLE ASQ

We have implemented an Andreev spin qubit, where the the spin degree of freedom of a quasi-particle in a quantum dot with superconducting leads encodes the qubit state. The qubit subspace is stabilized by the charging energy of the quantum dot and direct microwave driving of the transitions is possible without the requirement of auxiliary levels. The qubit coherence was found to be comparable to previous results for qubits implemented in InAs or InSb nanowires [123, 227, 317]. Our results suggest that the nuclear environment contributes strongly to the ASQ decoherence, although the contribution of charge noise can not be fully neglected. This limitation motivates future investigation of alternative material platforms for ASQs, such as superconductor-proximitized nuclear-spin-free semiconductors [71], e.g. isotopically purified germanium [128, 277, 311].

We furthermore observed direct strong coherent coupling between the ASQ and a transmon qubit. Such strong coupling showcases the advantage of the intrinsic spin-supercurrent coupling, allowing the ASQ to be readily integrated into a circuit QED architecture. Our results open avenues towards multi-qubit devices: we propose to leverage the fact that transmon qubits can be readily coupled together using capacitive coupling, useful for mediating interactions between multiple ASQ. Furthermore, our results are a crucial step towards the coupling of distant Andreev spin qubits through bus resonators or a shared inductance [234], as well as short-distance coupling through wavefunction overlap [297].

7.6. SUPPLEMENTARY INFORMATION

MODELING OF JOINT ASQ-TRANSMON SYSTEM

NUMERICAL DIAGONALIZATION

In order to obtain the transition frequencies of the joint ASQ-transmon system, we combine the Hamiltonian of the ASQ [Eq. (7.1) in the main text] with the Hamiltonian of the transmon, as indicated in Eq. (7.2) of the main text. This combined Hamiltonian is numerically diagonalized in the phase basis following the procedure in Ref. [169] and chapter 4. This results in the transmon and ASQ energy levels E_n, as well as the associated transition frequencies $f_{nm} = (E_m - E_n)/h$. These frequencies are used in Figs. 6.1 and 7.4 to fit the spectroscopy measurements.

ESTIMATE OF QUBIT-QUBIT COUPLING STRENGTH

As demonstrated in Fig. 7.4, we observe avoided crossings between the transmon and the ASQ transitions, which is indicative of strong coherent coupling. In this section we derive how the coupling strength depends on the model parameters.

We start by combining Eq. (7.1) and (7.2) of the main text into the effective Hamiltonian

$$H_{\rm tot} = H_{\rm tmon} + H_{\rm Z} + H_{\rm coupling}, \tag{7.3}$$

with the individual terms given as

$$H_{\rm tmon} = -4E_{\rm c}\partial_\phi^2 - E_{\rm J}\cos(\phi) - E_0\cos\left(\phi - \phi_{\rm ext}\right), \tag{7.4}$$

$$H_{\rm Z} = \frac{1}{2}\begin{pmatrix} E_{\rm Z}^{\perp} & E_{\rm Z}^{\parallel} \\ E_{\rm Z}^{\parallel} & -E_{\rm Z}^{\perp}\end{pmatrix} = \frac{|\vec{E}_{\rm Z}|}{2}\begin{pmatrix}\sin(\theta) & \cos(\theta) \\ \cos(\theta) & -\sin(\theta)\end{pmatrix} \tag{7.5}$$

$$H_{\rm coupling} = -E_{\rm SO}\sin(\phi - \phi_{\rm ext})\sigma_x. \tag{7.6}$$

Here, σ_x is the x Pauli matrix and θ is the angle between the Zeeman field $\vec{E}_{\rm Z}$ and the spin-orbit direction, such that $E_{\rm Z}^{\parallel} = |\vec{E}_{\rm Z}|\cos\theta$ and $E_{\rm Z}^{\perp} = |\vec{E}_{\rm Z}|\sin\theta$. Next, we write the coupling term $H_{\rm coupling}$ in the eigenbasis of $H_{\rm Z}$, which is given by the states

$$|v_1\rangle = [\cos(\theta/2), \sin(\theta/2)], \; |v_2\rangle = [-\sin(\theta/2), \cos(\theta/2)]. \tag{7.7}$$

We identify that

$$\langle v_1|\sigma_x|v_2\rangle = \langle v_2|\sigma_x|v_1\rangle = \cos\theta \tag{7.8}$$

and

$$\langle v_1|\sigma_x|v_1\rangle = -\langle v_2|\sigma_x|v_2\rangle = \sin\theta, \tag{7.9}$$

such that σ_x becomes $\cos(\theta)\sigma_{\overline{x}} + \sin(\theta)\sigma_{\overline{z}}$ in the $\{|v_1\rangle, |v_2\rangle\}$ spin basis.

We rewrite $H_{\rm coupling}$ and expand to first order in ϕ, valid in the transmon limit $E_{\rm J} \gg E_{\rm c}$, where $\langle\phi\rangle \ll 1$, which results in

$$\begin{aligned} H_{\rm coupling} &= E_{\rm SO}\left[\cos(\phi)\sin(\phi_{\rm ext}) - \cos(\phi_{\rm ext})\sin(\phi)\right]\sigma_x \qquad (7.10)\\ &\approx E_{\rm SO}\left[\sin(\phi_{\rm ext}) - \phi\cos(\phi_{\rm ext})\right]\sigma_x. \qquad (7.11)\end{aligned}$$

Therefore, in the spin eigenbasis, we obtain

$$H_{\text{coupling}} \approx E_{\text{SO}} \left[\sin(\phi_{\text{ext}}) - \phi \cos(\phi_{\text{ext}})\right] \left[\cos(\theta)\sigma_{\overline{x}} + \sin(\theta)\sigma_{\overline{z}}\right]. \tag{7.12}$$

This term of the Hamiltonian couples the ASQ to the transmon via the phase operator ϕ of the transmon and is, thus, reminiscent of a dipole coupling. In the transmon regime, we can express the operator ϕ in terms of the zero point fluctuations of the phase, ϕ_{zpf}, and the bosonic creation and annihilation transmon operators, $c^\dagger$ and c respectively: $\phi = \phi_{\text{zpf}}\left(c^\dagger + c\right)$. Inserting this operator into Eq. (7.12), we obtain

$$\begin{aligned} H_{\text{coupling}} &\approx \left[E_{\text{SO}} \sin(\phi_{\text{ext}}) - E_{\text{SO}}\phi_{\text{zpf}}\left(c^\dagger + c\right)\cos(\phi_{\text{ext}})\right] \left[\cos(\theta)\sigma_{\overline{x}} + \sin(\theta)\sigma_{\overline{z}}\right] && (7.13) \\ &= E_{\text{SO}} \sin(\phi_{\text{ext}}) \left[\cos(\theta)\sigma_{\overline{x}} + \sin(\theta)\sigma_{\overline{z}}\right] + \hbar J_{\overline{x}}\left(c^\dagger + c\right)\sigma_{\overline{x}} + \hbar J_{\overline{z}}\left(c^\dagger + c\right)\sigma_{\overline{z}}. && (7.14) \end{aligned}$$

In this expression, we have the transversal and longitudinal coupling strengths

$$\hbar J_{\overline{x}} = E_{\text{SO}} \cos(\phi_{\text{ext}})\phi_{\text{zpf}} \cos(\theta), \; \hbar J_{\overline{z}} = E_{\text{SO}} \cos(\phi_{\text{ext}})\phi_{\text{zpf}} \sin(\theta). \tag{7.15}$$

From fitting the spectroscopy data we find a charging energy of $E_{\text{c}}/h = 284$ MHz and a Josephson energy of $E_{\text{J}}/h = 13.1$ GHz, which results in $\phi_{\text{zpf}} = [2E_{\text{c}}/E_{\text{J,eff}}(\phi_{\text{ext}})]^{1/4} \leq 0.46$ where

$$E_{\text{J,eff}}(\phi_{\text{ext}}) = (E_{\text{J}} + E_0)\sqrt{\cos^2(\phi_{\text{ext}}) + \left(\frac{E_{\text{J}} - E_0}{E_{\text{J}} + E_0}\right)^2 \sin^2(\phi_{\text{ext}})}. \tag{7.16}$$

For $E_{\text{SO}}/h = 309$ MHz, this results on a transverse coupling of up to $J_{\overline{x}}/(2\pi) = 145$ MHz when $\phi_{\text{ext}} = 0$ and the magnetic field is applied perpendicular to the spin-orbit direction. In the fit of Fig. 7.4 we instead find an avoided crossing of $2J_{\overline{x}}/(2\pi) = 2 \times 52$ MHz, corresponding to a Zeeman field at an angle of $\theta = 35.6°$ with respect to the spin-orbit direction.

DEVICE AND EXPERIMENTAL SETUP

DEVICE OVERVIEW

Fig. 7.5 shows an overview of the device including the different elements forming the superconducting circuit used for readout and control of the qubits. The device under investigation in this work is the same as the one used in chapter 6, where further details about its physical implementation and fabrication can be found.

CRYOGENIC AND ROOM TEMPERATURE MEASUREMENT SETUP

The device was measured in a Triton dilution refrigerator with a base temperature of $\approx 20\,\mathrm{mK}$. Details of the wiring at room and cryogenic temperatures are shown in Fig. 7.6. The setup contains an input radio-frequency (RF) line, an output RF line, an extra RF line for the spin-flip drive tone and multiple direct current (DC) lines, used to tune the electrostatic gate voltages. The DC gate lines are filtered at base temperature with multiple low-pass filters connected in series. The input and drive RF lines contain attenuators and low-pass filters at different temperature stages, as indicated. In turn, the output RF line contains amplifiers at different temperature stages: a travelling wave parametric amplifier (TWPA) at the mixing chamber plate ($\approx 20\,\mathrm{mK}$), a high-electron-mobility transistor (HEMT) amplifier at the $4\,\mathrm{K}$ stage, and an additional amplifier at room temperature. A three-axis vector magnet (x-axis not shown) is thermally anchored to the $4\,\mathrm{K}$ temperature stage, with the device under study mounted at its center. The three magnet coils are controlled with Yokogawa GS610 current sources. At room temperature, a vector network analyzer (VNA) is connected to the input and output RF lines for spectroscopy at frequency f_r. On the input line, this signal is then combined with the IQ-modulated transmon drive tone at frequency $f_\mathrm{t,drive}$. A separate IQ-modulated tone at f_r, only used for time-domain measurements, is also combined onto this line. The IQ-modulated spin-flip drive tone at frequency f_drive is sent through the drive line. For time-domain measurements the output signal is additionally split off into a separate branch and down-converted to be measured with a Quantum Machines OPX.

BASIC CHARACTERIZATION AND TUNE UP

The basic characterization and tune-up of the device proceeds such as detailed in chapter 5, while the specific tune-up of the quantum dot resonance investigated in this device is detailed in the supplement of chapter 6, where it is labeled as resonance A. A brief summary is as follows: We first characterize the gate dependence of the reference junction with the dot fully closed, and fix V_J such that $E_\mathrm{J} \gg \sqrt{E_0^2 + E_\mathrm{SO}^2}$, to ensure the phase drop set by ϕ_ext happens mostly at the quantum dot junction. Furthermore, we choose E_J such that the transmon frequency f_t is close to the readout resonator frequency ≈ 6.11 GHz to obtain a large dispersive shift for two-tone spectroscopy and qubit readout. For the results shown in this work, we used $V_\mathrm{J} = 3860\,\mathrm{mV}$. We then investigate the gate dependence of the quantum dot junction with the reference junction fully closed, determining the pinchoff voltages of the three quantum dot gates. Next, we open the reference junction to its gate set-point and explore the quantum dot junction gate space at both $\phi_\mathrm{ext} = 0$ and $\phi_\mathrm{ext} = \pi$ to identify regions that show a π-shift in phase. For a given π-shifted region, we measure explicit ϕ_ext dependence of the transmon to identify a resonance with a spin splitting comparable to the spin-independent Josephson energy. Finally, we choose a

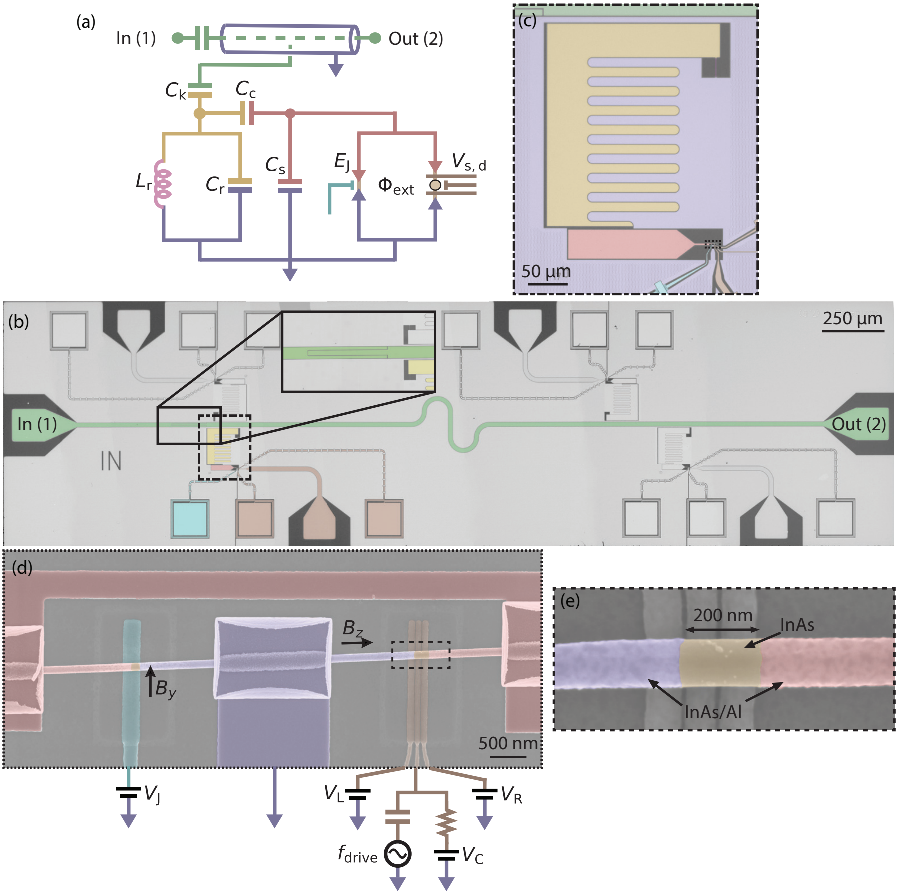

Figure 7.5: **Device overview.** (a) Diagram of the microwave circuit. A coplanar waveguide transmission line with an input capacitor (green center conductor) is capacitively coupled to a grounded LC resonator. The resonator consists of an island (yellow) capacitively and inductively (pink) shunted to ground (blue). The resonator is in turn capacitively coupled to a transmon island (red), which is shunted to ground capacitively as well as via two parallel Josephson junctions. (b) Chip containing four nearly identical devices coupled to the same transmission line, which has a capacitor at its input port, enlarged in the inset. (c) False-colored optical microscope image of the device showing the qubit island, the resonator island, the resonator inductor, the transmission line, the electrostatic gates and ground. (d) False-colored scanning electron micrograph (SEM) of the measured device, showing the InAs/Al nanowire into which the junctions are defined. The B_y component of the magnetic field is used to tune Φ_ext [333]. B_z is the magnetic field component parallel to the nanowire. (e) False-colored SEM of the measured device, showing the junction in which the quantum dot is gate defined. The three bottom gates have a width and spacing of 40 nm, although this is obfuscated by the dielectric layer placed on top.

gate set-point in the selected resonance. For the results shown here, the setpoint chosen for the three quantum dot gates was $V_\mathrm{L} = 363\,\mathrm{mV}$, $V_\mathrm{C} = 1000\,\mathrm{mV}$ and $V_\mathrm{C} = 81\,\mathrm{mV}$, which corresponds to $V_\mathrm{T,A} = -423.6\,\mathrm{mV}$, $V_\mathrm{P,A} = 909.5\,\mathrm{mV}$ in the rotated gate frame shown in Fig. 6.13 of chapter 6.

EXTENDED DATASET

EXTENDED TWO-TONE SPECTROSCOPY DATA

Fig. 7.7 shows extended two-tone spectroscopy measurements at the setpoint of main text Fig. 7.4(b), performed over a range of 20 GHz. It reveals several additional transition frequencies: panels (a) and (b) contain the higher-lying transmon transitions f_{03} and f_{02}, respectively, while panel (c) shows five different transitions. These are the four transitions also shown in Fig. 7.4(b) and, above that, the resonator transition frequency. Panel (d) exhibits two low-frequency transitions: the bright top transition is the direct spin-flip transition with the transmon in its ground state, while the dark lower transition results from the direct spin-flip transition with the transmon in its excited state. The latter transition is visible as a result of a residual excited state population of the transmon. No other auxiliary transitions are found between 0 and 20 GHz, nor does any transition develop for magnetic fields up to 65 mT. We further note that the measurement of panel (d) requires a large drive power (31 dBm more than for the measurement shown in Fig. 6.1 of the main text), and that visibility is reduced compared to panel (c), which is expected since the matrix elements for the EDSR driving is suppressed in the absence of an external magnetic field.

SINGLE SHOT ASSIGNMENT FIDELITY

The time domain measurements in the main text are obtained by averaging over many shots. We now estimate the assignment fidelity of ASQ readout at the setpoint used for the coherence measurements in the main text ($B_z = 65$ mT and $\phi_{\text{ext}} = 3\pi/2$). To do so, we measure the IQ quadrature response of the readout resonator for the qubit prepared in the ground state [Fig. 7.8(a)] and for the qubit prepared in the excited state [Fig. 7.8(b)], after applying an 8-ns π-pulse. In both cases we read out for 500 ns, more than 40 times shorter than T_1, and wait for $5T_1$ between different measurements to let the qubit decay back to its ground state. We find an assignment fidelity of $F = 1 - (P(\downarrow \mid \uparrow) - P(\uparrow \mid \downarrow))/2 = 80\%$ [Fig. 7.8(d)], where $P(a|b)$ denotes the probability of measuring the qubit to be in state a after preparing it in state b. The fidelity is predominantly set by assignment errors for the excited state limited by decoherence during the excitation as the π-pulse duration is comparable to T_2. Longer readout times therefore do not significantly improve the assignment fidelity. However, shorter π pulses would likely lead to improved performance although this experiment was not performed on the current device.

PARITY LIFETIME

One of the advantages of using a quantum dot junction over a semiconducting weak link is that the charging energy of the quantum dot allows us to select an operational setpoint for which the doublet states are the lowest energy states of the system [234]. Therefore, the charging energy is expected to protect against qubit leakage via quasiparticle escape or recombination, which would take the junction outside of the computational space of the qubit. To confirm this protection, we measure the quasiparticle poisoning times of the junction around the gate setpoint used in the main text.

Shown in Fig. 7.9(a), two resonances are visible as the central quantum dot gate V_C is varied around its setpoint $V_C = 1000$ mV, at $\phi_{\text{ext}} = 0$. Following the methods of chapter 5, we identify the outer two V_C regions as having a singlet ground state (spin-zero) and the central region as having a doublet ground state (spin-1/2). For each gate point, we subsequently monitor the transmon circuit in real time and determine the switching time of the quantum dot junction parity. T_s and T_d denote the characteristic times for which the quantum dot maintains a singlet or doublet occupation, respectively. The extracted times are shown in Fig. 7.9(b). Note that this measurement is performed at $\phi_\mathrm{ext} = 0$, where the $|\uparrow\rangle$ and $|\downarrow\rangle$ states result in equal transmon frequencies, thus becoming indistinguishable using our readout scheme. The spin-flip times T_spin are therefore not resolved here, as opposed to the experiments of Ref. [124].

We observe that, for the outer two regions, where the ground state is the spin-0 state, the doublet switching time T_d ranges from a few µs to hundreds of µs, but is always much shorter than the singlet switching time T_s. Close to the singlet-doublet ground state transition, both times become similar and of the order of 1 ms, which can be seen in Fig. 7.9(c) for $V_\mathrm{C} = 996$ mV, where the histogram of a continuous time trace, integrated in time bins of $t_\mathrm{int} = 4.3$ µs, shows two Gaussians with equal amplitudes. In the central region, where the doublet states are the lowest energy states, the situation is reversed and, away from the singlet-doublet transition, T_d is consistently above 1 ms. The imbalance between average singlet and doublet occupation is shown in Fig. 7.9(d) for the setpoint used in the main text, $V_\mathrm{C} = 1000$ mV. In this case we measure $T_\mathrm{s} = 59$ µs and $T_\mathrm{d} = 2.8$ ms. The latter is much larger than that of weak-link junctions, typically found to be in the range 10-500 µs [122–124, 136, 334], and thus demonstrates the advantage of using a quantum dot junction. In particular, for the weak-link ASQ [123] the authors measured a parity lifetime $T_\mathrm{parity} = 22$ µs and a spin-flip time $T_\mathrm{spin} = 17$ µs, such that the parity lifetime was a relevant limitation to the qubit T_1. In contrast, we find that $T_\mathrm{d} \gg T_1$ such that the lifetime of the ASQ studied in this work is not limited by parity switches.

EXCITED STATE POPULATION

Similar to what is found in previous works investigating the doublet states of SNS junctions [123, 124, 333], we observe that both $|\uparrow\rangle$ and $|\downarrow\rangle$ of the quantum dot junction are occupied at $B_z = 0$ mT, even in the absence of a drive. As such, we observe simultaneously both of the transmon branches corresponding to each spin state [see Fig. 7.4(b)]. We hypothesize that this residual excited state population is the result of excitations of either thermal or non-equilibrium origin, as the maximum zero-field ASQ transition frequency $f_\mathrm{s} \approx 600$ MHz, when expressed in units of temperature ($T_\mathrm{eff} = hf_\mathrm{s}/k_\mathrm{B}$, where k_B is Boltzmann's constant), corresponds to an effective temperature scale of $T_\mathrm{eff} \approx 30$ mK, below the typical electron temperatures found in transport and transmon [139] experiments, 35–100 mK.

To investigate the residual population further, we monitor the transmon circuit in real-time, now at $\phi_\mathrm{ext} = 3\pi/2$ so that we are maximally sensitive to changes in the spin state. At $B_z = 0$ mT, the IQ histogram of 2.5×10^5 sequential measurements confirms the presence of two populated states, as shown in Fig. 7.10(a). From a double Gaussian fit, we extract a ratio of state occupations of $P(\uparrow)/P(\downarrow) = 0.7$. Upon increasing the qubit frequency f_s with the magnetic field B_z, we find that the excited state population is strongly reduced, in line with expectation [Fig. 7.10(d)]. However, the ASQ frequency first crosses the transmon and then the resonator frequencies between 20 and 30 mT, preventing the measurement of the spin states occupancy over a range of frequencies. Measuring again at $B_z = 65\,\mathrm{mT}$, where $f_\mathrm{s} = 11.53\,\mathrm{GHz}$, we find at most 4% remaining excited state population, see Fig. 7.10(b). Here, the remaining excited state population is expected to be predominantly due to assignment errors, similar to those found in Fig. 7.8(a).

To extract the effective temperature of the ASQ, we subsequently fit the frequency dependence of the ratio of populations to a Boltzmann distribution, $P(\uparrow)/P(\downarrow) = \exp\left(-hf_\mathrm{s}/(k_\mathrm{B}T_\mathrm{eff})\right)$, where h and k_B are the Planck and Boltzmann constants, respectively. This leads to reasonable agreement with the data, resulting in an effective temperature of $T_\mathrm{eff} = 100 \pm 8\,\mathrm{mK}$ [see Fig. 7.10(d)].

CP DATA

In this section we provide further data for the CP measurements shown in Fig. 7.3(d) in the main text. As discussed, the CP sequence is constructed as follows: for each n_π, we apply a $\pi/2$-pulse, followed by n_π equidistant π-pulses and a final $\pi/2$-pulse. All pulses are composed of a Gaussian envelope and have a FWHM of 2 ns and 4 ns for the $\pi/2$- and π-pulses, respectively. The separation between the centers of consecutive π-pulses is τ/n_π and the separation between a $\pi/2$ pulse and its nearest π pulse is $\tau/(2n_\pi)$, resulting in a total delay time τ between the center of the two $\pi/2$ pulses. Fig. 7.11 shows CP measurements for n_π values ranging from 2 to 7, accompanied by a fit to the expression

$$a\cos\left(\tau\Omega - \phi\right)\exp\left(-(\tau/T_2)^{d+1}\right) + c + e\tau, \tag{7.17}$$

from which we extract the $T_2(n_\pi)$ values reported in Fig. 7.3(d). Note that the maximum waveform generator output power puts a limit on the minimum delay time τ for which the sequence can be generated, as the Gaussian pulses overlap for short delay times compared to the pulse width. This results in the absence of data for short τ in Fig. 7.11.

TRANSMON QUBIT COHERENCE

We characterize the transmon performance at the flux and gate bias point used in the main text using standard time-domain techniques, see Fig. 7.12.

ASQ COHERENCE VERSUS CONTROL PARAMETERS

In this section we provide additional data showing the dependence of the ASQ lifetime and coherence times on different control parameters. They are extracted by fitting their respective time evolutions using the same expressions employed in Fig. 7.3 of the main text:

$$T_1: \quad a\exp\left(t/T_1\right) + c \tag{7.18}$$

$$T_{2\mathrm{R}}: \quad a\cos\left(t\Omega - \phi\right)\exp\left(-(t/T_{2\mathrm{R}})^{d+1}\right) + c \tag{7.19}$$

$$T_{2\mathrm{E}}: \quad a\cos\left(t\Omega - \phi\right)\exp\left(-(t/T_{2\mathrm{E}})^{d+1}\right) + c + et \tag{7.20}$$

Here, a, c, d, e, ϕ, Γ, T_1, $T_{2\mathrm{R}}$ and $T_{2\mathrm{E}}$ are fit parameters. For $T_{2\mathrm{R}}$ and $T_{2\mathrm{E}}$, Ω accounts for the combination of detuning and the oscillations introduced by adding a phase proportional to the delay time for the final $\pi/2$-pulse.

ASQ LIFETIME VERSUS MAGNETIC FIELD

We start by investigating the evolution of the ASQ lifetime T_1 versus magnetic fields between 0 and 65 mT. As shown in Fig. 7.13(b), the qubit lifetime varies strongly, from around 1 µs close to zero magnetic field and up to 40 µs at intermediate fields, before once-more decreasing to approximately 20 µs. For intermediate magnetic fields between 15 mT and 35 mT, the measurement of the qubit lifetime is hindered by the vicinity to the transmon and resonator transition frequencies. In this region it is not possible to drive the ASQ independently as, due to the capacitance between the gate drive line and the transmon island, the transmon qubit is also excited. This simultaneous driving of both qubits impedes the distinction of the response coming from each of them.

The strong reduction of T_1 at low fields is potentially due to resonant exchange with the nuclear spins in InAs [303]; given the large g-factor of the ASQ, this process only takes places at low magnetic fields. This is supported by the finding that at elevated magnetic fields, in the range 45–50 mT, we find the ASQ lifetime to exceed 40 µs. Further investigation would be needed to determine the origin of the magnetic field dependence of T_1 near zero field. At even higher fields we observe a drop of the lifetime to around 20 µs. As discussed in the main text, we conjecture the ASQ lifetime found in these regimes is limited by Purcell-like decay from coupling to the transmon, given the short transmon lifetime of around 250 ns [Fig. 7.12(b)].

To support the assertion that the reduction in the ASQ lifetime for qubit frequencies in the proximity of the transmon transitions is due to Purcell-like decay, we investigate whether the transmon lifetime is enhanced by proximity to the ASQ. Fig. 7.14 shows the transmon lifetime T_1^{t} for three different detunings between transmon and ASQ. When the qubits are detuned from each other, we measure $T_1^{\mathrm{t}} \approx 250\,\mathrm{ns}$. However, when the transmon is resonant with the ASQ, its lifetime is enhanced by almost factor of two, reaching $470 \pm 5\,\mathrm{ns}$. This is consistent with hybridization of the two qubits, given that $T_1^{\mathrm{s}} \gg T_1^{\mathrm{t}}$, and supports that the lifetime of the ASQ can be decreased by vicinity to the transmon modes. These findings furthermore compliment the the observations discussed surrounding main text Fig. 7.4, serving as an additional signature of coherent coupling.

INDEPENDENCE OF ASQ COHERENCE ON GATE VOLTAGES, MAGNETIC FIELD AND FLUX

We investigate the effect of different sources of noise by measuring the dependence of the $T_{2\mathrm{R}}$ and $T_{2\mathrm{E}}$ coherence times on gate voltage, magnetic field, and flux.

The B_z dependence of coherence times is shown in Fig. 7.15(a), for which we do not observe a measurable dependence over the B_z range investigated. Therefore charge noise is likely not the dominant contribution to qubit dephasing since, if it was the case, an increase in B_z would increase the effectiveness of EDSR at coupling charge noise to the qubit, which would result on a reduction of the decoherence times. In contrast, this B_z-independence of coherence times is compatible with nuclear magnetic noise being a strong contribution to qubit dephasing; due to the small magnetic moment of the nuclei spin, a magnetic fields of 65 mT do not yet lead to a significant nuclear splitting. As a result of this we do not reach the regime of strong nuclear spin polarization, such that the precession of the nuclear bath in the external fields still leads to a significant Overhauser field for the range of fields explored. Additionally, the Overhauser field could have a field-independent component originating from the quadrupolar coupling of the nuclei to electric field gradients, induced by strain in the nanowire [173, 303]. A more complete understanding of the system will require further investigation.

Next, we consider the dependence of coherence times on the external flux ϕ_{ext}. As shown in Fig. 7.15(b), we again do not find a pronounced dependence of the coherence times. In particular, we do not observe an increase of the T_2 times near the sweet spots at $\phi_{\text{ext}} = \pm\pi/2$. From this we conclude that flux noise does not strongly contribute to dephasing.

Finally we investigate the dependence of coherence times on the voltages applied to the three gate electrodes situated underneath the quantum dot junction [see Fig. 7.5(e)]. As shown in Fig. 7.16, we do not find a clear correlation between $T_{2\text{R}}$ or $T_{2\text{E}}$ and the slope of the qubit frequency versus any of the three gate voltages. This indicates that voltage noise also does not provide a large contribution to the dephasing rate. However, although we measure T_2 in the vicinity of the available sweet spots of the individual gate electrodes, we did not find a simultaneous sweet spot for all three quantum dot gates, and the effect of voltage noise cannot be entirely ruled out. Further investigation of the qubit's susceptibility to voltage and magnetic noise based on the Rabi decay times are discussed in the next section.

ESTIMATING THE AMPLITUDE OF CHARGE AND MAGNETIC NOISE FLUCTUATIONS

A method for estimating upper bounds on the amplitude of fluctuations originating from different noise sources is provided in Ref. [205], where the authors study the relation between the Rabi frequency, $f_\text{R} = \Omega_\text{R}/2\pi$, and the Rabi decay time, T_R. These quantities, respectively shown in Figs. 7.17(a) and (b), can be extracted from a fit to the Rabi signal with the expression $a\cos(t\Omega_R)\exp(\text{t}/\text{T}_\text{R}) + c$, where t denotes the full-width half maximum of the applied Gaussian pulse, see Fig. 7.2. We fit the extracted decay times to the model of Ref. [205]

$$\left(\frac{1}{T_\text{R}}\right)^2 = \frac{\sigma_f^4}{4f_\text{R}^2} + C^2 f_\text{R}^2, \tag{7.21}$$

where σ_f is the standard deviation of the fluctuations of the qubit frequency f_s due to noise in the control and model parameters and C is a measure of noise of the drive field. The data is fitted up to the region where the Rabi frequency stops being linear as a function of the pulse amplitude A, indicated with grey markers in Fig. 7.17, and extract $\sigma_f = 39.7\,\text{MHz}$ and $C = 0.25$.

If we assume that the dominating contribution to σ_f originates from noise in just one control parameter, we can obtain upper bounds on the noise amplitude for various types of noise. Since the coherence time is mostly independent on the external flux [Fig. 7.15], we focus only on two possible origins of decoherence: voltage noise and nuclear magnetic noise. We first determine the susceptibility of the qubit frequency with respect to the external parameters (V_L, V_C, V_R, $B_\parallel$ and $B_\perp$) at the ASQ operational setpoint, calculated as the partial derivatives of the qubit frequency with respect to each parameter. From two-tone spectroscopy measurements, we find the susceptibilities with respect to the left, central and right quantum dot gates of $S_\text{L} \approx 0.16\,\text{GHz/mV}$, $S_\text{C} \approx 0.07\,\text{GHz/mV}$ and $S_\text{R} \approx 0.08\,\text{GHz/mV}$, respectively, and the susceptibilities to the parallel and perpendicular magnetic fields of $S_\parallel \approx 0.18\,\text{GHz/mT}$ and $S_\perp \approx 0.05\,\text{GHz/mT}$, respectively.

We start by evaluating the contribution of voltage noise on the DC lines. Considering noise from the gate with highest susceptibility we obtain an upper bound of $\sigma_\mathrm{L} < \sigma_f / S_\mathrm{L} = 0.25\,\mathrm{mV}$ for the standard deviation of the gate voltage fluctuations. While this agrees with the gate noise observed in Ref. [123], where the estimated standard deviation of the voltage gate fluctuations was $\sigma_V = 0.24\,\mathrm{mV}$, we do not expect fluctuations of this magnitude to be present in our system. Previous experiments measured in the same experimental setup [Fig. 7.6] observed gate stability below 60 μeV for similar device geometries (see chapter 4). Furthermore, the DC lines used to control the gate electrodes are strongly filtered with a sequence of 9 kHz RC filters, 80 MHz to 5 GHz π filters and, finally, custom made copper powder filters, all mounted at the mixing chamber stage. and an additional set of 80 MHz π filter on the printed circuit board. The left and right gates additionally have first order LC filters on-chip, with an expected cutoff frequency of 200 MHz. We therefore suspect that the dominant contribution to σ_f does not arise from gate voltage fluctuations on the DC lines. However, charge fluctuations on the device, unrelated to the gate control, could still limit the coherence time.

Alternatively, the gate voltage noise could originate from the RF drive line connected to the central gate electrode. This would result in an upper bound to gate voltage noise of $\sigma_\mathrm{C} < \sigma_f / S_\mathrm{C} = 0.57\,\mathrm{mV}$, which corresponds to an effective power of −53 dBm at the sample. Given the −55 dB attenuation of the drive line [Fig. 7.6], this would correspond to a noise power of 2 dBm at the fridge input, which we consider implausible. Furthermore, the RF line is connected via both a DC block and a bias tee, providing strong high-pass filtering.

Next, we consider the contribution of nuclear magnetic noise. We estimate upper bounds to the longitudinal and transverse magnetic fluctuations of $\sigma_\parallel < \sigma_f / S_\parallel = 0.22\,\mathrm{mT}$ and $\sigma_\perp < \sigma_f / S_\perp = 0.80\,\mathrm{mT}$, respectively. These estimates are comparable to the values obtained for InAs and InSb spin-orbit qubits in previous works: $\sigma_B = 0.66\,\mathrm{mT}$ [227] and $\sigma_B = 0.16\,\mathrm{mT}$ [317], respectively. Nuclear magnetic noise is therefore a plausible dominating contribution to the dephasing observed in the ASQ. However, we emphasize that these calculations are only an estimate and that further investigation is needed to discern between the different possible causes of dephasing.

VIRTUAL-PHOTON-MEDIATED ASQ–RESONATOR COUPLING

In this section we provide additional data showing coherent coupling between the readout resonator and the Andreev spin qubit. As shown in Fig. 7.18, we observe avoided crossings between the ASQ and resonator transitions when they are on resonance, at $B_z = 36.5\,\mathrm{mT}$. This coherent coupling is of note, as the ASQ and readout resonator are not directly coupled. However, both are directly and strongly coupled to the transmon qubit, detuned by 900 MHz in this case, which mediates a strong virtual coupling. This effect is analogous to the work of Ref. [180] where, instead, a resonator mediated virtual coupling between a transmon and a spin qubit.

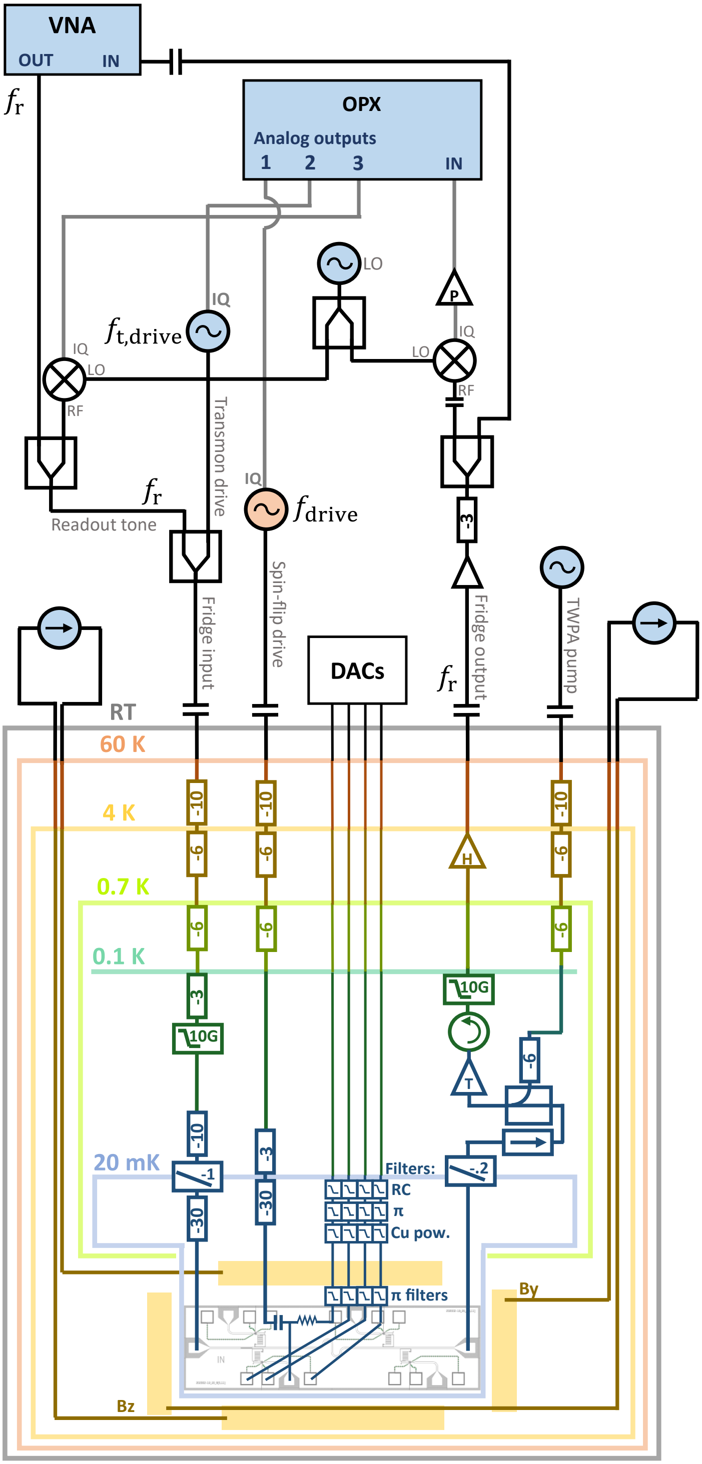

Figure 7.6: Measurement setup at cryogenic and room temperatures.

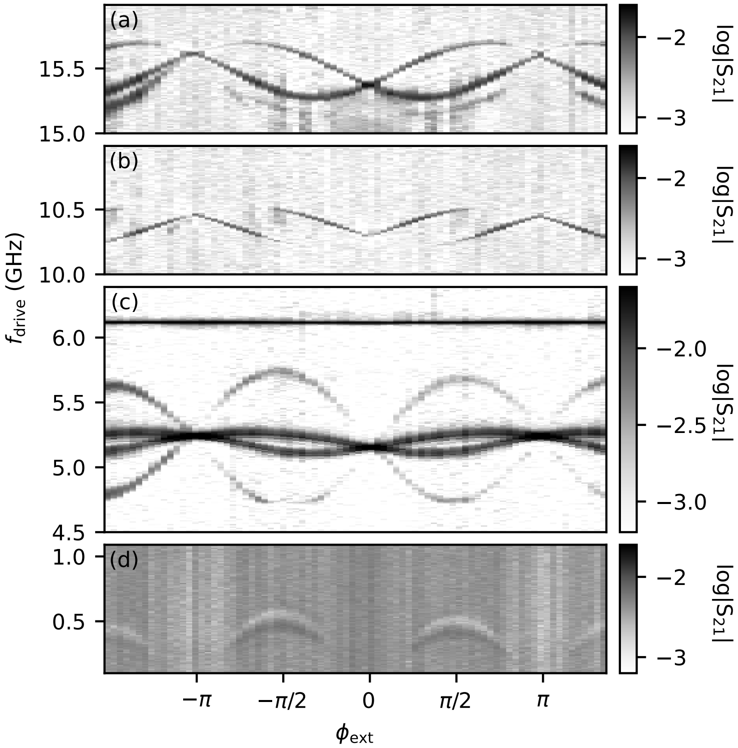

Figure 7.7: Normalized two-tone spectroscopy measurement of the transition spectrum versus external flux. Input power at the top of the spin-flip drive line is −36 dBm for (a-b), −46 dBm for (c) and −6 dBm for (d).

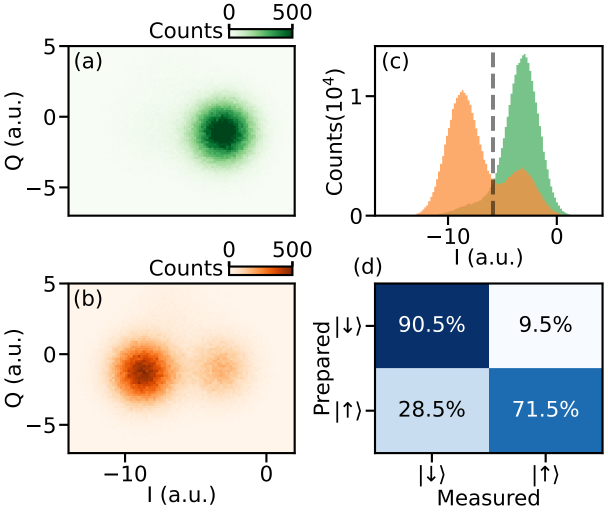

Figure 7.8: Single shot assignment fidelity. (a) Histogram in the complex plane of 3×10^5 sequential shots separated by 200 μs and integrated for 500 ns in the absence of an excitation pulse. (b) Same as (a) in the presence of a π-pulse with a FWHM of 8 ns preceding each shot. (c) Histograms of the I-quadrature response of the preceding panels. Green and orange colors correspond to panels (a) and (b), respectively. (d) Extracted single-shot fidelity's based on the threshold indicated in (c) with a gray dashed line.

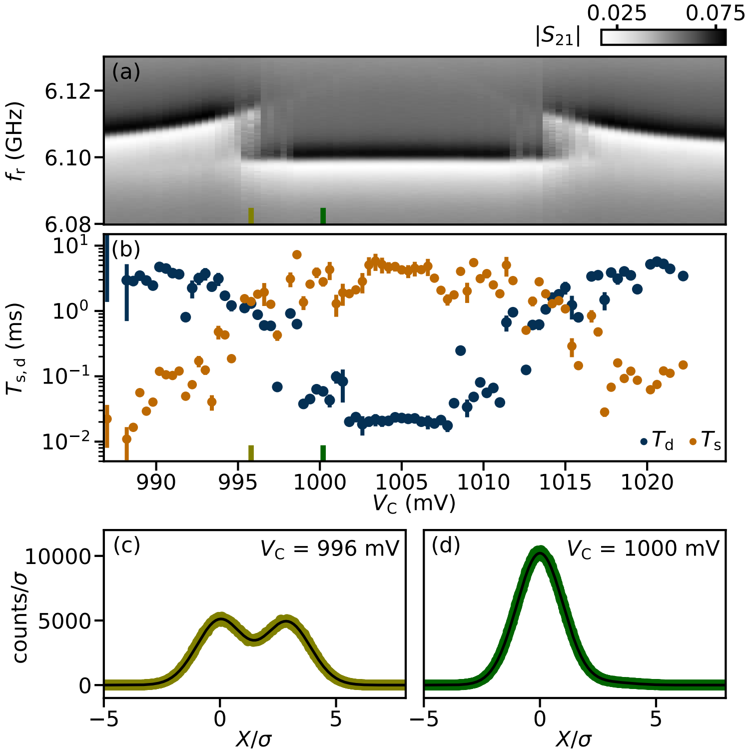

Figure 7.9: Gate dependence of parity lifetimes. (a) V_C dependence of $|S_{21}|$ at $\phi_{ext} = 0$. (b) V_C dependence of the extracted lifetimes. Markers indicate the mean while error bars indicate the maximum and minimum values of 10 consecutive time traces. (c) In yellow, 1D histogram of a continuously measured 17 s-long time trace integrated in time bins of $t_{int} = 4.3\,\mu s$, at $V_C = 996\,mV$. In black, best fit to a double Gaussian shape. (d) Same as (c) but at $V_C = 1000\,mV$.

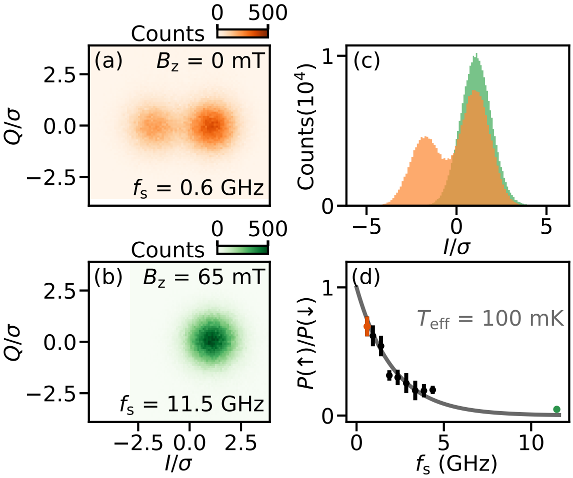

Figure 7.10: Excited state population of the spin states. (a) Histogram in the complex plane of 2.5×10^5 sequential shots, integrated for 500 ns in the absence of an excitation pulse. Measured at $B_z = 0$ mT and $f_s = 0.6$ GHz. (b) Same as (a) at $B_z = 65$ mT and $f_s = 11.5$ GHz. (c) Histograms of the I-quadrature response of the preceding panels (a in orange, b in green). (d) Extracted excited state population versus spin qubit frequency f_s, as tuned with the magnetic field B_z. Data (markers) are fit with a Boltzmann equation (see text) resulting in an effective temperature of 100 mK.

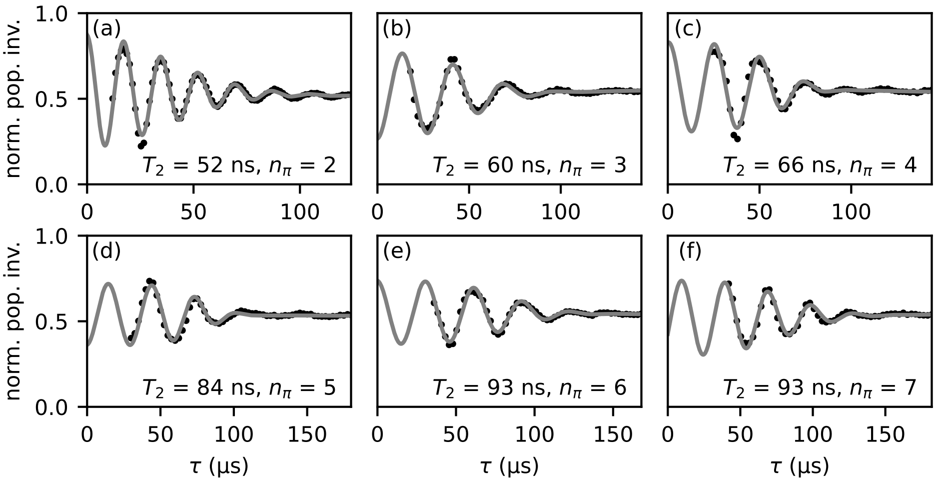

Figure 7.11: Extended CP experiment data. Solid lines indicate fits to the data (see text). All data is normalized to the visibility of a preceding Rabi oscillation measurement, and the data is obtained using a π-pulse ($\pi/2$-pulse) with a FWHM of 4 ns (2 ns). The oscillations are introduced into the decay by adding a phase proportional to the delay time for the final $\pi/2$-pulse.

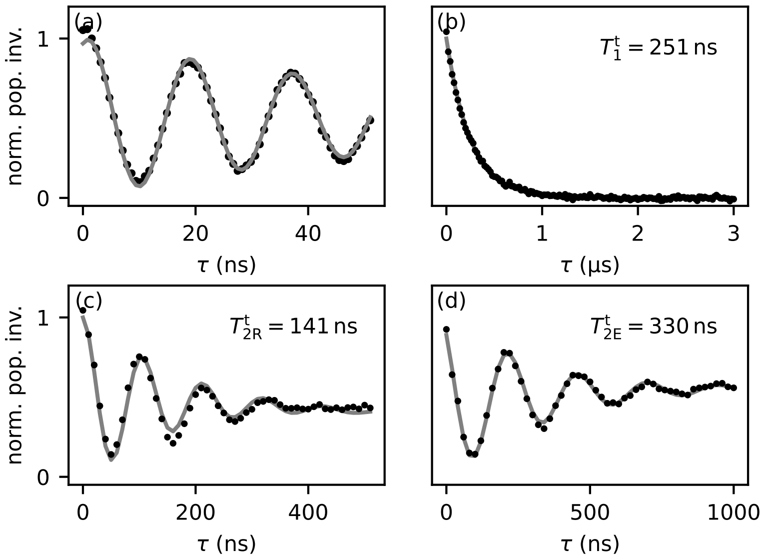

Figure 7.12: Coherence of the transmon qubit at $B_z = 65\,\text{mT}$. (a) Rabi oscillations, (b) qubit lifetime, (c) Ramsey and (d) Hahn-echo experiments. Solid lines indicate fits to the data. For (c-d) oscillations are introduced into the decay by adding a phase proportional to the delay time for the final $\pi/2$-pulse. We plot the normalized population inversion, where each sub-panel is individually normalized to the resulting fit. $\phi_{\text{ext}} = 3\pi/2$ for all panels.

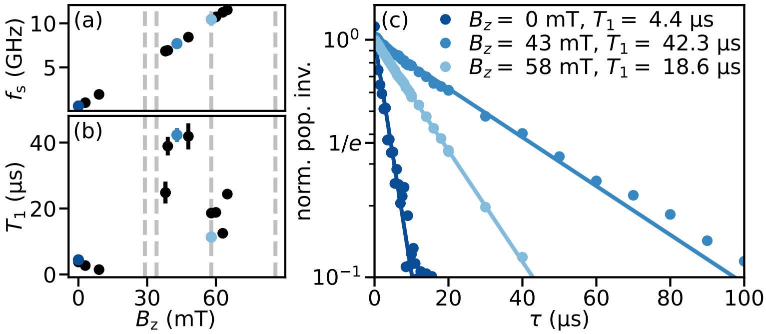

Figure 7.13: (a) Spin qubit frequency, f_s, as a function of magnetic field, B_z. (b) Spin qubit lifetime, T_1 as a function of magnetic field. Dashed lines in (a-b) indicate the magnetic fields at which f_s crosses the first three transmon frequencies f_{0j} and the resonator frequency [c.f. Fig. 7.7]. (c) Representative qubit lifetime measurements, fit with an exponential decay.

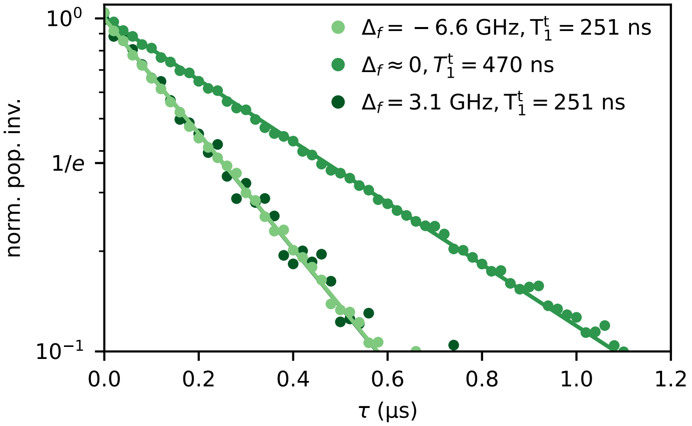

Figure 7.14: Transmon qubit lifetime T_1^t at $\phi_{\text{ext}} = 3\pi/2$ and as a function of detuning $\Delta_f = f_t - f_s$ from the spin qubit frequency as tuned with the magnetic field. Detunings $\Delta_f = 3.1$, 0 and -6.6 GHz correspond to $B_z = 9$, 28 and 65 mT, respectively.

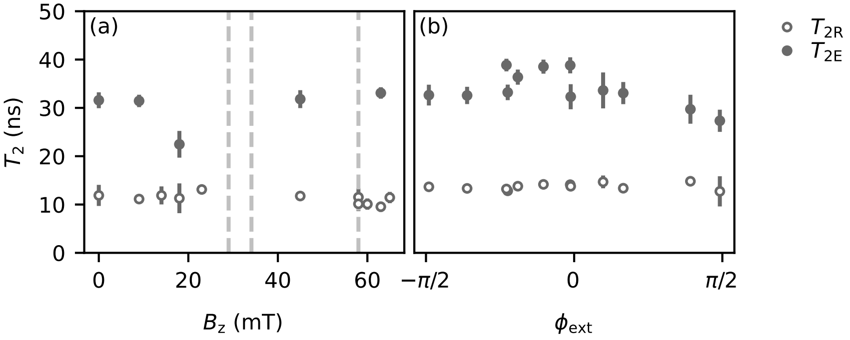

Figure 7.15: Dependence of the spin qubit coherence on the external magnetic field (a) and the external flux (b). The dashed lines in (a) indicate the magnetic fields at which f_s crosses the transmon transition frequencies f_{01} and f_{02} as well as the resonator frequency.

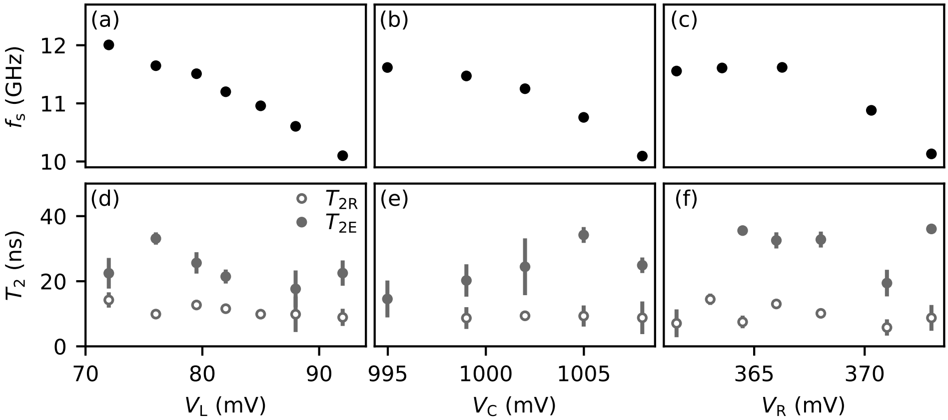

Figure 7.16: Dependence of the spin qubit coherence on the three quantum dot gates. (a-c) Spin qubit frequency versus gate voltage. (d-f) Ramsey and Hahn echo T_2 times versus gate voltage.

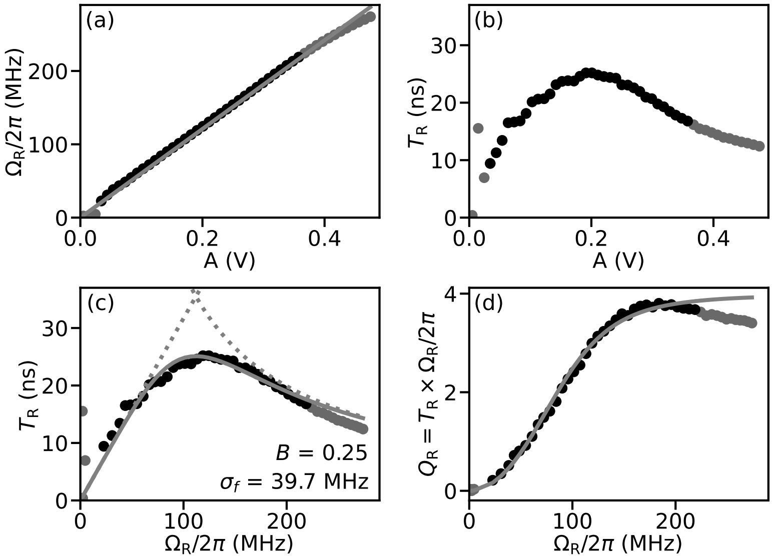

Figure 7.17: (a) Rabi frequency versus pulse amplitude (markers) and fit to a linear dependence (line). Same data as in Fig. 7.2. (b) Rabi decay time versus pulse amplitude (markers). Grey markers denote the points for which the data deviates from the linear dependence in (a). (c) Rabi decay time versus Rabi frequency (markers) an result of a fit of the black markers to Eq. 7.21 (continuous line). The dotted lines show the individual contributions of the two summands in Eq. 7.21. (d) Rabi quality factor $Q = T_R f_R$ versus Rabi frequency (markers) and result of the same fit as in (c) (line).

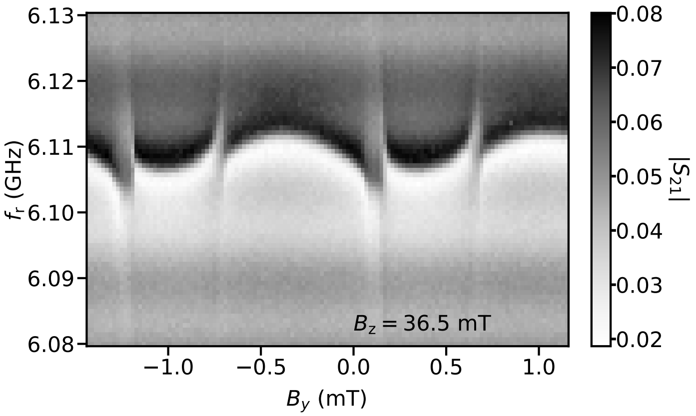

Figure 7.18: Single-tone spectroscopy of the readout resonator versus the magnetic field in the chip plane and perpendicular to the nanowire, B_y, for $B_z = 36.5\,\mathrm{mT}$.

8

MITIGATION OF QUASIPARTICLE LOSS IN SUPERCONDUCTING QUBITS BY PHONON SCATTERING

Quantum error correction will be an essential ingredient in realizing fault-tolerant quantum computing. However, most correction schemes rely on the assumption that errors are sufficiently uncorrelated in space and time. In superconducting qubits this assumption is drastically violated in the presence of ionizing radiation, which creates bursts of high energy phonons in the substrate. These phonons can break Cooper-pairs in the superconductor and, thus, create quasiparticles over large areas, consequently reducing qubit coherence across the quantum device in a correlated fashion. A potential mitigation technique is to place large volumes of normal or superconducting metal on the device, capable of reducing the phonon energy to below the superconducting gap of the qubits. To investigate the effectiveness of this method we fabricate a quantum device with four nominally identical nanowire-based transmon qubits. On the device, half of the niobium-titanium-nitride ground plane is replaced with aluminum (Al), which has a significantly lower superconducting gap. We deterministically inject high energy phonons into the substrate by voltage biasing a galvanically isolated Josephson junction. In the presence of the low gap material, we find a factor of 2-5 less degradation in the injection-dependent qubit lifetimes, and observe that undesired excited qubit state population is mitigated by a similar factor. We furthermore turn the Al normal with a magnetic field, finding no change in the phonon-protection. This suggests that the efficacy of the protection in our device is not limited by the size of the superconducting gap in the Al ground plane. Our results provide a promising foundation for protecting superconducting qubit processors against correlated errors from ionizing radiation.

The work in this chapter has been published as: A. Bargerbos, L. Splitthoff, M. Pita-Vidal, J. Wesdorp, Y. Liu, P. Krogstrup, L. Kouwenhoven, C.K. Andersen, and L. Grünhaupt, Mitigation of quasiparticle loss in superconducting qubits by phonon scattering, Physical Review Applied **19**, 024014 (2023).

8.1. INTRODUCTION

Superconducting qubits are one of the prime candidates in the global effort towards building a quantum computer. Tremendous technological advances have been achieved over the last decade, heralding the advent of noisy intermediate-scale quantum technologies [13, 161, 257]. In order to go beyond this intermediate scale and harness the full potential of quantum computers, fault-tolerant quantum computing will be required. Remarkable progress has been made in terms of implementing error detection and correction in recent years using superconducting circuits [1, 6, 57, 170, 208, 306]. A key assumption of most quantum error correction schemes is that qubit errors are spatially and temporally uncorrelated, however that appears to be drastically violated in large scale superconducting qubit arrays. In [214] it has been shown that cosmic rays and ambient radioactivity can deposit large amounts of energy into the substrate of the device in the form of phonons. These phonons travel over distances of centimeters, breaking up Cooper pairs and leading to decreased qubit coherence over timescales of milliseconds, causing correlated error events [49, 211, 214, 226, 307, 322, 337].

Several mitigation strategies have been proposed to combat these ionizing impact events at the level of the quantum device, such as the direct trapping of quasiparticles through gap engineering [235, 264, 265, 325] as well as impeding the propagation of phonons by substrate modification [60, 150, 261, 267]. A complementary approach is the use of so-called phonon traps [72, 129, 150, 211, 238]. Made from a normal or superconducting material with a small superconducting gap, phonon traps dissipate the phonon energy through scattering events until the resulting phonons have too little energy to break Cooper pairs in the qubit layer. A key difference of phonon traps compared to the direct trapping of quasiparticles is that the traps target the phonons also while they are en-route to the qubits, before error events occur. Phonon traps furthermore do not have to be galvancially connected to the circuit, nor do they even have to be embedded into the same plane of the chip, as long as they connect to the substrate. It is therefore possible to design phonon traps without introducing qubit dissipation from coupling to lossy materials [264], and with no added strain on the increasing complex task of control line routing [42].

8.2. EXPERIMENTAL SETUP & METHOD

To date, the efficacy of phonon traps has been demonstrated for superconducting resonators [129, 238] and kinetic inductance detectors [150]. In this article we set out to investigate their effectiveness in protecting superconducting qubits by fabricating a $6 \times 6\,\text{mm}^2$ chip containing four nanowire transmon qubits [70, 182], one in each corner of the device [Fig. 8.1(a)]. All transmons have identical geometries [Fig. 8.1(b)] and are excited and read out via individual coplanar waveguide resonators coupled to a common feedline. The transmon islands, resonators and feedline are dry etched from a 20 nm thick niobium-titanium-nitride (NbTiN) thin film deposited on a 525 µm thick high-resistivity silicon substrate. We implement the phonon traps by partially removing the NbTiN groundplane on one half of the chip, replacing it with 200 nm of aluminium (Al) deposited by electron beam evaporation and patterned by lift-off [cf. Fig. 8.1(e)]. The Al and NbTiN layers are furthermore galvanically connected by a 20 µm wide region of overlap between them. We leave a 290 µm region of NbTiN around all qubit islands to suppress direct quasiparticle trapping in the Al layer surrounding the qubit [264, 265]. While quasiparticle trapping can be of great use in practical qubit applications, the goal of this study is to evaluate the effect of phonon trapping only. Finally, the full backside of the chip is glued to a solid copper block using thermally conductive silver epoxy. Through the copper, the chip and surrounding enclosure are thermally anchored to the mixing chamber of a dilution refrigerator at ~ 20 mK.

Each transmon island is connected to ground via a nominally 10 µm long epitaxial semiconductor-superconductor nanowire, consisting of a 110 nm wide hexagonal InAs core and a 6 nm-thick Al shell covering two of its facets [173]. By selectively removing a 100 nm long segment from the Al shell we define a semiconducting Josephson junction, whose Josephson energy can be tuned with a single bottom gate electrode via the field effect [70, 182]. A second gate electrode is present under an InAs-Al region of the nanowire, allowing for capacitive tuning of the island's offset charge and aiding in the estimation of the qubit parameters (see Sec. 8.7). The choice for nanowire-based junctions over conventional tunnel junctions is motivated by their magnetic field compatibility [203, 252, 313], allowing us to study the dependence of phonon trapping efficacy on the size of the superconducting gap in the 200 nm thick Al ground plane without strongly affecting the qubit parameters (see Fig. 8.10).

A key feature of our device is two additional semiconducting junctions used for phonon injection. Identical to those used for the transmons, the junctions are located at the top and bottom of the front side of the chip, but galvanically isolated from the qubit ground plane [see Fig. 8.1(a)]. They are connected to source and drain leads made from the NbTiN base-layer to allow for voltage biasing and current sensing, while the resistance of the junctions can be tuned with a bottom gate electrode (see Fig. 8.8). In this article only the top junction is used, as the bottom junction is not functional. Given that the four qubits can be uniquely identified based on their distance from the top junction (1.8 mm or 4.4 mm (see Fig. 8.5) and whether their ground plane is made from Al or NbTiN, we label them as the $\mathrm{Near_{Al}}$, $\mathrm{Near_{NbTiN}}$, $\mathrm{Far_{Al}}$, and $\mathrm{Far_{NbTiN}}$ qubits in what follows.

The top junction serves to inject phonons over a broad spectral distribution up to energies $\leq eV_{\mathrm{bias}} - 2\Delta_{\mathrm{nw}}$ into the substrate of the chip, where Δ_{nw} is the superconducting gap of the injector junction [233]. This technique originates in the investigation of non-equilibrium phonon dynamics [87, 88, 329] and has more recently been adapted for experiments involving superconducting quantum circuits [190, 238, 331]. The purpose of the injection junction is to qualitatively reproduce the phonon spectrum present several microseconds after a cosmic ray impact event. By virtue of the phononic dispersion relation and interactions with the superconducting layers, at this stage most of the energy will have been converted into phonons with a broad energy spectrum ranging up to several meV [211], similar to the spectrum resulting from the phonon injection by voltage biasing a Josephson junction. However, the total energy of an impact event, ranging up to MeV scales, remains difficult to experimentally generate using Josephson junctions [211, 233].

As the phonon injection and propagation process is central to this experiment, we briefly discuss the operation mechanism here, which is visually represented in Fig. 8.1(f-h). We set the junction's bottom gate voltage such that we operate in the tunneling

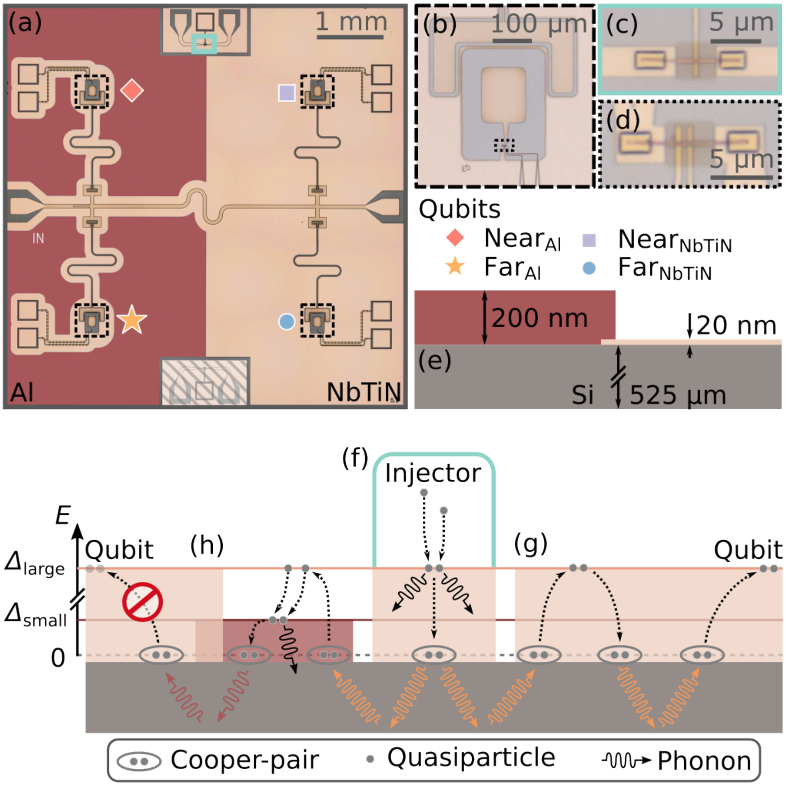

Figure 8.1: False colored device overview (a-e) and sketch of the phonon mitigation process (f-h). (a) Four nanowire transmon qubits [dashed boxes, see (b)] are coupled to individual readout resonators which in turn are coupled to a common feedline. Two nanowire-based junctions are additionally present for phonon injection [turquoise boxes, see (c)] and are galvanically isolated from the qubit ground plane (bottom junction not operational). All structures are patterned from NbTiN (light orange), except for the majority of the left half of the ground plane, which is made from a thick aluminum film (red) [see device cross-section in (e), lateral dimension not to scale]. Electrostatic gates below the junctions tune the resistance of the phonon injector (c) and Josephson energy of the qubits [d, zoom-in of (b)], respectively. A second gate per qubit allows for independent tuning of the qubit charge offsets. (f) Quasiparticles excited by voltage biasing the injector relax to the superconducting gap edge and recombine, emitting phonons (black and orange arrows, respectively). (g) The emitted phonons propagate via the substrate, and those with energies larger than twice the superconducting gap $> 2\Delta_{large}$ induce Cooper-pair breaking, relaxation and recombination cycles, eventually exciting quasiparticles in the qubits. (h) In the presence of a small gap superconductor, these cycles produce phonons of energy $\leq 2\Delta_{small}$ instead (red arrows), which cannot break Cooper-pairs in the qubits.

regime, where the supercurrent at bias voltage $V_{\mathrm{bias}} = 0$ is fully suppressed (see Fig. 8.8). For voltages $V_{\mathrm{bias}} < |2\Delta_{\mathrm{nw}}|/e$ applied between the leads of the junction there is thus no current, where Δ_{nw} is the superconducting gap of the InAs-Al nanowires. However, for voltages $V_{\mathrm{bias}} \geq |2\Delta_{\mathrm{nw}}|/e$ Cooper pairs can be broken up and a quasiparticle current will run across the junction [see Fig. 8.2(a)]. The quasiparticles then diffuse around the vicinity of the junction and its leads, scattering and relaxing to the gap edge of the superconductors, producing relaxation phonons of energies up to $E = eV_{\mathrm{bias}} - \Delta_{\mathrm{nw}}$ in the process, see Fig. 8.1(f) [233]. The now-relaxed quasiparticles can subsequently also recombine with other quasiparticles, emitting recombination phonons of energy $E = 2\Delta_{\mathrm{nw}}$ [1]. These phonons either break up new Cooper pairs in the metal layer, or they escape into the substrate where they can rapidly travel over distances of several times the size of the chip, scattering off the boundaries [210]. The phonons can thus end up at the qubits, creating quasiparticles and inducing losses proportional to the excess quasiparticle density x_{qp} [105], see Fig. 8.1(h). However, if the phonons encounter the Al traps en-route to the qubits, part of their energy can be dissipated in further cycles of Cooper pair breaking, relaxation, and recombination [Fig. 8.1(g)]. The resulting phonons of energy $E \leq 2\Delta_{\mathrm{trap}}$ can no longer excite quasiparticles in the qubit structures, for which the superconducting gaps of the islands $\Delta_{\mathrm{NbTiN}} \geq 1500\,\mu\mathrm{eV}$ and of the nanowires $\Delta_{\mathrm{nw}} = 270\,\mu\mathrm{eV}$ are larger than that of the traps $\Delta_{\mathrm{trap}} = 180\,\mu\mathrm{eV}$ [207, 299, 319].

We note that at cryogenic temperatures, phonons move through the silicon substrate virtually unimpeded with a velocity of $\sim 6\,\mathrm{mm}\,\mu\mathrm{s}^{-1}$ and thus traverse the chip on μs timescales. Additionally, we expect the scattering length of phonons in the Al film to be comparable to the thickness of the Al trapping region, such that they have a significant probability to escape the film without creating quasiparticles [211]. Thus, we anticipate the phonons to be able to fully traverse the chip, with the main impediments to their propagation coming from the probability of scattering into quasiparticles and from the probability to escape through the silver epoxy on the backside of the sample. However, accurate modeling of the phonon distribution in the substrate would critically rely on phonon transfer rates through the various interfaces, the scattering lengths in the different materials, and adequate numerical simulations of phonon propagation trajectories (cf. [210]).

8.3. QUBIT LIFETIME VERSUS QUASIPARTICLE INJECTION

To investigate the effectiveness of the Al ground plane to protect against high energy phonons, we perform qubit lifetime (T_1) experiments on all four qubits while we apply a constant bias to the phonon injector, which causes the T_1 time to decrease as shown in Fig. 8.2(b). For bias voltages within the gap, T_1 remains essentially constant, see Fig. 8.2(c), while T_1 drastically decreases at the onset of the quasiparticle current, with a kink at $2\Delta_{\mathrm{nw}}$ originating from the enhanced conductance at the gap edge. As the qubit is over 4 mm away from the galvanically isolated injector junction, this suggests that the losses indeed originate from phonons that traveled through the substrate [238]. We then compare the added loss rate $\Gamma_1(V_{\mathrm{bias}}) = 1/T_1(V_{\mathrm{bias}}) - 1/T_1(V_{\mathrm{bias}} < |2\Delta_{\mathrm{nw}}/e|)$ of each qubit,

---

[1] When quasiparticles recombine they can also emit photons rather than phonons. However, as the final density of states corresponding to this process is much smaller than the density of states for phonon emission, we neglect this effect.

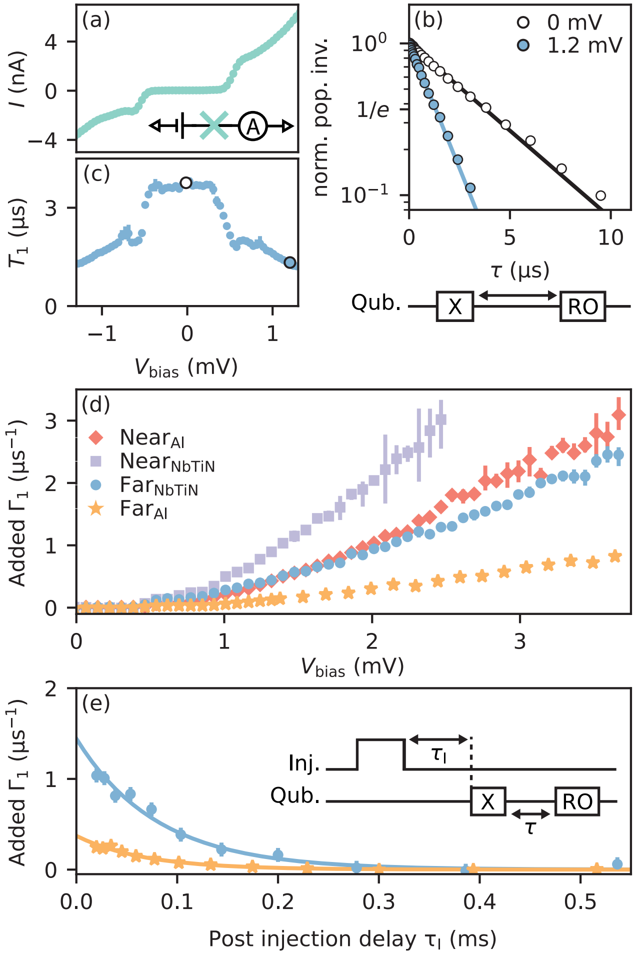

Figure 8.2: Added qubit loss due to phonon injection. (a) I-V characteristics of the Josephson junction used to inject phonons measured using the circuit shown in the inset. (b) Representative qubit lifetime (T_1) measurements on the $\mathrm{Far}_{\mathrm{NbTiN}}$ qubit for bias voltages V_{bias} of 0 and 1.2 mV applied across the injector. The data (markers) is fit with an exponential decay (solid lines), yielding lifetimes of 3.8 μs and 1.3 μs respectively. (c) Qubit lifetime T_1 of the $\mathrm{Far}_{\mathrm{NbTiN}}$ qubit as a function of V_{bias}. (d) Added qubit loss rate Γ_1 as a function of V_{bias} for all 4 qubits (labels apply to all panels). We define added Γ_1 as the bias voltage dependent loss rate minus the average base line value for $|eV_{\mathrm{bias}}| < 2\Delta_{\mathrm{nw}}$ [cf. panel (c)]. (e) Added Γ_1 as a function of the delay time τ_{I} after a square injection pulse with a duration of 20 μs and an amplitude of ≈ 3 mV. The loss rates are fit with an exponential decay (solid line), yielding recovery times of (80 ± 9) μs (blue) and (67 ± 5) μs (orange). Error bars in panels (c-e) denote the standard deviation over 5 repetitions.

where we subtract the baseline loss rate measured inside the superconducting gap. As can be seen in Fig. 8.2(d), the $\mathrm{Far}_{\mathrm{Al}}$ qubit has up to 8 times smaller added loss rate than the $\mathrm{Near}_{\mathrm{NbTiN}}$ qubit. However, this comparison involves both a larger separation from the injector and the presence of phonon traps. To disentangle the two effects, we compare the qubits at equal distance from the injector. The $\mathrm{Near}_{\mathrm{Al}}$ qubit has up to 2.5 times smaller added loss rate than the $\mathrm{Near}_{\mathrm{NbTiN}}$ qubit, supporting that the presence of the Al phonon traps leads to resilience against phonon induced losses. For the $\mathrm{Far}_{\mathrm{NbTiN}}$ and $\mathrm{Far}_{\mathrm{Al}}$ qubits the improvement even reaches up to 5, suggesting that an increased area of the trapping region increases the efficacy (see Fig. 8.9). We note that the improvements are bias dependent, tending towards a constant value for bias voltages above 1.5 mV, several times the size of Δ_{nw}.

So far, we have focused on phonons that are continuously injected into the chip by applying a constant bias voltage across the injector. However, in the impact events of ionizing radiation the phonons are created in bursts. To test whether our findings still hold under such circumstances, we repeat the same experiment using a pulsed phonon injection scheme. We now apply a square pulse of duration 20 µs at an amplitude of approximately 3 mV across the injector. This would result in an energy of ~ 5 keV if all energy was transduced into phonons - about two orders of magnitude smaller than during a typical high-energy particle impact, but with a spectrum similar to that some µs after the initial impact [211, 233]. Subsequently, we measure the qubit loss as a function of delay time after the injection event [Fig. 8.2(e)]. The recovery of added loss rate with delay time follows an exponential form, suggesting a recovery dominated by quasiparticle relaxation rather than by recombination, for which the recovery is governed by a hyperbolic cotangent function [325]. We find that at zero delay time the $\mathrm{Far}_{\mathrm{NbTiN}}$ qubit is affected 4 times more than the $\mathrm{Far}_{\mathrm{Al}}$ qubit, consistent with the results for continuous injection. We further note that that the recovery times are approximately equal at (80 ± 9) µs [(67 ± 5) µs] for the $\mathrm{Far}_{\mathrm{NbTiN}}$ [$\mathrm{Far}_{\mathrm{Al}}$] qubit. We do not observe any significant enhancement of recovery time due to the presence of the Al phonon traps, such that the recovery time might instead be dominated by quasiparticle dynamics near the junction, such as quasiparticle trapping and diffusion rates. The latter could be addressed with quasiparticle traps rather than with phonon traps [264, 265]. Alternatively, the phonon traps could have a similar effect on recovery times across the device, as the phonons can traverse the chip on timescales of a few microseconds [211]. We note that the timescale for phonons to leave the chip is also several microseconds, and this is therefore unlikely to be the limiting mechanism of the observed the recovery time.

8.4. EXCITED STATE POPULATION

In the measurements of the qubit loss rates we additionally find that the qubit readout signal becomes smaller with increasing bias voltages, requiring substantially more repetitions to obtain the same signal-to-noise ratio (SNR) at elevated bias. To investigate this effect we monitor the resonator response of the $\mathrm{Far}_{\mathrm{NbTiN}}$ qubit using single-shot readout in the absence of any qubit excitation tones. For 0 mV bias this results in a double Gaussian distribution of measurement outcomes, with 93% of the outcomes located in a single Gaussian [Fig 8.3(a)]. We interpret this output as the signal corresponding to the ground state population of the transmon qubit, indicating a residual excited state

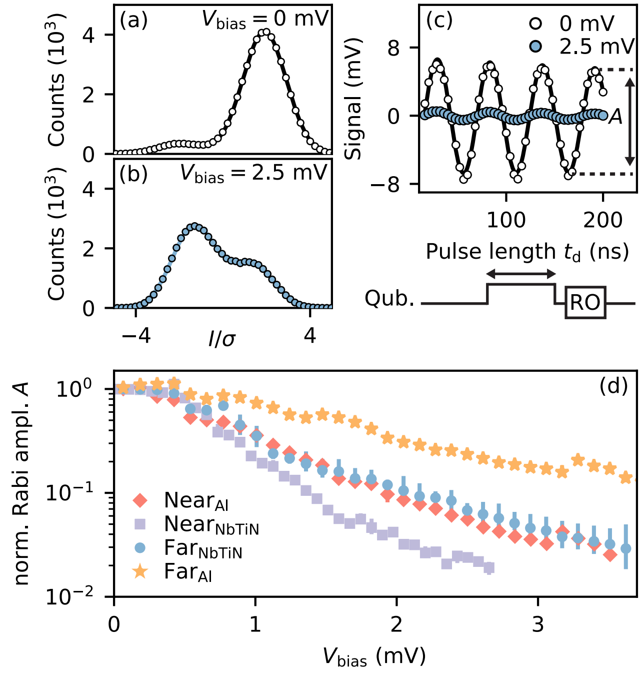

Figure 8.3: Increased excited state population due to phonon injection. (a) Histogram of the resonator response for the Far$_{\text{NbTiN}}$ qubit at $V_{\text{bias}} = 0$ mV. Each individual shot corresponds to the integrated output signal for a readout time of 500 ns. The resulting histogram (markers) is fit with a double Gaussian function (solid line), from which we estimate a ground state population of 93%. (b) Same as (a) for $V_{\text{bias}} = 2.5$ mV, from which we estimate a ground state population of 35%. (c) Representative time-Rabi experiments on the Far$_{\text{NbTiN}}$ qubit for the values of V_{bias} used in panels (a-b). The data (markers) is fit with an exponentially decaying cosine (solid line). (d) Extracted Rabi oscillation amplitude A normalized to its value at zero bias, measured as a function of V_{bias} for all 4 qubits. Error bars in panel (d) denote the standard deviation over 5 repetitions.

population of 7%. When we apply a constant bias of 2.5 mV the distribution changes significantly: the transmon is now in the ground state only 35% of the time. This is consistent with previous findings showing that non-equilibrium quasiparticles with energies in excess of $2\Delta_{\mathrm{nw}}$ can lead to an increased excited state population [139, 287, 331]. The fact that the ground state population is less than 50% could furthermore indicate that the transmon now also has a sizeable population outside of the two-level qubit subspace, and that non-equilibrium quasiparticles resulting from high energy phonons serve to reduce the unwanted excited state population induced by the generation of non-equilibrium quasiparticles by phonons. We note that such energetic quasiparticles are likely only produced during the initial phase following an impact event [211, 214], while they are constantly observed in this experiment due to the continuous injection of high energy phonons.

To gain insight into the effectiveness of the traps in reducing unwanted excited population, while constrained by limited SNR, we perform a time-Rabi experiment between the transmons' ground and first excited state as a function of the injection bias voltage. The amplitude of the Rabi oscillation A is proportional to the difference in the population of the transmon states involved, and additionally decreases in the presence of qubit leakage. The evolution of A with V_{bias} is thus indicative of the change in the state populations. As shown in Fig 8.3(c), the amplitude of the oscillations for the $\mathrm{Far}_{\mathrm{NbTiN}}$ qubit indeed decreases significantly at $V_{\mathrm{bias}} = 2.5\,\mathrm{mV}$ compared to that at 0 mV. We repeat this experiment for all qubits, normalizing the Rabi amplitude to its value at zero injection voltage. We find results comparable to those of the added qubit loss rates, with the $\mathrm{Near}_{\mathrm{Al}}$ qubit again showing a reduction in Rabi amplitude of up to 5 times larger than that of the $\mathrm{Far}_{\mathrm{NbTiN}}$ qubit. This difference indicates that phonon traps can thus also protect against phonon-induced excited state population.

8.5. MAGNETIC FIELD DEPENDENCE

Having established a moderate protection due to the Al traps, we investigate how the difference in superconducting gap between the trapping and qubit materials influences the effectiveness of the trapping process. For the trapping process to be of use, the superconducting gap of the trap must be smaller than that of the qubit layer [cf. Fig. 8.2(f-h)]. Furthermore, as the relaxation rate of quasiparticles excited inside the trap grows with their energy above the gap edge [149, 264], one would assume that the absolute size of gap should also be a relevant metric. Ignoring potentially detrimental effects from electromagnetic coupling, a normal metal (with no spectral gap) might thus be particularly suitable as a trapping material [211, 238]. We investigate this hypothesis in-situ, making use of the inherent magnetic field compatibility of the nanowire transmon qubits and their readout circuit, which have been shown to be operable up to parallel fields in excess of 1 T [174, 203, 252, 313]. This is in contrast to the 200 nm thick Al, which turns normal at significantly lower fields of ≈ 30 mT [see Fig. 8.4(b)] [219].

We repeat the measurements of added loss rate in the presence of a constant bias voltage for different applied magnetic fields. Contrary to expectation, the added loss rate does not appear to change after passing the critical parallel field of the thick Al [Fig. **??**(a)]. In fact, we do not detect any significant change as a function of magnetic field between 0 and 70 mT, far in excess of the critical field [Fig. **??**(c)]. To elucidate the

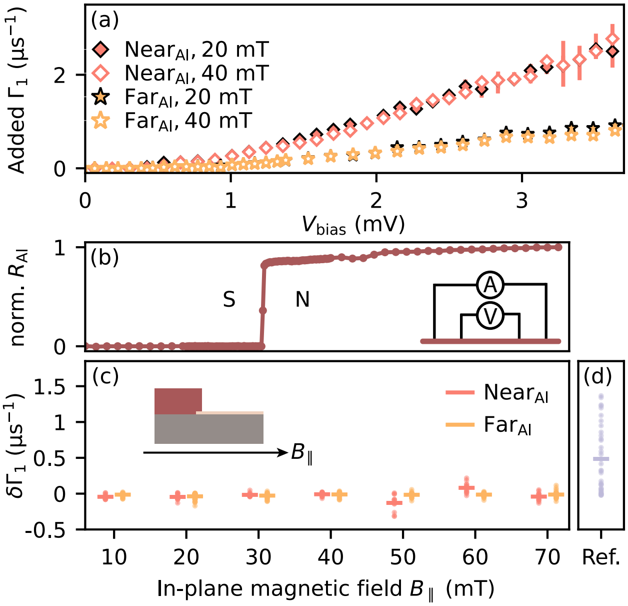

Figure 8.4: Magnetic field independence of added qubit loss. (a) Added Γ_1 as a function of V_{bias} for the two qubits with an aluminum ground plane at magnetic fields $B_{\parallel}$ of 20 and 40 mT applied in the plane of the chip [cf. inset panel (c)]. (b) Four-point measurement of the normalized aluminum film resistance R_{Al} as a function of $B_{\parallel}$. (c) Scatter plot showing the differences between the V_{bias} dependence of Γ_1 at 0 and elevated $B_{\parallel}$ for the two qubits with an aluminum ground plane. Each data point represents the difference in rates $\delta\Gamma_1$ evaluated at equal V_{bias}. The horizontal line indicates the mean of $\delta\Gamma_1$ over all V_{bias}. Inset: direction of the applied magnetic field with respect to the cross-section of the chip. (d) Same type of plot as (c), but showing the difference between the Near$_{\mathrm{Al}}$ and Near$_{\mathrm{NbTiN}}$ qubits at 0 applied magnetic field [data shown in Fig. 8.2(d)]. This serves as a reference for the data in panel (c).

implications of these findings, we conservatively estimate the relaxation rate of quasiparticles at energy $2\Delta_{\mathrm{nw}}$ to be at least 30% faster in normal state Al than in zero-field superconducting Al due to the reduction in gap size [264]. Given that despite this no improvement is observed, we conclude that the the rate at which excited quasiparticles relax inside the phonon trap is not what sets the effectiveness of our phonon traps.

We instead consider that the bottleneck for the trapping efficacy is the rate at which phonons are able to scatter and excite quasiparticles in the trapping layer. This rate has two primary components: the scattering rate of phonons into quasiparticles inside the Al, and the transmission probability for phonons to cross from the silicon substrate into the Al. The first component is predicted to moderately decrease when entering the normal state [211]; a negative change in trapping efficacy would thus have been observed if this were the limiting factor. The second component, the transmission probability, is not expected to be a function of field. Consequently, we hypothesize that the trapping is limited by the poor interface between the substrate and the Al layer [148, 210], making it difficult for phonons to enter the traps. In our device this is potentially exacerbated by the dry etching procedure used to remove the NbTiN layer before Al deposition, which roughens the underlying silicon, reducing phonon transmission across the metal-substrate interface. We again note that the magnetic field experiment is performed using continuous injection rather than using pulsed injection. Potential improvements during the phase where most phonons have been reduced to energies of $2\Delta_{\mathrm{nw}}$ might thus be obfuscated by the constant influx of new high energy phonons.

8.6. CONCLUSIONS

In conclusion, we find a factor of 2-5 improvement in the protection against phonon-induced degradation of qubit lifetimes for transmon qubits surrounded by Al phonon traps. This level of improvement is in line with previous results on phonon trapping for superconducting resonators [129, 238] and kinetic inductance detectors [150], here demonstrated at the level of sensitivity of transmon qubits. Additionally, we demonstrate that phonon traps can also be used to combat the increase in excited state population due to the generation of energetic quasiparticles from phonons. While the obtained improvements are modest, we emphasize that this is a conservative estimate for realistic multi-qubit arrays. With mean-free paths exceeding several times the size of the chip, phonons in the silicon are able to travel vast distances, and thus it is likely that the two NbTiN-based qubits also benefit from the presence of the Al traps. Therefore, we believe the improvement found is a lower bound on what could be obtained when comparing different chips with and without traps, which we choose not to do to exclude unintended differences between devices and thermal anchoring of the respective chips. Furthermore, we deliberately thermally anchor the full backside of the chip, allowing phonons to leave the device via the substrate. This is in contrast to most superconducting qubit implementations, where the chips are mounted in a floating configuration [193, 211, 330]. In these devices the main path for the phonons to escape the device is through the wirebonds at the perimeter of the chip, a slow process that enhances the probability for the phonons to interact with the traps in such devices.

During the writing of this manuscript we became aware of a similar experiment by Iaia et al. [132]. In their work the authors compare the impact of high energy phonons on two separate transmon chips, where one chip has a 10 μm thick Cu film deposited on its backside. For the Cu-covered device they find a reduction in phonon-induced qubit errors by more than a factor of 20. These findings strongly complement the results of this paper, where we instead investigate the effect of superconducting traps. Furthermore, by comparing transmons on a single chip we provide a conservative measure of what trapping efficacy can be achieved. Together these works show that phonon traps offer a promising path towards reducing correlated errors to below the level required for fault-tolerant operation.

Finally, we highlight that phonon traps are also relevant for transmons realized with conventional Al/AlOx Josephson junctions [207], as well as for other types of superconducting qubits, such as fluxoniums [255] and novel protected qubit designs [113]. The enhanced rates of quasiparticle poisoning events following an impact event are also expected to be highly detrimental for parity-based qubits such as Andreev qubits [123, 136], as well as topologically protected Majorana qubits [154, 262]. The current generation of devices used in these qubit platforms rely on the same type of superconductor-semiconductor nanowires as used in this experiment. Furthermore, while not directly sensitive to superconductor-based quasiparticles, spin qubits are known to suffer phonon-mediated back-action [110, 280] and might also suffer from correlated errors due to phonon impacts, although to what extent remains to be investigated.

8.7. SUPPLEMENTARY INFORMATION

DEVICE AND EXPERIMENTAL SETUP

DEVICE OVERVIEW

An extended optical image of the full $6 \times 6\,\mathrm{mm}^2$ chip is shown in Fig. 8.5(a). As discussed in the main text, it contains four grounded nanowire transmon qubits coupled to individual coplanar waveguide resonators. The coplanar waveguide resonators are coupled to a common feedline, which contains a capacitor at its input port to improve the directionality of the signal [126]. The nanowire transmons each have two gate electrodes; the first is used to control the Josephson potential with voltage V_j, the second to control the offset-charge on the island with voltage V_n [Fig. 8.5(b)].

At the top and bottom of the chip there are two additional nanowire junctions that are galvanically isolated from the rest of the ground plane [Fig. 8.5(c)]. The junctions are connected to two leads: the source and drain. The source is connected to a pulsed and constant voltage sources via a bias tee, while the drain is connected to a current measurement module. An additional gate electrode is present to tune the out-of-gap resistance of the junction via the field effect.

NANOFABRICATION DETAILS

The device fabrication is done using standard nanofabrication techniques. The substrate is 525 μm thick high-resistivity silicon, on top of which a 20 nm thick NbTiN film is sputtered. From this base layer the circuit elements are patterned using an electron-beam lithography mask and SF_6/O_2 reactive ion etching. In this step we also remove the NbTiN in the places where the Al phonon traps are to be placed. Immediately before deposition of the 200 nm thick Al by electron beam evaporation, we remove surface oxide

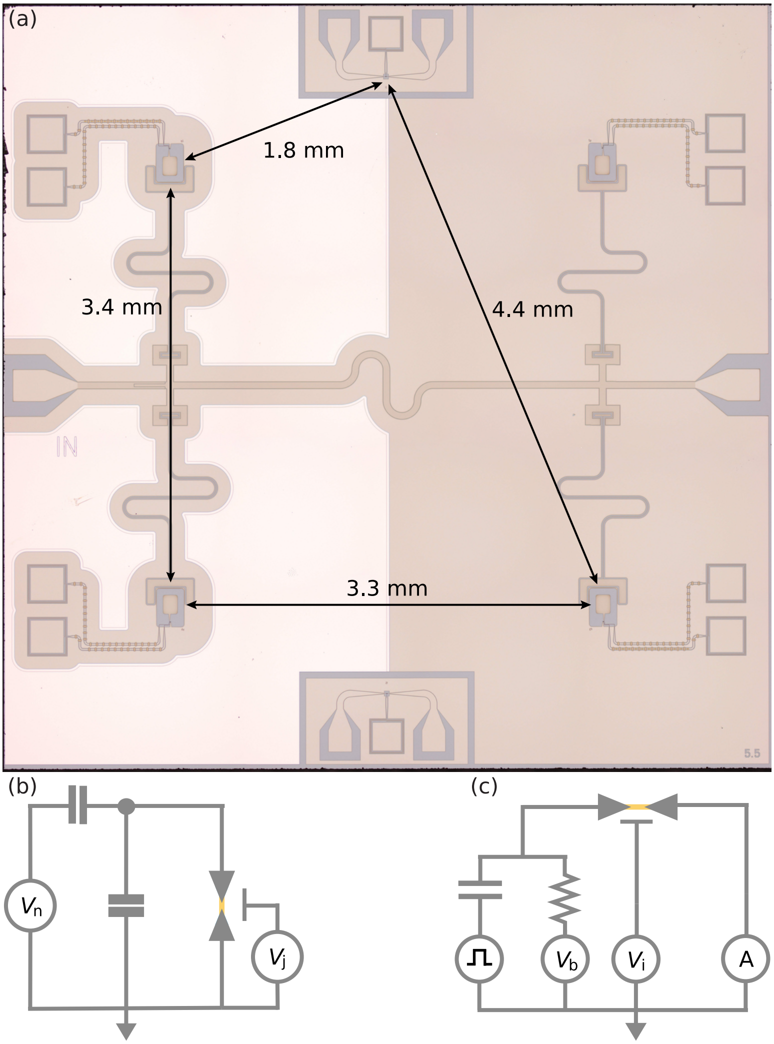

Figure 8.5: **Extended device overview.** (a) Optical micrograph of the device before wire-bonding. The composite image is stitched together from 36 separate images. For each image the contrast is adjusted to that of its neighboring images, but no further processing is performed. (b) Circuit diagram of the nanowire transmon qubit coupled to junction and island gate electrodes. (c) Circuit diagram of the nanowire phonon injector coupled to source and drain leads as well as an additional gate electrode.

on the substrate by a 30 s dip in 20:1 diluted buffered oxide. The Al layer is then patterned by lift-off. After this 30 nm of Si_3N_4 dielectric is deposited to form the insulation of the junction gate electrodes using plasma enhanced chemical vapor deposition, which is patterned by wet etching with buffered oxide etch using negative electron-beam lithography. The nanowires are then deterministically placed on top of the dielectric using a nanomanipulator and an optical microscope. For this we use an approximately 10 µm-long vapour-liquid-solid (VLS) hexagonal InAs nanowire with a diameter of 110 nm and a 6 nm-thick epitaxial Al shell covering two facets [173]. After placement, a 100 nm section of the aluminium shell is selectively removed by wet etching with MF-321 developer to create the Josephson junctions. After the junction etch the nanowires are contacted by an argon milling step followed by the deposition of 150 nm thick sputtered NbTiN. Finally, the chip is diced into $6 \times 6\ \mathrm{mm}^2$, glued onto a solid copper block with silver epoxy, and connected to a custom-made printed circuit board using aluminium wirebonds.

CRYOGENIC AND ROOM TEMPERATURE MEASUREMENT SETUP

The device is measured in a commercial dilution refrigerator with a base temperature of 20 mK. Shown in Fig. 8.6, the setup contains an input RF line, an output RF line, an extra RF line for the pulsed injection, and multiple DC lines for voltage biasing, current sensing, and the tuning of gate voltages. Digital-to-analog (DAC) voltage sources developed in-house are connected to the DC gate electrode lines, which are filtered at base temperature with multiple low-pass filters. The injector junction drain lead contains the same filtering and is connected to a current measurement module also developed in-house. It is further connected to a Keithley 2400 multimeter and a Stanford Research Instruments SR830 Lock in amplifier (not shown). The input and pulse RF lines contain attenuators and filters at different temperature stages, as indicated. The output RF line contains a traveling wave parametric amplifier (TWPA) acquired from the MIT Lincoln Laboratory at the 20 mK temperature stage, a Low Noise Factory high-electron-mobility transistor (HEMT) amplifier at the 4 K stage, and two additional Narda-MITEQ low noise amplifiers at room temperature. A three-axis vector magnet (x-axis not shown) is thermally anchored to the 4 K temperature stage, with the device under study mounted at its center. The three magnet coils are controlled with MercuryiPS current sources. At room temperature, a vector network analyzer (VNA) is connected to the input and output RF lines for spectroscopy at frequency f_r. On the input line, this signal is then combined with the IQ-modulated transmon drive tone at frequency f_t. A separate IQ-modulated tone at f_r, only used for time-domain measurements, is also combined onto this line. The pulsed injection signal is directly sent into the fridge at baseband frequencies. For time-domain measurements the output signal is additionally split off into a separate branch measured with a commercial quantum system measurement platform.

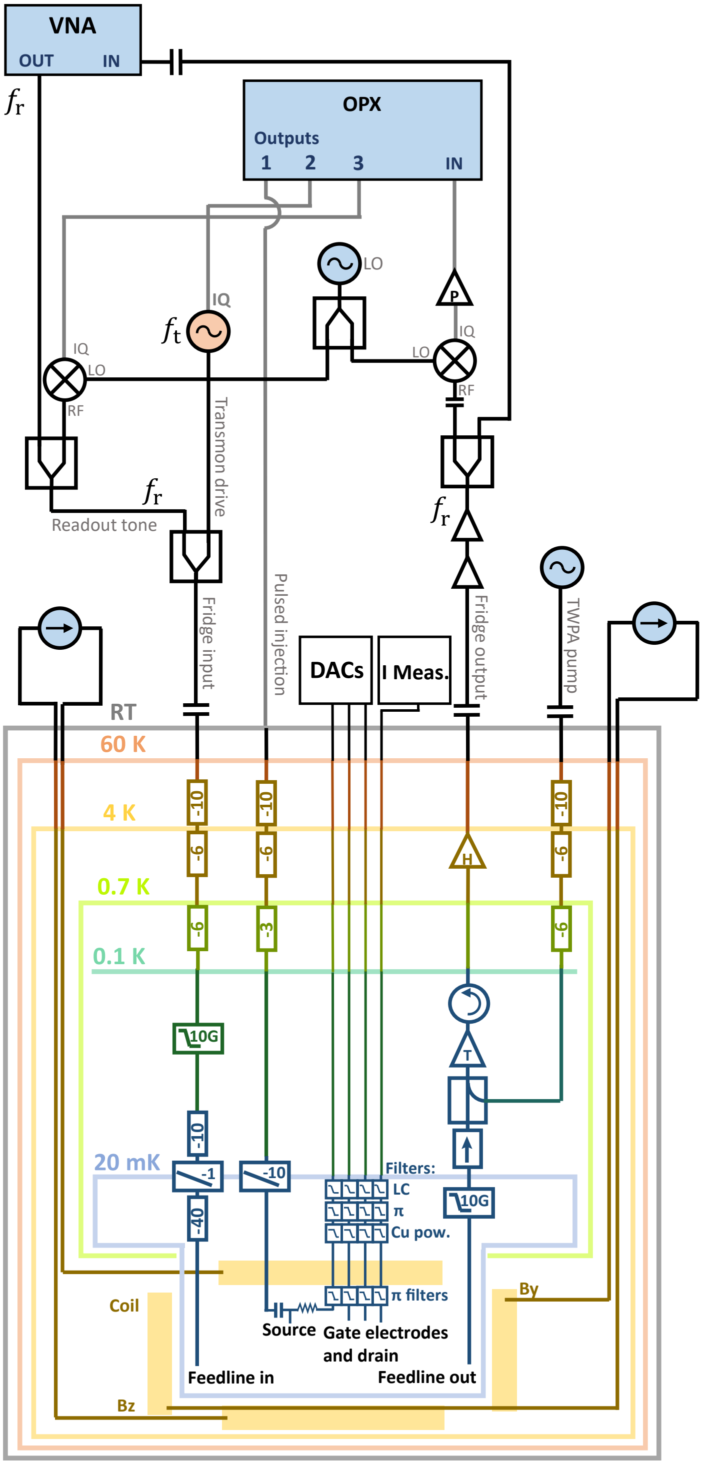

Figure 8.6: Measurement setup at cryogenic and room temperatures.

BASIC CHARACTERIZATION

QUBITS

In this section we discuss the characterization of the four qubits at the setpoints used in the experiments. In practice, the choice for the setpoints is governed by several factors: the frequency dependence of the qubit lifetimes through Purcell and dielectric losses, the suppression of offset-charge sensitivity to allow for parity-insensitive qubit manipulation, and the need for inter-qubit frequency detuning to allow for individual control of the qubits through a single feedline. Under these constraints, we empirically find the optimal range of qubit frequencies to be in the range 3.7–4.0 GHz. The resulting readout resonator frequencies f_r, qubit frequencies f_{01}, and average qubit lifetimes T_1 in the absence of phonon injection are listed in Table 8.1.

However, in order to compare the effect of phonon injection on each qubit on equal footing, we further need to consider that the interaction between the phonon-induced quasiparticles and the qubits depends on the values of the qubit parameters. Specifically, for transmon qubits based on superconductor-insulator-superconductor (SIS) junctions with a Josephson energy E_J significantly larger than the charging energy E_c, the added qubit loss due to quasiparticles is given by [105]

$$\Gamma_{10} = \frac{16E_\mathrm{J}}{\hbar\pi}\sqrt{\frac{E_\mathrm{c}}{8E_\mathrm{J}}}\sqrt{\frac{\Delta}{2hf_{01}}}x_\mathrm{qp} = Dx_\mathrm{qp} \tag{8.1}$$

where f_{01} is the qubit frequency and x_qp the density of quasiparticles. While the validity of this equation for the semiconducting Josephson junctions used in this work has not been investigated, we choose our qubit setpoints in accordance with this equation in an attempt to ensure comparable sensitivity to quasiparticles (see the estimated values of D in Tab. 8.1).

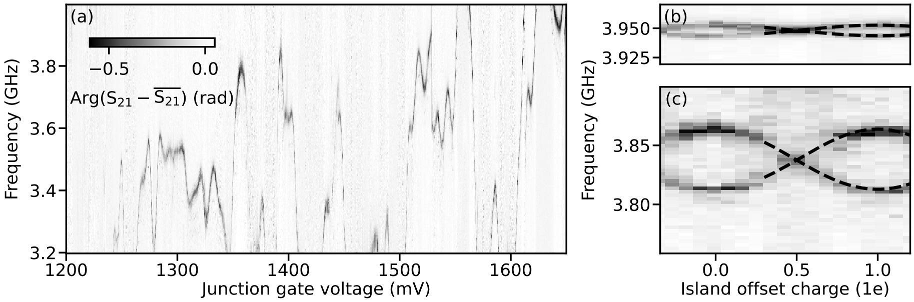

Figure 8.7: Characterization of the nanowire transmon qubits. (a) Representative junction gate dependence of the Near$_\mathrm{Al}$ qubit near its setpoint at 1659 mV used in the main text. (b-c) Offset charge dependence of the f_{01} (top) and $f_{02}/2$ transition frequencies of the Near$_\mathrm{Al}$ qubit as capacitively tuned with the island gate electrode, measured at the setpoint used in the main text. Partially overlaid are fits with Eqs. (5.1) and (8.4), used to determine the parameters listed in Tab. 8.1.

The tuning of the qubits is performed in-situ via the field effect, making use of the bottom gate electrode located below the qubit's Josephson junction [70, 182]. As shown in Fig. 8.7(a), this results in mesoscopic fluctuations of the qubit frequency as a function of gate voltage, allowing for fine tuned control. When possible, we choose to place qubits at a local maximum or minimum in gate voltage, reducing sensitivity to charge noise [203]. Next we characterize the Hamiltonian parameters of the qubits in more detail by fitting the measured qubit frequency. This is done by numerically diagonalizing the transmon Hamiltonian

$$H = -4E_{\mathrm{c}}\partial_{\phi}^{2} + V(\phi) \tag{8.2}$$

where $V(\phi)$ is the Josephson potential of the junction, dependent on the superconducting phase difference across the junction ϕ. For SIS junctions it takes on the simple form $V(\phi) = E_{\mathrm{J}}\left[1 - \cos(\phi)\right]$, allowing one to uniquely determine the transmon's Hamiltonian parameters through a measurement of the qubit frequency f_{01} and its anharmonicity $f_{21} - f_{01}$. However, for the semiconducting weak link Josephson junctions employed in the experiment the situation is more complex. Here the Josephson potential is governed by a limited number of possibly highly transparent Andreev bound states, requiring a more complex potential strongly dependent on the microscopics of the junction [167]. In the limit where the length of the junction is much shorter than the coherence length, one often employs a potential of the form

$$V(\phi) = -\sum_{i=1}^{N} \Delta_i \sqrt{1 - T_i \sin^2\left(\phi/2\right)}. \tag{8.3}$$

This equation describes N non-interacting channels with normal state transmission T_i and superconducting gap Δ_i [26]. For the case of a a single channel this type of expression has been shown to lead to good agreement with experiments, but when $N > 1$ it becomes highly non-trivial to uniquely determine the junction parameters from the transmon spectra alone [118, 296]. In order to circumvent this problem we operate the qubits near the pinch-off voltage of the junctions, where only a single level strongly contributes. Nevertheless, this leads to an additional complication: near pinch-off, the behavior of the junction is typically governed by accidental quantum dots, resulting in near-unity transparencies due to resonant tunneling (see Ref. [169] and chapter 4). In this case the charge dispersion of the transmon qubit can be drastically reduced beyond what is expected from its effective Josephson energy due to non-adiabatic phase dynamics. This effect is also encountered in our experiment, and has to be included in order to accurately fit the data. For this we extend the Josephson potential to include the presence of the higher lying Andreev bound states:

$$V(\phi) = \widetilde{\Delta}\begin{pmatrix} \cos\frac{\phi}{2} & \sqrt{1-T}\sin\frac{\phi}{2} \\ \sqrt{1-T}\sin\frac{\phi}{2} & -\cos\frac{\phi}{2} \end{pmatrix} \tag{8.4}$$

Here $\widetilde{\Delta}$ is an effective gap energy of the Andreev bound states, potentially reduced below that of the superconducting leads Δ_{nw} by confinement and charging effects (see Ref. [169] and chapter 4).

Having established the model for the nanowire transmon qubits, we now characterize the qubit parameters by measuring the remaining offset-charge dependence of the f_{01} and the two-photon $f_{02}/2$ transition frequencies for each of the qubits. We then

Qubit	f_r (GHz)	f_{01} (GHz)	T_1 (µs)	$E_\mathrm{J}^\mathrm{eff}/h$ (GHz)	$E_\mathrm{J}^\mathrm{eff}/E_c$	D (ns^{-1})
$\mathrm{Near}_\mathrm{Al}$	7.028	3.948	3.4	5.26	13.1	7.5
$\mathrm{Near}_\mathrm{NbTiN}$	6.873	3.864	2.6	5.07	12.8	7.4
$\mathrm{Far}_\mathrm{NbTiN}$	6.803	3.784	4.0	5.15	13.8	7.3
Far_Al	6.762	3.892	4.5	4.92	11.7	7.5

Table 8.1: Extracted qubit parameters at zero applied magnetic field. Estimated from the qubit's charge dispersion through Eqs. (8.1) and (8.4).

diagonalize the Hamiltonian of (8.2) using the potential of (8.4) and fit this to the measurements, resulting in a unique set of qubit parameters. These parameters are also tabulated in Table 8.1. We find that the qubits have comparable charging energies, close to the targeted value of 400 MHz. Furthermore, their effective Josephson energies $E_\mathrm{J}^\mathrm{eff} = \widetilde{\Delta}T/4$ are again similar, resulting in comparable quasiparticle proportionally constants D. Although the validity of Eq. (8.1) for weak link Josephson junctions is not strictly established, these estimates indicate that the chosen qubit setpoints do not bias the experiment towards positive effects of the phonon traps. Based on the obtained values of D and the loss rates reported in main text Fig. 2(d), we further estimate that the phonon injection creates non-equilibrium quasiparticle densities x_qp of up to 5×10^{-4} at the $\mathrm{Near}_\mathrm{NbTiN}$ qubit.

INJECTOR

We now discuss the setpoint chosen for the phonon injection junction. To start, we measure the so called 'pinchoff curve' of the junction by applying a constant bias voltage of $V_\mathrm{bias} = 1\,\mathrm{mV}$, several times beyond the expected superconducting gap of the nanowire. We then measure the current while varying the gate voltage applied to the junction [Fig. 8.8(a)]. For negative voltages, no current flows, until around −0.5 V where we observe an oscillatory onset of current. For larger gate voltages the current grows, eventually saturating and reaching several tens of nano-amperes. The oscillatory behaviour near pinch-off is once-more indicative of accidental quantum dots forming inside the junction region, similar to that seen in Fig. 8.7(a).

Further insight into the behavior of the junction is obtained by measuring the bias voltage dependent differential conductance G using lock-in amplification. As shown in Fig. 8.8(b-c), around zero bias voltage the junction portrays a region of strongly reduced conductance, indicative of a transport gap. The width of this region as a function of junction gate voltage is set by the superconducting gap of the nanowire Δ_nw, modified by an interplay of Coulomb effects and multiple Andreev reflection. For the setpoint used in the experiments we fix the junction gate voltage in the regime where the size of the transport gap is maximal, resulting in an estimated $\Delta_\mathrm{nw} = 270\,\mu\mathrm{eV}$ [Fig. 8.8(d)]. We note that the size of this gap could include residual effects of Coulomb blockade, however the value extracted is comparable to results found on nanowires from the same growth batch [299].

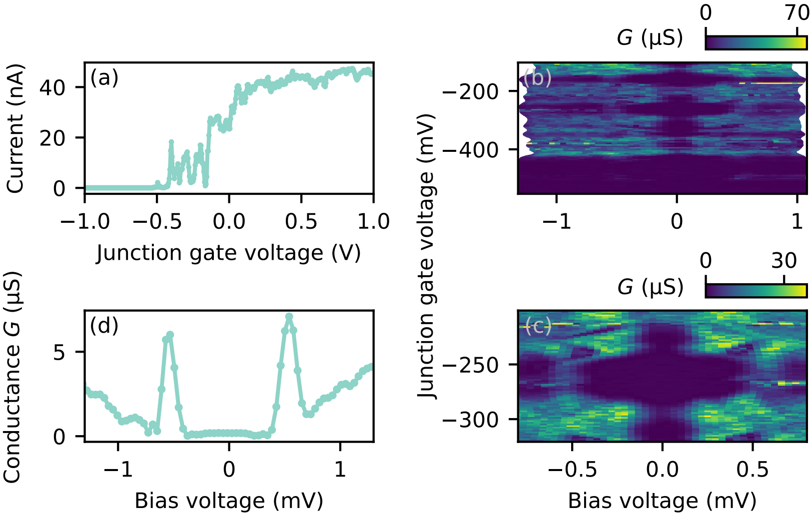

Figure 8.8: Characterization of the injector Josephson junction. (a) Pinchoff curve of the measured current at $V_{\text{bias}} = 1\,\text{mV}$. (b-c) 2D maps of differential conductance G as a function of the junction gate voltage and the bias voltage, where (c) shows a higher resolution zoom-in of the region used in the experiment. (d) Differential conductance versus bias voltage at a junction gate voltage of −251 mV, the setpoint used in the experiment. Note that this panel is not a linecut of panel (c); it is measured simultaneously with main text Fig. 2(a,c), and its position is slightly shifted with respect to the other panels due to hysteresis.

EXTENDED DATA

RATIOS OF LOSS RATES

Fig. 8.9 shows different ratios of added loss rate in the presence of a constant bias voltage across the injector junction. All six scenario's are compared. As discussed in the main text, this shows that the largest difference occurs between the Near$_{\text{NbTiN}}$ and the Far$_{\text{Al}}$ qubits, reaching up to 8 times more added loss for the Near$_{\text{NbTiN}}$ qubit, although this is potentially due to a combination of distance from the injector as well as the presence of the phonon traps. On equal footing, the Near$_{\text{Al}}$ qubit has up to 2.5 times smaller added loss rate than the Near$_{\text{NbTiN}}$ qubit, and the Far$_{\text{Al}}$ has up to 5 times smaller loss than the Far$_{\text{NbTiN}}$ suggesting that an increased area of the trapping region increases the efficacy. Furthermore, the Far$_{\text{NbTiN}}$ qubit performs up to 2 times better than the Near$_{\text{NbTiN}}$. As both qubits are not directly next to the Al phonon traps, this supports previous findings that qubit errors are strongest close to the position where the phonons originate [211, 214, 337]. Finally, we note that the ratio of added loss rates is a function of the bias voltage, the exact cause of which remains to be investigated.

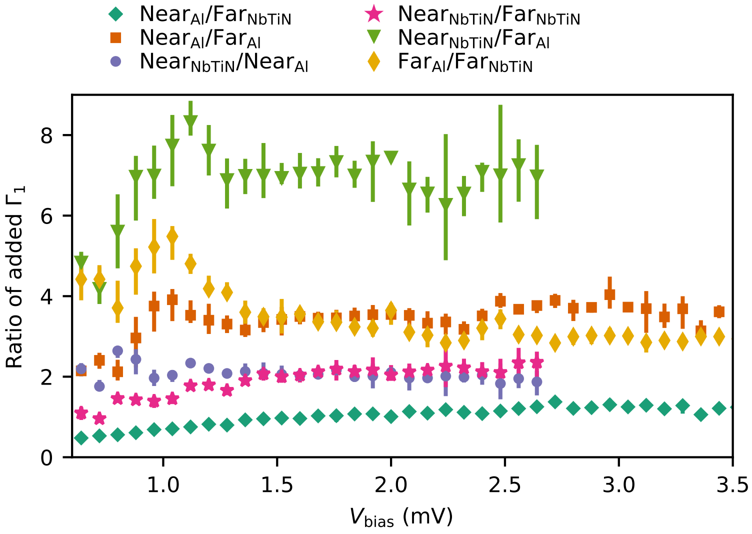

Figure 8.9: Ratio of added loss rates as measured for constant injection voltages at zero applied magnetic field [c.f. Fig. 2(d)]. The colors and symbols used in this figure do not match those used to identify the qubits throughout the text.

MAGNETIC FIELD DEPENDENCE

As discussed in the main text, we make use of the inherent magnetic field compatibility of the nanowire transmon qubits and their readout circuit to investigate the effect of the Al phonon traps turning normal. In previous works, nanowire-based superconducting qubits have been shown to be operable up to parallel fields in excess of 1 T [203, 252, 313]. In Fig. 8.10 we show the evolution of the four nanowire transmon qubits used in this work as a function of the magnetic field. Up to 70 mT, only modest changes in qubit frequency of less than 5% are found, leading to a negligible change in the quasiparticle proportionality constant D of Eq. (8.1). This shows that the absence of changes in the added loss rates versus magnetic field can indeed be attributed to the phonon traps having a constant effect at all investigated fields, rather than to a field dependence canceled out by changes in qubit sensitivity. Furthermore, we note that the qubits do not all have the same field evolution; in particular the Far_{Al} qubit appears more resilient over the range of fields explored. We hypothesize this occurs because the magnetic field evolution of the nanowires is governed not only by the reduction of the superconducting gap in the Al shell, but also by orbital effects that depend on the spatial profile of the occupied transport channels inside the nanowire [355].

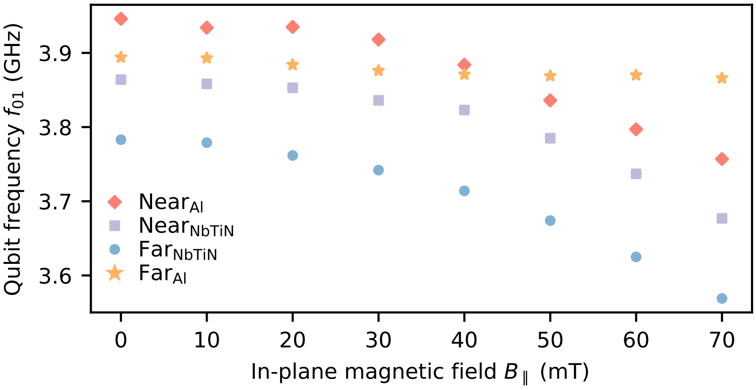

Figure 8.10: Magnetic field dependence of nanowire transmon qubit frequencies f_{01}.

9

CONCLUSION & OUTLOOK

> *Beware of the man who works hard to learn something, learns it, and finds himself no wiser than before.*
>
> Bokonon, Cat's Cradle

In this concluding chapter we summarize the key results of each experimental chapter and discuss possible avenues of future research.

9.1. CHAPTER 4

In this chapter, we experimentally investigate and observe the proposed vanishing of Coulomb oscillations in a nearly-open superconducting island. To do so we measure the charge dispersion of an island connected to ground via a semiconducting weak-link hosting a resonant level. The device constitutes an offset-charge-sensitive nanowire transmon, whose junction transparency is set by tunneling through the resonant level and can be accurately tuned in-situ using an electrostatic gate. For elevated junction transparencies, we observe rapid suppression of the charge dispersion consistent with the proposed scaling law resulting from diabatic phase evolution of Andreev bound states.

The demonstration of junctions with near-unity transparency motivates follow-up experiments that exploit the resulting non-standard energy-phase relationship, for example to construct what are known as protected superconducting qubit designs. A first instance of such a protected design, colloquially known as the $\cos(2\phi)$ qubit, encodes its qubit states in the parity of Cooper pairs [29, 45, 281, 295]. In short, this encoding results in a strongly reduced overlap between the computational states (composed of even and odd Cooper pair number states), suppressing transition matrix elements and thereby enhancing the qubit lifetime [see Fig. 9.1(c)]. However, a challenge with designs that realize an effective $\cos(2\phi)$ potential using conventional circuit elements (i.e. SIS junctions) is the need for complex circuit topologies with demanding constraints on parameter disorder [112]. These constraints can be strongly simplified through the usage of a transparent semiconducting weak-link [see Fig. 9.1(a)] [181]. In this design the higher harmonics of the Josephson potential that develop at large junction transparencies [c.f. Eq. (2.20)] are combined with the destructive interference that takes place in a SQUID at $\phi_{\mathrm{ext}} = \pi$, fully canceling the leading $E_{\mathrm{J}}^{(1)}\cos(\phi)$ term. This results in a circuit with the desired Hamiltonian

$$H = 4E_{\mathrm{c}}\left(N - N_{\mathrm{g}}\right)^2 + E_{\mathrm{J}}^{(2)}\cos(2\phi), \tag{9.1}$$

up to corrections from higher harmonics of the potential. A challenge with this implementation is the strong dependence on fine-tuned junction properties, which are known to be sensitive to charge noise [203]. Additionally, achieving a large enough $E_{\mathrm{J}}^{(2)}/E_{\mathrm{c}}$ ratio to suppress offset-charge sensitivity would require a very large capacitance, due to the smallness of the second harmonic. Finally, at the point of maximal protection ($\phi_{\mathrm{ext}} = \pi$) conventional qubit operation poses a challenge, as the built-in protection decouples the qubit from the environment. However, this is a challenge that many protected designs face, for which novel schemes of qubit manipulation will have to be developed [236, 295].

An alternative follow-up experiment focuses on a direct measurement of the evolution of 2π and 4π quantum phase slip rates with increasing junction transparency, which underpin the suppression of charge dispersion investigated in this chapter. Indeed, as was pointed out by dr. Bernard van Heck after publication, the underlying connection between charge dispersion and quantum phase slips can be understood from the Aharonov-Casher effect. At the expense of mathematical rigor, one can picture a phase slip as a fluxon encircling the transmon island, thus "picking up" the offset charge (similar to how a charge going around a loop "picks up" the flux in the Aharanov-Bohm effect). The suppressed amplitude of 2π phase slips as the transparency approaches one is thus what leads to the observed suppression in sensitivity to the offset charge, such that charge dispersion is effectively a measure of the combined phase slip rates. We

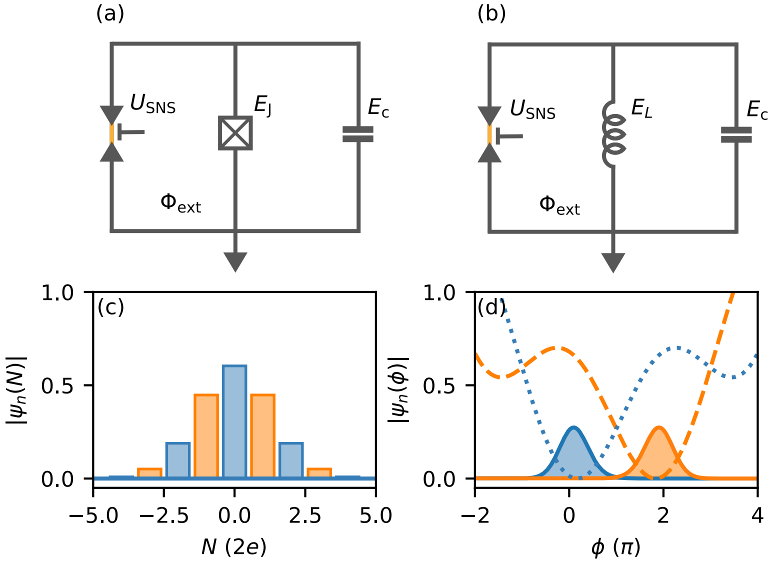

Figure 9.1: Protected qubit designs based on semiconducting weak-links. (a) Circuit diagram implementing the proposed $\cos(2\phi)$ qubit. A weak-link with Josephson potential $U_{\rm SNS}$ is tuned to the high-transparency regime with a nearby gate-electrode and placed in parallel to an SIS junction with Josephson energy $E_{\rm J}$. An external flux $\Phi_{\rm ext}$ threads the resulting SQUID loop, which is shunted by a capacitance with a charging energy $E_{\rm c}$. (b) Circuit diagram implementing the proposed $\cos(\phi/2)$ qubit. A weak-link with Josephson potential $U_{\rm SNS}$ is tuned to the high-transparency regime with a nearby gate-electrode and placed in parallel to an inductor with inductive energy E_L. An external flux $\Phi_{\rm ext}$ threads the resulting loop, which is shunted by a capacitance with charging energy $E_{\rm c}$. (c) Absolute value of the wavefunction for the first two levels of Eq. 9.1 expressed in the Cooper pair number basis. (d) Absolute value of the wavefunction for the first two levels of Eq. 9.2 expressed in the phase basis. Potential is shown in dotted/dashed lines (not to scale).

propose that a direct measurement of the phase slip rate could instead be made by embedding a high transparency Josephson junction not into a transmon but into fluxonium circuit [see Fig. 9.1(b)] [252]. In this system both the 2π and 4π phase slip rates become explicitly observable in the transition frequency spectrum, measurable as independent quantities through standard spectroscopy techniques [206]. A direct study of the phase slip rate as the transparency approaches unity would allow for a deeper understanding of the crossover between 2π and 4π periodicity that takes place in the junction.

If one is able to approach the limit of full transparency, the circuit of Fig. 9.1(b) would furthermore allow for investigation of an additional protected qubit design. Taking the high transparency limit of Eq. (2.21), the circuit is governed by the Hamiltonian

$$H = 4E_{\rm c}N^2 + \frac{1}{2}E_L\left(\phi - \phi_{\rm ext}\right)^2 - |\Delta|\cos(\phi/2)\sigma_z. \tag{9.2}$$

This idealized Hamiltonian gives rise to what is colloquially known as the $\cos(\phi/2)$ qubit or the bifluxon [146]. It is essentially the dual to the $\cos(2\phi)$ qubit discussed above, where the qubit states are now protected by the parity of fluxons rather than Cooper pairs. Indeed, for a perfect $\cos(\phi/2)$ junction 2π-phase slips are fully suppressed, such that the two neighboring fluxon parities are decoupled, which should once-more lead to enhanced qubit lifetimes [see Fig. 9.1(d)]. The implementation of the bifluxon circuit with conventional SIS junctions again places stringent requirements on the targeting of circuit parameters [146], which would be alleviated in this nanowire-based design. Whether a sufficient degree of protection is achievable for realistic parameter values, however, is subject to a more detailed investigation.

9.2. CHAPTER 5

In this chapter we show that a transmon circuit can act as a sensitive probe for quantum impurities, specifically of quantum dots with superconducting leads. Compared to the vast body of experiments that preceded our measurements, we demonstrate a significantly enhanced time and energy resolution, down to microseconds and megahertz scales. This allows us to explore regimes of the phase diagram of the system that, to our knowledge, have never before been accessed experimentally, and also to measure the dynamics of quasi-particles tunneling into and out of the quantum dot in real-time. Our use of a transmon circuit to understand a paradigmatic quantum impurity model furthermore demonstrates that circuit-QED techniques can be applied to fundamental questions in mesoscopic physics as well as condensed matter in general, and that in doing so they can supplement conventional quantum transport experiments.

Several continuations of these experiments are put forward at the end of the chapter, such as the enticing concept of creating the charging energy protected Andreev spin qubit studied in chapter 7. An additional avenue of exploration we now put forward is to use fast gate-based switching to implement two-qubit gates in transmon devices. At the time of writing, large circuits containing many tens of transmon qubits [1, 133] often make use of flux-tunable coupling, which can be turned on and off on demand using fast pulses [see Fig. 9.2(a)] [56, 62, 301, 341]. However, such schemes necessarily involve sizeable currents running through the control lines and the ground plane of the chip, which is problematic due to cross-coupling to other devices, and additionally produce non-negligible dissipation [171]. An all-electric alternative coupling element would alleviate both of these problems, as gate voltages can be applied locally and via high-impedance electrodes. A first option is to use a semiconducting weak link, for which the Josephson energy (and thus the coupling) can be controlled with a gate voltage [see Fig. 9.2(b)]. However, a downside of this approach is that one often requires comparatively large voltage swings to tune the junction from pinched off to open, potentially tens to hundreds of millivolts, and that the generally encountered gate-dependencies are highly non-monotonic, see e.g. Fig. 5.17. This type of implementation is thus particularly susceptible to gate-hysteresis, and would not easily allow for net-zero pulse schemes [266].

An alternative is to use a quantum dot with superconducting leads as the tunable element, operated close to the singlet-doublet transition [see Fig. 9.2(c)]. As demonstrated in this chapter, in the vicinity of the singlet-doublet transition switches between vanishing and sizable Josephson energy can be enacted with voltages on the single millivolt scale, potentially with enough contrast to enable fast and high-fidelity coupling elements. Stability and hysteresis is also not a limitation, as evidenced by the large two-dimensional gate maps of e.g. Fig. 5.5, which show no signs of hysteresis over tens of millivolts, nor any charge jumps over timescales of days. Net-zero schemes should even be

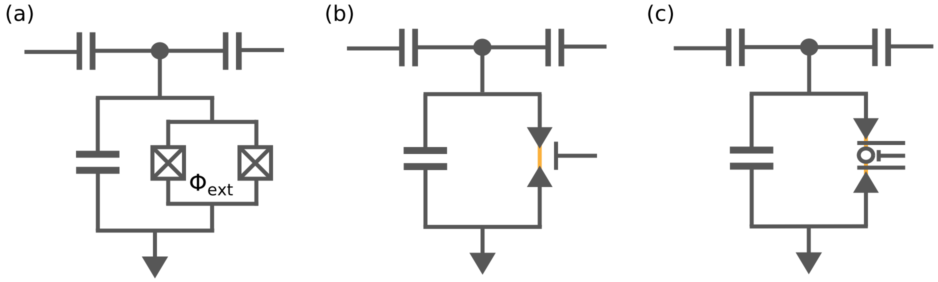

Figure 9.2: Tunable qubit-qubit couplers. (a) Coupling element based on SIS junctions, with flux-tunable Josephson energy by virtue of the SQUID. (b) Coupling element based on a semiconducting weak-link, with gate-tunable Josephson energy by virtue of the field effect. (c) Coupling element based on a quantum dot with superconducting leads, with gate-tunable Josephson energy by virtue of the singlet-doublet transition.

achievable with improved decoupling of the electostatic gates [131], as the ideal plunger gate response is symmetric around half-filling of the dot. One can however question whether the quasiparticle dynamics deep inside the singlet and doublet regimes are fast enough to adjust the parity during rapid (tens of ns) gate sequences. If they are not, then perhaps such a scheme can instead be used to probe quasiparticle dynamics beyond the μs timescales resolved in this chapter. Finally, we note that both of these proposals reintroduce charge sensitivity into the charge-insensitive transmon platform, the costs of which have to be weighed against those of flux control and sensitivity [203].

Finally, as an alternative route of further exploration we note that determining the ground state properties of a quantum dot with superconducting leads is numerically expensive. Indeed, even though the calculations in this chapter applied only to a single quantum dot level, the NRG calculations consumed many CPU hours on a high performance cluster [350]. The computations were nevertheless still tractable. This could be made more strenuous by investigating hybrid systems containing multiple relevant dot orbitals, chains of quantum dots, or those in which the superconducting leads are genuine superconducting islands, both with sizable charging energy and a finite level spacing. In this case even more computationally expensive density-matrix renormalization group (DMRG) calculations with strongly simplified models for the leads are likely the best that can be employed [239, 352]. If one were to add spin-orbit interaction and Zeeman fields to this, lifting various of the model symmetries, the relevant phase diagrams might quickly becomes untractable. Yet in principle they remain measurable using the techniques introduced in this chapter, with many of the parameters tune-able in situ. Additionally, S-QD-S chains map to a variety of Hamiltonians from solid state physics, such as finite Hubbard chains and Luttinger liquids, which are of definite interest [209]. Follow up experiments investigating this direction could therefore constitute viable near-term analog quantum simulators of computationally hard problems. One has to admit, however, that their outcomes might also be hard to verify.

9.3. CHAPTER 6

In this chapter we have implemented a superconducting transmon qubit with a fully controllable quantum dot as its Josephson element to once-more exploit the high energy resolution circuit QED techniques. Thanks to our sensitive measurement circuit, we are able to resolve the predicted spin splitting of the quantum dot's doublet states due to the spin-orbit interaction in InAs. Furthermore, in the presence of magnetic field we elucidate and demonstrate the appearance of the anomalous Josephson effect. These findings are all well-described by an analytical model, and their physical origin is understood through numerical renormalization group calculations. Moreover, we show that the spin states can be directly manipulated by applying microwaves to a bottom gate, which facilitates the novel and improved implementation of Andreev spin qubits in chapter 7.

In addition to coherent manipulation of the spin states, another avenue of exploration (both theoretical and experimental) became apparent in the post-analysis of the experiments. While investigating the NRG calculations detailed in Sec. 6.7, we encountered an unanticipated effect at elevated Zeeman energies. As shown in Fig. 9.3, we find that as the Zeeman energy is increased, the phase ϕ at which the spin-flip transition takes on its minimum (maximum) value moves away from its $\pi/2$ ($3\pi/2$) baseline value governed by the $\sin(\phi)$ term underlying the spin splitting, instead moving towards π (2π) governed by e.g. a $\cos(\phi)$ term. In addition, the frequency dispersion with phase grows as a function of Zeeman energy.[1] These findings are not consistent with the minimal model of Eq. (6.1) where the Zeeman energy enters as a phase-independent contribution. However, the observed behavior can be reproduced with a simple modification to the Hamiltonian

$$\frac{1}{2}\vec{E}_Z\cdot\vec{\sigma} \rightarrow \frac{1}{2}\vec{E}_Z\cdot\vec{\sigma}\left[1+\kappa\cos(\phi)\right], \tag{9.3}$$

where κ is a phenomenological parameter. Indeed, setting $\kappa = 0.22$, the modified analytical model is able to reproduce the numerical results.

In recent work we have shown that this effect can be understood as the impurity Knight shift: an energy shift resulting from the hybridization between the quantum dot and its superconducting leads [240]. Given that the dot and the leads have a different g-factor, their hybridization results in an effective g-factor renormalization. And as the hybridization between the dot and the leads is phase dependent (as evidenced by e.g. the divergent doublet phase of Fig. 5.5), this renormalized g-factor also has a phase-dependent contribution, resulting in the observed modification to the analytical model. This effect had not previously been reported in the literature, with the impurity Knight shift only having been studied for N-QD and S-QD geometries, but not for the phase-dependent S-QD-S system [223].

Calculations show that this effect is present already in the single-impurity Anderson model, without the extensions of multi-level effects and spin-orbit coupling. It only requires a difference in g-factors between the dot and its leads. This is of relevance because the modification given in Eq. (9.3) leads to an energy shift that is both spin and phase dependent, precisely the type of dependence for which Andreev spin qubits have thus far

---

[1] In this calculation the size of the superconducting gap $|\Delta|$ is assumed to be constant as a function of Zeeman energy.

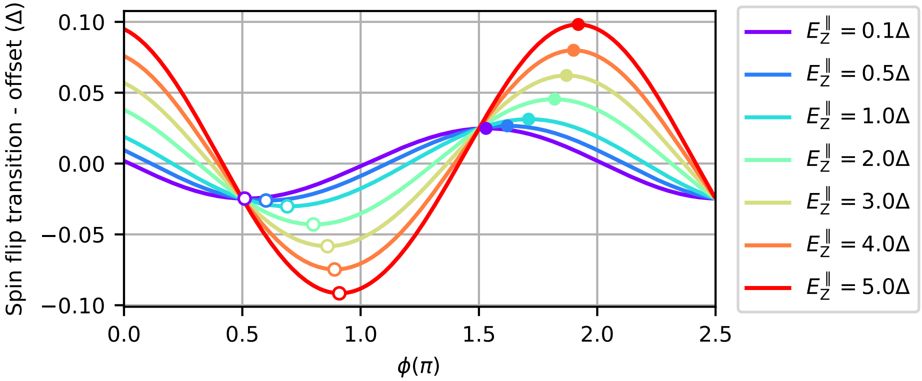

Figure 9.3: Evolution of the spin-flip transition energy versus phase difference ϕ as a function of a Zeeman term parallel to the spin-orbit direction. The average, phase-independent transition energy offset is subtracted to facilitate comparison. Open (filled) markers indicate the minimum (maximum) transition energy versus phase. Calculations are performed for the extended SIAM model using the NRG method outlined in Sec. 6.7.

relied on spin-orbit coupling. Indeed, if the factor κ is made large (through e.g. a careful tuning of the microscopic parameters of the S-QD-S system), this effect could allow for the implementation of Andreev spin qubits in materials other than those with strong spin-orbit coupling. While large g-factors and strong spin-orbit coupling often go together, we note that one merely requires a strong variation in g-factors between the dot and the leads, which could potentially be achieved through strong confinement [159]. While at this stage it remains speculative, this could expand the Andreev spin qubit platform towards a much broader range of materials, in particular those not plagued by the large nuclear spin of III-V semiconductors.

9.4. CHAPTER 7

In this chapter we have made significant progress in the experimental realization of superconducting spin qubits, also known as Andreev spin qubits (ASQ). We demonstrate the essential requirement of stabilizing the qubit subspace by incorporating a large $U_{ee}/|\Delta|$ quantum dot inside the Josephson junction. This establishes a fundamentally novel approach for overcoming qubit leakage through charging energy, improving the ASQ parity lifetime by more than two orders of magnitude. Additionally, using an external magnetic field, we can control the qubit frequency over a range of more than 10 GHz. We furthermore achieve direct coherent manipulation of the spin-flip transition, resulting in qubit control more than an order of magnitude faster than in the previous realization of the ASQ. We finally demonstrate that this novel qubit can be used to achieve its main promised feature: direct qubit-qubit coupling mediated by supercurrent.

As a continuation of the experiments in this chapter, an exciting avenue of further exploration is the coupling of the ASQ to other qubits. Our calculations in Sec. 7.6 indicate that the regime of ultrastrong coupling (where the coupling is a significant fraction of the qubit frequencies) between ASQ and transmon should already achievable through modest modifications to the experiment, allowing one to probe the limits of light-matter

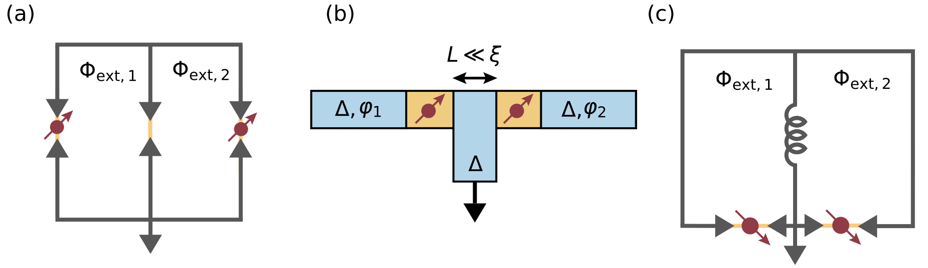

Figure 9.4: Coherent coupling between Andreev spin qubits. (a) Circuit diagram of inductively coupled Andreev spin qubits, with a tunable coupling mediated by external flux and a semiconducting weak-link [234]. (b) Schematic depiction of a spinful Andreev molecule, constructed from two closely spaced Andreev spin qubits separated via a grounded superconductor. (c) Circuit diagram of Andreev spin qubits coupled via wavefunction overlap, with a tunable coupling tuned by external flux.

interaction beyond the rotating-wave-approximation. This is of particular interest given the two-level nature of the ASQ. Additionally, engineering the coupling between two different ASQ would allow for the demonstration of two-qubit gates within this nascent qubit platform. Two approaches for coupling have been proposed in the literature: one can make use of inductive coupling, relying on the supercurrent carried by each qubit [234], or one can place the ASQ in close vicinity to each other, relying on direct wavefunction overlap across a short superconducting segment [297].

The first type of coupling could be implemented as shown in Fig. 9.4(a). Here two ASQ are defined in separate junctions, and are embedded in a double loop structure to allow for individual control of the phases across each junction. The presence of a third, gate-tunable junction based on a semiconducting weak-link allows for tuning of the inductive coupling strength in-situ. The approach based on direct wavefunction overlap instead builds on proposals for Andreev molecules, originally formulated for the singlet states of the junction [164, 247, 248]. As depicted in Fig. 9.4(b), it involves two junctions hosting ASQ that are separated by a narrow (shorter than the superconducting coherence length ξ) region of superconductor, connected to ground such that the interaction between the modes is not suppressed by the charging energy of the superconductor. Once-more embedding this system into a loop, coherent coupling between the ASQ could be made visible using standard spectroscopy techniques, see Fig. 9.4(c). In this design, motivated by experiments on a “fluxonium molecule” [165], the presence of an additional inductor again allows for control of the phases across each individual junction with external flux. Furthermore, we note that the same geometry can be used to study conventional (spinless) Andreev molecules, for which at the time of writing only an implementation without external flux dependence been realized [178]. If the ASQ are implemented using quantum dots with superconducting leads, both types of molecule are even configurable in-situ by tuning the occupation of the dot from doublet to singlet. Finally, we note a close connection between this geometry and recent experiments on artificial Kitaev chains and triplet pairing [85, 197, 326], signatures of which might also be accessible via microwave spectroscopy in related geometries.

A separate but related avenue of exploration is the study of double quantum dots with superconducting leads: an S-DQD-S junction. Such junctions essentially come in three types.[2] As illustrated in Fig. 9.5, one can consider a single quantum dot with multiple interacting orbitals, two quantum dots placed in parallel, and two quantum dots placed in series. While in particular the latter system has seen initial experimental investigation [39, 270], much of the predicted physics remains unexplored. Of particular interest is the presence of a singlet-triplet transition, leading to the formation of a triplet ground state in which both levels host an aligned spin. In bulk superconductors triplet spin pairing corresponds to orbital p-wave symmetry, which can give rise to the onset of topological superconductivity and the appearance of Majorana zero modes [326]. The latter holds promise for topologically protected quantum computing schemes, and investigating its building blocks in simple model systems is of great value in this active field of research. We refer the interested reader to Ref. [93] for a recent review of the field, whose introduction lists eight additional review articles.

Experiments aiming to investigate triplet pairing in S-DQD-S systems face two primary challenges: realizing the triplet ground state, and producing a measurable triplet supercurrent. The first challenge depends primarily on the geometry of the DQD. Serial DQD systems tend to exhibit antiferromagnetic super-exchange between the dots, such that the zero-field ground state is a singlet, and the presence of a properly aligned external magnetic field is thus required in order to reach a triplet ground state [151]. At the same time, in this system most of the degrees of freedom (such as tunnel couplings and relative energy levels) are spatially separated and individually tune-able with gate electrodes. For both a strongly interacting parallel and a multi-orbital configuration the situation is different. Here interactions between the levels can be ferromagnetic by virtue of Hund's rule, and as such these geometries can exhibit a triplet ground state even in the absence of a magnetic field, simplifying their study [188, 259]. Yet the multi-orbital case faces the largest challenges when it comes to in-situ control of parameters, as each level is controlled by the same gate electrodes. The case of parallel dots instead introduces the formation of a loop, which might lead to intricate interference effects, both interesting and challenging [310].

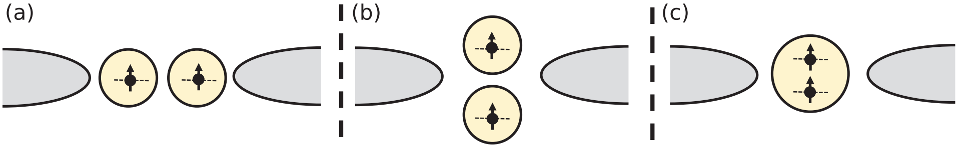

Figure 9.5: Three configurations of spin-triplet S-DQD-S junctions: serial (a), parallel (b), and multi-orbital (c).

The challenge of finding a measurable supercurrent is that of overcoming Pauli spin blockade. Indeed, when both quantum dots are occupied by the same spin, spin-conserving cotunneling trajectories that transfer a Cooper pair tend to involve double occupancy of one of the levels [39]. For large values of U_{ee} this is energetically unfavorable, which strongly suppresses the supercurrent. However, for N-DQD-N systems it is known that the presence of SOI (among other elements) may lift spin-blockade [66], and it has since

---

[2] It could be argued that an S-QD-S-QD-S implementation of Fig.9.4(b) is a fourth type.

been proposed that its inclusion in an S-DQD-S system would also lead to a finite triplet supercurrent [84]. While its magnitude might still be small, it should be readily measurable in the transmon geometry of chapters 5 to 7, with which picoampere sensitivity should be attainable.

9.5. CHAPTER 8

In this chapter we experimentally investigate a recently proposed mitigation method that serves to protect superconducting qubit processors against correlated errors from ionizing radiation [211]. Specifically, we implement so-called phonon traps using a galvanically isolated material with a small superconducting gap, and demonstrate their effectiveness in protecting transmon qubits against deterministically injected high energy phonons. Our work shows that phonon traps are a promising candidate for mitigating correlated errors, which can be implemented without introducing qubit dissipation from coupling to lossy materials, and with little added strain on the increasing complex task of control line routing.

Our results furthermore demonstrate that technology previously developed in microwave kinetic inductance detectors (MKID) can be made applicable to transmon qubits, highlighting the potential benefits of cross-pollination between these two domains of research. This motivates investigating other methods of phonon control pursued for MKIDs, such as placing the phonon-sensitive elements on a thin SiN membrane [72, 150]. As the first implementations of membranes in superconducting circuits have already been demonstrated [244], such an approach should also be readily applicable to transmon islands [see Fig. 9.6(a)]. Here one should aim to make the electric field participation ratio of the potentially lossy membrane as small as possible, however.

Other avenues of substrate engineering have also been proposed for MKIDs, such as phononic crystals [127, 261], and the usage of bilayer metal films with vastly different Debye temperatures, blocking phonons by virtue of there being no modes for them to occupy [353]. An idea that, to our knowledge, has yet to be proposed in this context, is that of an acoustic Bragg reflector [see Fig. 9.6(b)]. By interchanging layers of insulating material with vastly different acoustic properties, phononic stopbands could be created that target phonons at energy $2\Delta_{\mathrm{qubit}}$. We profess that such a layered approach might be difficult to reconcile with the aforementioned sensitivity of transmon qubits to lossy dielectric materials.

Finally we note that for all approaches which make it difficult for phonons to enter the transmon island, it is imperative that the few phonons that do make it through can be rapidly disposed of. The phonons would otherwise end up trapped in the qubit layer, stuck in repeating cycles of Cooper pair breaking and recombination, leading to strongly lengthened recovery times following (now infrequent) error events. This is readily solved by placing galvanically connected quasiparticle traps on the qubit electrodes, which dissipate the energy of phonons that do manage to excite quasiparticles in the qubit [211, 264, 265].

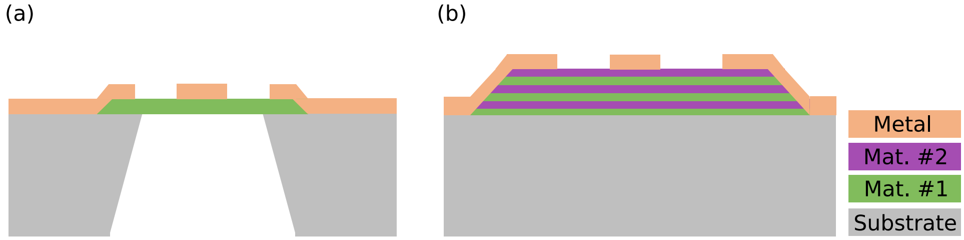

Figure 9.6: Phonon mitigation through substrate engineering. (a) Schematic depiction of a superconducting circuit placed on a membrane. (b) Schematic depiction of a superconducting circuit placed on an acoustic Bragg reflector. Panels depict device cross-sections and are not to scale.

BIBLIOGRAPHY

[1] R. Acharya, I. Aleiner, R. Allen, T. I. Andersen, M. Ansmann, et al. Suppressing quantum errors by scaling a surface code logical qubit. *arXiv e-prints*, July 2022.

[2] I. Affleck, J.-S. Caux, and A. M. Zagoskin. Andreev scattering and Josephson current in a one-dimensional electron liquid. *Phys Rev B*, 62, 2000.

[3] R. Aguado. A perspective on semiconductor-based superconducting qubits. *Appl Phys Lett*, 117(24), Dec. 2020.

[4] S. Ahn, H. Pan, B. Woods, T. D. Stanescu, and S. Das Sarma. Estimating disorder and its adverse effects in semiconductor Majorana nanowires. *Phys. Rev. Materials*, 5, Dec. 2021.

[5] I. Aleiner and L. Glazman. Mesoscopic charge quantization. *Phys Rev B*, 57(16), Apr. 1998.

[6] C. K. Andersen, A. Remm, S. Lazar, S. Krinner, N. Lacroix, G. J. Norris, M. Gabureac, C. Eichler, and A. Wallraff. Repeated quantum error detection in a surface code. *Nat Phys*, 16, June 2020.

[7] P. Anderson. Special effects in superconductivity. In *Lectures on the Many-body Problems*, pages 113–135. Elsevier, 1964.

[8] P. W. Anderson. Random-phase approximation in the theory of superconductivity. *Physical Review*, 112(6):1900–1916, dec 1958.

[9] P. W. Anderson. How Josephson discovered his effect. *Physics Today*, 23(11):23–29, nov 1970.

[10] P. W. Anderson. More is different. *Science*, 177(4047):393–396, aug 1972.

[11] P. W. Anderson and J. M. Rowell. Probable observation of the Josephson superconducting tunneling effect. *Phys Rev Lett*, 10(6):230–232, mar 1963.

[12] A. E. Antipov, A. Bargerbos, G. W. Winkler, B. Bauer, E. Rossi, and R. M. Lutchyn. Effects of Gate-Induced Electric Fields on Semiconductor Majorana Nanowires. *Phys. Rev. X*, 8(3), Aug. 2018.

[13] F. Arute, K. Arya, R. Babbush, D. Bacon, J. C. Bardin, et al. Quantum supremacy using a programmable superconducting processor. *Nature*, 574(7779), Oct. 2019.

[14] D. V. Averin. Coulomb blockade in superconducting quantum point contacts. *Phys Rev Lett*, 82(18), May 1999.

[15] D. V. Averin, A. B. Zorin, and K. K. Likharev. Bloch oscillations in small Josephson junctions. *Zh. Eksp. Teor. Fiz*, 88(August 1984), Aug. 1985.

[16] J. Avila, E. Prada, P. San-Jose, and R. Aguado. Majorana oscillations and parity crossings in semiconductor-nanowire-based transmon qubits. *Phys. Rev. Research*, 2(3), Mar. 2020.

[17] J. Avila, E. Prada, P. San-Jose, and R. Aguado. Superconducting islands with semiconductor-nanowire-based topological Josephson junctions. *Phys Rev B*, 102(9), Mar. 2020.

[18] P. F. Bagwell. Suppression of the Josephson current through a narrow, mesoscopic, semiconductor channel by a single impurity. *Phys Rev Lett*, 46(19), Nov. 1992.

[19] H. Barakov and Y. V. Nazarov. Supercurrent in the presence of direct transmission and a resonant localized state. *arXiv e-prints*, Jan. 2022.

[20] J. Bardeen. Electron-phonon interactions and superconductivity. In *Cooperative Phenomena*, pages 63–78. Springer Berlin Heidelberg, 1973.

[21] J. Bardeen, L. N. Cooper, and J. R. Schrieffer. Theory of superconductivity. *Physical Review*, 108(5):1175–1204, dec 1957.

[22] C. Barthel, J. Medford, C. M. Marcus, M. P. Hanson, and A. C. Gossard. Interlaced dynamical decoupling and coherent operation of a singlet-triplet qubit. *Phys Rev Lett*, 105, Dec. 2010.

[23] J. Baselmans, S. Yates, P. Diener, and P. de Visser. Ultra low background cryogenic test facility for far-infrared radiation detectors. *J Low Temp Phys*, 167(3-4), Jan. 2012.

[24] G. Batey and G. Teleberg. Principles of dilution refrigeration. Oxford Instruments, 2015.

[25] J. Bauer, A. Oguri, and A. C. Hewson. Spectral properties of locally correlated electrons in a Bardeen-Cooper-Schrieffer superconductor. *J. Phys.: Condens. Matter*, 19(48):486211, nov 2007.

[26] C. W. Beenakker. Universal limit of critical-current fluctuations in mesoscopic Josephson junctions. *Phys Rev Lett*, 67(27), Dec. 1991.

[27] C. W. J. Beenakker and H. van Houten. Resonant Josephson Current Through a Quantum Dot. *Sprin S Ele*, Sept. 1992.

[28] C. W. J. Beenakker and H. van Houten. The Superconducting Quantum Point Contact. *Nanostructures and Mesoscopic Systems*, Dec. 1992.

[29] M. T. Bell, J. Paramanandam, L. B. Ioffe, and M. E. Gershenson. Protected josephson rhombus chains. *Phys Rev Lett*, 112(16), Apr. 2014.

[30] F. S. Bergeret, A. L. Yeyati, and A. Martín-Rodero. Interplay between Josephson effect and magnetic interactions in double quantum dots. *Phys Rev B*, 74(13):132505, oct 2006.

[31] B. Béri, J. H. Bardarson, and C. W. J. Beenakker. Splitting of Andreev levels in a Josephson junction by spin-orbit coupling. *Phys Rev B*, 77(4), Jan. 2008.

[32] R. Bianchetti, S. Filipp, M. Baur, J. M. Fink, M. Göppl, P. J. Leek, L. Steffen, A. Blais, and A. Wallraff. Dynamics of dispersive single-qubit readout in circuit quantum electrodynamics. *Phys Rev A*, 80(4), Oct. 2009.

[33] A. Blais, A. L. Grimsmo, S. Girvin, and A. Wallraff. Circuit quantum electrodynamics. *Rev Mod Phys*, 93(2), May 2021.

[34] A. Blais, A. L. Grimsmo, S. M. Girvin, and A. Wallraff. Circuit quantum electrodynamics. *Rev Mod Phys*, 93, May 2021.

[35] A. Blais, R.-S. Huang, A. Wallraff, S. M. Girvin, and R. J. Schoelkopf. Cavity quantum electrodynamics for superconducting electrical circuits: An architecture for quantum computation. *Phys Rev A*, 69, June 2004.

[36] F. Borjans, X. G. Croot, X. Mi, M. J. Gullans, and J. R. Petta. Resonant microwave-mediated interactions between distant electron spins. *Nature*, 577(7789), Jan. 2020.

[37] F. Borsoi, G. P. Mazur, N. van Loo, M. P. Nowak, L. Bourdet, K. Li, S. Korneychuk, A. Fursina, J. Wang, V. Levajac, E. Memisevic, G. Badawy, S. Gazibegovic, K. van Hoogdalem, E. P. A. M. Bakkers, L. P. Kouwenhoven, S. Heedt, and M. Quintero-Pérez. Single-shot fabrication of semiconducting–superconducting nanowire devices. *Adv Funct Mater*, 31(34), June 2021.

[38] V. Bouchiat, D. Vion, P. Joyez, D. Esteve, and M. H. Devoret. Quantum Coherence with a Single Cooper Pair. *Phys Scripta*, T76(1), Jan. 1998.

[39] D. Bouman, R. J. J. van Gulik, G. Steffensen, D. Pataki, P. Boross, P. Krogstrup, J. Nygård, J. Paaske, A. Pályi, and A. Geresdi. Triplet-blockaded josephson supercurrent in double quantum dots. *Phys Rev B*, 102(22):220505, dec 2020.

[40] A. I. Braginski. Consequences of Brian Josephson's theoretical discovery. *Journal of Superconductivity and Novel Magnetism*, 34(6):1597–1600, dec 2020.

[41] J. Braumüller, L. Ding, A. P. Vepsäläinen, Y. Sung, M. Kjaergaard, T. Menke, R. Winik, D. Kim, B. M. Niedzielski, A. Melville, J. L. Yoder, C. F. Hirjibehedin, T. P. Orlando, S. Gustavsson, and W. D. Oliver. Characterizing and optimizing qubit coherence based on SQUID geometry. *Phys. Rev. Applied*, 13(5), May 2020.

[42] T. Brecht, W. Pfaff, C. Wang, Y. Chu, L. Frunzio, M. H. Devoret, and R. J. Schoelkopf. Multilayer microwave integrated quantum circuits for scalable quantum computing. *npj Quantum Inf.*, 2(1), Feb. 2016.

[43] L. Bretheau. *Localized Excitations in Superconducting Atomic Contacts : Probing the Andreev Doublet.* PhD thesis, Paris-Saclay University, 2013.

[44] L. Bretheau, Ç. Ö. Girit, H. Pothier, D. Esteve, and C. Urbina. Exciting Andreev pairs in a superconducting atomic contact. *Nature*, 499(7458), July 2013.

[45] P. Brooks, A. Kitaev, and J. Preskill. Protected gates for superconducting qubits. *Phys Rev A*, 87(5), May 2013.

[46] A. Brunetti, A. Zazunov, A. Kundu, and R. Egger. Anomalous Josephson current, incipient time-reversal symmetry breaking, and Majorana bound states in interacting multilevel dots. *Phys Rev B*, 88(14), Oct. 2013.

[47] R. Bulla, T. A. Costi, and T. Pruschke. The numerical renormalization group method for quantum impurity systems. *Rev Mod Phys*, 80(2), Apr. 2008.

[48] J. Bylander, S. Gustavsson, F. Yan, F. Yoshihara, K. Harrabi, G. Fitch, D. G. Cory, Y. Nakamura, J.-S. Tsai, and W. D. Oliver. Noise spectroscopy through dynamical decoupling with a superconducting flux qubit. *Nat Phys*, 7(7), July 2011.

[49] L. Cardani, F. Valenti, N. Casali, G. Catelani, T. Charpentier, M. Clemenza, I. Colantoni, A. Cruciani, G. D'Imperio, L. Gironi, L. Grünhaupt, D. Gusenkova, F. Henriques, M. Lagoin, M. Martinez, G. Pettinari, C. Rusconi, O. Sander, C. Tomei, A. V. Ustinov, M. Weber, W. Wernsdorfer, M. Vignati, S. Pirro, and I. M. Pop. Reducing the impact of radioactivity on quantum circuits in a deep-underground facility. *Nat Commun*, 12(1), May 2021.

[50] H. Y. Carr and E. M. Purcell. Effects of diffusion on free precession in nuclear magnetic resonance experiments. *Phys Rev*, 94, May 1954.

[51] F. J. M. Cañadas, C. Metzger, S. Park, L. Tosi, P. Krogstrup, J. Nygård, M. F. Goffman, C. Urbina, H. Pothier, and A. Levy Yeyati. Signatures of interactions in the Andreev spectrum of nanowire Josephson junctions. *arXiv e-prints*, 2021.

[52] J. Cerrillo, M. Hays, V. Fatemi, and A. L. Yeyati. Spin coherent manipulation in Josephson weak links. *Phys. Rev. Research*, 3(2), May 2021.

[53] W. Chang, S. M. Albrecht, T. S. Jespersen, F. Kuemmeth, P. Krogstrup, J. Nygård, and C. M. Marcus. Hard gap in epitaxial semiconductor-superconductor nanowires. *Nat Nanotechnol*, 10(3), Jan. 2015.

[54] W. Chang, V. E. Manucharyan, T. S. Jespersen, J. Nygård, and C. M. Marcus. Tunneling spectroscopy of quasiparticle bound states in a spinful Josephson junction. *Phys Rev Lett*, 110(21), May 2013.

[55] M. Chauvin, P. Vom Stein, D. Esteve, C. Urbina, J. C. Cuevas, and A. L. Yeyati. Crossover from josephson to multiple andreev reflection currents in atomic contacts. *Phys Rev Lett*, 99(6), Aug. 2007.

[56] Y. Chen, C. Neill, P. Roushan, N. Leung, M. Fang, R. Barends, J. Kelly, B. Campbell, Z. Chen, B. Chiaro, A. Dunsworth, E. Jeffrey, A. Megrant, J. Mutus, P. O'Malley, C. Quintana, D. Sank, A. Vainsencher, J. Wenner, T. White, M. R. Geller, A. Cleland, and J. M. Martinis. Qubit architecture with high coherence and fast tunable coupling. *Phys Rev Lett*, 113(22), Nov. 2014.

[57] Z. Chen, K. J. Satzinger, J. Atalaya, A. N. Korotkov, A. Dunsworth, et al. Exponential suppression of bit or phase errors with cyclic error correction. *Nature*, 595(7867), July 2021.

[58] M.-S. Choi, M. Lee, K. Kang, and W. Belzig. Kondo effect and Josephson current through a quantum dot between two superconductors. *Phys Rev B*, 70, July 2004.

[59] N. M. Chtchelkatchev and Y. V. Nazarov. Andreev Quantum Dots for Spin Manipulation. *Phys Rev Lett*, 90(22), June 2003.

[60] Y. Chu, C. Axline, C. Wang, T. Brecht, Y. Y. Gao, L. Frunzio, and R. J. Schoelkopf. Suspending superconducting qubits by silicon micromachining. *Appl Phys Lett*, 109(11), Sept. 2016.

[61] J. P. Cleuziou, W. Wernsdorfer, V. Bouchiat, T. Ondarcuhu, and M. Monthioux. Carbon nanotube superconducting quantum interference device. *Nat Nanotechnol*, 1(1), Oct. 2006.

[62] M. C. Collodo, J. Herrmann, N. Lacroix, C. K. Andersen, A. Remm, S. Lazar, J.-C. Besse, T. Walter, A. Wallraff, and C. Eichler. Implementation of conditional phase gates based on tunable zz interactions. *Phys Rev Lett*, 125(24), Dec. 2020.

[63] L. N. Cooper. Bound electron pairs in a degenerate Fermi gas. *Phys Rev*, 104(4):1189–1190, nov 1956.

[64] S. Csonka, L. Hofstetter, F. Freitag, S. Oberholzer, C. Schönenberger, T. S. Jespersen, M. Aagesen, and J. Nygård. Giant fluctuations and gate control of the g-factor in InAs nanowire quantum dots. *Nano Lett.*, 8(11), Oct. 2008.

[65] L. Cywiński, R. M. Lutchyn, C. P. Nave, and S. Das Sarma. How to enhance dephasing time in superconducting qubits. *Phys Rev B*, 77, May 2008.

[66] J. Danon and Y. V. Nazarov. Pauli spin blockade in the presence of strong spin-orbit coupling. *Phys Rev B*, 80(4), July 2009.

[67] I. M. Dayton, T. Sage, E. C. Gingrich, M. G. Loving, T. F. Ambrose, N. P. Siwak, S. Keebaugh, C. Kirby, D. L. Miller, A. Y. Herr, Q. P. Herr, and O. Naaman. Experimental demonstration of a Josephson magnetic memory cell with a programmable π-junction. *IEEE Magnetics Letters*, 9, 2018.

[68] D. de Jong. *Gate-based readout of hybrid quantum dot systems*. PhD thesis, 2021.

[69] D. de Jong, C. G. Prosko, D. M. A. Waardenburg, L. Han, F. K. Malinowski, P. Krogstrup, L. P. Kouwenhoven, J. V. Koski, and W. Pfaff. Rapid microwave-only characterization and readout of quantum dots using multiplexed gigahertz-frequency resonators. *Phys. Rev. Applied*, 16(1), July 2021.

[70] G. De Lange, B. Van Heck, A. Bruno, D. J. Van Woerkom, A. Geresdi, S. R. Plissard, E. P. Bakkers, A. R. Akhmerov, and L. DiCarlo. Realization of Microwave Quantum Circuits Using Hybrid Superconducting-Semiconducting Nanowire Josephson Elements. *Phys Rev Lett*, 115(12), Sept. 2015.

[71] N. P. de Leon, K. M. Itoh, D. Kim, K. K. Mehta, T. E. Northup, H. Paik, B. S. Palmer, N. Samarth, S. Sangtawesin, and D. W. Steuerman. Materials challenges and opportunities for quantum computing hardware. *Science*, 372, Apr. 2021.

[72] P. J. de Visser, S. A. de Rooij, V. Murugesan, D. J. Thoen, and J. J. Baselmans. Phonon-trapping-enhanced energy resolution in superconducting single-photon detectors. *Phys. Rev. Applied*, 16(3), Sept. 2021.

[73] R. S. Deacon, Y. Tanaka, A. Oiwa, R. Sakano, K. Yoshida, K. Shibata, K. Hirakawa, and S. Tarucha. Tunneling spectroscopy of Andreev energy levels in a quantum dot coupled to a superconductor. *Phys Rev Lett*, 104(7), Feb. 2010.

[74] R. Delagrange, D. J. Luitz, R. Weil, A. Kasumov, V. Meden, H. Bouchiat, and R. Deblock. Manipulating the magnetic state of a carbon nanotube Josephson junction using the superconducting phase. *Phys Rev B*, 91(24), June 2015.

[75] R. Delagrange, R. Weil, A. Kasumov, M. Ferrier, H. Bouchiat, and R. Deblock. $0-\pi$ Quantum transition in a carbon nanotube Josephson junction: Universal phase dependence and orbital degeneracy. *Phys. B Condens. Matter*, 536, May 2018.

[76] M. L. Della Rocca, M. Chauvin, B. Huard, H. Pothier, D. Esteve, and C. Urbina. Measurement of the current-phase relation of superconducting atomic contacts. *Phys Rev Lett*, 99, Sept. 2007.

[77] L. Dell'Anna, A. Zazunov, R. Egger, and T. Martin. Josephson current through a quantum dot with spin-orbit coupling. *Phys Rev B*, 75(8), Feb. 2007.

[78] M. T. Deng, S. Vaitiekenas, E. B. Hansen, J. Danon, M. Leijnse, K. Flensberg, J. Nygård, P. Krogstrup, and C. M. Marcus. Majorana bound state in a coupled quantum-dot hybrid-nanowire system. *Science*, 354, Dec. 2016.

[79] M. T. Deng, S. Vaitiekenas, E. B. Hansen, J. Danon, M. Leijnse, K. Flensberg, J. Nygård, P. Krogstrup, and C. M. Marcus. Majorana bound state in a coupled quantum-dot hybrid-nanowire system. *Science*, 354(6319), Dec. 2016.

[80] M. A. Despósito and A. L. Yeyati. Controlled dephasing of Andreev states in superconducting quantum point contacts. *Phys Rev B*, 64(14), Sept. 2001.

[81] M. H. Devoret. Does Brian Josephson's gauge-invariant phase difference live on a line or a circle? *Journal of Superconductivity and Novel Magnetism*, 34(6):1633–1642, may 2021.

[82] I. A. Devyatov and M. Y. Kupriyanov. Resonant Josephson tunneling through S-I-S junctions of arbitrary size. *J Exp Theor Phys*, 85(1), July 1997.

[83] Y. J. Doh, J. A. Van Dam, A. L. Roest, E. P. Bakkers, L. P. Kouwenhoven, and S. De Franceschi. Applied physics: Tunable supercurrent through semiconductor nanowires. *Science*, 309(5732), July 2005.

[84] S. Droste, S. Andergassen, and J. Splettstoesser. Josephson current through interacting double quantum dots with spin–orbit coupling. *J. Phys.: Condens. Matter*, 24(41):415301, sep 2012.

[85] T. Dvir, G. Wang, N. van Loo, C.-X. Liu, G. P. Mazur, A. Bordin, S. L. D. ten Haaf, J.-Y. Wang, D. van Driel, F. Zatelli, X. Li, F. K. Malinowski, S. Gazibegovic, G. Badawy, E. P. A. M. Bakkers, M. Wimmer, and L. P. Kouwenhoven. Realization of a minimal kitaev chain in coupled quantum dots. *arXiv e-prints*, June 2022.

[86] A. Eichler, R. Deblock, M. Weiss, C. Karrasch, V. Meden, C. Schönenberger, and H. Bouchiat. Tuning the Josephson current in carbon nanotubes with the Kondo effect. *Phys Rev B*, 79, Apr. 2009.

[87] W. Eisenmenger. Superconducting tunneling junctions as phonon generators and detectors. *Phys Acoustics*, 1976.

[88] W. Eisenmenger and A. H. Dayem. Quantum generation and detection of incoherent phonons in superconductors. *Phys Rev Lett*, 18(4), Jan. 1967.

[89] S. D. Escribano, A. Levy Yeyati, R. Aguado, E. Prada, and P. San-Jose. Fluxoid-induced pairing suppression and near-zero modes in quantum dots coupled to full-shell nanowires. *Phys Rev B*, 105, Jan. 2022.

[90] C. Fasth, A. Fuhrer, L. Samuelson, V. N. Golovach, and D. Loss. Direct measurement of the spin-orbit interaction in a two-electron InAs nanowire quantum dot. *Phys Rev Lett*, 98(26), June 2007.

[91] V. Fatemi, P. D. Kurilovich, M. Hays, D. Bouman, T. Connolly, S. Diamond, N. E. Frattini, V. D. Kurilovich, P. Krogstrup, J. Nygard, A. Geresdi, L. I. Glazman, and M. H. Devoret. Microwave susceptibility observation of interacting many-body Andreev states. *arXiv e-prints*, Dec. 2021.

[92] K. Flensberg. Capacitance and conductance of mesoscopic systems connected by quantum point contacts. *Phys Rev B*, 48(15), Jan. 1993.

[93] K. Flensberg, F. von Oppen, and A. Stern. Engineered platforms for topological superconductivity and majorana zero modes. *Nature Reviews Materials*, 6(10):944–958, jul 2021.

[94] C. Flindt, A. S. Sørensen, and K. Flensberg. Spin-orbit mediated control of spin qubits. *Phys Rev Lett*, 97(24), Dec. 2006.

[95] P. Forn-Díaz, L. Lamata, E. Rico, J. Kono, and E. Solano. Ultrastrong coupling regimes of light-matter interaction. *Rev Mod Phys*, 91(2):025005, jun 2019.

[96] FraSchelle. Topology and Superconductor Symmetry Breaking. `https://physics.stackexchange.com/q/284957`, Apr. 2017.

[97] I. C. Fulga, A. Haim, A. R. Akhmerov, and Y. Oreg. Adaptive tuning of Majorana fermions in a quantum dot chain. *New J Phys*, 15, Apr. 2013.

[98] A. Furusaki and M. Tsukada. A unified theory of clean Josephson junctions. *Phys. B Condens. Matter*, 165-166, Aug. 1990.

[99] Y. Y. Gao, M. A. Rol, S. Touzard, and C. Wang. Practical guide for building superconducting quantum devices. *PRX Quantum*, 2, Nov. 2021.

[100] A. García Corral, D. M. T. van Zanten, K. J. Franke, H. Courtois, S. Florens, and C. B. Winkelmann. Magnetic-field-induced transition in a quantum dot coupled to a superconductor. *Phys. Rev. Research*, 2, Mar. 2020.

[101] I. Giaever. Electron tunneling between two superconductors. *Phys Rev Lett*, 5(10):464–466, nov 1960.

[102] E. Ginossar and E. Grosfeld. Microwave transitions as a signature of coherent parity mixing effects in the Majorana-transmon qubit. *Nat Commun*, 5(1), Sept. 2014.

[103] V. L. Ginzburg and L. D. Landau. On the theory of superconductivity. In *On Superconductivity and Superfluidity*, pages 113–137. Springer Berlin Heidelberg, 1950.

[104] L. Glazman and K. Matveev. Resonant Josephson current through Kondo impurities in a tunnel barrier. *JETP Lett*, 49(10), May 1989.

[105] L. I. Glazman and G. Catelani. Bogoliubov quasiparticles in superconducting qubits. *SciPost Phys. Lect. Notes*, 2021.

[106] M. F. Goffman, C. Urbina, H. Pothier, J. Nygard, C. M. Marcus, and P. Krogstrup. Conduction channels of an InAs-Al nanowire Josephson weak link. *New J Phys*, 19(9), Sept. 2017.

[107] V. N. Golovach, M. Borhani, and D. Loss. Electric-dipole-induced spin resonance in quantum dots. *Phys Rev B*, 74(16), Oct. 2006.

[108] A. A. Golubov, M. Y. Kupriyanov, and E. Il'ichev. The current-phase relation in Josephson junctions. *Rev Mod Phys*, 76(2), Apr. 2004.

[109] L. P. Gor'kov. Microscopic derivation of the Ginzburg-Landau equations in the theory of superconductivity. *Soviet Physics - JETP*, 9(6), Jan. 1959.

[110] G. Granger, D. Taubert, C. E. Young, L. Gaudreau, A. Kam, S. A. Studenikin, P. Zawadzki, D. Harbusch, D. Schuh, W. Wegscheider, Z. R. Wasilewski, A. A. Clerk, S. Ludwig, and A. S. Sachrajda. Quantum interference and phonon-mediated back-action in lateral quantum-dot circuits. *Nat Phys*, 8(7), June 2012.

[111] M. Greiter. Is electromagnetic gauge invariance spontaneously violated in superconductors? *Annals of Physics*, 319(1):217–249, sep 2005.

[112] P. Groszkowski, A. D. Paolo, A. L. Grimsmo, A. Blais, D. I. Schuster, A. A. Houck, and J. Koch. Coherence properties of the $0-\pi$ qubit. *New J Phys*, 20(4), Apr. 2018.

[113] A. Gyenis, P. S. Mundada, A. Di Paolo, T. M. Hazard, X. You, D. I. Schuster, J. Koch, A. Blais, and A. A. Houck. Experimental realization of a protected superconducting circuit derived from the $0-\pi$ qubit. *PRX Quantum*, 2, Mar. 2021.

[114] E. L. Hahn. Spin echoes. *Phys Rev*, 80, Nov. 1950.

[115] L. Han, M. Chan, D. de Jong, C. Prosko, G. Badawy, S. Gazibegovic, E. P. A. M. Bakkers, L. P. Kouwenhoven, F. K. Malinowski, and W. Pfaff. Variable and orbital-dependent spin-orbit field orientations in a InSb double quantum dot characterized via dispersive gate sensing. *arXiv e-prints*, Mar. 2022.

[116] R. Hanson, L. P. Kouwenhoven, J. R. Petta, S. Tarucha, and L. M. K. Vandersypen. Spins in few-electron quantum dots. *Rev Mod Phys*, 79, Oct. 2007.

[117] T. Hansson, V. Oganesyan, and S. Sondhi. Superconductors are topologically ordered. *Ann Phys-new York*, 313(2):497–538, oct 2004.

[118] S. Hart, Z. Cui, G. Ménard, M. Deng, A. E. Antipov, R. M. Lutchyn, P. Krogstrup, C. M. Marcus, and K. A. Moler. Current-phase relations of InAs nanowire Josephson junctions: From interacting to multimode regimes. *Phys Rev B*, 100(6), Aug. 2019.

[119] P. Harvey-Collard, J. Dijkema, G. Zheng, A. Sammak, G. Scappucci, and L. M. Vandersypen. Coherent spin-spin coupling mediated by virtual microwave photons. *Phys. Rev. X*, 12(2), May 2022.

[120] F. Hassler, A. R. Akhmerov, and C. W. Beenakker. The top-transmon: A hybrid superconducting qubit for parity-protected quantum computation. *New J Phys*, 13, Sept. 2011.

[121] M. Hays. *Realizing an Andreev Spin Qubit*. PhD thesis, Yale University, 2021.

[122] M. Hays, G. De Lange, K. Serniak, D. J. Van Woerkom, D. Bouman, P. Krogstrup, J. Nygård, A. Geresdi, and M. H. Devoret. Direct Microwave Measurement of Andreev-Bound-State Dynamics in a Semiconductor-Nanowire Josephson Junction. *Phys Rev Lett*, 121(4), July 2018.

[123] M. Hays, V. Fatemi, D. Bouman, J. Cerrillo, S. Diamond, K. Serniak, T. Connolly, P. Krogstrup, J. Nygård, A. L. Yeyati, A. Geresdi, and M. H. Devoret. Coherent manipulation of an Andreev spin qubit. *Science*, 373(6553), July 2021.

[124] M. Hays, V. Fatemi, K. Serniak, D. Bouman, S. Diamond, G. de Lange, P. Krogstrup, J. Nygård, A. Geresdi, and M. H. Devoret. Continuous monitoring of a trapped, superconducting spin. *Nat Phys*, 16(11), Aug. 2019.

[125] S. Heedt, M. Quintero-Pérez, F. Borsoi, A. Fursina, N. van Loo, G. P. Mazur, M. P. Nowak, M. Ammerlaan, K. Li, S. Korneychuk, J. Shen, M. A. Y. van de Poll, G. Badawy, S. Gazibegovic, N. de Jong, P. Aseev, K. van Hoogdalem, E. P. A. M. Bakkers, and L. P. Kouwenhoven. Shadow-wall lithography of ballistic superconductor–semiconductor quantum devices. *Nat Commun*, 12(1), Aug. 2021.

[126] J. Heinsoo, C. K. Andersen, A. Remm, S. Krinner, T. Walter, Y. Salathé, S. Gasparinetti, J.-C. Besse, A. Potočnik, A. Wallraff, and C. Eichler. Rapid high-fidelity multiplexed readout of superconducting qubits. *Phys. Rev. Applied*, 10, Sept. 2018.

[127] S. Heiskanen, T. Puurtinen, and I. J. Maasilta. Controlling thermal conductance using three-dimensional phononic crystals. *arXiv e-prints*, Apr. 2021.

[128] N. W. Hendrickx, D. P. Franke, A. Sammak, M. Kouwenhoven, D. Sabbagh, L. Yeoh, R. Li, M. L. V. Tagliaferri, M. Virgilio, G. Capellini, G. Scappucci, and M. Veldhorst. Gate-controlled quantum dots and superconductivity in planar germanium. *Nat Commun*, 9(1), July 2018.

[129] F. Henriques, F. Valenti, T. Charpentier, M. Lagoin, C. Gouriou, M. Martínez, L. Cardani, M. Vignati, L. Grünhaupt, D. Gusenkova, J. Ferrero, S. T. Skacel, W. Wernsdorfer, A. V. Ustinov, G. Catelani, O. Sander, and I. M. Pop. Phonon traps reduce the quasiparticle density in superconducting circuits. *Appl Phys Lett*, 115(21), Nov. 2019.

[130] C. Hermansen, A. Levy Yeyati, and J. Paaske. Inductive microwave response of Yu-Shiba-Rusinov states. *Phys Rev B*, 105, Feb. 2022.

[131] T. K. Hsiao, C. J. van Diepen, U. Mukhopadhyay, C. Reichl, W. Wegscheider, and L. M. K. Vandersypen. Efficient orthogonal control of tunnel couplings in a quantum dot array. *Phys. Rev. Applied*, 13(5), May 2020.

[132] V. Iaia, J. Ku, A. Ballard, C. P. Larson, E. Yelton, C. H. Liu, S. Patel, R. McDermott, and B. L. T. Plourde. Phonon downconversion to suppress correlated errors in superconducting qubits. *arXiv e-prints*, Mar. 2022.

[133] IBM Quantum. Compute resources. `https://quantum-computing.ibm.com/services?services=systems`. Accessed: 2022-06-13.

[134] D. A. Ivanov and M. V. Feigel'man. Coulomb effects in a ballistic one-channel S-S-S device. *Phys. Usp.*, 41(2), Feb. 1998.

[135] D. A. Ivanov and M. V. Feigel'man. Two-level hamiltonian of a superconducting quantum point contact. *Phys Rev B*, 59(13), Oct. 1999.

[136] C. Janvier, L. Tosi, L. Bretheau, Ç. O. Girit, M. Stern, P. Bertet, P. Joyez, D. Vion, D. Esteve, M. F. Goffman, H. Pothier, and C. Urbina. Coherent manipulation of Andreev states in superconducting atomic contacts. *Science*, 349(6253), Sept. 2015.

[137] S. Jezouin, Z. Iftikhar, A. Anthore, F. D. Parmentier, U. Gennser, A. Cavanna, A. Ouerghi, I. P. Levkivskyi, E. Idrisov, E. V. Sukhorukov, L. I. Glazman, and F. Pierre. Controlling charge quantization with quantum fluctuations. *Nature*, 536(7614), Aug. 2016.

[138] Y. Jiang, S. Yang, L. Li, W. Song, W. Miao, B. Tong, Z. Geng, Y. Gao, R. Li, F. Chen, Q. Zhang, F. Meng, L. Gu, K. Zhu, Y. Zang, R. Shang, Z. Cao, X. Feng, Q.-K. Xue, D. E. Liu, H. Zhang, and K. He. Selective area epitaxy of PbTe-Pb hybrid nanowires on a lattice-matched substrate. *Phys. Rev. Materials*, 6(3):034205, mar 2022.

[139] X. Jin, A. Kamal, A. Sears, T. Gudmundsen, D. Hover, J. Miloshi, R. Slattery, F. Yan, J. Yoder, T. Orlando, S. Gustavsson, and W. Oliver. Thermal and residual excited-state population in a 3d transmon qubit. *Phys Rev Lett*, 114(24), June 2015.

[140] H. I. Jørgensen, K. Grove-Rasmussen, K. Flensberg, and P. E. Lindelof. Critical and excess current through an open quantum dot: Temperature and magnetic-field dependence. *Phys Rev B*, 79, Apr. 2009.

[141] H. I. Jørgensen, T. Novotný, K. Grove-Rasmussen, K. Flensberg, and P. E. Lindelof. Critical current 0-π transition in designed Josephson quantum dot junctions. *Nano Lett.*, 7(8), Aug. 2007.

[142] B. Josephson. Possible new effects in superconductive tunnelling. *Phys Lett*, 1(7):251–253, jul 1962.

[143] P. Joyez, V. Bouchiat, D. Esteve, C. Urbina, and M. H. Devoret. Strong tunneling in the single-electron transistor. *Phys Rev Lett*, 79(7), Aug. 1997.

[144] A. Kadlecová, M. Žonda, V. Pokorný, and T. Novotný. Practical guide to quantum phase transitions in quantum-dot-based tunable Josephson junctions. *Phys. Rev. Applied*, 11, Apr. 2019.

[145] A. Kadlecová, M. Žonda, and T. Novotný. Quantum dot attached to superconducting leads: Relation between symmetric and asymmetric coupling. *Phys Rev B*, 95(19), May 2017.

[146] K. Kalashnikov, W. T. Hsieh, W. Zhang, W.-S. Lu, P. Kamenov, A. D. Paolo, A. Blais, M. E. Gershenson, and M. Bell. Bifluxon: Fluxon-parity-protected superconducting qubit. *PRX Quantum*, 1(1), Sept. 2020.

[147] R. Kalra, A. Laucht, J. P. Dehollain, D. Bar, S. Freer, S. Simmons, J. T. Muhonen, and A. Morello. Vibration-induced electrical noise in a cryogen-free dilution refrigerator: Characterization, mitigation, and impact on qubit coherence. *Rev. Sci. Instrum.*, 87(7), July 2016.

[148] S. B. Kaplan. Acoustic matching of superconducting films to substrates. *J Low Temp Phys*, 37(3-4), Nov. 1979.

[149] S. B. Kaplan, C. C. Chi, D. N. Langenberg, J. J. Chang, S. Jafarey, and D. J. Scalapino. Quasiparticle and phonon lifetimes in superconductors. *Phys Rev B*, 14(11), Dec. 1976.

[150] K. Karatsu, A. Endo, J. Bueno, P. J. de Visser, R. Barends, D. J. Thoen, V. Murugesan, N. Tomita, and J. J. A. Baselmans. Mitigation of cosmic ray effect on microwave kinetic inductance detector arrays. *Appl Phys Lett*, 114(3), Jan. 2019.

[151] C. Karrasch, S. Andergassen, and V. Meden. Supercurrent through a multilevel quantum dot close to singlet-triplet degeneracy. *Phys Rev B*, 84(13), 2011.

[152] C. Karrasch and V. Meden. Supercurrent and multiple singlet-doublet phase transitions of a quantum dot Josephson junction inside an Aharonov-Bohm ring. *Phys Rev B*, 79(4), Jan. 2009.

[153] C. Karrasch, A. Oguri, and V. Meden. Josephson current through a single Anderson impurity coupled to BCS leads. *Phys Rev B*, 77, 2008.

[154] T. Karzig, W. S. Cole, and D. I. Pikulin. Quasiparticle poisoning of Majorana qubits. *Phys Rev Lett*, 126(5), Feb. 2021.

[155] T. Karzig, C. Knapp, R. M. Lutchyn, P. Bonderson, M. B. Hastings, C. Nayak, J. Alicea, K. Flensberg, S. Plugge, Y. Oreg, C. M. Marcus, and M. H. Freedman. Scalable designs for quasiparticle-poisoning-protected topological quantum computation with Majorana zero modes. *Phys Rev B*, 95, June 2017.

[156] A. Keselman, C. Murthy, B. van Heck, and B. Bauer. Spectral response of Josephson junctions with low-energy quasiparticles. *SciPost Physics*, 7(4), May 2019.

[157] S. A. Khan, C. Lampadaris, A. Cui, L. Stampfer, Y. Liu, S. J. Pauka, M. E. Cachaza, E. M. Fiordaliso, J.-H. Kang, S. Korneychuk, T. Mutas, J. E. Sestoft, F. Krizek, R. Tanta, M. C. Cassidy, T. S. Jespersen, and P. Krogstrup. Transparent gatable superconducting shadow junctions. *arXiv e-prints*, Mar. 2020.

[158] G. Kiršanskas, M. Goldstein, K. Flensberg, L. I. Glazman, and J. Paaske. Yu-Shiba-Rusinov states in phase-biased superconductor–quantum dot–superconductor junctions. *Phys Rev B*, 92, Dec. 2015.

[159] A. A. Kiselev, E. L. Ivchenko, and U. Rössler. Electron g factor in one- and zero-dimensional semiconductor nanostructures. *Phys. Rev. B.*, 58(24), Dec. 1998.

[160] M. Kjaergaard, F. Nichele, H. J. Suominen, M. P. Nowak, M. Wimmer, A. R. Akhmerov, J. A. Folk, K. Flensberg, J. Shabani, C. J. Palmstrøm, and C. M. Marcus. Quantized conductance doubling and hard gap in a two-dimensional semiconductor–superconductor heterostructure. *Nat Commun*, 7(1), Sept. 2016.

[161] M. Kjaergaard, M. E. Schwartz, J. Braumüller, P. Krantz, J. I.-J. Wang, S. Gustavsson, and W. D. Oliver. Superconducting qubits: Current state of play. *Annu Rev Conden Ma P*, 11(1), 2020.

[162] J. Koch, T. M. Yu, J. Gambetta, A. A. Houck, D. I. Schuster, J. Majer, A. Blais, M. H. Devoret, S. M. Girvin, and R. J. Schoelkopf. Charge-insensitive qubit design derived from the Cooper pair box. *Phys Rev A*, 76(4), Oct. 2007.

[163] S. Komiyama, O. Astafiev, V. Antonov, T. Kutsuwa, and H. Hirai. A single-photon detector in the far-infrared range. *Nature*, 403(6768), Jan. 2000.

[164] V. Kornich, H. S. Barakov, and Y. V. Nazarov. Overlapping Andreev states in semiconducting nanowires: competition of 1D and 3D propagation. *Phys Rev B*, 101(19), Dec. 2019.

[165] A. Kou, W. Smith, U. Vool, R. Brierley, H. Meier, L. Frunzio, S. Girvin, L. Glazman, and M. Devoret. Fluxonium-based artificial molecule with a tunable magnetic moment. *Phys. Rev. X*, 7(3), Aug. 2017.

[166] L. P. Kouwenhoven, N. C. van der Vaart, A. T. Johnson, W. Kool, C. J. Harmans, J. G. Williamson, A. A. Staring, and C. T. Foxon. Single electron charging effects in semiconductor quantum dots. *Zeitschrift für Physik B Condensed Matter*, 85(3), Oct. 1991.

[167] A. Kringhøj, L. Casparis, M. Hell, T. W. Larsen, F. Kuemmeth, M. Leijnse, K. Flensberg, P. Krogstrup, J. Nygård, K. D. Petersson, and C. M. Marcus. Anharmonicity of a superconducting qubit with a few-mode Josephson junction. *Phys Rev B*, 97(6), Feb. 2018.

[168] A. Kringhøj, T. W. Larsen, B. van Heck, D. Sabonis, O. Erlandsson, I. Petkovic, D. I. Pikulin, P. Krogstrup, K. D. Petersson, and C. M. Marcus. Controlled DC Monitoring of a Superconducting Qubit. *Phys Rev Lett*, 124(5), Oct. 2019.

[169] A. Kringhøj, B. van Heck, T. W. Larsen, O. Erlandsson, D. Sabonis, P. Krogstrup, L. Casparis, K. D. Petersson, and C. M. Marcus. Suppressed charge dispersion via resonant tunneling in a single-channel transmon. *Phys Rev Lett*, 124, June 2020.

[170] S. Krinner, N. Lacroix, A. Remm, A. D. Paolo, E. Genois, C. Leroux, C. Hellings, S. Lazar, F. Swiadek, J. Herrmann, G. J. Norris, C. K. Andersen, M. Müller, A. Blais, C. Eichler, and A. Wallraff. Realizing repeated quantum error correction in a distance-three surface code. *Nature*, 605(7911), May 2022.

[171] S. Krinner, S. Storz, P. Kurpiers, P. Magnard, J. Heinsoo, R. Keller, J. Lütolf, C. Eichler, and A. Wallraff. Engineering cryogenic setups for 100-qubit scale superconducting circuit systems. *EPJ Quantum Technology*, 6(1), may 2019.

[172] H. Krishna-murthy, J. Wilkins, and K. Wilson. Renormalization-group approach to the Anderson model of dilute magnetic alloys. i. static properties for the symmetric case. *Phys Rev B*, 21(3), Feb. 1980.

[173] P. Krogstrup, N. L. Ziino, W. Chang, S. M. Albrecht, M. H. Madsen, E. Johnson, J. Nygård, C. M. Marcus, and T. S. Jespersen. Epitaxy of semiconductor-superconductor nanowires. *Nat. Mater.*, 14(4), Jan. 2015.

[174] J. Kroll, F. Borsoi, K. van der Enden, W. Uilhoorn, D. de Jong, M. Quintero-Pérez, D. van Woerkom, A. Bruno, S. Plissard, D. Car, E. Bakkers, M. Cassidy, and L. Kouwenhoven. Magnetic-Field-Resilient Superconducting Coplanar-Waveguide Resonators for Hybrid Circuit Quantum Electrodynamics Experiments. *Phys. Rev. Applied*, 11(6), June 2019.

[175] I. Kulik. Macroscopic quantization and the proximity effect in SNS junctions. *Soviet Journal of Experimental and Theoretical Physics*, 30:944, 1969.

[176] A. Kumar, M. Gaim, D. Steininger, A. Levy Yeyati, A. Martín-Rodero, A. K. Hüttel, and C. Strunk. Temperature dependence of Andreev spectra in a superconducting carbon nanotube quantum dot. *Phys Rev B*, 89, Feb. 2014.

[177] P. D. Kurilovich, V. D. Kurilovich, V. Fatemi, M. H. Devoret, and L. I. Glazman. Microwave response of an Andreev bound state. *Phys Rev B*, 104, Nov. 2021.

[178] O. Kürtössy, Z. Scherübl, G. Fülöp, I. E. Lukács, T. Kanne, J. Nygård, P. Makk, and S. Csonka. Andreev molecule in parallel InAs nanowires. *Nano Lett.*, 21(19):7929–7937, sep 2021.

[179] A. J. Landig, J. V. Koski, P. Scarlino, U. C. Mendes, A. Blais, C. Reichl, W. Wegscheider, A. Wallraff, K. Ensslin, and T. Ihn. Coherent spin–photon coupling using a resonant exchange qubit. *Nature*, 560(7717), Aug. 2018.

[180] A. J. Landig, J. V. Koski, P. Scarlino, C. Müller, J. C. Abadillo-Uriel, B. Kratochwil, C. Reichl, W. Wegscheider, S. N. Coppersmith, M. Friesen, A. Wallraff, T. Ihn, and K. Ensslin. Virtual-photon-mediated spin-qubit–transmon coupling. *Nat Commun*, 10(1), Nov. 2019.

[181] T. W. Larsen, M. E. Gershenson, L. Casparis, A. Kringhøj, N. J. Pearson, R. P. G. McNeil, F. Kuemmeth, P. Krogstrup, K. D. Petersson, and C. M. Marcus. Parity-protected superconductor-semiconductor qubit. *Phys Rev Lett*, 125, July 2020.

[182] T. W. Larsen, K. D. Petersson, F. Kuemmeth, T. S. Jespersen, P. Krogstrup, J. Nygård, and C. M. Marcus. Semiconductor-Nanowire-Based Superconducting Qubit. *Phys Rev Lett*, 115(12), Sept. 2015.

[183] N. Lauk, N. Sinclair, S. Barzanjeh, J. P. Covey, M. Saffman, M. Spiropulu, and C. Simon. Perspectives on quantum transduction. *Quantum Sci. Technol.*, 5(2), Mar. 2020.

[184] W. Lawrie. *Spin Qubits in Silicon and GermaniumTitle.* PhD thesis, 2022.

[185] E. J. Lee, X. Jiang, M. Houzet, R. Aguado, C. M. Lieber, and S. De Franceschi. Spin-resolved Andreev levels and parity crossings in hybrid superconductor-semiconductor nanostructures. *Nat Nanotechnol*, 9(1), Dec. 2014.

[186] E. J. H. Lee, X. Jiang, R. Aguado, G. Katsaros, C. M. Lieber, and S. De Franceschi. Zero-bias anomaly in a nanowire quantum dot coupled to superconductors. *Phys Rev Lett*, 109, Oct. 2012.

[187] E. J. H. Lee, X. Jiang, R. Žitko, R. Aguado, C. M. Lieber, and S. De Franceschi. Scaling of subgap excitations in a superconductor-semiconductor nanowire quantum dot. *Phys Rev B*, 95(18), May 2017.

[188] M. Lee, T. Jonckheere, and T. Martin. Josephson effect through a multilevel quantum dot near a singlet-triplet transition. *Phys Rev B*, 81(15):155114, apr 2010.

[189] A. J. Leggett. *Quantum Liquids.* Oxford University Press, USA, 2006.

[190] M. Lenander, H. Wang, R. C. Bialczak, E. Lucero, M. Mariantoni, M. Neeley, A. D. O'Connell, D. Sank, M. Weides, J. Wenner, T. Yamamoto, Y. Yin, J. Zhao, A. N. Cleland, and J. M. Martinis. Measurement of energy decay in superconducting qubits from nonequilibrium quasiparticles. *Phys Rev B*, 84(2), July 2011.

[191] S. Li, N. Kang, P. Caroff, and H. Q. Xu. $0-\pi$ phase transition in hybrid superconductor–InSb nanowire quantum dot devices. *Phys Rev B*, 95, Jan. 2017.

[192] D. Liang and X. Gao. Strong tuning of Rashba spin–orbit interaction in single InAs nanowires. *Nano Lett.*, 12(6), May 2012.

[193] B. Lienhard, J. Braumuller, W. Woods, D. Rosenberg, G. Calusine, S. Weber, A. Vepsalainen, K. O'Brien, T. P. Orlando, S. Gustavsson, and W. D. Oliver. Microwave packaging for superconducting qubits. *2019 IEEE MTT-S International Microwave Symposium (IMS)*, June 2019.

[194] K. K. Likharev. Single-electron devices and their applications. *Proc. IEEE*, 87(4), Apr. 1999.

[195] J. S. Lim and M.-S. Choi. Andreev bound states in the Kondo quantum dots coupled to superconducting leads. *J. Phys.: Condens. Matter*, 20(41), Sept. 2008.

[196] J. Linder and J. W. A. Robinson. Superconducting spintronics. *Nature Physics*, 11(4):307–315, apr 2015.

[197] C.-X. Liu, G. Wang, T. Dvir, and M. Wimmer. Tunable superconducting coupling of quantum dots via andreev bound states. *arXiv e-prints*, Feb. 2022.

[198] F. London. On the Bose-Einstein condensation. *Phys Rev*, 54(11):947–954, dec 1938.

[199] T. Lorenz, S. Sprenger, and E. Scheer. Coulomb Blockade and Multiple Andreev Reflection in a Superconducting Single-Electron Transistor. *J Low Temp Phys*, 191(5-6), Dec. 2018.

[200] D. Loss and D. P. DiVincenzo. Quantum computation with quantum dots. *Phys Rev A*, 57, Jan. 1998.

[201] W. Lu, Z. Ji, L. Pfeiffer, K. W. West, and A. J. Rimberg. Real-time detection of electron tunnelling in a quantum dot. *Nature*, 423(6938), May 2003.

[202] D. J. Luitz, F. F. Assaad, T. Novotný, C. Karrasch, and V. Meden. Understanding the Josephson current through a Kondo-correlated quantum dot. *Phys Rev Lett*, 108, May 2012.

[203] F. Luthi, T. Stavenga, O. W. Enzing, A. Bruno, C. Dickel, N. K. Langford, M. A. Rol, T. S. Jespersen, J. Nygård, P. Krogstrup, and L. DiCarlo. Evolution of Nanowire Transmon Qubits and Their Coherence in a Magnetic Field. *Phys Rev Lett*, 120(10), May 2018.

[204] F. K. Malinowski, F. Martins, L. Cywiński, M. S. Rudner, P. D. Nissen, S. Fallahi, G. C. Gardner, M. J. Manfra, C. M. Marcus, and F. Kuemmeth. Spectrum of the nuclear environment for gaas spin qubits. *Phys Rev Lett*, 118, Apr. 2017.

[205] F. K. Malinowski, F. Martins, P. D. Nissen, S. Fallahi, G. C. Gardner, M. J. Manfra, C. M. Marcus, and F. Kuemmeth. Symmetric operation of the resonant exchange qubit. *Phys Rev B*, 96, July 2017.

[206] V. E. Manucharyan, J. Koch, L. I. Glazman, and M. H. Devoret. Fluxonium: Single cooper-pair circuit free of charge offsets. *Science*, 326(5949), Oct. 2009.

[207] G. Marchegiani, L. Amico, and G. Catelani. Quasiparticles in superconducting qubits with asymmetric junctions. *arXiv e-prints*, May 2022.

[208] J. F. Marques, B. M. Varbanov, M. S. Moreira, H. Ali, N. Muthusubramanian, C. Zachariadis, F. Battistel, M. Beekman, N. Haider, W. Vlothuizen, A. Bruno, B. M. Terhal, and L. DiCarlo. Logical-qubit operations in an error-detecting surface code. *Nat Phys*, 18(1), Dec. 2021.

[209] A. Martín-Rodero and A. Levy Yeyati. Josephson and Andreev transport through quantum dots. *Adv Phys*, 60(6), Dec. 2011.

[210] M. Martinez, L. Cardani, N. Casali, A. Cruciani, G. Pettinari, and M. Vignati. Measurements and simulations of athermal phonon transmission from silicon absorbers to aluminum sensors. *Phys. Rev. Applied*, 11(6), June 2019.

[211] J. M. Martinis. Saving superconducting quantum processors from decay and correlated errors generated by gamma and cosmic rays. *npj Quantum Inf.*, 7(1), June 2021.

[212] K. A. Matveev. Coulomb blockade at almost perfect transmission. *Phys Rev B*, 51(3), Apr. 1995.

[213] R. Maurand, T. Meng, E. Bonet, S. Florens, L. Marty, and W. Wernsdorfer. First-order $0-\pi$ quantum phase transition in the Kondo regime of a superconducting carbon-nanotube quantum dot. *Phys. Rev. X*, 2, Feb. 2012.

[214] M. McEwen, L. Faoro, K. Arya, A. Dunsworth, T. Huang, et al. Resolving catastrophic error bursts from cosmic rays in large arrays of superconducting qubits. *Nat Phys*, 18(1), Dec. 2021.

[215] V. Meden. The Anderson–Josephson quantum dot—a theory perspective. *J. Phys.: Condens. Matter*, 31(16), Feb. 2019.

[216] J. Medford, L. Cywiński, C. Barthel, C. M. Marcus, M. P. Hanson, and A. C. Gossard. Scaling of dynamical decoupling for spin qubits. *Phys Rev Lett*, 108, Feb. 2012.

[217] T. Meng, S. Florens, and P. Simon. Self-consistent description of Andreev bound states in Josephson quantum dot devices. *Phys Rev B*, 79(22), 2009.

[218] M. Meschke, J. Engert, D. Heyer, and J. P. Pekola. Comparison of Coulomb blockade thermometers with the international temperature scale PLTS-2000. *Int J Thermophys*, 32(7-8), July 2011.

[219] R. Meservey and P. M. Tedrow. Properties of very thin aluminum films. *J Appl Phys*, 42(1), Jan. 1971.

[220] C. Metzger. *Spin and charge effects in Andreev bound states*. PhD thesis, Paris-Saclay University, 2022.

[221] C. Metzger, S. Park, L. Tosi, C. Janvier, A. A. Reynoso, M. F. Goffman, C. Urbina, A. L. Yeyati, and H. Pothier. Circuit-QED with phase-biased Josephson weak links. *Phys. Rev. Research*, 3(1), Jan. 2021.

[222] X. Mi, M. Benito, S. Putz, D. M. Zajac, J. M. Taylor, G. Burkard, and J. R. Petta. A coherent spin–photon interface in silicon. *Nature*, 555(7698), Mar. 2018.

[223] C. P. Moca, I. Weymann, M. A. Werner, and G. Zaránd. Kondo cloud in a superconductor. *Phys Rev Lett*, 127(18), Oct. 2021.

[224] C. M. Moehle, C. T. Ke, Q. Wang, C. Thomas, D. Xiao, S. Karwal, M. Lodari, V. van de Kerkhof, R. Termaat, G. C. Gardner, G. Scappucci, M. J. Manfra, and S. Goswami. InSbAs two-dimensional electron gases as a platform for topological superconductivity. *Nano Lett.*, 21(23), Nov. 2021.

[225] L. W. Molenkamp, K. Flensberg, and M. Kemerink. Scaling of the Coulomb energy due to quantum fluctuations in the charge on a quantum dot. *Phys Rev Lett*, 75(23), Dec. 1995.

[226] D. C. Moore, S. R. Golwala, B. Bumble, B. Cornell, P. K. Day, H. G. LeDuc, and J. Zmuidzinas. Position and energy-resolved particle detection using phonon-mediated microwave kinetic inductance detectors. *Appl Phys Lett*, 100(23), 2012.

[227] S. Nadj-Perge, S. M. Frolov, E. P. A. M. Bakkers, and L. P. Kouwenhoven. Spin–orbit qubit in a semiconductor nanowire. *Nature*, 468(7327), Dec. 2010.

[228] Y. V. Nazarov. Coulomb blockade without tunnel junctions. *Phys Rev Lett*, 82(6), Feb. 1999.

[229] J. Nicol, S. Shapiro, and P. H. Smith. Direct measurement of the superconducting energy gap. *Phys Rev Lett*, 5(10):461–464, nov 1960.

[230] D. Noble. *The Music of Life.* Oxford University Press, USA, 2008.

[231] K. C. Nowack, F. H. L. Koppens, Y. V. Nazarov, and L. M. K. Vandersypen. Coherent control of a single electron spin with electric fields. *Science*, 318(5855), 2007.

[232] A. Oguri, Y. Tanaka, and A. C. Hewson. Quantum phase transition in a minimal model for the Kondo effect in a Josephson junction. *J. Phys. Soc. Jpn.*, 73, Nov. 2004.

[233] O. O. Otelaja, J. B. Hertzberg, M. Aksit, and R. D. Robinson. Design and operation of a microfabricated phonon spectrometer utilizing superconducting tunnel junctions as phonon transducers. *New J Phys*, 15(4), Apr. 2013.

[234] C. Padurariu and Y. V. Nazarov. Theoretical proposal for superconducting spin qubits. *Phys Rev B*, 81, Apr. 2010.

[235] X. Pan, H. Yuan, Y. Zhou, L. Zhang, J. Li, S. Liu, Z. H. Jiang, G. Catelani, L. Hu, and F. Yan. Engineering superconducting qubits to reduce quasiparticles and charge noise. *arXiv e-prints*, 120, Feb. 2022.

[236] A. D. Paolo, A. L. Grimsmo, P. Groszkowski, J. Koch, and A. Blais. Control and coherence time enhancement of the $0-\pi$ qubit. *New J Phys*, 21(4):043002, apr 2019.

[237] S. Park and A. L. Yeyati. Andreev spin qubits in multichannel Rashba nanowires. *Phys Rev B*, 96(12), Sept. 2017.

[238] U. Patel, I. V. Pechenezhskiy, B. L. T. Plourde, M. G. Vavilov, and R. McDermott. Phonon-mediated quasiparticle poisoning of superconducting microwave resonators. *Phys Rev B*, 96(22), Dec. 2017.

[239] L. Pavešić, D. Bauernfeind, and R. Žitko. Subgap states in superconducting islands. *Phys Rev B*, 104(24):l241409, dec 2021.

[240] L. Pavešić, M. Pita-Vidal, A. Bargerbos, and R. Žitko. Impurity knight shift in quantum dot josephson junctions. *arXiv e-prints*, Dec. 2022.

[241] L. Pavešić and R. Žitko. Qubit based on spin-singlet Yu-Shiba-Rusinov states. *Phys Rev B*, 105, Feb. 2022.

[242] D. Pekker, C. Y. Hou, V. E. Manucharyan, and E. Demler. Proposal for coherent coupling of majorana zero modes and superconducting qubits using the 4π Josephson effect. *Phys Rev Lett*, 111(10), Sept. 2013.

[243] J. P. Pekola, O. P. Saira, V. F. Maisi, A. Kemppinen, M. Möttönen, Y. A. Pashkin, and D. V. Averin. Single-electron current sources: Toward a refined definition of the ampere. *Rev Mod Phys*, 85(4), Oct. 2013.

[244] M. Peruzzo, A. Trioni, F. Hassani, M. Zemlicka, and J. M. Fink. Surpassing the resistance quantum with a geometric superinductor. *Phys. Rev. Applied*, 14(4), Oct. 2020.

[245] D. Pikulin, K. Flensberg, L. I. Glazman, M. Houzet, and R. M. Lutchyn. Coulomb Blockade of a Nearly Open Majorana Island. *Phys Rev Lett*, 122(1), Jan. 2019.

[246] D. I. Pikulin, B. van Heck, T. Karzig, E. A. Martinez, B. Nijholt, T. Laeven, G. W. Winkler, J. D. Watson, S. Heedt, M. Temurhan, V. Svidenko, R. M. Lutchyn, M. Thomas, G. de Lange, L. Casparis, and C. Nayak. Protocol to identify a topological superconducting phase in a three-terminal device. *arXiv e-prints*, Mar. 2021.

[247] J. D. Pillet, V. Benzoni, J. Griesmar, J. L. Smirr, and C. O. Girit. Nonlocal Josephson Effect in Andreev Molecules. *Nano Lett.*, 19(10), Oct. 2019.

[248] J. D. Pillet, V. Benzoni, J. Griesmar, J. L. Smirr, and Ç. Ö. Girit. Scattering description of Andreev molecules. *SciPost Physics Core*, 2(2), Feb. 2020.

[249] J.-D. Pillet, P. Joyez, R. Žitko, and M. F. Goffman. Tunneling spectroscopy of a single quantum dot coupled to a superconductor: From Kondo ridge to Andreev bound states. *Phys Rev B*, 88, 2013.

[250] J. D. Pillet, C. H. L. Quay, P. Morfin, C. Bena, A. Levy Yeyati, and P. Joyez. Andreev bound states in supercurrent-carrying carbon nanotubes revealed. *Nat Phys*, 6(12), Nov. 2010.

[251] A. B. Pippard. The historical context of Josephson's discovery. In *Superconductor Applications: SQUIDs and Machines*, pages 1–20. Springer US, 1977.

[252] M. Pita-Vidal, A. Bargerbos, C.-K. Yang, D. J. van Woerkom, W. Pfaff, N. Haider, P. Krogstrup, L. P. Kouwenhoven, G. de Lange, and A. Kou. Gate-tunable field-compatible fluxonium. *Phys. Rev. Applied*, 14(6), Dec. 2020.

[253] S. Plugge, A. Rasmussen, R. Egger, and K. Flensberg. Majorana box qubits. *New J Phys*, 19(1), Jan. 2017.

[254] N. R. Poniatowski. Superconductivity, broken gauge symmetry, and the higgs mechanism. *Am J Phys*, 87(6):436–443, jun 2019.

[255] I. M. Pop, K. Geerlings, G. Catelani, R. J. Schoelkopf, L. I. Glazman, and M. H. Devoret. Coherent Suppression of Electromagnetic Dissipation Due to Superconducting Quasiparticles. *Nature*, 508(7496), Apr. 2014.

[256] E. Prada, P. San-Jose, M. de Moor, A. Geresdi, E. Lee, J. Klinovaja, D. Loss, J. Nygård, R. Aguado, and L. Kouwenhoven. From Andreev to Majorana bound states in hybrid superconductor–semiconductor nanowires. *Nature Reviews Physics*, 2(10), 2020.

[257] J. Preskill. Quantum computing in the NISQ era and beyond. *Quantum*, 2, Aug. 2018.

[258] J. Preskill. The physics of quantum information. *arXiv e-prints*, Aug. 2022.

[259] B. Probst, F. Domínguez, A. Schroer, A. L. Yeyati, and P. Recher. Signatures of nonlocal Cooper-pair transport and of a singlet-triplet transition in the critical current of a double-quantum-dot josephson junction. *Phys Rev B*, 94(15):155445, oct 2016.

[260] A. Proutski, D. Laroche, B. Van 'T Hooft, P. Krogstrup, J. Nygård, L. P. Kouwenhoven, and A. Geresdi. Broadband microwave spectroscopy of semiconductor nanowire-based Cooper-pair transistors. *Phys Rev B*, 99(22), June 2019.

[261] T. A. Puurtinen, K. Rostem, P. J. de Visser, and I. J. Maasilta. A Composite Phononic Crystal Design for Quasiparticle Lifetime Enhancement in Kinetic Inductance Detectors. *J Low Temp Phys*, 199(3), May 2020.

[262] D. Rainis and D. Loss. Majorana qubit decoherence by quasiparticle poisoning. *Phys Rev B*, 85(17), May 2012.

[263] E. I. Rashba and A. L. Efros. Orbital mechanisms of electron-spin manipulation by an electric field. *Phys Rev Lett*, 91(12), Sept. 2003.

[264] R.-P. Riwar and G. Catelani. Efficient quasiparticle traps with low dissipation through gap engineering. *Phys Rev B*, 100(14), Oct. 2019.

[265] R.-P. Riwar, A. Hosseinkhani, L. D. Burkhart, Y. Y. Gao, R. J. Schoelkopf, L. I. Glazman, and G. Catelani. Normal-metal quasiparticle traps for superconducting qubits. *Phys Rev B*, 94(10), Sept. 2016.

[266] M. Rol, F. Battistel, F. Malinowski, C. Bultink, B. Tarasinski, R. Vollmer, N. Haider, N. Muthusubramanian, A. Bruno, B. Terhal, and L. DiCarlo. Fast, high-fidelity conditional-phase gate exploiting leakage interference in weakly anharmonic superconducting qubits. *Phys Rev Lett*, 123(12):120502, sep 2019.

[267] K. Rostem, P. J. de Visser, and E. J. Wollack. Enhanced quasiparticle lifetime in a superconductor by selective blocking of recombination phonons with a phononic crystal. *Phys Rev B*, 98(1), July 2018.

[268] A. Rozhkov and D. Arovas. Interacting-impurity Josephson junction: Variational wave functions and slave-boson mean-field theory. *Phys Rev B*, 62, Sept. 2000.

[269] A. I. Rusinov. Superconductivity near a paramagnetic impurity. *JETP Lett*, 9(2):146, Jan. 1969.

[270] J. E. Saldaña, A. Vekris, G. Steffensen, R. Žitko, P. Krogstrup, J. Paaske, K. Grove-Rasmussen, and J. Nygård. Supercurrent in a double quantum dot. *Phys Rev Lett*, 121(25):257701, dec 2018.

[271] J. C. E. Saldaña, A. Vekris, L. Pavešič, R. Žitko, K. Grove-Rasmussen, and J. Nygård. Two Bogoliubov quasiparticles entangled by a spin. *arXiv e-prints*, Feb. 2022.

[272] N. Samkharadze, A. Bruno, P. Scarlino, G. Zheng, D. P. DiVincenzo, L. DiCarlo, and L. M. K. Vandersypen. High-kinetic-inductance superconducting nanowire resonators for circuit QED in a magnetic field. *Phys. Rev. Applied*, 5, Apr. 2016.

[273] N. Samkharadze, G. Zheng, N. Kalhor, D. Brousse, A. Sammak, U. C. Mendes, A. Blais, G. Scappucci, and L. M. K. Vandersypen. Strong spin-photon coupling in silicon. *Science*, 359(6380), 2018.

[274] K. Satori, H. Shiba, O. Sakai, and Y. Shimizu. Numerical renormalization group study of magnetic impurities in superconductors. *J. Phys. Soc. Jpn.*, 61, 1992.

[275] J. D. Sau and S. D. Sarma. Realizing a robust practical Majorana chain in a quantum-dot-superconductor linear array. *Nat Commun*, 3, July 2012.

[276] J. A. Sauls. Andreev bound states and their signatures. *Philos. Trans. Royal Soc. A*, 376(2125), June 2018.

[277] G. Scappucci, C. Kloeffel, F. A. Zwanenburg, D. Loss, M. Myronov, J.-J. Zhang, S. De Franceschi, G. Katsaros, and M. Veldhorst. The germanium quantum information route. *Nat. Rev. Mater.*, 6(10), Oct. 2021.

[278] P. Scarlino, J. Ungerer, D. van Woerkom, M. Mancini, P. Stano, C. Müller, A. Landig, J. Koski, C. Reichl, W. Wegscheider, T. Ihn, K. Ensslin, and A. Wallraff. In-situ tuning of the electric-dipole strength of a double-dot charge qubit: Charge-noise protection and ultrastrong coupling. *Phys. Rev. X*, 12(3):031004, jul 2022.

[279] S. G. Schellingerhout, E. J. de Jong, M. Gomanko, X. Guan, Y. Jiang, M. S. M. Hoskam, S. Koelling, O. Moutanabbir, M. A. Verheijen, S. M. Frolov, and E. P. A. M. Bakkers. Growth of PbTe nanowires by molecular beam epitaxy. *arXiv e-prints*, Oct. 2021.

[280] G. J. Schinner, H. P. Tranitz, W. Wegscheider, J. P. Kotthaus, and S. Ludwig. Phonon-mediated nonequilibrium interaction between nanoscale devices. *Phys Rev Lett*, 102(18), May 2009.

[281] C. Schrade, C. M. Marcus, and A. Gyenis. Protected hybrid superconducting qubit in an array of gate-tunable josephson interferometers. *PRX Quantum*, 3(030303), June 2022.

[282] J. A. Schreier, A. A. Houck, J. Koch, D. I. Schuster, B. R. Johnson, J. M. Chow, J. M. Gambetta, J. Majer, L. Frunzio, M. H. Devoret, S. M. Girvin, and R. J. Schoelkopf. Suppressing charge noise decoherence in superconducting charge qubits. *Phys Rev B*, May 2008.

[283] M. D. Schroer, K. D. Petersson, M. Jung, and J. R. Petta. Field tuning the g factor in InAs nanowire double quantum dots. *Phys Rev Lett*, 107(17), Oct. 2011.

[284] J. Schulenborg and K. Flensberg. Absence of supercurrent sign reversal in a topological junction with a quantum dot. *Phys Rev B*, 101(1), Jan. 2020.

[285] K. Serniak. *Nonequilibrium Quasiparticles in Superconducting Qubits*. PhD thesis, Yale University, 2019.

[286] K. Serniak, S. Diamond, M. Hays, V. Fatemi, S. Shankar, L. Frunzio, R. J. Schoelkopf, and M. H. Devoret. Direct dispersive monitoring of charge parity in offset-charge-sensitive transmons. *Phys. Rev. Applied*, 12(1), July 2019.

[287] K. Serniak, M. Hays, G. de Lange, S. Diamond, S. Shankar, L. Burkhart, L. Frunzio, M. Houzet, and M. Devoret. Hot nonequilibrium quasiparticles in transmon qubits. *Phys Rev Lett*, 121(15), Oct. 2018.

[288] J. Shabani, M. Kjaergaard, H. J. Suominen, Y. Kim, F. Nichele, K. Pakrouski, T. Stankevic, R. M. Lutchyn, P. Krogstrup, R. Feidenhans'l, S. Kraemer, C. Nayak, M. Troyer, C. M. Marcus, and C. J. Palmstrøm. Two-dimensional epitaxial superconductor-semiconductor heterostructures: A platform for topological superconducting networks. *Phys Rev B*, 93(15), Apr. 2016.

[289] S. Shapiro. Josephson currents in superconducting tunneling: The effect of microwaves and other observations. *Phys Rev Lett*, 11(2):80–82, jul 1963.

[290] S. V. Sharov and A. D. Zaikin. Parity effect and spontaneous currents in superconducting nanorings. *Physica E: Low-dimensional Systems and Nanostructures*, 29(1):360–368, 2005. Frontiers of Quantum.

[291] H. Shiba. Classical Spins in Superconductors. *Prog Theor Phys*, 40(3):435–451, sep 1968.

[292] H. Shiba. A Hartree-Fock theory of transition-metal impurities in a superconductor. *Prog Theor Phys*, 50(5):1776–1776, nov 1973.

[293] Y. M. Shukrinov. Anomalous Josephson effect. *Physics-Uspekhi*, 65(4):317–354, apr 2022.

[294] T. B. Smith, M. C. Cassidy, D. J. Reilly, S. D. Bartlett, and A. L. Grimsmo. Dispersive readout of Majorana qubits. *PRX Quantum*, 1, Nov. 2020.

[295] W. C. Smith, A. Kou, X. Xiao, U. Vool, and M. H. Devoret. Superconducting circuit protected by two-cooper-pair tunneling. *npj Quantum Inf.*, 6(1), Jan. 2020.

[296] E. M. Spanton, M. Deng, S. Vaitiekenas, P. Krogstrup, J. Nygård, C. M. Marcus, and K. A. Moler. Current-phase relations of few-mode InAs nanowire Josephson junctions. *Nat Phys*, 13(12), Aug. 2017.

[297] M. Spethmann, X.-P. Zhang, J. Klinovaja, and D. Loss. Coupled superconducting spin qubits with spin-orbit interaction. *arXiv e-prints*, May 2022.

[298] B. I. Spivak and S. A. Kivelson. Negative local superfluid densities: The difference between dirty superconductors and dirty Bose liquids. *Phys Rev B*, 43, Feb. 1991.

[299] L. J. Splitthoff, A. Bargerbos, L. Grünhaupt, M. Pita-Vidal, J. J. Wesdorp, Y. Liu, A. Kou, C. K. Andersen, and B. van Heck. Gate-tunable kinetic inductance in proximitized nanowires. *arXiv e-prints*, Feb. 2022.

[300] P. Sriram, S. S. Kalantre, K. Gharavi, J. Baugh, and B. Muralidharan. Supercurrent interference in semiconductor nanowire josephson junctions. *Phys Rev B*, 100(15):155431, oct 2019.

[301] J. Stehlik, D. Zajac, D. Underwood, T. Phung, J. Blair, S. Carnevale, D. Klaus, G. Keefe, A. Carniol, M. Kumph, M. Steffen, and O. Dial. Tunable coupling architecture for fixed-frequency transmon superconducting qubits. *Phys Rev Lett*, 127(8), Aug. 2021.

[302] J. P. T. Stenger, B. D. Woods, S. M. Frolov, and T. D. Stanescu. Control and detection of Majorana bound states in quantum dot arrays. *Phys Rev B*, 98, Aug. 2018.

[303] R. Stockill, C. L. Gall, C. Matthiesen, L. Huthmacher, E. Clarke, M. Hugues, and M. Atatüre. Quantum dot spin coherence governed by a strained nuclear environment. *Nat Commun*, 7, Sept. 2016.

[304] E. Strambini, A. Iorio, O. Durante, R. Citro, C. Sanz-Fernández, C. Guarcello, I. V. Tokatly, A. Braggio, M. Rocci, N. Ligato, V. Zannier, L. Sorba, F. S. Bergeret, and F. Giazotto. A Josephson phase battery. *Nat Nanotechnol*, 15(8), June 2020.

[305] S. Strogatz, S. Walker, J. M. Yeomans, C. Tarnita, E. Arcaute, M. D. Domenico, O. Artime, and K.-I. Goh. Fifty years of 'more is different'. *Nature Reviews Physics*, 4(8):508–510, jul 2022.

[306] N. Sundaresan, T. J. Yoder, Y. Kim, M. Li, E. H. Chen, G. Harper, T. Thorbeck, A. W. Cross, A. D. Córcoles, and M. Takita. Matching and maximum likelihood decoding of a multi-round subsystem quantum error correction experiment. *arXiv e-prints*, Mar. 2022.

[307] L. J. Swenson, A. Cruciani, A. Benoit, M. Roesch, C. S. Yung, A. Bideaud, and A. Monfardini. High-speed phonon imaging using frequency-multiplexed kinetic inductance detectors. *Appl Phys Lett*, 96(26), 2010.

[308] D. B. Szombati, S. Nadj-Perge, D. Car, S. R. Plissard, E. P. Bakkers, and L. P. Kouwenhoven. Josephson $\phi 0$-junction in nanowire quantum dots. *Nat Phys*, 12(6), June 2016.

[309] Y. Tanaka, A. Oguri, and A. C. Hewson. Kondo effect in asymmetric Josephson couplings through a quantum dot. *New J Phys*, 9, 2007.

[310] D. Tomaszewski, P. Busz, R. López, R. Žitko, M. Lee, and J. Martinek. Aharonov-Bohm and Aharonov-Casher effects in a double quantum dot Josephson junction. *Phys Rev B*, 98(17):174504, nov 2018.

[311] A. Tosato, V. Levajac, J.-Y. Wang, C. J. Boor, F. Borsoi, M. Botifoll, C. N. Borja, S. Martí-Sánchez, J. Arbiol, A. Sammak, M. Veldhorst, and G. Scappucci. Hard superconducting gap in a high-mobility semiconductor. *arXiv e-prints*, June 2022.

[312] L. Tosi, C. Metzger, M. F. Goffman, C. Urbina, H. Pothier, S. Park, A. L. Yeyati, J. Nygård, and P. Krogstrup. Spin-orbit splitting of Andreev states revealed by microwave spectroscopy. *Phys. Rev. X*, 9(1), Oct. 2018.

[313] W. Uilhoorn, J. G. Kroll, A. Bargerbos, S. D. Nabi, C.-K. Yang, P. Krogstrup, L. P. Kouwenhoven, A. Kou, and G. de Lange. Quasiparticle trapping by orbital effect in a hybrid superconducting-semiconducting circuit. *arXiv e-prints*, May 2021.

[314] T. Vakhtel and B. van Heck. Quantum phase slips in a resonant josephson junction. *arXiv e-prints*, Nov. 2022.

[315] M. Valentini, F. Peñaranda, A. Hofmann, M. Brauns, R. Hauschild, P. Krogstrup, P. San-Jose, E. Prada, R. Aguado, and G. Katsaros. Nontopological zero-bias peaks in full-shell nanowires induced by flux-tunable Andreev states. *Science*, 373, July 2021.

[316] J. A. Van Dam, Y. V. Nazarov, E. P. Bakkers, S. De Franceschi, and L. P. Kouwenhoven. Supercurrent reversal in quantum dots. *Nature*, 442(7103), Aug. 2006.

[317] J. W. G. van den Berg, S. Nadj-Perge, V. S. Pribiag, S. R. Plissard, E. P. A. M. Bakkers, S. M. Frolov, and L. P. Kouwenhoven. Fast spin-orbit qubit in an indium antimonide nanowire. *Phys Rev Lett*, 110(6), Feb. 2013.

[318] J. van Veen, D. de Jong, L. Han, C. Prosko, P. Krogstrup, J. D. Watson, L. P. Kouwenhoven, and W. Pfaff. Revealing charge-tunneling processes between a quantum dot and a superconducting island through gate sensing. *Phys Rev B*, 100(17), Nov. 2019.

[319] D. J. van Woerkom, A. Geresdi, and L. P. Kouwenhoven. One minute parity lifetime of a NbTiN cooper-pair transistor. *Nat Phys*, 11(7), May 2015.

[320] D. J. Van Woerkom, A. Proutski, B. Van Heck, D. Bouman, J. I. Väyrynen, L. I. Glazman, P. Krogstrup, J. Nygård, L. P. Kouwenhoven, and A. Geresdi. Microwave spectroscopy of spinful Andreev bound states in ballistic semiconductor Josephson junctions. *Nat Phys*, 13(9), Sept. 2017.

[321] E. Vecino, A. Martín-Rodero, and L. Yeyati. Josephson current through a correlated quantum level: Andreev states and π junction behavior. *Phys Rev B*, 68(11), July 2003.

[322] A. P. Vepsäläinen, A. H. Karamlou, J. L. Orrell, A. S. Dogra, B. Loer, F. Vasconcelos, D. K. Kim, A. J. Melville, B. M. Niedzielski, J. L. Yoder, S. Gustavsson, J. A. Formaggio, B. A. VanDevender, and W. D. Oliver. Impact of ionizing radiation on superconducting qubit coherence. *Nature*, 584(7822), Aug. 2020.

[323] R. Žitko and T. Pruschke. Energy resolution and discretization artefacts in the numerical renormalization group. *Phys Rev B*, 79, 2009.

[324] A. Wallraff, D. I. Schuster, A. Blais, L. Frunzio, R.-. S. Huang, J. Majer, S. Kumar, S. M. Girvin, and R. J. Schoelkopf. Strong coupling of a single photon to a superconducting qubit using circuit quantum electrodynamics. *Nature*, 431(7005), Sept. 2004.

[325] C. Wang, Y. Y. Gao, I. M. Pop, U. Vool, C. Axline, T. Brecht, R. W. Heeres, L. Frunzio, M. H. Devoret, G. Catelani, L. I. Glazman, and R. J. Schoelkopf. Measurement and control of quasiparticle dynamics in a superconducting qubit. *Nat Commun*, 5(1), Dec. 2014.

[326] G. Wang, T. Dvir, G. P. Mazur, C.-X. Liu, N. van Loo, S. L. D. ten Haaf, A. Bordin, S. Gazibegovic, G. Badawy, E. P. A. M. Bakkers, M. Wimmer, and L. P. Kouwenhoven. Singlet and triplet cooper pair splitting in superconducting-semiconducting hybrid nanowires. *arXiv e-prints*, May 2022.

[327] J. I. Wang, D. Rodan-Legrain, L. Bretheau, D. L. Campbell, B. Kannan, D. Kim, M. Kjaergaard, P. Krantz, G. O. Samach, F. Yan, J. L. Yoder, K. Watanabe, T. Taniguchi, T. P. Orlando, S. Gustavsson, P. Jarillo-Herrero, and W. D. Oliver. Coherent control of a hybrid superconducting circuit made with graphene-based van der Waals heterostructures. *Nat Nanotechnol*, 14(2), Feb. 2019.

[328] P. Welch. The use of fast fourier transform for the estimation of power spectra: A method based on time averaging over short, modified periodograms. *IEEE Transactions on Audio and Electroacoustics*, 15(2), June 1967.

[329] M. Welte, K. Lassemann, and W. Eisenmenger. Emission of high frequency relaxation phonons by superconducting aluminium tunneling junctions. *J. Phys. Colloq.*, 33(C4), Oct. 1972.

[330] J. Wenner, M. Neeley, R. C. Bialczak, M. Lenander, E. Lucero, A. D. O'Connell, D. Sank, H. Wang, M. Weides, A. N. Cleland, and J. M. Martinis. Wirebond crosstalk and cavity modes in large chip mounts for superconducting qubits. *Supercond. Sci. Technol.*, 24(6), Mar. 2011.

[331] J. Wenner, Y. Yin, E. Lucero, R. Barends, Y. Chen, B. Chiaro, J. Kelly, M. Lenander, M. Mariantoni, A. Megrant, C. Neill, P. J. J. O'Malley, D. Sank, A. Vainsencher, H. Wang, T. C. White, A. N. Cleland, and J. M. Martinis. Excitation of superconducting qubits from hot nonequilibrium quasiparticles. *Phys Rev Lett*, 110(15), Apr. 2013.

[332] M. Werninghaus, D. J. Egger, F. Roy, S. Machnes, F. K. Wilhelm, and S. Filipp. Leakage reduction in fast superconducting qubit gates via optimal control. *npj Quantum Inf.*, 7(1), Jan. 2021.

[333] J. Wesdorp, L. Grünhaupt, A. Vaartjes, M. Pita-Vidal, A. Bargerbos, L. J. Splitthoff, B. van Heck, and G. de Lange. Andreev spectroscopy of an InAs junction in a magnetic field. *In preparation*, Feb. 2022.

[334] J. J. Wesdorp, L. Grünhaupt, A. Vaartjes, M. Pita-Vidal, A. Bargerbos, L. J. Splitthoff, P. Krogstrup, B. van Heck, and G. de Lange. Dynamical polarization of the fermion parity in a nanowire Josephson junction. *arXiv e-prints*, Dec. 2021.

[335] A. M. Whiticar, A. Fornieri, A. Banerjee, A. C. C. Drachmann, S. Gronin, G. C. Gardner, T. Lindemann, M. J. Manfra, and C. M. Marcus. Zeeman-driven parity transitions in an Andreev quantum dot. *arXiv e-prints*, Jan. 2021.

[336] E. P. Wigner. The unreasonable effectiveness of mathematics in the natural sciences. *Commun. Pure Appl. Math.*, 13(1):1–14, feb 1960.

[337] C. D. Wilen, S. Abdullah, N. A. Kurinsky, C. Stanford, L. Cardani, G. D'Imperio, C. Tomei, L. Faoro, L. B. Ioffe, C. H. Liu, A. Opremcak, B. G. Christensen, J. L. DuBois, and R. McDermott. Correlated charge noise and relaxation errors in superconducting qubits. *Nature*, 594(7863), June 2021.

[338] K. G. Wilson. The renormalization group: Critical phenomena and the Kondo problem. *Rev Mod Phys*, 47, 1975.

[339] G. W. Winkler, A. E. Antipov, B. van Heck, A. A. Soluyanov, L. I. Glazman, M. Wimmer, and R. M. Lutchyn. Unified numerical approach to topological semiconductor-superconductor heterostructures. *Phys Rev Lett*, 99(24), June 2019.

[340] G. W. Winkler, D. Varjas, R. Skolasinski, A. A. Soluyanov, M. Troyer, and M. Wimmer. Orbital contributions to the electron g factor in semiconductor nanowires. *Phys Rev Lett*, 119(3), July 2017.

[341] F. Yan, P. Krantz, Y. Sung, M. Kjaergaard, D. L. Campbell, T. P. Orlando, S. Gustavsson, and W. D. Oliver. Tunable coupling scheme for implementing high-fidelity two-qubit gates. *Phys. Rev. Applied*, 10(5), Nov. 2018.

[342] T. Yokoyama, M. Eto, and Y. V. Nazarov. Anomalous josephson effect induced by spin-orbit interaction and zeeman effect in semiconductor nanowires. *Phys. Rev. B*, 89:195407, May 2014.

[343] T. Yoshioka and Y. Ohashi. Numerical renormalization group studies on single impurity Anderson model in superconductivity: a unified treatment of magnetic, nonmagnetic impurities, and resonance scattering. *J. Phys. Soc. Jpn.*, 69, 2000.

[344] L. Yu. Bound state in superconductors with paramagnetic impurities. *Acta Phys Sin-ch Ed*, 21(1):75, 1965.

[345] A. D. Zaikin and L. S. Kuzmin. Strong tunneling and coulomb blockade in a single-electron transistor. *Phys Rev B*, 59(16), Apr. 1999.

[346] P. Zalom, V. Pokorný, and T. c. v. Novotný. Spectral and transport properties of a half-filled Anderson impurity coupled to phase-biased superconducting and metallic leads. *Phys Rev B*, 103, Jan. 2021.

[347] A. Zazunov, R. Egger, T. Jonckheere, and T. Martin. Anomalous Josephson current through a spin-orbit coupled quantum dot. *Phys Rev Lett*, 103, Oct. 2009.

[348] A. Zazunov, V. S. Shumeiko, E. N. Bratus', J. Lantz, and G. Wendin. Andreev Level Qubit. *Phys Rev Lett*, 90(8), Feb. 2003.

[349] R. Žitko. NRG Ljubljana, May 2021.

[350] R. Žitko. Josephson potentials for single impurity Anderson impurity in a junction between two superconductors, Jan. 2022.

[351] R. Žitko and M. Fabrizio. Non-Fermi-liquid behavior in quantum impurity models with superconducting channels. *Phys Rev B*, 95, Feb. 2017.

[352] R. Žitko and L. Pavešić. Yu-Shiba-Rusinov states, the BCS-BEC crossover, and the exact solution in the flat-band limit. *arXiv e-prints*, Apr. 2022.

[353] N. Zobrist, W. H. Clay, G. Coiffard, M. Daal, N. Swimmer, P. Day, and B. A. Mazin. Membraneless phonon trapping and resolution enhancement in optical microwave kinetic inductance detectors. *Phys Rev Lett*, 129(1), July 2022.

[354] H. Zu, W. Dai, and A. de Waele. Development of dilution refrigerators—a review. *Cryogenics*, 121, Jan. 2022.

[355] K. Zuo, V. Mourik, D. B. Szombati, B. Nijholt, D. J. van Woerkom, A. Geresdi, J. Chen, V. P. Ostroukh, A. R. Akhmerov, S. R. Plissard, D. Car, E. P. Bakkers, D. I. Pikulin, L. P. Kouwenhoven, and S. M. Frolov. Supercurrent interference in few-mode nanowire Josephson junctions. *Phys Rev Lett*, 119(18), Nov. 2017.

[356] A. M. J. Zwerver, T. Krähenmann, T. F. Watson, L. Lampert, H. C. George, R. Pillarisetty, S. A. Bojarski, P. Amin, S. V. Amitonov, J. M. Boter, R. Caudillo, D. Correas-Serrano, J. P. Dehollain, G. Droulers, E. M. Henry, R. Kotlyar, M. Lodari, F. Lüthi, D. J. Michalak, B. K. Mueller, S. Neyens, J. Roberts, N. Samkharadze, G. Zheng, O. K. Zietz, G. Scappucci, M. Veldhorst, L. M. K. Vandersypen, and J. S. Clarke. Qubits made by advanced semiconductor manufacturing. *Nature Electronics*, 5(3), Mar. 2022.

ACKNOWLEDGEMENTS

The chapters presented in this dissertation are the culmination of several years of work. Work both inside and outside of the lab, both one-on-one and in large collaborations, and both on physics and on myself. I am deeply grateful to all of those who have contributed; my colleagues, both former and present, my friends, new and old, and my family and loved ones, always present. It is through your passion, support, and encouragement that I was able to grow as a scientist and as a person. Thank you all for having made my PhD journey an unforgettable experience.

In what follows, I hope you will indulge me as I take you on a brief tour of how I ended up pursuing my PhD in the first place. I will then reminisce about those of you I have met in and around the lab, and finally turn to those who have been there for me outside of work. To start with, I turn to **Leo**. Your role in my PhD will seem obvious to most, in offering me the opportunity to be part of your fantastic team and laboratory. While the last years might have been tumultuous, there has not been a day during which I was not happy and proud to be taking part in your research. It has been an experience I will forever cherish. But not everyone will know that your role in this PhD started much earlier; in fact, there were many moments in life where you sparked my curiosity for experimental physics. The first of such moments I recall is in 2007, when I was 14 years old, and you received your Spinoza prize. During your acceptance speech you told me (and the audience) that you could make electrons colder than the vacuum of outer space, trap them in tiny boxes on demand, and make them traverse both sides of a ring at the same time. This came at a time when all I associated with physics was the friction of sleds, and trick questions about resistors placed in various parallel configurations. I vividly remember realizing that there was much more to physics.

What followed was a quest to get a glimpse into what this “more” entailed, in which **Wolfgang** played an important role. Then a PhD candidate, you were kind enough to spend several afternoons with a high school student who wanted to write a report on (all of) quantum physics. In a room with blacked-out windows, laser beams, and incomprehensible CHSH statistics, you took me on my first journey into the non-classical world. I recently looked up our email conversations from 2010, which included my report. It is safe to say your assessment was kind! I’m very thankful for this experience; it offered me an early glimpse into the scientific world, a luxury not given to most.

What came next was a bachelor’s degree at the Amsterdam University College, with a major in physics and mathematics. While this introduced me to various interesting topics, the most memorable of which were taught by **Forrest**, the majority of this time was spent in the world of theory. My first up-close encounter with experimental physics came in 2014, when **Ronald** was kind enough to offer me a bachelor student project in his research group. Here **Machiel** took me into the lab, where he showed me diamonds, lasers, quantum jumps and single photon detectors. I would like to say thank you to both of you, especially now that I realize bachelor students are often more of a burden than a benefit! It was a pivotal experience for me, and ultimately where I decided that I wanted to work on experimental quantum physics.

I then moved to ETH Zurich for a master's in physics. Given the goal I had set out for myself, I sent emails to the professors I could identify online as working on quantum. **Andreas**, you replied and even took time out of your extremely busy schedule. As a newly arrived student, you showed me around the campus and the lab, and gave guidance on what courses to pick. It was perhaps not a coincidence that we met again during your Quantum Systems for Information Technology course, where we spoke about potential research projects in your group. In the year that followed, you paired me up with **Michele** and **Anton**, which was a fantastic experience. Thank you for having me in your lab. **Michele**, you were forever patient and kind, showing me what was basic for you and novel for me, from dipstick measurements to VNA calibrations. It was a perfect introduction to the lab. **Anton**, you quite literally took me to the next level. First of all, you inspired me to be daring as a researcher. You carved out a piece of your own in a prestigious and competitive lab, and boldly pursued a perhaps atypical but fascinating topic, to great success. What is more, you let me, a new-to-the-show master student, feel like an integral part of top level research. You let me design, tinker, measure, analyze and write alongside you. You let me see what an experimental physics PhD would be like, and that that is what I wanted to do. I'm very grateful for this experience.

Armed with this newfound conviction, I took a brief but memorable trip. Firstly it was a trip into the theory and numerics of Majorana physics, and secondly a trip to Microsoft Station Q in Santa Barbara. **Kevin**, in preparation for this you patiently let me play around with COMSOL and kwant, teaching me my first things about semiconductors, quantum dots, charging energies and Fermi level pinning. I enjoyed all of our exchanges, from talking about expensive watches to tedious meshing. It is your preparation that allowed me to make something of my internship with **Roman** and **Andrey**. Both highly distinguished researchers working at the frontiers of knowledge, you let a novice like myself into your world with open arms. You gave me an intriguing project to work on, a fascinating paper to participate in, and you even let me join your 9PM wine and physics meetings. **Andrey**, you additionally took me to Rattlesnake canyon, to metal concerts in LA, and even to your wedding in Moscow, which was an event I will forever cherish. I thank you both for three fantastic months.

It was during this times that **Leo** and I spoke about pursuing a PhD in Delft. What sparked my interested in particular was that several senior scientists were about to join the research effort, soon to arrive fresh from Yale. With intimate knowledge about circuit QED, they would take the Majorana research into the microwave domain, and I wanted to be a part of that. It is in this way that I met **Wolfgang** once again, as well as meeting my soon-to-be supervisors **Gijs** and **Angela** for the first time. **Gijs**, you took me under your wing for the first year, teaching me that Josephson junctions are not just about wavefunction overlap but about Andreev bound states, giving me the pragmatic but highly effective coding skills an experimental physicist must have, and showing me how to recognize that a cold trap is starting to block ahead of time. I'm very thankful for the months in which I got to work beside you at the measurement station, and for all our exchanges that followed since. You taught me many important skills, both technical and personal. I hope to keep hearing about the great results coming out of your team in Delft, and to see you at the next high school reunion! **Angela**, early on in my PhD you took over from Gijs, after which you created what was (for me) the core of our cQED team. While I have had the pleasure of learning from many during my PhD, I think you are the one that taught me the most. While doing so you were always patient, good-humored and kind, even if disaster struck and a load-lock was left open. I think it is in this way that a multi-year search for signatures that were never found became a fun and successful learning experience. I'm happy I got the chance to learn from you, and grateful to have you on my defense committee. I wish you and Wolfgang all the best in your beautiful wood-finished labs, and in your blue house. Oh, and I promise to always cut off the tails of cable-ties! **Bernard**, I first got to know you and **Monica** during my stay in Santa Barbara. You invited me into your home to watch the seasons finale of Game of Thrones, and while in hindsight this evening signaled the end of a good show, meeting you both was the start of good times to come. I have been lucky enough to learn from you during the start of my PhD, when your manuals and notebooks about Majorana transmon and fluxonium qubits formed the foundation of my theoretical understanding. You then took over supervision from Angela when I was mid-way through. This was a difficult time for all of the cQED team, and I imagine also for you, as you had enough on your plate already. Nevertheless, you helped us through this phase with much support, both in terms of encouragements and endless theoretical insights. I know you sometimes say that I did not need much help, but if we were to append the questions I wrote to you during that time to this thesis, it would be much longer still (I have been told it is already quite long). I wish you and your family all the best in Rome, and I hope we meet again soon. **Christian**, you joined at the end of my PhD and got what might have seemed like the dubious pleasure of taking over from Bernard. Starting up your own team while also taking on a group of semi-grown doctoral candidates in the middle of projects and several manuscripts, that is no easy feat. In truth, I was a little afraid we would wear out your patience, given you had so much more to take care of and so many ideas of your own to pursue. But the opposite has been true. You quickly adapted to the role, answered our many and varied questions at any moment, and helped us push our teams' abilities to the max. In the time we spent together you taught me a lot, and I am sure I would have learned even more had I been around for longer. I want to thank you for all your effort, and for being my copromotor. I wish you and your protected qubits team long life and coherence times! **Michael**, we first met when I was working on kwant simulations with Kevin. I remember how I anxiously showed you my code, sure to be a disappointment. Instead, I was met with great words of encouragement; it was not bad at all, compared to what you often had to deal with in your mailing list! Thank you for all your help and your guidance; as head of QuRe, as teacher to provide assistance to, and finally as my promotor.

Next I would like to turn to my colleagues that I worked with the most, those in our self-named cQED team. **James**, the first word you spoke to me was nepotism, and I immediately knew that we were off to a good start. While we did not get to do much lab work, I have many good and obscure memories of our times together. From ginger ales to Scooby snacks, and from ducks being free to Giovanni Giorgio, we have had many meaningful exchanges. I hope to see you and **Deniz** soon, and to have many more memorable days and nights. **Willemijn**, while perhaps I was not yours, you were my original parter-in-PhD. You taught me how to do (some) fab and (many) measurements, and while doing so you shared with me your defining optimism and positive attitude. Together we sat through infinite charge dispersions and endless Risk games, while we drank excessively strong ginger teas and awful Sarsaparillas. I hope you keep enjoying life as fully as I have often seen you do, and that soon we will meet again! **Marta**, with whom I coauthored most of these 200+ pages. I remember well when you first arrived in the lab and joined Angela, Willemijn and me. As a student you were clever, determined, hard working, and seemingly in possession of Hermione's time-turner necklace; within a year you essentially put together a complete paper, all by yourself. Yet despite your unquestionable solo success, I managed to convince you that working together would be much more fun (and much more productive)! I am happy that I managed. We spent a lot of time together behind the measurement computer, a lot of time behind our paper writing machines, and by now also a lot of time giving back-to-back talks. All the while having many Teams' chats about work, and many WhatsApp chats about not-work. I will cherish these times, for even though I did not always show it as clearly as you would have liked, I thoroughly enjoyed them all. Thank you for being my paranymph, and I am sure I will see you and **Hugo** soon. Ideally for tamales! **Lukas G**, the postdoc of our team. You came to us at what would soon turn out to be a challenging time. Looking to do a *super-PhD* in an exciting new topic, your job also quickly became one of senior management and supervision, which you executed fantastically. You introduced us to team retro's and to postdoc appreciation days, to the horror of cosmic rays and to the measurements of contact resistance. In exchange we introduced you to a Slack channel without threads, to fridges full of pulse tube noise, to social distancing behind the measurement pc, and to long food truck lines. Despite all that, we all had a ton of fun together, and managed to do good research. I sleep peacefully knowing that the German metrology institute is in good hands, and that Veldhoven is now finally safe. **Lukas S**, or our young Lukas. Without you and your steady hands, not a single device past chapter 4 would have been made. This thesis is essentially built on the many hours you spent in the basement of the TU Delft, for which I am deeply thankful. But I get to be thankful for much more than your wire deposition skills. While working together, you have shared with me a deep passion for physics, have shown what it means to be highly resilient to (many) setback, and demonstrated that if someone really wants to, they can go virtually anywhere (by bike). It was great to spend time together, in and outside of the lab, eating dried fruits and drinking bourbon. I wish you much gain and topology in the phases that lies ahead of you! **Jaap**, I come to you last as you were, in a sense, the final member of the cQED team. Indeed, it took us a while to convince you to leave behind your selective area friends, but I am happy that we managed. In our years together you were the resident Andreev bound state expert, and your work helped pave the way for many of the experiments presented here. But luckily we also got to spend time outside of work, as in retrospect that meant good times were guaranteed. Whether it was car bombs in Chicago, horse racing in Belgium, or improvised empanadas in Rotterdam, I have a lot of great moments to look back on. Best of luck in what lies ahead, I am sure you and **Ilse** will do great no matter where you go!

These were the colleagues I directly worked with. But there were many more that contributed to my stay, and many more that made it fun. **Damaz**, first my spatial (but not temporal) companion in Santa Barbara, then in the lab, and now in the house of quantum. You taught me about the frustration of Alazar cards, about the nuances of gate-based readout, about the fantastic investment opportunities in emerging virtual currencies, and about the dangers ESD. You have been a great colleague and a great friend. Now that I am done, I hope that the four of us can get together sometime to have a peaceful dinner at your new place! **Alex**, you set a great example on how the measurement floor was the ideal workspace, as I too spent virtually all my time there. During my PhD we often spoke about the intricacies of Cooper pair boxes, about our favorite sci-fi books and authors, and about the latest in football (even though there is one specific night we do not mention). I'm happy that since then we have been able to continue this over the occasional bowl of ramen, because we still have a lot to talk about. Let's make sure that it is said! **Christian M**, one of the several colleagues I had the pleasure of going on a fantastic roadtrip with. I am happy that we did, and that we occasionally got the chance to crank up the voltage a little further than supposed to! Keep doing what can be done, even if it isn't always pretty. **Michiel**, who gave me my spot on my first experimental Majorana paper, and who paved the way for me checking the arXiv on a daily basis. Thanks for all the stimulating talks, and for never saying no to another beer. **Jouri**, thanks for getting lost with me, and being an integral part of an unforgettable snowball fight. **Daniël**, thank you for bringing Tim and Eric into my life. For this me and my friends are forever grateful. **Srijit**, thank you for showing me that senior scientists can also have fun! **Fokko**, thank you for telling me to take charge of my PhD; this was sage advice! And **Guan**, thank you for being there from start to finish, I look forward to our joint celebration! I also want to thank every other member that made topo great. **Di, Francesco, Jasper, Christian P, Lin, Vukan, Nick, Alberto, David, Jiyin, Greg, Filip, Ivan, Ting, Prasanna, Qing, Tom, Jie, Michael, Sebastian, John, Jonne, Cristina, Dominique, Kongyi, Alexandra, Avradeep, Nikolai**, thank you for all of our discussions, questions, interactions and explanations. I think we made a pretty good team!

I would also like to thank our excellent permanent staff, without whom the institute wouldn't be nearly as great. **Olaf**, I thoroughly enjoyed designing our light-tight boxes, and all the talks we had about fridges and about life in general. **Jason**, you were always ready to patiently help reverse engineer what it was I actually needed help with. **Nico**, you made an endless stream of masterfully machined copper. **Raymond**, you were ever-friendly and ever-knowledgeable, and taught me much about interference. **Matt**, you were kind enough to convey some of your record-breaking cryogenic knowledge, and made me appreciate the nuances of infrared filtering. **Csilla**, you were always ready to help and to figure out a solution that was best for the PhDs, as challenging as that might have been. **Lydia**, you would often be at the other end of the conversation, but despite that you were always kind and understanding, and tried to make things work out as best as you could. And finally **Jenny**, you offered me great support from day one, while never getting tired of answering the same questions you had been asked many times before. Thank you!

In the context of my physics journey I would also like to acknowledge in particular three groups of friends, in the order in which I met them. **Wouter**, **Mats**, **Timo**, **Pelle**, **Jasper**, oftewel mijn middelbare school vrienden, dat zullen jullie beamen. Confetti-sur-la-mer, zeven dagen lang tennis, jackfruit al pastor, een gorgelend wederzien met

Oosterheem, en champignons enorm fijn snijden. Een kleine greep uit wat jullie gedaan hebben om mij door zware tijden heen te helpen, bijvoorbeeld als er problemen waren met helium-drie, of als het water kapot bleek. Bedankt voor jullie jaren van vriendschap en steun. En gras. **Pietro**, **Danu**, **Ward**, **Tycho**, **John**. During our bachelor degree we found each other in being perplexed by the complexity of the three dimensional world. While we have since then made use of these dimensions to go our separate ways, I am happy that we have recently found the chance to meet up again. I thank you for making our (sometimes lacking) physics degree into a complete experience, and also for trusting me with your IOTA. **Daniele**, **Federico**, **Johannes**, **Leo**, **Thanos**. My friends from Italy, Germany, and Greece, who made studying at the daunting institution of ETH a breeze. From the basement at the Bulachstrasse to Malaga, and from neon painted t-shirts to glamorous weddings, the times we spent together were fantastic. COVID has not done us many favors, but I am not worried. I am sure that soon the next one of you will be united in Holy Matrimony, and that we will see each other again.

Ik wil ook graag mijn familie bedanken. Bedankt voor jullie eindeloze interesse, voor het altijd willen weten hoe het gaat, wat ik gedaan heb, hoe dat was, en wat ik nu dan wil gaan doen. **Opa**, ik durf te stellen dat niemand een groot-vader heeft die zoveel over zijn proefschrift wil weten, en die het vervolgens ook nog begrijpt. De foutjes die her en der in het proefschrift staan zijn uiteraard met opzet gemaakt, en zijn voor jou en je radiovrienden om te ontdekken! **Oma**, mijn hele leven al de fijnste oma die er is, daar kan geen twijfel over bestaan. Maar ook nog degene die mij tijdens mijn PhD nog leerde dat het niet arsenide is maar arsenicum, en niet antimonide maar antimoon. Bedankt voor alle jaren heerlijke kip (altijd een 10), en voor het uitstekende oma-zijn! Mijn ouders en zusje, **Wim**, **Ineke**, en **Kiki**. Volgens mij kan niemand zich een fijner thuis wensen. Jullie hebben mij bijgestaan van Papendal tot in Zürich, mij voorgedaan hoe je (met overtuiging!) je proefschrift verdedigt, en mij eindeloos (zingend) gezelschap gehouden terwijl ik op de achterbank zat. Bedankt voor alle steun en het vertrouwen, en voor het mogelijk maken van. Dankzij jullie ben ik waar ik ben.

Als laatste, mijn lieve vriendin **Maureen**. Al zes geweldige jaren samen, en dus ook mijn gehele PhD. Bedankt voor je luisterend oor, al je hulp, al je steun, en al je liefde. In goede en slechte tijden, je bent er altijd. Ik kijk uit naar alle mooie dingen die de toekomst ons samen gaat brengen!

Arno

Curriculum Vitæ

Arno Bargerbos

28-11-1993	Born in Zoetermeer, The Netherlands
2005–2011	Pre-university secondary education (VWO) Erasmus College, Zoetermeer, the Netherlands
2011–2014	Bachelor of Science Amsterdam University College (AUC), the Netherlands *Thesis:* Real-time monitoring of nuclear spin quantum jumps in a nitrogen vacancy center *Supervisors:* Dr. F. Bradbury, Dr. M. Blok, and Prof. dr. R. Hanson
2014–2016	Master of Science in Physics Swiss Federal Institute of Technology in Zürich (ETH), Switzerland *Thesis:* Analog quantum simulation of noise assisted transport in light harvesting structures with superconducting circuits *Supervisors:* Dr. A. Potočnik and Prof. dr. A. Wallraff
JUN - AUG 2017	Research internship Microsoft Station Q, Santa Barbara, United States of America *Topic:* Modeling superconductor-semiconductor heterostructures in the presence of gate-induced electric fields *Supervisors:* Dr. A. Antipov and Dr. R.M. Lutchyn
2017–2022	PhD in Physics Delft University of Technology, Delft, the Netherlands *Thesis:* Nanowire Josephson junctions in superconducting circuits *Supervisors:* Dr. G. de Lange, Prof. dr. A. Kou, Dr. B. van Heck, Dr. C.K. Andersen and Prof. dr. L.P. Kouwenhoven

LIST OF PUBLICATIONS

14. **A. Bargerbos**, L.J. Splitthoff, M. Pita-Vidal, J.J. Wesdorp, Y. Liu, P. Krogstrup, L.P. Kouwenhoven, C.K. Andersen, and , L. Grünhaupt, Mitigation of quasiparticle loss in superconducting qubits by phonon scattering, Physical Review Applied **19**, 024014 (2023).

13. L. Pavešić, M. Pita-Vidal, **A. Bargerbos**, and R. Žitko, Impurity Knight shift in quantum dot Josephson junctions, arXiv:2212.07185 (2022).

12. M. Pita-Vidal*, **A. Bargerbos***, R. Žitko, L.J. Splitthoff, L. Grünhaupt, J.J. Wesdorp, Y. Liu, L.P. Kouwenhoven, R. Aguado, B. van Heck, A. Kou, and C.K. Andersen, Direct manipulation of a superconducting spin qubit strongly coupled to a transmon qubit, arXiv:2208.10094 (2022).

11. **A. Bargerbos***, M. Pita-Vidal*, R. Žitko, L.J. Splitthoff, L. Grünhaupt, J.J. Wesdorp, Y. Liu, L.P. Kouwenhoven, R. Aguado, C.K. Andersen, A. Kou, and B. van Heck, Spectroscopy of spin-split Andreev levels in a quantum dot with superconducting leads, arXiv:2208.09314 (2022).

10. J.J. Wesdorp, F.J. Matute-Canadas, A. Vaartjes, L. Grünhaupt, T. Laeven, S. Roelofs, L.J. Splitthoff, M. Pita-Vidal, **A. Bargerbos**, D.J. van Woerkom, P. Krogstrup, L.P. Kouwenhoven, C.K. Andersen, A. Levy Yeyati, B. van Heck, G. de Lange, Microwave spectroscopy of interacting Andreev spins, arXiv:2208.11198 (2022).

9. **A. Bargerbos***, M. Pita-Vidal*, R. Žitko, J. Ávila, L.J. Splitthoff, L. Grünhaupt, J.J. Wesdorp, C.K. Andersen, Y. Liu, P. Krogstrup, L.P. Kouwenhoven, R. Aguado, A. Kou, and B. van Heck, Singlet-doublet transitions of a quantum dot Josephson junction revealed in a transmon circuit, PRX Quantum **3**, 030311 (2022).

8. L.J. Splitthoff, **A. Bargerbos**, L. Grünhaupt, M. Pita-Vidal, J.J. Wesdorp, Y. Liu, A. Kou, C.K. Andersen, B. van Heck, Gate-tunable kinetic inductance in proximitized nanowires, Physical Review Applied **18**, 024074 (2022).

7. J.J. Wesdorp, L. Grünhaupt, A. Vaartjes, M. Pita-Vidal, **A. Bargerbos**, L.J. Splitthoff, P. Krogstrup, B. van Heck, and G. de Lange, Dynamical polarization of the fermion parity in a nanowire Josephson junction, arXiv:2112.01936 (2021).

6. W. Uilhoorn, J.G. Kroll, **A. Bargerbos**, S.D. Nabi, C.K. Yang, P. Krogstrup, L.P. Kouwenhoven, A. Kou, and G. de Lange, Quasiparticle trapping by orbital effect in a hybrid superconducting-semiconducting circuit, arXiv:2105.11038 (2021).

5. **A. Bargerbos**, W. Uilhoorn, C.K. Yang, P. Krogstrup, L.P. Kouwenhoven, G. de Lange, B. van Heck, and A. Kou, Observation of Vanishing Charge Dispersion of a Nearly Open Superconducting Island, Physical Review Letters **124**, 246802 (2020).

4. M. Pita-Vidal, **A. Bargerbos**, C.K. Yang, D.J. van Woerkom, W. Pfaff, N. Haider, P. Krogstrup, L.P. Kouwenhoven, G. de Lange, and A. Kou, Gate-Tunable Field-Compatible Fluxonium, Physical Review Applied **14**, 064038 (2020).

3. M.W.A. de Moor*, J.D.S. Bommer*, D. Xu*, G.W. Winker, A.E. Antipov, **A. Bargerbos**, G. Wang, N. van Loo, R.L.M. Op het Veld, S. Gazibegovic, D. Car, J.A. Logan, M. Pendharkar, J.S. Lee, E.P.A.M. Bakkers, C.J. Palmstrøm, R.M. Lutchyn, L.P. Kouwenhoven, and H. Zhang, Electric field tunable superconductor-semiconductor coupling in Majorana nanowires, New Journal of Physics **20** 103049 (2018).

2. A.E. Antipov, **A. Bargerbos**, G.W. Winkler, B. Bauer, E. Rossi, and R. Lutchyn, Effects of Gate-Induced Electric Fields on Semiconductor Majorana Nanowires, Physical Review X **8**, 031041 (2018).

1. A. Potočnik*, **A. Bargerbos***, F.A.Y.N. Schröder, S.A. Khan, M.C. Collodo, S. Gasparinetti, Y. Salathé, C. Creatore, C. Eichler, H.E. Türeci, A.W. Chin and A. Wallraff, Studying light-harvesting models with superconducting circuits, Nature Communications **9**, 904 (2018).

---

* These authors contributed equally to this work.